DESIGN & FABRICATION OF NANOSTRUCTURED HYDROGELS FROM BIOPOLYMER NANOPARTICLE BUILDING BLOCKS FOR BIOMEDICAL AND ENVIRONMENTAL APPLICATIONS

DESIGN & FABRICATION OF NANOSTRUCTURED HYDROGELS FROM BIOPOLYMER NANOPARTICLE BUILDING BLOCKS FOR BIOMEDICAL AND ENVIRONMENTAL APPLICATIONS

BY: MICHAEL MAJCHER, B.Sc
A Thesis Submitted to the School of Graduate Studies in Partial Fulfillment of the Requirements for the Degree Ph.D. of Chemical Engineering

McMaster University Ph.D. OF ENGINEERING (2021) Hamilton, Ontario (Chemical Engineering)
TITLE: DESIGN & FABRICATION OF NANOSTRUCTURED HYDROGELS FROM BIOPOLYMER NANOPARTICLE BUILDING BLOCKS FOR BIOMEDICAL AND ENVIRONMENTAL APPLICATIONS
AUTHOR: Michael Joseph Majcher (McMaster University)
SUPERVISOR: Professor Todd R. Hoare
INTERNAL COMMITTEE MEMBERS: Professor Michael A Brook and Professor Heather Sheardown
NUMBER OF PAGES: 239 (single spaced)
NUMBER OF WORDS: 71,926 (including bibliography)
NUMBER OF REFERENCES: 520

Lay Abstract

This thesis describes the chemical and physical modification of commercially-available starch nanoparticles (SNPs) to rationally create novel hydrogel systems. These gel-like networks are made by chemically connecting starch nanoparticles (with sizes on the 10^{-8} m length scale) by introducing various reactive chemical groups onto the surface of SNPs, enabling the creation of hydrogels with well-defined structures, features, and properties. Careful selection of the crosslinking chemistry made it possible to tune hydrogel properties to specific application requirements, such as the targeted delivery of pharmaceuticals (including the intranasal delivery of antipsychotic drugs to the brain, a key technical challenge to improve the quality of life of patients with mental health challenges) and agrochemical agents or as an anti-fouling coating. The hydrogels created herein are attractive since they directly incorporate nanoscale particles generated from a sustainable source and are generally regarded as safe (GRAS) in terms of their degradation products once they break down, a rare trait for nanoparticles of this size. The existing industrial-scale production of the SNPs also enables facile scaling of these strategies for ultimate commercial translation.

Abstract

In recent years, there has been a growing interest within the field of soft materials engineering on the development of advanced hydrogel systems with well-defined chemistries and morphologies that can be customized to suit various applications ranging from biomedical to environmental to personal care. In any case, careful selection of the building block materials, crosslinking chemistry, degradation pathway, and overall hydrogel architecture is essential to ensure the final design (and the resulting degradation components if relevant) are safe/non-toxic, mechanically tunable, and overall translatable for their intended end use given industry safety/production standards.

In this thesis, the utility of starch nanoparticles created by a reactive extrusion process was explored as one such building block for creating renewable hydrogels. Starch was reactively extruded by *EcoSynthetix Inc.* to create starch nanoparticles (SNPs) that are attractive as hydrogel building blocks due to their inherent small size (25-50 nm), generally safe degradation products, overall net neutral charge, high deformability/viscoelastic properties, stability in solution without collapsing or changing size (on the order of months), and the ability to be manufactured at a multiple kg/hr rate; in comparison, other manufacturing methods of SNPs suffer from a lack of scalability or require the use of potentially toxic solvents, making them less amenable to biological or environmental/agricultural applications. The amorphous nature of the starch also allows for facile functionalization to further chemically modify and/or crosslink the SNPs through surface functional group (i.e. hydroxyl) modification chemistries.

The nanoparticle nature of the SNP building block, coupled with the facile functionalizability of the SNPs, also makes SNPs ideal building blocks for the design and fabrication of nanoparticle network hydrogels (NNHs) in which NPs create an interconnected network on their own on, in addition to, other polymeric networks at any desired length scale. There are a variety of NNH architectures that can be achieved through careful design considerations. More specifically, herein colloidal NNHs were created using UV photopolymerization post-functionalization with methacrylic anhydride, which leaves a vinyl group on the SNP surface. Alternately, plum pudding NNHs were created by mixing aldehyde-functionalized SNPs with amine-bearing O-carboxymethyl chitosan that were able to chemically react via hydrolytically labile imine bonds.

The properties of various types of colloidal and plum-pudding hydrogels based on SNPs were tested and subsequently compared through a range of different performance tests such as rheological and micromechanical force testing, swelling/degradation kinetics, their potential for controlled bioactive release, and overall toxicity (cell and organ level). In addition to these macroscopic performance tests, the internal morphologies of both colloidal and plum pudding NNHs were assessed with small angle and very small angle neutron scattering experiments to glean insight into how these internal structures correlate to macroscopic properties. For all experiments, the effect of using SNPs versus typical cold water-soluble branched starch (SS) was assessed to further understand the impact of

making hydrogels from nanoscale rather than soluble polymer building blocks, with the small size of SNPs compared to the large hydrodynamic radius of SS consistently allowing for greater control over the range of potential hydrogel properties.

The results of these studies suggest that SNP-based NNHs are promising materials for studying the encapsulation and release of small molecules in both *in vitro* and *in vivo* settings. For example, the photopolymerization of methacrylated SNP-based NNH coatings can be fabricated at much higher concentrations than possible with conventional starch (35% for SNP, 10% for SS), leading to denser and stiffer gels compared to SS controls albeit with slightly longer gelation times due to the reduced conformational mobility of the polymerizable methacrylate groups on the SNPs. The addition of charge (cationic or anionic) to the SNP surface further increases the bulk gelation time while significantly reducing the observed changes in SNP deformation during photogelation as confirmed via very small angle neutron scattering experiments. Other functional groups were also demonstrated to be introduced to SNPs to enable different types of gelation for different applications. For example, in situ-gelling and degradable bulk nanoparticle network hydrogels consisting of oxidized starch nanoparticles (SNPs) and carboxymethyl chitosan (CMCh) were created for intranasal delivery that could be delivered into the nose via a commercial atomization device to enable high nasal mucosal retention and functional controlled release of the peptide drug PAOPA, a positive allosteric modulator of dopamine D2 receptor. Selected gels shown to alleviate negative behavioural abnormalities associated with for up to 72 hours in pre-clinical rat models of schizophrenia at a low drug dosage (0.5 mg/kg), compared to just a few hours with the drug alone. Finally, the functionalization of SNPs with hydrophobic groups (via grafting the starch with octenyl succinic acid (OSAn) or succinic anhydride (SAn)) was demonstrated as a promising delivery system for agricultural applications. Hydrophobization increased the contact angle of a sprayed watermelon and pumpkin leaves from <60˚ (unmodified) to ~80˚ when modified (DS 0.25), while confocal fluorescence microscopy confirmed that the hydrophobized SNPs can both adhere to the leaf surface as well as penetrate into the leaves when sprayed due to their small size (25-50 nm).

Future work will look at other methods of crosslinking SNPs (i.e. Michael addition, hydrazone, and alkyne-azide “click” chemistry, amongst others) to see if there are beneficial differences compared to analogous hydrogels made from macroscopic alternatives (i.e. polymers alone) and to follow-up the findings already gleaned within this thesis. Further information on the impact and potential follow-up experiments for the work conducted in this thesis will be explained in Chapter 6 on final outlooks and conclusions of the following work.

Acknowledgements

I would like to thank Dr. Hoare and Dr. Niels Smeets in particular for being supervisors of my research and for agreeing to sign me onto this project in 2015. I would also like to thank Professor Sheardown and Professor Brook for being excellent members of my thesis committee and for their guidance on key technical issues such as project flow planning, publishing, and presentation.

I would like to thank the many colleagues and classmates I have had within the Department of Chemical Engineering and McMaster University in general. There are honestly too many students I have met from different departments, and it would be unfair to even attempt to guess all the names or only highlight a handful. You know who you are and how you have helped. Thank you for all that you do.

I would also like to thank the rest of the Chemical Engineering faculty and staff, there are a handful of people and professors who have helped guide me on my life journey and help show me the path that is in the highest good for me. In particular, the Chem Eng office staff have always gone above and beyond to help me out with anything I was dealing with. I cannot thank Kristina, Michelle, and Linda enough for their guidance and emotional support, you are all angels dressed in plainclothes.

I would like to thank and show respect for all of the funding sources who have either directly or indirectly had a large part in making the execution of these research projects possible. In particular, I'd like to acknowledge *EcoSythetix Inc.* for their in-kind contributions of chemicals and equipment, the NSERC Strategic Grant of which I was hired on, and the Ontario Ministry of Research and Innovation.

I would also like to thank the technical staff and assistance of our colleagues from other universities who have helped with the research explained herein. More specifically:

- Neutron scattering collaborators (Maikel Rheinstadter group and NCNR users)
- Marcia West for the training on the Faculty of Health Sciences Electron Microscope
- Nicholas Burke from Dr. Stover's group for training and giving me assess to the Stover group confocal and thorough training.
- The McMaster Department of Chemistry's NMR staff (Dr. Bob Berno, Dr. Hilary Jenkins, Dr. Dan Sorensen) for training and guidance.
- The Biointerfaces Institute – primarily Elna Luckham and Dr. Marta Princz for training on various instruments.
- The Department of Biology's Greenhouse, in particular Dr. Susan Dudley for her assistance in our research projects and allocating us space to conduct our research.
- MacPherson Institute for their guidance on my development as a TA, lecturer, pedagogical researcher, and lifelong learner. In particular, I'd like to thank Kris Knorr, Rebecca Taylor, and Erin Allard for their continued support.

I would like to thank the McMaster University Student Wellness Centre and all of the staff, doctors, counsellors, and nurses there. I would like to particularly thank Aven Armstrong-Sutton for being my counsellor, therapist, and spiritual mentor during the last two and half years of my graduate degree. I will never let you exit my life for you have given me the most amount of clarity and knowledge that you have bestowed unto me. Your life lessons will never leave my heart or my psyche, they have been fully integrated with your help. Also thank you to Dr. Sara Rudge, Dr. McLeod, and Dr. Snellgrove for their help along the way as well.

I would like to thank my friends and family back home in Cleveland, OH for wishing me well during graduate school. It was very difficult to deal with deaths and illnesses in the family and with my friends alongside the PhD, but one can only hope that this will leave our family unit and friendships stronger than ever. No matter it all, I still send you love and forgiveness for your past traumas and mistakes. We will make it though everything together.

I would like to thank the Hamilton Art Scene for introducing me to one of my greatest passions in life and for helping me overcome my largest emotional hurdles. Through the Art Gallery of Hamilton (AGH), Hamilton Art Crawl, crafternoons, etc., I have been able to learn my craft. Within the art community I would like to personally thank Julia Veenstra, Anthony Haley, Robyn Lightwalker, Nicholas Zyla, Geoff Carmichael, Mackenzie Taylor, and others for welcoming me as a novice to the local art community. Keep creating Hamilton and don't let the city and gentrifiers ruin your artcrawl nights on James St N. I hope it is still kicking when I visit in the future!

Lastly, I would like to thank the Great Spirit running through all things and keeping order in the world. I thank the life-giving nature of the God and Goddess as well as their spiritual messengers and workers in this world and beyond. In particular, I would like to thank the American Crow/Corvid for being my spirit guide on this physical plane and for always sending me messages/spiritual intuitions when I need them the most. I am very thankful for the lessons you have taught me thus far, and I am indebted to your intuitive ways. Hail and farewell.

Table of Contents

List of Figures
Chapter 1 - Introduction

Figure 2S.3: XRD data of selected SS and SNP samples showing that the samples are largely amorphous post-fabrication in the reactive extruder.

Samples were analyzed using a Bruke D8 DISCOVER with DAVINCI Design with a Co sealed tube (wavelength = 1.79026A). The instrument settings used are as follows: 35 kV and 45 mA power settings, parallel focus Goebel Mirror, Micro Slit (1 mm), Short collimator (0.5 mm), Vertical D8 goniometer, Chi cradle with phi rotation on an X/Y/Z translation stage, Laser-Video sample alignment, and a Vantec 500 (MiKroGap TM technology) area detector. The experiment parameters are as follows: 2θ (fixed θ = 8 deg), number of frames: 3, frame exposure: 900s/frame, range collected: 6-60 deg, and detector distance: 20 cm. All 2D frames were collected with DIFFRAC Measurement Centre Version 6.5 software and integrated to 1D using DIFFRAC.EVA Version 4.2.

Figure 2S.4: Comparison of the experimental versus theoretical degree of substitution (DS) from ^{1}H-NMR for both SS and SNPs (see **Table 2S.1** for tabulated data). The dotted line represents stoichiometric functionalization.

Figure S2.5(a,b): DLS results on the methacrylated SNPs in 1 mM NaCl with DS values ranging from 0 to 0.25 at concentrations of 1, 0.5, and 0.1 wt% based on (a) the intensity-weighted average particle diameter or (b) the number-weighted average particle diameter (assuming RI = 1.4 for particle). The data suggest that esterification does not significantly alter particle size in the process and that altering the wt% during the DLS experiment has little effect on the resulting particle size within the range tested.

Figure S2.6: Representative nanoparticle tracking analysis (NTA) curves showing the concentration (particles/mL) vs. particle diameter (binned) of SNPs with different DS values.

Figure S2.7: Storage (a, b) and loss (c, d) modulus data for selected hydrogel formulations at their swollen equilibrium state (after 3 days of incubation in 10 mM PBS at 37 ˚C). (a, c) SNP-based hydrogels; (b, d) SS-based hydrogels

Figure 2S.8(a-c): Swelling kinetics and equilibrium degrees of swelling (relative to the dry state) for hydrogels prepared with (a) SS and SNP building blocks at equivalent 10 wt%/DS 0.25 conditions; (b) SNP building blocks at different wt% and DS values (c) SS building blocks at different wt% and DS values.

Figure 2S.9: 30 m SANS scattering profiles of colloidal dispersions of SNPs before (light blue) and after (dark blue) methacrylation (DS = 0.05). While the background and low *q* scales are slightly altered before and after modification, both curves have the same general shape. This corroborates the NTA, DLS, TEM, and GPC results that the SNP size/structure is not substantially altered due to methacrylation.

compared to the anomeric carbon (I = 5.4 ppm, ^{1}H) intensity to calculate the degree of substitution (DS) [254].

Figure 3.4 (a,d): Viscosity versus shear rate flow sweeps to determine the relationship between shear and viscosity for (a) 35 wt% homogenous gels (SNP building blocks); (b) 25 wt% homogenous gels (SNP building blocks); (c) SS-based homogenous gels at different concentrations (10 and 7.5 wt%); and (d) 10 wt% heterogenous gels (mixtures of SS and SNP building blocks).

Figure 3.5 (a-d): Post-gelation mechanical properties for SS and/or SNP-based hydrogel systems fabricated at concentrations of (a) 35 wt% (SNP only); (b) 25 wt% (SNP only); (c) 10 wt% and 7.5 wt% (SS only); (d) 10% (mixed SS/SNP).

Figure 3.6: Schematic showing the evolution of network formation when going from concentrated SNP colloids to crosslinked SNP gels after 30 s exposure to 365 nm light.

Figure 3.7 (a, b): Measured changes in the a. fluid scale over 30 s UV exposure and b. $1/\tau$ for all homogenous SNP hydrogels formed in situ in the beamline.

Figure 3.8 (a,b): Measured changes in the a. fluid scale over 30 s of UV exposure and b. $1/\tau$ for all homogenous SS hydrogels formed in situ in the beamline.

Figure 3.9 (a,b): Measured changes in the a. fluid scale over 30 s UV exposure and b. $1/\tau$ for all heterogenous SS/SNP hydrogels formed in situ in the beamline.

Chapter 3 Supporting Information

Figure S3.1: Confirmation of the structure of synthesized pyridinium methyl sulfate (Py-Me-S). The ^{1}H-NMR indicates a pure sample of correct structure with a small amount of residual DMSO, which is used as the solvent for the functionalization reaction.

Figure S3.2 (a, b): Elemental analysis results for a CHNS scan of the cationic (a) or anionic (b) modified starch particles. To view the differences in nitrogen and sulfur, the carbon peak was omitted (C was in the range of 50-55 mol% for all samples).

Figure S3.3 (a-h): G'/G" (storage modulus to loss modulus) ratio as a function of time over the duration of UV exposure for: (a, b) 35 wt% homogenous SNP gels over the full modulus range (a) or zoomed in (b); (c,d) 25 wt% homogenous SNP gels at over the full modulus range (c) or zoomed in (d); (e, f) 10 and 7.5 wt% SS homogenous gels over the full modulus range (e) or zoomed in (f); and (g, h) 10 wt% heterogeneous SS:SNP gels over the full modulus range (g) or zoomed in (h). The bulk gelation time was measured based on the inflection point, which represents the shift from primarily viscous to primarily elastic behavior.

Figure S3.4 (a-e): Rheological flow sweeps described in a decade format for easier comparison between samples: (a) 35 wt% SNP (homogenous); (b) 25 wt% SNP (homogeneous); (c) 10 wt% SS (homogenous); (d) 7.5 wt% SS (homogeneous) ; and (e) 10% (heterogenous). Notice that the x axis range is the same for all graphs, but the y-axis of panels c and d are more extended than those in panels A, B, and E due to differences in starting sample viscosity due to the starch type used.

Figure S3.5 (a,b): Measured changes in (a) the fluid correlation length over 30 s UV exposure and (b) the time constant of the exponential best-fit line ($1/\tau$) for all homogenous SNP hydrogels formed in situ in the beamline; see **Figure 3.7 (a,b)** for the corresponding data on the fluid scale.

Figure S3.6 (a,b): The percent change in (a) the Porod exponent and (b) the fluid (Lorentzian) exponent over 30 s of UV irradiation for 35 wt% homogenous SNP hydrogels

Figure S3.7 (a,b): The percent change in (a) the Porod exponent and (b) the fluid (Lorentzian) exponent over 30 s of UV irradiation for 25 wt% homogenous SNP hydrogels

Figure S3.8 (a,b): Measured changes in (a) the fluid correlation length over 30 s UV exposure and (b) the time constant of the exponential best-fit line ($1/\tau$) for all homogenous SS hydrogels formed in situ in the beamline; see **Figure 3.8 (a,b)** for the corresponding data on the fluid scale.

Figure S3.9 (a,b): The percent change in (a) the Porod exponent and (b) the fluid (Lorentzian) exponent over 30 s of UV irradiation for homogeneous SS hydrogels.

Figure S3.10 (a,b): Measured changes in (a) the fluid correlation length over 30 s UV exposure and (b) the time constant of the exponential best-fit line ($1/\tau$) for all heterogeneous SS:SNP hydrogels formed in situ in the beamline; see **Figure 3.9 (a,b)** for the corresponding data on the fluid scale.

Figure S3.11 (a,b): The percent change in (a) the Porod exponent and (b) the fluid (Lorentzian) exponent over 30 s of UV irradiation for heterogenous hydrogels.

Chapter 4 - In Situ-Gelling Starch Nanoparticle (SNP) and O-Carboxymethyl Chitosan Plum Pudding Hydrogels for the Intranasal Delivery of Antipsychotic Peptides

Figure 4.GA: A hydrogel formulation based on O-carboxymethyl chitosan (CMCh, green), aldehyde-functionalized starch nanoparticles (SNP-CHO, yellow), and PAOPA (red) is reported that can gel in situ (< 10 min) following spray or pipetting into the rat nasal cavity. Using an MK-801-induced pre-clinical rat model of schizophrenia and

tracking changes in animal social interaction time, PAOPA-loaded intranasally-delivered hydrogels alleviated the negative symptoms of schizophrenia for 3-4 days (red points in graph), while free drug administered at the same dosage alleviated symptoms for only a few hours (blue points in graph).

Figure 4.1: Schematic diagram of the IN delivery strategy to administer PAOPA to the brain using *in situ*-gelling SNP-CHO/CMCh hydrogels.

Figure 4.2 (a-c): Characterization of oxidized starch nanoparticles (SNP-CHO): (A) gel permeation chromatography analysis of the relative hydrodynamic diameter of SNP-CHO prepared at different degrees of oxidation; (B) representative transmission electron microscopy image of SNP-CHO-0.25 in the presence of background PMMA nanoparticles used to prevent SNP-CHO film formation during drying (100 nm scale bar); (C) intensity average (blue) and number average (red) particle size distribution of SNP-CHO-0.25 via dynamic light scattering.

Figure 4.3 (a-c): Gelation times (via vial inversion) for CMCh/SNP-CHO hydrogels prepared using various CMCh and SNP-CHO concentrations: (A) SNP-CHO-0.25-based hydrogels; (B) SNP-CHO-0.5-based hydrogels; (C) SNP-CHO-1-based hydrogels

Figure 4.4 (a,b): Gravimetric *in vitro* swelling/degradation profiles in 10 mM PBS at 37 ˚C for CMCh/SNP-CHO hydrogels based on (A) SNP-CHO-0.25 and (B) SNP-CHO-0.5.

Figure 4.5 (a-d): Mechanical properties of CMCh/SNP-CHO hydrogels. (A, B) Shear storage modulus (G') as a function of frequency for CMCh/SNP-CHO hydrogels prepared with (A) SNP-CHO-0.25; (B) SNP-CHO-0.5; (C) Work of mucoadhesion for selected CMCh/SNP-CHO hydrogels with relevant gelation/degradation properties for IN delivery.

Figure 4.6: Cell viability resazurin assay for SNO-CHO-0.25 (red) and SNP-CHO-0.5 (blue) with SH-SY5Y neuroblastoma cells.

Figure 4.7 (a,b): Spray pattern of a nebulized hydrogel at a various spray distances for (A) 2 wt% CMCh/35 wt% SNO-SNP-0.25 and (B) 4 wt% CMCh/35 wt% SNP-CHO-0.25, comparing the inner (hatched bar) area corresponding to the focused spray area in which most droplets are deposited and the outer (solid) spray area corresponding to the maximum diameter impacted by the atomization. Inset pictures represent characteristic images of spray patterns from the 15 cm distance best modeling the human nasal cavity (food coloring is added for visualization).

Figure 4.8 (a,d): Effect of CMCh/SNP-CHO hydrogels with or without 0.5 mg/kg PAOPA loading on reversing MK-801-induced social interaction schizophrenia symptoms in Sprague-Dawley rats. (A) Controls of untreated rats, 2 wt% CMCh/35 wt% SNP-CHO hydrogels alone, 4 wt% CMCh/35 wt% SNP-CHO hydrogels alone, and 0.5

mg/kg PAOPA without MK-801 knockdown indicate the hydrogels or drug alone do not alter rat behavior; (B) 0.5 mg/kg PAOPA in solution can reverse MK-801-induced schizophrenia social withdrawal (relative to the aCSF series) for short times but has no benefit after 24 hours; (C) 2 wt% CMCh/35 wt% SNP-CHO-0.25 hydrogel loaded with 0.5 mg/kg PAOPA can fully reverse MK-801-induced social deficits for at least 3 days, with positive effects persisting over 5 days; (D) 4 wt% CMCh/35 wt% SNP-CHO-0.25 hydrogel loaded with 0.5 mg/kg PAOPA can sustain some positive effects of PAOPA for up to 5 days but does not fully recover the control interaction times and has an induction time at shorter testing intervals. n=4 for all test groups; statistical comparisons at different confidence intervals are shown by different symbols on the graphs. The dashed line in B-D represents the average social interaction time from A in the absence of MK-801 model induction for easier comparison of social interaction recovery upon PAOPA treatment.

Figure 4.9 (a,b): Biodistribution of SNP-CHO-0.25 nanoparticles 1 day (light series) or 3 days (dark series) following IN administration for (A) 2 wt% CMCh/35 wt% SNP-CHO-0.25 hydrogels and (B) 4 wt% CMCh/35 wt% SNP-CHO-0.25 hydrogels.

Chapter 4 Supporting Information

Figure S4.1 (a-j): Sample holder design kit consisting of: a) mold backplate, b) backplate with support for mucin-coated PDMS membranes, c) assembly in (b) with PDMS wafers inserted with tape, d) insertion of mold walls and polymer precursors solution (pink), e) second PDMS wafer added, f) top plate added to secure the second PDMS wafer (assembly screwed together until gelation occurs), g) removal of the back plate and top plate post-gelation, h) removal of mold walls post-gelation, i) insertion of mounting screw on top of assembly (same for bottom), and j) mounting of the test assembly to the instrument.

Figure S4.2 (a-d): The individual components (a) and assembled acrylic sample holder (b) to gel a sample *in situ* for mucoadhesion testing. The device is then removed and the mucin-modified silicone sheets connected by the gel are mounted onto the MACH-1 micromechanical tester to perform the lap shear test (c, d).

Figure S4.3 (a-c): ^{1}H-NMR data for (a) a raw, unmodified SNP, (b) SNP-CHO-0.25, and (c) SNP-CHO-0.5 showing the confirmation of the aldehyde functionality on the SNP surface. By comparing a native, unmodified SNP (a) to SNP-CHO (b, c), a clear peak at 9-9.1 ppm is observed due to the imparted functionality that is not normally present and increases at higher DS values, as indicated by the red arrows.

Figure S4.4 (a-f): Raw mucoadhesion data from small-amplitude stress relaxation experiments; the area under each curve was used to calculate the work of adhesion. Panels (a-c) represent the data for the 35 wt% SNP-CHO-0.25 mixed with 2 wt% (a), 4 wt% (b), and 6 wt% (c) CMCh. Panels (d-f) represent the data for the 35 wt% SNP-

CHO-0.5 mixed with 2 wt% (d), 4 wt% (e), and 6 wt% (f) CMCh. For each formulation, selected replicates are shown to show the reproducibility of the mucoadhesion experiments. Note that the y-axis changes for each sample since the total distance moved will vary depending on the stress relaxation properties of each gel.

Figure S4.5 (a-c): HPLC chromatograms of free PAOPA prepared fresh (D0), after 1 day (D1), and after 6 days (D6) when loaded in (A) free solution in aCSF, (B) 2 wt% CMCh/35 wt% SNP-CHO-0.25 and (C) 2 wt% CMCh/35 wt% SNP-CHO-0.5 hydrogels.

Figure S4.6: Baseline auto-fluorescence of target tissues for the in vivo biodistribution study. These fluorescence intensities were subtracted from the fluorescence intensities measured with F-SNP-CHO nanoparticles to produce the biodistribution data shown in **Fig. 4.9** in the main manuscript.

Chapter 5 - Hydrophobized Starch Nanoparticles (SNPs) Engineered for Foliar Plant Delivery

Figure 5.1 (a,b): A summary of the foliar and root entry routes for plant-based agricultural delivery mechanisms (a) as well as a summary of the reported size ranges for particle size exclusion limits for internal barriers to nanoparticle translocation (b). Adapted from Wang et al (2016) [28].

Figure 5.2 (a,b): Degree of substitution of anhydride-modified SNPs: (A) Comparison of actual versus theoretical DS values for succinic anhydride-modified SNPs (SAn) functionalized at pH 10-11 (blue) and pH 8-9 (green, texture); (B) Comparison of actual versus theoretical DS values for both succinic anhydride and octyl succinic anhydride-modified SNPs functionalized at pH 8-9; the green dotted line represents 100% grafting efficiency.

Figure 5.3: Contact angle (CA) measurements for hydrophobized SNPs following drying of an SNP suspension on a leaf surface.

Figure 5.4 (a,b): Photodegradation of the FITC-SNP fluorescence signal for hydrophobized SNPs tagged with either 1 mg or 2 mg of FITC isomer I (A) in natural greenhouse conditions; and (B) under simulated sunlight on benchtop.

Figure 5.5 (a, b): Humic acid (HA) release from hydrophobized SNPs as measured through (A) a 3.5-5 kDa dialysis membrane and (B) a 100 kDa dialysis membrane (b).

Figure 5.6 (a, b): Preliminary retention data for (A) pumpkin leaves and (B) watermelon leaves for hydrophobized FITC-SNPs.

Figure 5.7 (a-f): Confocal images of transport of FITC-OSAn-0.25 starch nanoparticles following foliar spray on (A,B) the leaf surface; (C,D) the stomata; and (E,F) the root

capillary. Green coloration represents the location of the SNPs (FITC filter) while red represents chloroplasts (TRITC filter).

Chapter 5 Supporting Information

Figure S5.1: The chemical structures for the main additives used in this study, succinic anhydride or SAn (top) and octenyl succinic anhydride or OSAn (bottom).

Figure S5.2: The functionalization reaction scheme for OSAn-modified starch, adapted from Sweedman et al. (2013) [329]. The same reaction would also take place with the SAn-modified starch, just without the extra alkenyl chain.

Figure S5.3 (a-d): Conductometric titration data (pH and conductivity vs. volume of NaOH added) for SAn-0.10 (a), SAn-0.25 (b), OSAn-0.10 (c), and OSAn-0.25 (d).

Figure S5.4: Standard curves for (a) FITC-tagged SNPs at 1 and 2 mg FITC isomer I to 50 mg SNP showing both undialyzed (U) and dialyzed (D) SNPs to show the effect in loss of fluorescence and (b) the relative fluorescence for the tagged SNPs (all at 2 mg FITC/50 mg polymer) post-hydrophobization at comparable concentrations.

Figure S5.5: Standard curve for the starch-iodine test using 0.0125 M iodine and varying wt%'s of HA. Note that concentrations of up to 0.5 wt% were tested, but concentrations above the range of this graph did not give a linear calibration.

Figure S5.6: Schematic of the experimental protocol for the contact angle measurements to clear up any confusion with the measurements on top of the leaf surface.

Figure S5.7: Example of the leaf sections in their 48 well plate before being quantified for their relative FITC fluorescent intensity values.

Figure S5.8: Calibration curve run using UV-vis spectroscopy (plotting the difference in absorbances at 465 and 665 nm) for humic acid (HA).

List of Tables

Chapter 1 (Introduction)

N/A

Chapter 2 - UV Photopolymerized Starch Nanoparticle (SNP) Network Hydrogels for Biomedical Applications

Chapter 2 Supporting Information

Chapter 3 - Investigating the Kinetics and Structure of Network Formation in UV-Photopolymerizable Starch Nanogel Network Hydrogels via Very Small Angle Neutron Scattering (vSANS) and Dynamic Hybrid Rheology (DHR)

Table 3.1: Effective diameter (by intensity or number weighting), electrophoretic mobility, and surface charge density of native and functionalized starch nanoparticle (SNPs) used for hydrogel fabrication. Hence, all precursor starches have the same degree of methacrylation and all charged SNPs have equivalent surface charge densities, allowing direct comparisons to be made between the samples.

Table 3.2: Gelation time (G'/G" = 1) for methacrylated starch photogelation as a function of starch concentration, morphology (SS or SNP), and charge.

Chapter 3 Supporting Information

Table S3.1: Charge titration results from various anionic-modified SNPs designed to match the charge density of the provided cationic SNP sample using poly(DADMAC) as the positively charged titrant/polyelectrolyte. Note that the "SNP-SO4-5-d" sample was chosen for the subsequent work in the manuscript given that the absolute surface charge measured matches with that of the commercially-acquired (+)SNP, allowing direct comparisons between the cationic and anionic SNP-based hydrogels.

Table S3.2: (0) SNP, 35wt% raw vSANS best fit parameters.

Table S3.3: (0) SNP, 25wt% raw vSANS best fit parameters.

Table S3.4: (+) SNP, 35wt% raw vSANS best fit parameters.

Table S3.5: (+) SNP, 25wt% raw vSANS best fit parameters.

Table S3.6: (-) SNP, 35wt% raw vSANS best fit parameters.

Table S3.7: (-) SNP, 25wt% raw vSANS best fit parameters.

Table S3.8: (0) SS, 10wt% raw vSANS best fit parameters.

Table S3.9: (0) SS, 7.5wt% raw vSANS best fit parameters.

Table S3.10: 2:1 SS:SNP, 10wt% raw vSANS best fit parameters.

Table S3.11: 1:1 SS:SNP, 10wt% raw vSANS best fit parameters.

Table S3.12: 1:2 SS:SNP, 10wt% raw vSANS best fit parameters.

Chapter 4 - In Situ-Gelling Starch Nanoparticle (SNP) and O-Carboxymethyl Chitosan Plum Pudding Hydrogels for the Intranasal Delivery of Antipsychotic Peptides

N/A

Chapter 4 Supporting Information

Table S4.1: Total social interaction time following MK-801 knockdown of rats treated with various IN doses of PAOPA dissolved in aCSF.

Chapter 5 – Hydrophobized Starch Nanoparticles (SNPs) Engineered for Foliar Plant Delivery

Table 5.1: Dynamic light scattering (DLS) results for 0.5 wt% (top half) and 1 wt% (bottom half) anhydride-functionalized SNPs reported in terms of intensity averages or number averages. Results are given for dispersions in DMSO (left) and water (right).

Table 5.2: Electrophoretic mobility and zeta potential measurements for unmodified SNPs and OSAn modified SNPs at a DS of 0.10.

Chapter 5 Supporting Information

N/A

List of Terminology, Symbols, and Abbreviations

Chapter 1 - Introduction:

AGUs; anhydrous glucose units
APS; ammonium persulfate
CNS; central nervous system
CAN; ceric ammonium nitrate,
DCC; dynamic constitutional chemistry
DHR; dynamic hybrid rheology
DNA; deoxyribonucleic acid
DLS; dynamic light scattering
ECH; epichlorohydrin
ECM; extracellular matrix
FRP; free radical polymerization
GelMA; gelatin methacrylated
GRAS; “generally regarded as safe”
IPN; interpenetrating network
IV; intravenous
KPS; potassium persulfate
NC; nanocomposite hydrogels
NP; nanoparticle
NNHs; nanoparticle network hydrogels
OSAn; octenyl succinic anhydride
PE; polyethylene
PNIPAM; poly-N-isopropylacrylamide
PP; polypropylene
PVA; poly(vinyl alcohol),
RGD; arginine-glycine-aspartate tripeptide
SANS; Small angle neutron scattering
SAXS; small angle X-ray scattering
STPP; sodium polyphosphate
STMP; sodium trimetaphosphate
SNP; starch nanoparticle
SAn; succinic anhydride
SPIONs; superparamagnetic iron oxide nanoparticles
TEMED; tetramethylethylenediamine
UV; ultraviolet
vSANS; very small angle neutron scattering

Chapter 2 - UV Photopolymerized Starch Nanoparticle (SNP) Network Hydrogels for Biomedical Applications:

AA; acrylic acid,
BIS; N,N-methylenebis(acrylamide)
ADH; adipic dihydrazide,
AGU; anhydrous glucose unit
DLS; dynamic light scattering
DMEM; Dulbecco's modified Eagle's medium
DMSO; dimethyl sulfoxide
DS; degree of substitution
FBS; fetal bovine serum
FITC; fluorescein isothiocyanate
GPC; gel permeation chromatography
^{1}H-NMR; proton nuclear magnetic resonance
IPN; interpenetrating network
KPS; potassium persulfate
MAAn; methacrylic anhydride
NTA; nanoparticle tracking analysis
pMMA; poly(methyl methacrylate)
pNIPAM; poly(N-isopropylacrylamide)
PVAm; poly(vinylamine)
PS; penicillin streptomycin
PSNPs; potato starch nanoparticles
SANS; small angle neutron scattering
SDS; sodium dodecyl sulfate
SNP; starch nanoparticle
SS; soluble starch
TDA; N,N'-bis(acryloyl) cystamine
TEM; transmission electron spectroscopy
UV; ultra-violet
WCSNPs; waxy corn starch nanoparticles;

Chapter 3 - Investigating the Kinetics and Structure of Network Formation in UV-Photopolymerizable Starch Nanogel Network Hydrogels via Very Small Angle Neutron Scattering (vSANS) and Dynamic Hybrid Rheology (DHR):

DHR; dynamic hybrid rheometer
DMAPA; 3-dimethylaminopropylamine
DMSO;dimethylsulfoxide,
EDC; 1-(3-dimethylaminopropyl)-3-ethylcarbodiimide hydrochloride
FRP; free radical polymerization
LVE; linear viscoelastic region
MAAn; methacrylic anhydride
MWCO; Molecular weight cut off
MQW; Milli-Q Water
NIST; National Institute of Standards and Technology
Py-Me-S; pyridinium-methyl-sulfate
SNPs; starch nanoparticles
SS; cold water-soluble starch,
t_{gel}; gelation time
UV; Ultra-violet
vSANS; very small angle neutron scattering

Chapter 4 - In Situ-Gelling Starch Nanoparticle (SNP) and O-Carboxymethyl Chitosan Plum Pudding Hydrogels for the Intranasal Delivery of Antipsychotic Peptides:

aCSF; artificial cerebrospinal fluid
ATR-FTIR; total reflectance Fourier transform infrared spectroscopy
ANOVA; one-way analysis of variance
BBB; blood-brain barrier
CMCh; O-carboxymethyl chitosan
D_2O; deuterium oxide
DMSO; dimethyl sulfoxide
DS; degree of substitution
DLS; Dynamic light scattering
F-SNP-CHO; Fluorescently tagged SNP-CHO
FITC; fluorescein isothiocyanate
GPC; gel permeation chromatography
^{1}H-NMR; Proton nuclear magnetic resonance
IN; Intranasal
IP; Intraperitoneal
MK-801; dizocilpine or ((+)-5-methyl-10,11-dihydro-5H-dibenzo [a,d]cyclohepten-5,10-imine maleate salt)
MQW; Millipore Milli-Q grade distilled deionized water

NMDA; N-methyl-D-aspartate
PAOPA; (3R)-2-Oxo-3-[[(2S)-2-Pyrrolidinylcarbonyl]amino]-1-pyrrolidineacetamide
PBS; Phosphate buffered saline
PMMA; poly(methyl methacrylate)
SNP; Starch nanoparticle
SNP-CHO; starch nanoparticle with aldehyde functionality
SS; Soluble starch
TEM; transmission electron microscopy
Wt%; weight percent
W/v%; weight/volume percent

Chapter 5 - Hydrophobized Starch Nanoparticles (SNPs) Engineered for Foliar Plant Delivery:

AGU; anhydrous glucose unit
CA; contact angle
DLS; dynamic light scattering
DMSO; dimethyl sulfoxide
DS; degree of substitution
FITC; fluorescein isothiocyanate isomer I
GPC; gel permeation chromatorgraphy
HA; humic acid
MQW; Mili-Q water
MW; molecular weight
MWCO; molecular weight cut off
OSAn; octenyl succinic anhydride
PBS; phosphate buffered saline
SAn; succinic anhydride
SNP; starch nanoparticle
UV; ultraviolet

Declaration of Academic Achievement

The majority of the written work herein recorded was conceived, carried out, analyzed, and written by the author of this thesis, in consultation with Dr. Hoare except for the following:

Chapter 1: All writing done by Michael Majcher and edited by Dr. Todd Hoare.

Chapter 2: All experimental work was completed by Michael Majcher along with the help of summer/thesis student Carter McInnis (2015/6). For the SANS experiments, Richard Alsop helped me collect the spectra and then Sebastian Himbert helped me analyze/plot them. All writing and manuscript preparation was done by Michael Majcher and edited with the help of Dr. Todd Hoare.

Chapter 3: Some of the physical interpretations of the SANS data was carried out by Sebastian Himbert who is our lab's SANS collaborator (also helped in **Chapter 2**). He helped to analyze, reduce, collect, and summarize the data at NIST for this study. Additionally, co-authors Matthew A. Campea and Ridhdhi Dave are acknowledged for helping to re-synthesize and characterize some of the missing anionic formulations. All the remaining experiments and data analysis was conducted by Michael Majcher. Francesco Vito is credited with helping to functionalize some of the SNP samples described in this paper for the DHR analysis.

Chapter 4: The co-first author, Ali Babar, helped write some of the manuscript and led the experimental *in vivo* and spray testing work, focusing mostly on the in vivo and spray testing results. Ashlyn Leung (2017) helped with the hydrogel performance testing and initial chemistry when she was my summer student. Xiaoyun Li helped acquire the HPLC data for the study's *in vitro* release curves. The majority of writing, conception, and execution of experimental procedures not already mentioned was done by Michael Majcher and edited by Dr. Hoare.

Chapter 5: All experimental work and nanoparticle chemistry was completed by Michael Majcher along with the help of summer/thesis student Cynthia Pham (2018). Dr. Susan Dudley allowed us to use the McMaster Greenhouse to complete our research and offered her professional opinions on the work when needed. All writing was done by Michael Majcher and edited with the help of Dr. Todd Hoare.

Chapter 6: All writing done by Michael Majcher and edited by Dr. Todd Hoare.

Chapter 1: Introduction

Preface

This introduction was written completely by the author on selected topics pertinent to the reader for proper comprehension of the other chapters of research presented herein. However, the introduction has been adapted from previous publications from the author, including the following works listed below. Further citations to reviews and useful studies will be highlighted in the main text for the reader interested in pursuing such topics further on their own accord.

1. **Majcher M.J.**, Hoare T. (2018) Advanced Hydrogel Structures. In: Jafar Mazumder M., Sheardown H., Al-Ahmed A. (eds) Functional Biopolymers. Polymers and Polymeric Composites: A Reference Series. Springer, Cham

2. **Majcher M.J.**, Hoare T. (2018) Applications of Hydrogels. In: Jafar Mazumder M., Sheardown H., Al-Ahmed A. (eds) Functional Biopolymers. Polymers and Polymeric Composites: A Reference Series. Springer, Cham

3. **Majcher M.J.**, Hoare T. (2018) Hydrogel Properties and Characterization Techniques. In: Jafar Mazumder M., Sheardown H., Al-Ahmed A. (eds) Functional Biopolymers. Polymers and Polymeric Composites: A Reference Series. Springer, Cham

4. **Majcher M.J.**, Hoare T. (2018) Hydrogel Synthesis and Design. In: Jafar Mazumder M., Sheardown H., Al-Ahmed A. (eds) Functional Biopolymers. Polymers and Polymeric Composites: A Reference Series. Springer, Cham

5. **Majcher, M.J**., Campea, M.C., Lofts, A., and Hoare, T.R., "A Review on the Design and Fabrication of Nanoparticle Network Hydrogels (NNHs) for Biomedical, Environmental, and Industrial Applications", Submitted to *Advanced Functional Materials*, Accepted on May 7, 2021 (adfm.202102355R1 and EMID:da6937010fe6d77d).

1.1 Starch Nanoparticles (SNPs) At a Glance

1.1.1 Starch/Carbohydrate Research and Development – Surveying the field

Starch is an attractive bio-based carbohydrate polymer for use in polymeric systems due to its tissue compatibility (low protein adsorption and inflammation), degradability, renewability, natural abundance, and overall low cost [1]. Despite the technical limitations of batch-to-batch variation amongst others, starch chemistry (and more broadly, carbohydrate chemistry) has attracted increasing interest in recent years due to the push for more simple, scalable, and "green" chemistries for end-product development [2]. A dominant engineering constraint associated with the use of starch for polymer chemistry is its inherent inhomogeneity, given that it is comprised of both amorphous and crystalline domains [3] that vary according to the source and processing technique of native starch granules [4,5]. As such, the heterogeneity of domains in the starting polysaccharide can typically complicate the relationship between starch structure and intended hydrogel properties.

The native structure of starch starts with the granule, a spherical structure typically on the size regime of micro to millimetres with alternating layers of amorphous and semicrystalline growth rings [6], **Figure 1.1** (reproduced with permission from ACS Biomacromolecules). Therefore, the granule will have crystalline regions with tightly packed amylopectin double helices and branching points or amorphous lamellae that can be exploited when designing nanoparticle-based hydrogels.

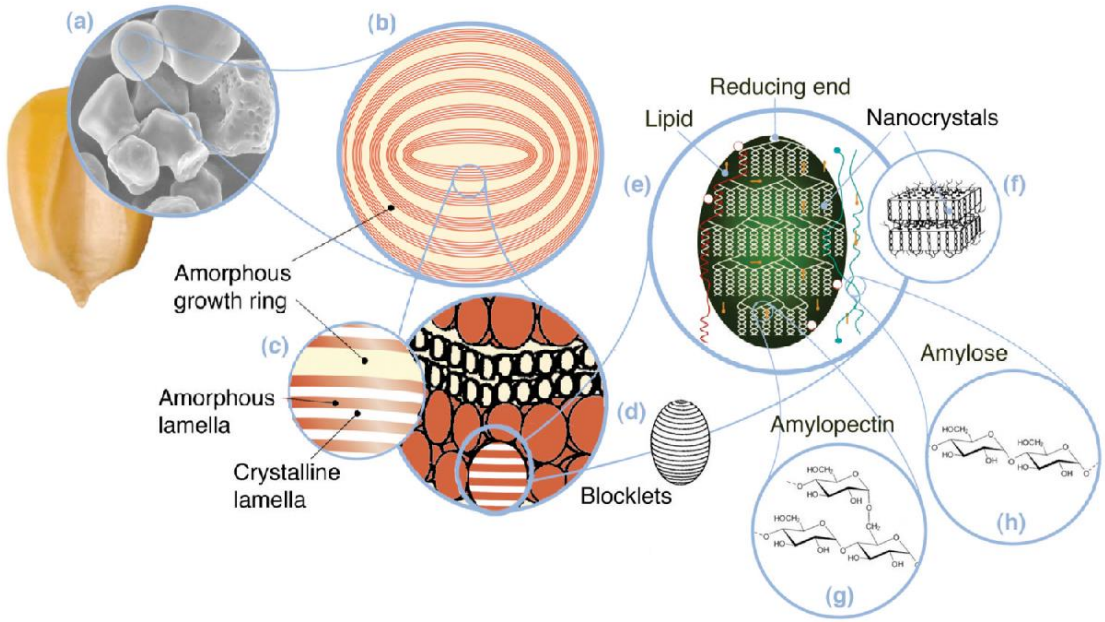

Figure 1.1: Starch organization starting from a. the granule (30 μm), b. the amorphous and semi-crystalline growth rings (120-500 nm), c. the amorphous and crystalline lamellae (9 nm), d. blockets (20-50 nm), e. amylopectin double helices forming the crystalline lamellae of blockets. and the molecular scale for f. nanocrystals from acid

hydrolysis, g. amylopectin (molecular structure), and h. amylose (molecular structure, 0.1-1 nm). Image reproduced with permission from *Biomacromolecules* [6].

Thus, the varying crystallinity of the granule is attributed to two macromolecules: linear amylose chains connected via α (1,4)-glycosidic links between anhydrous glucose units (AGUs), **Figure 1.2**, that typically form the amorphous domains and branched amylopectin connected via α (1,6)-glycosidic links between AGUs that typically form the crystalline domains; the amylopectin chains are typically larger (1×10^8 g/mol) compared to amylose (1×10^6 g/mol) [7,8]. When in granular form, the starch can attain either A-type packing (closer interactions, less water) or B-type packing (more open interactions, more water), or a combination thereof, depending on the amylopectin:amylose balance [9].

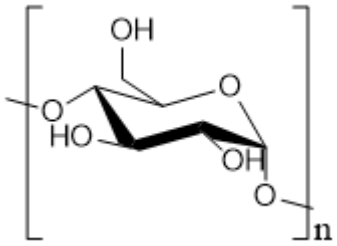

Figure 1.2: Chemical structure of the anhydrous glucose unit (AGU)

Starch can be sourced from a number of sources such as pea [10], yam [11], legume [12], pulses [13], banana [14,15], sago palm [16], roots (cassava [17]) and tubers [4], or cereals like corn, rice, or wheat/amaranth [18], all of which will exhibit different physiochemical properties due to the unique ratio of amylose vs. amylopectin content in their final form. In particular, the varying crystallinities of starch granules (around 30 μm) from different sources is attributed to two macromolecules: linear amylose chains and branched amylopectin chains. As shown in **Figure 1.1**, the amorphous lamellae of starch blocklets are rich in amylose (containing only linear α (1,4)-glycosidic linkages), while the crystalline lamella of starch blockets are rich in amylopectin (containing both linear α (1,4)-glycosidic linkages between anhydrous glucose units (AGUs) shown in **Figure 1.2**, as well as α (1,6)-glycosidic branching points). Additionally, the amylopectin chains are typically larger (1×10^8 g/mol) compared to amylose (1×10^6 g/mol) [7,8]; thus starches collected from different sources are expected to have unique and distinct molecular weight distributions (MWDs) and thus solution properties.

Starch can be extracted directly from plants using a variety of reported methods [11,12]. The impact of various processing parameters on the structure and function of starch is heavily reported in the literature, including how heat-moisture treatments and annealing can affect key properties such as solubility, pasting, morphology, or crystallinity [19]; new processing techniques are also being developed simultaneously [20]. The use of thermomechanical extrusion to process starch is especially critical to enable the production of starch at an industrial (kg/h) rate. The expected properties of starch post-extrusion such as structure (crystallinity, morphology, molecular weight) and physico-

chemical properties (expansion ratio, water absorption index, water soluble index, texture, pasting property, and digestion) are well understood [21]. In addition, a number of chemical modifications can be made to starch in order to offer chemical compatibility with the targeted application. Common modifications include oxidation, esterification, carboxymethylation, hydroxypropylation, and hydroxyethylation [22,23], with newer reports focusing on developing more environmentally-safe [24] or non-thermal [25] methods for starch chemical modification compared to the industrial standards currently employed. Regardless of the type of modification done, the high variability possible for starch properties requires strict characterization of the modified starches for comparison and reproducibility [26].

Starch products have been envisioned based on a wide variety of chain morphologies or structures including linear [27] or branched polymers [20], foams [28], thin films/membranes/edible coatings [29,30], and even hydrogels [31–33], the latter of which will be the focus of the work in this thesis. These unique forms have met applications in a wide range of general fields, including (but not limited to) pharmaceuticals [34] (typically using starch as the excipient for capsule formulations [35]), biomedical applications (i.e. drug delivery and tissue scaffolds) [34], biodegradable food packaging [36], food engineering and biotechnology [14,37], paper and wood coatings/binders for performance enhancement [38,39] [40,41], or papermaking purposes [42,43]. Other emerging applications of starch include using raw starch for ethanol [44] and biohydrogen production [45] to reduce the need for petroleum-based materials that have an unsustainable ecological fate.

While starch naturally possess many advantageous characteristics as a building block for advanced polymer systems, and an expansive library of knowledge around the processing and modification of starch is available, starch as a polymer still possesses some inherent limitations. For example, for certain applications the thermal and mechanical properties of starch are insufficient, typically requiring either blending or co-polymerization with other polymers such as polypropylene (PP), polyethylene (PE), or poly(vinyl alcohol) (PVA) to create thermoplastic starches with enhanced properties compared to the starting starch (but compromising the overall renewability of the system) [46]. Alternately, rather than only blending starch with other polymers or chemically modifying the starch, changing the packing and overall hydrophilic radius of starch through NP generation offers an intriguing alternative to better exploit starch in functional applications.

1.1.2 Starch Nanoparticles

While many synthetic routes (both bottom-up [47,48] and top-down [49–51]) have been reported in the literature to create SNPs, most of these methods lack scalability and industrial relevance due to the multiple steps involved (i.e. plasticization, extrusion, and pelletization in that order; each with their own workable concentration ranges), the duration/speed of processing, and/or environmental toxicity concerns with the process. To our knowledge, only three companies in the world currently produce starch nanoparticles at an industrial scale: EcoSynthetix Inc.(*EcoSphere* technology) [52–54],

Mirexus (phytoglycogen technology) [55–57], and NovaMont (*Mater-Bi* technology) [5,58].

Aside from the previous attributions of low cost and availability, *EcoSphere* technology is a particularly useful starting material for subsequent functionalization since: 1) it results in SNPs with a very small specific size (20-50 nm, depending on the method of analysis used and the degree of nanoparticle hydration); 2) it is fully amorphous, enabling facile functional group chemistry and post-processing (unlike native starch that possesses a mixture of amorphous and crystalline (15-45%) domains, the latter of which interfere with water binding and thus the availability of hydroxyl groups for functionalization depending on their packing [5,24,59]); 3) it may be enzymatically (α-amylase) or chemically (i.e. trifluoroacetic acid) degraded to make diverse structures; 4) it can be dispersed at much higher weight concentrations (~ 35-40 wt%) than typical starch without huge spikes in viscosity; and 5) it has many possibilities for post-functionalization chemistry due to the presence of only one main functional group on the surface (-OH), **Figure 1.3**.

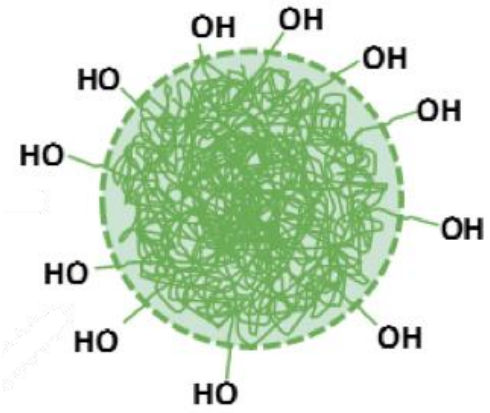

Figure 1.3: Cartoon representation of a native starch nanoparticle with an exterior surface rich in hydroxyl (-OH) groups and an interior rich with crosslinked glucose chains (green).

The specific benefits of *EcoSynthetix's* SNPs are related to the use of reactive extrusion for SNP manufacture. Reactive co-extrusion [60] has been applied to chemically modify and process starch extensively in the past and is now being used by *EcoSynthetix* to create SNPs by using a plasticizer to help solubilize the starch granules entering the twin-screw extruder. When inside the mixing chamber, the particles experience high shear due to changing screw sizes/geometries, high pressure due to hydrostatic pressure, and high heat as controlled by the operator. This process helps mechanically break down the crystalline regions in the native starch granules and allow for gelatinization of the starch via cooling [4,21], aided by the addition of crosslinkers depending on the application. By changing

these parameters, the particle size, charge, and other important physiochemical properties can be modified, offering a highly scalable way to make functional SNPs.

Of note, while there is a considerable number of papers that discuss various ways of making starch-based particles or crystals, all of the properties of these materials will be depend on the method used for processing and the source of the starch. In this thesis, we strictly apply *EcoSynthetix's* commercial grade SNPs to avoid this issue and promote higher practical reproducibility of the materials (and thus application performance) achieved.

1.2 Hydrogels and Hydrogel Architectures

1.2.1 Conventional Hydrogels

Hydrogels are three-dimensional polymeric networks that possess the ability to imbibe water due to their hydrophilic nature [61]. In recent years, research groups have investigated the synthesis and characterization of hydrogels extensively whilst exploiting a milieu of chemical modifications and polymerization mechanisms to produce specific physiochemical properties. Hydrogels can be formed based on any water-soluble polymer, including various synthetic polymers (e.g. namely poly(ethylene glycol) analogues [62] or environmentally-responsive smart polymers like poly(N-isopropylacrylamide [63] or poly(oligoethylene glycol methacrylate) [64]) as well as natural polymers such as chitosan [65], alginate [66], cellulose [67], dextran [68], and xanthan gum [69] to name a few. Hybrid hydrogels combining both natural and synthetic components have also been described for particular applications in the literature, deriving benefits from both components [70,71]. While the number of differences between hydrogels made from synthetic monomers versus those coming from natural or sustainable sources is oftentimes complicated and requires more information about the polymer and its intended end use to draw important comparisons, there is a broader push to create natural and sustainable alternatives [72,73] to synthetic hydrogels without compromising the mechanical [74] or stability properties achievable with synthetic polymers [75]. The use of biodegradable SNPs as fillers or (based on their hydrated network structures) nanoscale building blocks for hydrogel fabrication offers a potentially more renewable as well as more flexible alternative to create hydrogels with diverse and application-relevant properties while circumventing the need for certain blends [76] or co-polymerizations [77] to enable gel formation.

1.2.2 Nanocomposite Hydrogels (NCs)

Nanocomposite hydrogels (NC) are hydrogels in which one or more of the major components of the system is within the nanoscale size regime. A nanocomposite hydrogel is defined as a hydrogel that contains nanoparticles (NPs) or nanoscale structures of a different composition to the continuous phase [78]. While these systems can be designed with heterogenous or advanced functionalities, to have reproducible material properties the nanoscale additive typically must be homogenously dispersed within the gel matrix. Five main approaches have been used to create a uniform distribution of NPs within a gel

matrix [79]: (1) using an aqueous NP suspension as the solvent to prepare the hydrogel [80–82], (2) physically embedding NPs into the hydrogel after gelation [83–85], (3) fabricating NPs *in situ* within a preformed gel from NP precursors [86–88], (4) crosslinking functional groups on the surface of NPs to use NPs themselves as a building block for the overall hydrogel [89,90], and (5) entrapping NPs inside hydrogels formed by small molecule gelators [91]. The choice of NP and the method by which it is incorporated (primarily the degree to which it is dispersed and interacts with the surrounding hydrogel phase) will govern the mechanics and functionality of the resulting nanocomposite hydrogel. Examples have been reported in the literature of NC hydrogels made directly from polymeric nanoparticles including micelles [92], nanogels [93,94], core-shell particles [95], dendrimers [96], hyperbranched polymers [97], and liposomes [98], with further specific examples described in the drug delivery and tissue scaffold application descriptions below.

1.2.3 Nanoparticle Network Hydrogels (NNHs)

It is imperative that a distinction is made between conventional hydrogels or common morphologies versus nanoparticle network hydrogels (NNHs); specifically, in an NNH, the nanoparticle is used as the crosslinker directly to link together other NP(s) and/or linear polymer(s). Given the number of potential building blocks that can result, a variety of architectures can be achieved in which all the NPs are connected in some sense. Network hydrogels made from solely nanoparticles are of particular interest due to the differences in the physiochemical properties of such hydrogels in comparison to other nanocomposite hydrogels [99–101]. Each of the key properties of NNHs can be controlled by altering the core factors associated with NNH formation, such as the crosslinking density, NP size, NP-NP (“inter-NP”) and/or NP-polymer (“inter-network”) crosslinking chemistry, NP and polymer concentration, and the length scale of the NNH (i.e. bulk hydrogel, micro/nanogel, thin film gel, etc.). In general, these phenomena can be tuned to affect the overall hydrogel’s mechanics, mass transfer, swelling, degradation, and stimuli responsivity depending on the types of polymers, NPs, and crosslinking techniques employed [79]. Oftentimes, NPs are able to form their own networks or build new ones from polymeric matrices using a combination of strategies such as small molecule crosslinking agents, dynamic constitutional chemistry (DCC), free radical or controlled radical polymerizations, freeze thawing/cryogelation methods, electrostatic interactions, weak physical interactions, hydrophobic interactions, and coordination chemistry. The nanoparticles comprising NNHs can be assembled in different geometric orientations using any of the crosslinking strategies used above. In particular, the two main morphologies NNHs (and SNP-based NNHs described in this thesis) are the plum pudding [102,103] and colloidal [104] hydrogel structures.

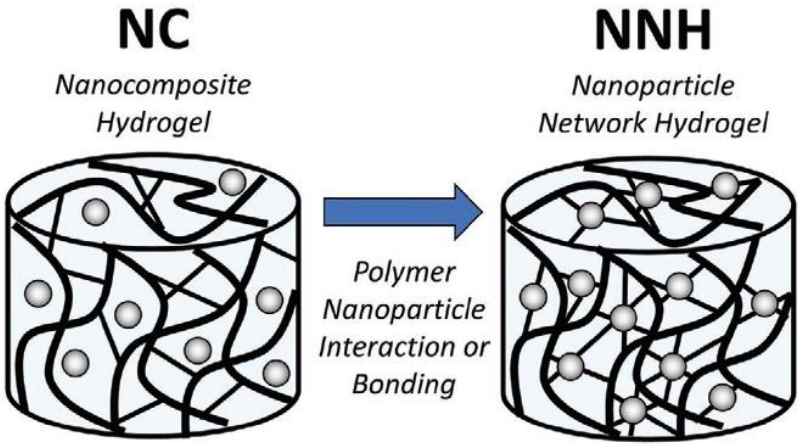

Figure 1.4: A cartoon to demonstrate the main difference between a nanocomposite (NC) vs. a nanoparticle network hydrogel (NNH) is that the NPs must actively perform in crosslinking and not simply be physically encapsulated or doped on the material surface. Image from previous publication by the group with permission from Advanced Functional Materials (AFM) under AFM's Creative Commons license [105].

1.2.3.1 Plum Pudding

The "plum pudding" morphology is named after the plum pudding model first proposed by J. J. Thompson in 1904 after the discovery of the electron [102]. The term is used in the context of nanocomposite hydrogels to describe randomly dispersed nanoparticles (plums) scattered through a conventional hydrogel network [103,106], see **Figure 1.5**. As such, the polymer matrix is denoted as the "pudding" since it encompasses a large volume of the overall system, while the smaller nano/microparticles dispersed throughout are the "plums". This orientation can be achieved with a variety of crosslinking methods; however, *in situ* gelation via reactive mixing was selected to create the plum pudding SNP-CHO/CMCh NNHs described in **Chapter 4** herein. Previous research in the lab guided the research design of these SNP hydrogels, based on the report of Maitland et al. on how SPION-based plum pudding gels can aid in pulsatile drug release [107].

1.2.3.2 Colloidal

Colloidal gels are NNHs formed by the direct crosslinking of nanogels or nanoparticles to form a network; relative to the plum pudding morphology, a colloidal gel is made of only the "plums" described in the previous example. This morphology can be imagined as a children's ball-pit with high porosity between spherical building blocks even when particles are tightly packed see **Figure 1.5**. Examples of this morphology are described in **Chapters 2-4,** fabricated by employing different lengths of linkages between the particles and methods for tethering the SNPs. Such hydrogels are often referred to as colloidal gels [108] to explain the remaining particle-like nature of the building blocks post-gelation, but can also be referred to macrogels [109] or polymer-nanoparticle hydrogels [110]; crosslinkers can also be used to directly crosslink nanoparticles together to form "raspberry-like" clusters [111,112]. The use of covalent crosslinkers between nanogels can increase NNH strength independent of the amount or ratio of nanoparticles; however,

using a large amount of polymeric crosslinkers transitions the colloidal nature of these clusters towards a plum pudding morphology [111]. Changing particle size can modify the porous nature or the hydrogel. For example, using two similarly sized large particles will increase the interparticle spacing while using one large and one small particle, the latter of which can pack within the free volume between the large NPs, results in significantly lower porosity. In addition to chemical crosslinking, physical methods are often used to form colloidal gel NNHs based on either attractive interactions (e.g. using nanogel building blocks that are oppositely charged [108]) or repulsive interactions (e.g. forming an IPN of a naturally collapsing polymer such as PNIPAM and a repulsive polymer that prevents complete collapse of the microgels into a bulk material [113,114]).

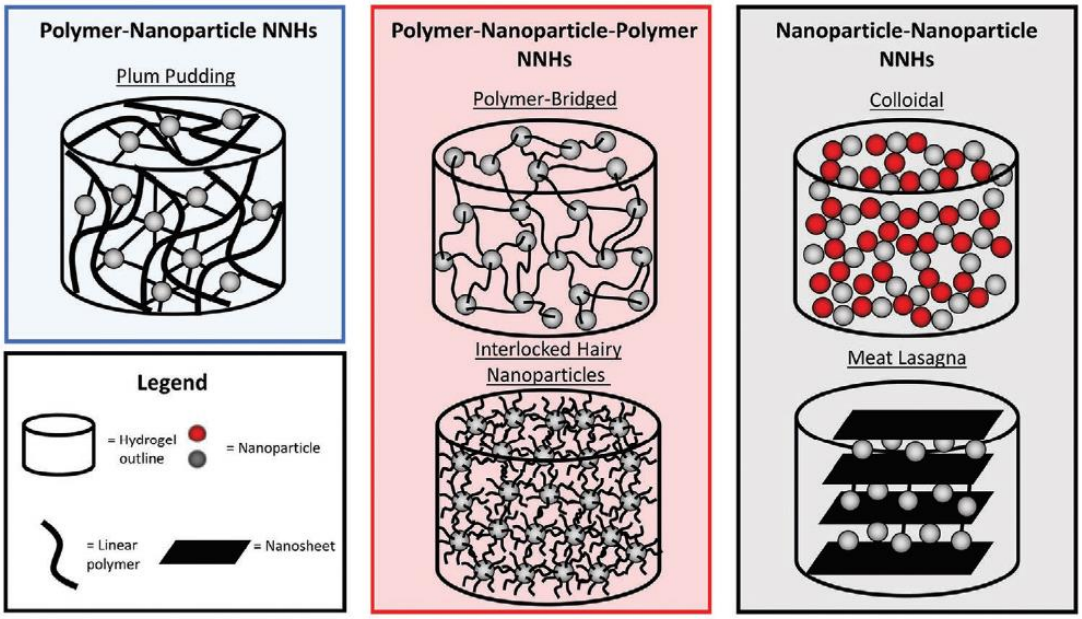

Figure 1.5: The possible NNH architectures that can be formed, two of which being plum pudding (polymer-nanoparticle) and colloidal (nanoparticle-nanoparticle) that are used the work described herein. Image from previous publication by the group reproduced here with permission from Advanced Functional Materials (AFM) under AFM's Creative Commons license [105].

1.2.4 Hydrogels Made from SNPs

Aside from one 2020 report of an SNP-stabilized poly(acrylamide) hydrogel bead Pickering emulsion [115], to the best of our knowledge there have prior to this thesis work been no papers that describe SNPs as a hydrogel building block. The closest example comes from Pixin Wang's group in which starch is modified and oxidized to enable grafting of cholesterol groups via addition of cholesteryl cholorformate and imidazole, which self-assembles in water to form a nanoparticle with a mean size of 143 nm. When in the presence of either PVAm [116] or O-carboxymethyl chitosan [117], a

Schiff base crosslinked hydrogel is formed. The starting material for both these papers is a hybrid of branched starch, starch NPs, and a "gelling" polymer rather than being a homogeneous colloidal gel made from reactive SNPs only. Hydrogels based on SNPs derived from mangrove fruit have also been made using free radical polymerization with N,N-methylene bisacrylamide; however, the SNPs used in this work were not well characterized, and their actual morphology as a nanoparticle is questionable based on the lack of particle sizing data and the low resolution of provided EM images in their paper [118]. An earlier example was also reported based on cassava starch in which starch was hydrolyzed in citric acid, SNPs were created using a bench scale precipitation method adapted from Ma et al. [119], and hydrogels were formed by gamma irradiation based on a method from Erizal et al. [120]. However, the resulting materials only have localized gel fractions and were not free standing bulk gels that could have sufficient mechanics for any of the applications described herein [121]. The last example applied *in situ* gelling chemistry in which SNPs were dispersed within matrices made from hydrazide-functionalized PNIPAM and aldehyde-functionalized dextran [122]; however, the SNPs themselves were not crosslinked into the network such that this material would not be categorized as an NNH. To our knowledge, no previous work describes the formation of hydrogels in which well-defined and industrially-scalable SNPs serve as the core hydrogel building block.

1.3 Hydrogels for Biomedical/Environmental Applications

1.3.1 Biomedical Implants

Biomedical implants serve to replace a missing biological structure, support a damaged biological structure, or enhance an existing biological structure through its design. Hydrogels are often categorized as biomedical implants when they are introduced to the *in vivo* environment to supplement the native soft tissues as fillers, lubricants, adhesives, etc. In addition to the advanced functionality that can be imparted on these materials, it is imperative that the overall implant possesses physiologically favourable properties such as low cytotoxicity and minimal mutagenic properties if resorbed for any reason (i.e. erosion, degradation, temperature effects, etc.) from the original implant. A common issue with all of these scaffolds, even if low toxicity materials are used, is local inflammation and foreign body rejection following implantation [123,124]; it is also not uncommon for implants to adhere to surrounding tissues, thus causing complications upon surgical removal or a lessening of the engineered properties over time. The end stage of the foreign body reaction for an implant is typically the formation of a fibrous capsule, which is an attempt by the body to wall off the implant from the surrounding cells/tissues to prevent further damage or cellular integration [125]. The process of fibrous encapsulation is not necessarily indicative of full rejection of the implant, however the walling off process will have noticeable effects on its *in vivo* functionality and if oftentimes considered a failure in terms of bio-integration. The development of a fibrous capsule is commonly accepted to go through various phases known as non-specific protein adsorption (>1 s after implantation), infiltration of immune cells (60 min), release of cytokines and chemokines from cells (1-5 days), recruitment of tissue

repair cells and macrophages (5-15 days), and finally fibrous encapsulation and granulation tissue formation (3-4 weeks) [126], **Figure 1.6.**

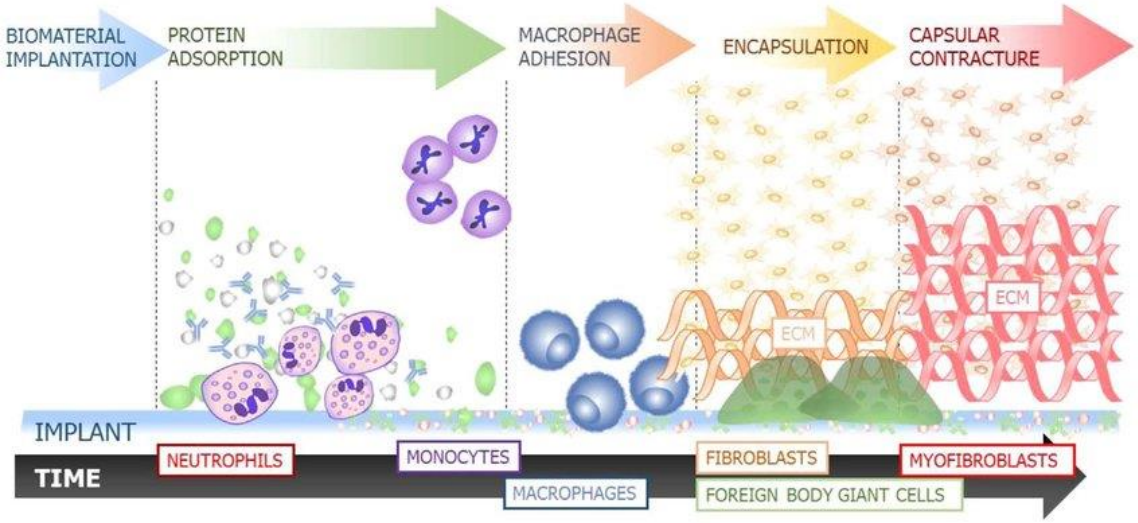

Figure 1.6: A summary of the timeline and major events implicating the foreign body reaction from biomaterial implantation up to capsular contracture when a fibrous capsule is formed in vivo. Image reproduced with permission under the Creative Commons CC-BY license by Elsevier [127].

As mentioned, it is widely accepted that the rejection of an implant first begins with non-specific protein adsorption to the implant within seconds of implantation [128,129]. Within the human body, there are around 3,700 plasma amphipathic proteins [130] in varying concentrations that have multiple types of functions, including structure/tissue mechanics, catalysis of reactions, cell motility and regulation, molecular transport, and immunological defense [131–134]. These chemically diverse proteins are built from amino acid building blocks which contain positive and negative charges, hydrophobic pockets, and polar regions which can interact with different surfaces *in vivo* due to the reversibility of its 3-D conformations and ability to form new bonds/interactions [128,135], **Figure 1.7**. Once the protein is near a surface (controlled by diffusion, thermal convection, flow, and coupled transport [135]), the combination of its ability to form new non-specific physical bonds with an interface and the ability to reduce the exposure of any internal hydrophobic domains within the protein to water drives adsorption of the protein to the interface, reducing the overall interfacial free energy of the system [128].

Given the link between protein adsorption and biomaterial failure, many scientists in the field of materials engineering are interested in designing and fabricating implants and hydrogels that possess favourable properties and advanced structures to increase the longevity of the implant's functionality once implanted. The most common method of protein passivation is through chemical modification of the surface of the implant with the ultimate aim of augmenting the hydration of the interface (Whitesides Rules). For

example, covering the interface with a bioinert hydrophilic coating such as poly(ethylene glycol) (PEG) [136] can enable the binding of significant water to the near-surface layer, making it both enthalpically (by limiting surface-protein interactions) and entropically (by limiting accessibility of the protein to the surface) more difficult for proteins to adsorb. PEG may work well in these applications, but it is not the ultimate solution to biomaterial design since it lacks the ability for subsequent functionalization [137], can degrade in the presence of oxygen or metal ions [138], yield toxic metabolites after enzymatic degradation or due to impurities from synthesis [139], and can potentially lead to hypersensitive bodily reactions in some cases [140].

Changing the surface topology and physical dimensions of a surface can also impact the extent of protein adsorption that occurs. It has been widely recognized that material-protein interactions are largely governed by nanoscale surface cues, while micro-scale features typically only have indirect influences [141]. The most general case to consider is spherical particulate matter, as it has been found that the surface curvature of nanoparticles can effectively reduce protein adsorption [142,143]. A curved profile within the size range of a classical protein (~ 5-10 nm) will lead to a reduction in the probability that a protein will make a stable binding event [144–146]. Multiple experiments with self-assembled monolayers of decorated gold nanoparticles [147,148] and native arterial vessel nanostructures [149,150] have successfully demonstrated these corollaries in practice. However, controlling the surface topography on the nanoscale alone is not typically sufficient for preventing protein adsorption.

Mimicking the charge of the extracellular matrix (ECM) [151,152] by using phospatidylcholine (PC) and its analogues or comparable zwitterionic polymers which contain both positive charges (like the amines on proteins) and negative charges (like the carboxylic acids in proteins) in close proximity is increasingly being used in a similar manner, a combination that enables extremely high water binding as well as “confused” electrostatic interactions with similarly zwitterionic proteins that thus promotes low protein adsorption [136,153–156]. A number of research groups at developing methods of creating synthetic PC analogues to attach to the surface of biomaterials [157] and as monolayers [158,159], the most popular of which being betaines (sulfo- [160], carboxy- [136,161], phospho- [162]). Polymers containing similar groups have also been discussed in the literature with examples like poly(methacryloyloxyethyl phosphorylcholine) or polyMPC [163], poly(sulfobetaine methacrylate) or polySBMA [164], poly(carboxybetaine acrylamide) (polyCBAA) [165], and poly(sulfobetaineacrylamide) or polySBAAm [166] for example. Many of these PC-looking polymers displayed excellent protein resistance, but their mechanical properties were largely limited and cannot be implemented in a reactive co-extrusion environment [167]. Compared to poly(ethylene glycol) and similar linear polyesters, zwitterions offer the ability for more chemical tunability and a broader choice of ionic groups, which can be arranged in different spatial orientations and deter long-term biofilm formation [161,168], despite having limited monomers available for synthesis [169]. The presence of ions with these coating can create high osmotic pressures at the interface, which can subsequently favour

the minimization of protein adsorption. Additionally, the ionic content can allow for better protection for dehydration via salts persistent in physiological conditions, unlike PEG-based analogues [170].

Changing the chirality (if possible) of the underlying polymer can further tune protein and water affinities, although this is not always possible depending on the polymer or building block being used [171,172]. For example, Wang et al. designed an N-acryolyl-valine brush polymer films with L- and D-amino acids to understand their effects on two adherent fibroblast-like cell lineages (COS-7 and COS-3End.B) [173]. The L-enantiomer yielded less cytotoxicity when compared to the D configuration, but the adhesion process was modulated differently for the different cell lines. Other studies have been performed using DNA (D-ribose and 3-D spiral) [174,175] and ECM proteins that suggest that L-amino acids have a much stronger interaction with both, likely due to differential hydrophobic interactions [176]. These results suggest that the effect of chirality may be linked to the affinity of cells in specific environments. However, the chiral effect may only influence the overall system if the cell interaction is strong, which may be a limitation this approach since the cells *in vivo* lie on a vast gradient of relative affinities and functionalities

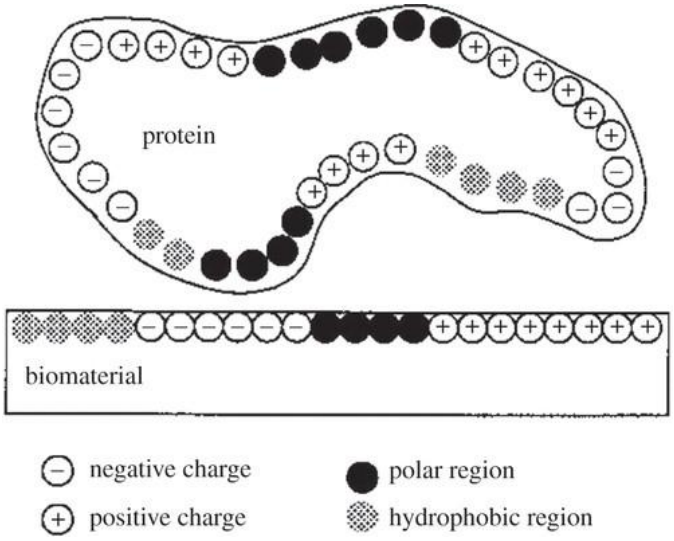

Figure 1.7: Representation of the heterogeneity of a protein surface with distinct regions such as negative or positive charges and polar or hydrophobic regions. Image reproduced with permission from Royal Society of Chemistry (RSC) [177].

Bioactive surfaces can also be fabricated using biomolecule tethering. For example, denatured proteins can be adsorbed or tethered to the interface to passively block binding sites for the adsorption of native proteins, at least in the shorter term [178]; bovine serum albumin (BSA) is typically used for this application since it is an abundant and relatively large (66.5 kDa and 583 amino acid residues) that is harder to displace by other proteins

[179]. Similar strategies can also be applied using immobilized antibodies, enzymes, peptides, nucleic acids, and even cell-signaling ligands [180]; depending on the intended functionality of the modified surface. An engineered bioactive surface must 1. Provide sufficiently high and well-controlled binding capacities for biomolecules, 2. Prevent denaturation of immobilized molecules, 3. And be based on convenient and efficient techniques for immobilization/regeneration [181].

The last main method of reducing protein adsorption involves the use of superhydrophobic or omniphobic surfaces which aim to reduce the surface energy of the material outright, without having an extra layer of bound water as discussed in method 1 above. Superhydrophobic interfaces typically present ordered roughness and hierarchical micro/nanoscale structures that alter the interfacial energy at the 3-phase (air, water, surface) wetting interface to make protein adsorption (or any kind of adsorption) less favourable [182,183]. However, a major limitation of these designs is that they typically involve trapped air (which is meta-stable) or require a lubricant/oil which can leak into the surrounded tissues (i.e. slippery lubricant-infused porous surfaces (SLIPs)), which limit the use of such interfaces in biomedical implant applications [183].

1.3.2 Cell Scaffolds for Tissue Engineering

Hydrogels are often employed to mimic the native extracellular matrix that surrounds cells within the native biological milieu. Hydrogels offer the ability to three-dimensionally control important parameters that make the ECM distinct such as its porosity, mechanical strength, degradation, and materials chemistry (in particular the capacity for dynamic or secondary functionalization [184]). Of these parameters pertinent to design, porosity is arguably one of the most important. Data from 2-D and 3-D cell studies show that, even if the materials used are carefully selected, if the pores are not large enough to allow for free diffusion of oxygen, nutrients and water, the cells will not able to survive and stay encapsulated within the hydrogel matrix [184–188]. Additionally, the size and/or shape of pores controls the selectivity of cell types that will infiltrate and grow within the scaffold [189]. Common methods for inducing porosity within hydrogel matrices includes the addition of sacrificial components that are selectively degraded either *in vitro* or *in vivo* [190,191], electrospinning [192–194], supercritical CO_2 foaming [195] or related gas-expanded supercritical CO_2 methods [196], porogens [197] such as salts [198] that can be selectively dissolved out after crosslinking [199]. However many of these methods leave behind residues of porogens with unknown biological fates, so new research is aimed at finding more biocompatible porogen alternatives like microbubbles [200]. Other modern research is looking at different ways to create these pores outside of using an additive, with some promising and emerging hydrogels for biomedical applications being created via 3-D or additive printing methods [201].

Another very important consideration for biomedical gels is the ultimate fate of the hydrogel and the timeline targeted for the implant. The degradative components of a hydrogel must be tested for toxicity [202] or be classified as “generally regarded as safe”

(GRAS) by the Food and Drug Administration or Health Canada to have no adverse side effects such as inflammation or immunological impact rejection [203]. The targeted rate of matrix degradation and its type (surface or bulk erosion [204]) will typically correlate with how quickly the cells can be predicted to remodel the construct by depositing new natural ECM. As with porosity, the relative rate of degradation can be tuned by the wt% or the amount of functionality of the polymer; specifically, more material or a higher crosslink density results in longer degradation times. The degradation rate can be tailored based on controlling the local environment around a degradable crosslink [205], the degree of crosslinking [206,207], or differences in backbone hydrophilicity to alter the microenvironment around the crosslinks [76]. Alternatively, the use of an enzymatically cleavable peptide crosslinker [151,208] or reductively labile crosslinks [209,210] have been widely reported.

Understanding the role of mechanical properties and how these can be altered to affect cell attachment, spreading, growth, viability, and differentiation pathways is also critical to control cell responses in hydrogel scaffolds [211,212]. Cell differentiation has been shown to be modified by mechanical cues in a number of well-studied cell lines [213,214]. In addition, the concept of mechanical matching is inherently important to the development of new tissues. If the mechanics of the underlying tissue are vastly different than the mechanics of the implanted hydrogels, bulk failures will be observed if the hydrogel is too weak or interfacial failures will be observed if the hydrogel is too strong [184].

A common approach to adding functionality to the surface of the hydrogels is to use polymers that bear additional functional groups not used up in the polymerization or network formation processes. In terms of tissue engineering scaffolds, it is quite common to include peptide and/or recognition sequences for integrins [215] such as RGD to promote adhesion and cell signalling [216–218]; other more complicated or multivalent peptides/ligands can be selected depending on the potential interactions with the biological milieu [219,220], overcoming some of the native limitations of using the polymers on their own [66,216].

1.3.3 Bioactive and Drug Delivery Vehicles

Hydrogels have long been used as a key material in drug delivery, in several cases also combining with functional micro/nanoparticles [221,222]. In general, the general construction and engineered design of the hydrogel is dependent on the physiochemical properties of the payload of interest as well as the requirements/limitations of the physical environment in which the gel is placed. The hydrogel serves as a reservoir or depot for an active agent of choice. By using targeted chemistry or signaling molecules, the drug can be held within the gel matrix and diffuse out over time at a rate depending on the drug-polymer affinity and the diffusion coefficient of drug inside the gel [223]. Thus, the predominant design considerations are the facile delivery of the gel to its site of action, the maximization of the types of cargoes possible for loading by controlling the physiochemical properties, and the achievement of tunable release kinetics, with zero-

order release kinetic profiles often preferred so there is an equilibrated plateau where most cumulative release occurs between the sub-therapeutic (lower limit) and toxic (higher limit) concentrations of drug [224], **Figure 1.8**.

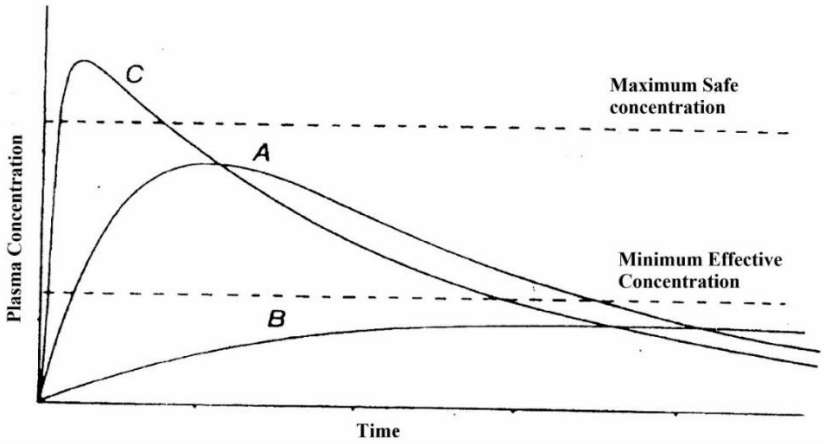

Figure 1.8: Graphical display of zero-order drug release kinetics as a function of plasma concentration (y) and time (x) with cases of ideal moderate-rate of release within the therapeutic window between minimum and maximum safe concentrations (A), of very slow drug absorption (B), and of extremely fast absorption (C), which goes above the toxic threshold. Image reproduced with permission from https://ukdiss.com/examples/zero-order-kinetics-drug-release.php

In terms of achieving facile delivery of the gel to its site of interest, one must first consider the route of administration. In some cases, one route of administration will offer a number of advantages compared to other possible alternatives. For example, the intranasal route of administration not only circumvents the blood brain barrier via the trigeminal and optic nerves [225–227] but also allows for quicker response times at lower dosages for certain CNS modulatory drug reactions since less drug is wasted to the vasculature (IV) or degraded by the stomach's acidic conditions and esophageal esterases (oral).

To improve cargo loading, delivery vehicles can be prepared using comonomers, chemistry, or cargoes that lead to strong affinities between the hydrogel and the drug, whether transient through physical means (i.e. electrostatic interaction between a charged drug and an oppositely charged polyelectrolyte) or more permanently via degradable covalent bonding [224]. For example, hydrogels can be prepared with ionizable functional groups in their polymeric backbones which can offer both pH-dependent control over mesh size/porosity (and thereby diffusion) [228] as well as electrostatic affinity with oppositely-charged drug [229,230]. Polyvalent ionic groups particularly increase the ability for the matrix to favor the loading of charge drugs [231,232]. For less transient affinity (depending on the site and duration of use), certain degradable covalent bonds can be formed either between the drug and matrix directly or through the use of

drug-polymer crosslinkers such as peptide sequences or DNA [79] in which careful selection of the type and quantity of linker used can control the hydrogel degradation and subsequent release of drug [224]. However, one limitation of using a transient crosslinker or molecule for this purpose is that there is always the potential for some polymer-based residues to remain on the surface of the drug once released, thereby potentially affecting its subsequent diffusional release and thereby activity [233].

Additionally, the rate of release of the drug can be controlled by diffusive/osmotic forces alone. In general, increasing the weight percentage of polymer or the number of crosslinkable functional groups will increase the amount of crosslinking that occurs within a specified volume or period of time, contributing to network strength. More crosslinking relates to reducing the amount of void space and pores, which will effectively slow diffusion-based drug release. Sometimes controlling diffusivity by crosslinking density alone is not sufficient to obtain desirable release curves. There are a handful of method to address this by introducing pores to the system either by using naturally porous materials alternatively [234] or those from pressurized gas expanded (PGX) liquids [196]. Other methods to introduce pores include but are not limited to using microbubbles [200], ice-templating [235], porogens [197] or leachates [198]. Regardless of the method employed to introduce the pores, the combination of introducing crosslinking and introducing porosity into a material increases the brittleness and decreases the mechanical strength of the hydrogel. Because of this trade-off, it is quite difficult to create a high strength hydrogel with large pores that is stable for a given application for an extended period of time. Without careful attention to this dichotomy, problems such as less than ideal or too rapid degradation of the matrix or lack of weight bearing capacity compared to a non-porous scaffold of the same materials may be observed, ultimately limiting the duration of by the native tissue [236,237]. Balancing these factors will be dependent on the specific polymer used, the method used to introduce pores, and the intended application for the material, and the timeline required for such an application.

Drug carrier designs that expand on the basic 3-D bulk hydrogel to incorporate nanoparticle drug carriers integrated into nanocomposites or nanoparticle network hydrogel morphologies (consistent with the definitions provided in section 1.2) can provide further control over drug release [238]. Examples of such carriers include microemulsions [239,240], liposomes [241,242], polymeric micelles [62,243], or microgels [93,244] dispersed within a hydrogel matrix or, in the case of certain nanoparticle network morphologies, used as the sole hydrogel building block [245]. Plum pudding hydrogel morphologies in particular allow for a two-step diffusion/partitioning pathway from the carrier particle into the hydrogel matrix and then from the hydrogel matrix to the surrounding tissues, enabling sustained release beyond that which is typically achievable with a bulk hydrogel [106,244].

1.3.3.1 The "Case" for Injectable and/or Sprayable Delivery

In general, hydrogels for biomedical applications can either be pre-cast (often using a mold) and surgically placed [124,196] or injected as a flowable, viscous liquid that is specifically designed to gel chemically [246–248] or physically [249] *in vivo*. Most hydrogel synthetic protocols rely on a bi- or multi-functional crosslinkers and a monomer or series of monomers, each of which can suffer from toxicity issues or the requirement for high temperature or high intensity UV light for initiation. As such, most conventional hydrogels used in biomedical applications are surgically implanted and cut into uniform size before use [233]. Although injectable designs introduce additional design constraints such as the need to precisely tune the gelation time (typically <30 minutes to avoid substantial dilution of the pre-gel solution prior to gelation) or ensuring biological orthogonality such that native tissues are not adversely affected by the *in situ* gelation process [250,251], they are both simpler for a doctor to administer and do not require any specialized steps with regards to administration [252]. Injectables are also on average less invasive [253] for the patient and thus cause less damage to surrounding tissues compared to surgery, which can dramatically impact recovery/healing times [254]. When considering delivery vehicles for agricultural/environmental applications, sprayability (which leverages much of the same scope of chemistries as injectability) is also commonly sought since a spray offers the potential for maximum foliar coverage during application while *in situ* gelation reduces run-off following rain or dew events to reduce the required frequency of re-administration.

1.3.3.2 Bioactive Delivery System Design Considerations

Having a clear understanding of the type of environment that the active agent and its delivery cargo will experience both during synthesis and during application is necessary for the successful translation of a controlled release vehicle. As first described in **Section 1.3.3**, some of the major advantages of using a delivery vehicle rather than a free drug/active agent include: (1) improved protection of the cargo to the surrounding environment; (2) prolonged or shortened circulation times, as desired; (3) better tunability of the drug concentration and release profile; and (4) the potential to increase the degree of target specificity if specific design elements are added, depending on the specific needs/requirements of the system. In this thesis, the two major general systems being studied are the animal biological milieu and the plant biological milieu and surrounding soil environment. While doing a full analysis on the specific details pertinent to both systems is outside of the scope of this literature review, some general design considerations will be outlined to show some of the major differences when engineering delivery vehicles for either application area.

For biomedical applications, the delivery vehicle must be designed to control for the target specificity, the concentration or dose of active agent required, the ideal shape/architecture/porosity of delivery vehicle (which influence both release kinetics and transport properties), and the desired time/release profile observed, all of which will be largely dictated by system through which delivery is occurring [255–257]. For the biological environment, it is important to ensure that: (1) the polymers/additives used are

both non-toxic and bio-orthogonal to prevent any unwanted side reactions within the body [258]; (2) the size is engineered to enable required transport or deformation to permeate specific size excluding membranes (i.e. renal clearance, blood brain barrier, cell-cell junctions, leaky tumour vasculature, etc.) [259]; and (3) the overall vehicle must facilitate desirable diffusion and/or degradation rates to accurately control the rate of cargo release at the site of interest [256]. The selected route of administration (depending on the application) will largely limit the acceptable ranges of the aforementioned parameters significantly [260].

For plant/agricultural applications, the same toxicity, size/deformability, and release profile considerations are still critical to consider but to different extents given the key differences between mammalian and plant cells. From a delivery standpoint the most important differences are size (i.e. plant cells are typically larger), shape (i.e. animal cells are round and irregular but plant cells are more rectangular and uniform), the transport barrier into the cell (i.e. animal cells have only cell membranes while plant cells have cell membranes and cell walls in plants vs. cell membrane only in animals), the presence of cell transport molecules (i.e. glyoxysomes in plants versus lysozomes in animals), the cell cell-cell spacing (i.e. tighter in plants), and the ability to create their own food (i.e. chloroplasts in plant cells, no such ability in animal cells) [261]. In addition to these parameters, agricultural delivery agents are also subjected to very different system conditions such as whole plant pest activity, soil microorganism degradation, variable rain and humidity that can change the partition/diffusion coefficients and wettability, contact with the sun which can cause photobleaching or bulk degradation over time via UV irradiation, and other mechanical forces (i.e. wind or storm conditions).

1.4 Crosslinking and Fabrication Techniques

A complete survey comparing and contrasting the possible methods and chemistries that can be used to create novel hydrogels is outside of the scope of this thesis; the interested reader is referred to the author's published book chapter on the topic [262]. However, a general description of the chemistries and fabrication methods used for the projects described in this thesis will be given for the reader to have context and a deeper understanding of the design considerations taken at each step. **Figure 1.9** below offers a summary of the crosslinking strategies used in this thesis along with other common crosslinking strategies as well.

1.4.1 Direct Crosslinking

One of the easiest ways to generate hydrogels is to use a crosslinker that can directly crosslink a pre-fabricated polymer without the need for any pre-functionalization reaction. There are many examples of these direct crosslinkers being used in the carbohydrate literature, including glutaraldehyde [263–265], epichlorohydrin (ECH) [266–268], sodium trimetaphosphate (STMP) [69,269], sodium polyphosphate (STPP) [270–272], and others. While not a major issue with polyphosphate crosslinkers, many others (in particular glutaraldehyde [273] and epichlorohydrin [274]) suffer from toxicity limitations to human and animal cells in certain dosages or over chronic exposure times.

1.4.2 Crosslinking via free-radical polymerization

Another very common crosslinking method employed for the generation of hydrogels is free radical polymerization (FRP). Free radical polymerization (FRP) is the process of creating radical groups on a typically unsaturated monomer (initiation), typically through the use of a radical initiator, to enable the formation of C-C bonds with other monomers (propagation) to achieve a specific polymer size (termination) [275]. FRP is broadly used to create both conventional and NNH hydrogels. The degree of polymerization can be controlled based on the mass amounts of monomers or through the addition of chain transfer agents like ascorbic acid [276], phenolic compounds (i.e. 4-methoxyphenol or MEHQ), or nitroxides (i.e. 4-hydroxy-2,2,6,6-tetramethylpiperidine 1-oxyl (tempol)) [277] to impact reaction time and radical scavenging capabilities.

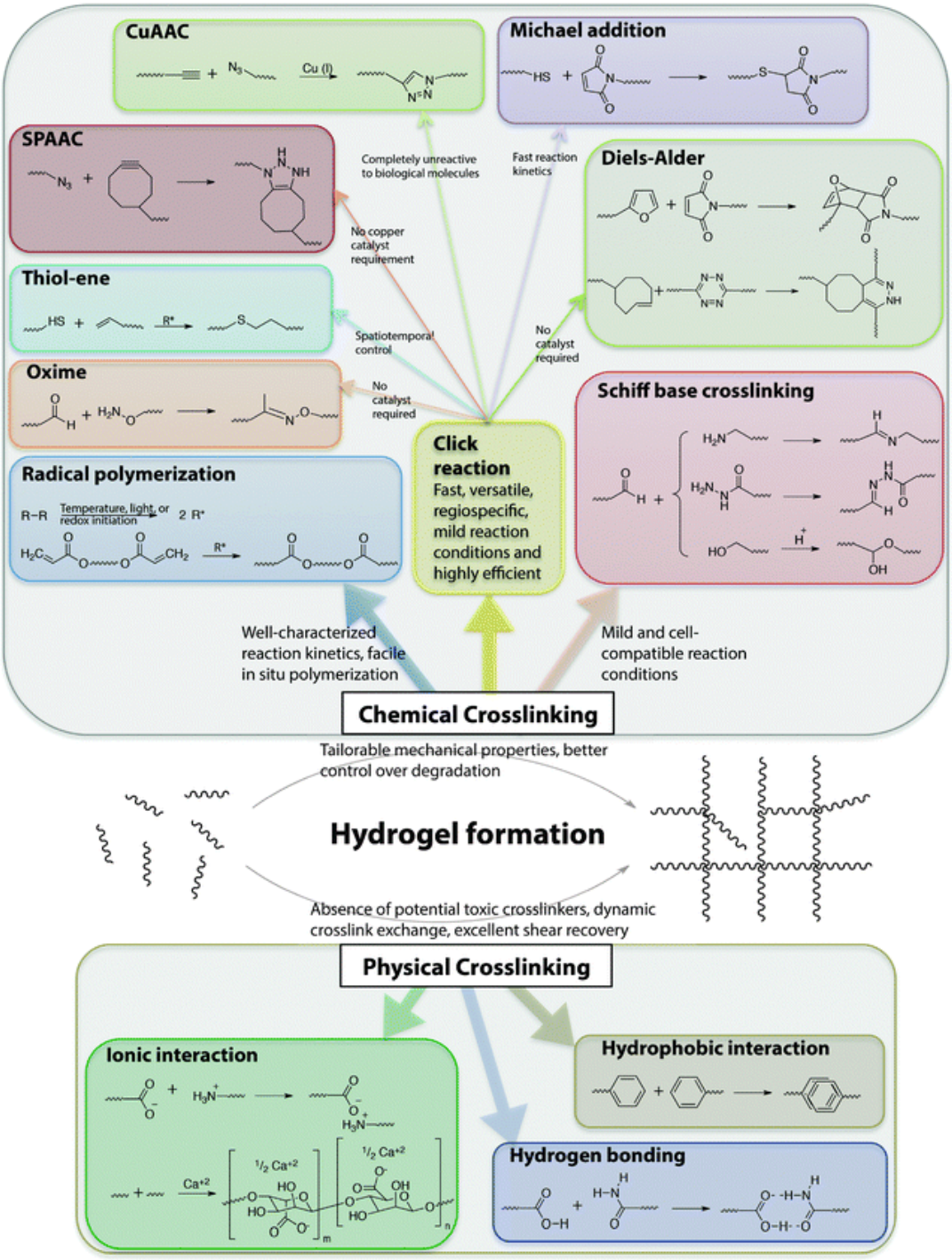

Figure 1.9: Summary of chemical and physical crosslinking strategies for hydrogel formation. The radical polymerization, Schiff base crosslinking, and physical crosslinking strategies were used in the research projects described herein. Image was reproduced with permission under Creative Commons agreement by the Royal Society of Chemistry (RSC) [152].

Radicals are most commonly generated via the temperature-driven degradation of a thermal free radical initiator such as of radical initiators like ceric ammonium nitrate (CAN) [278,279], ammonium persulfate (APS) [280,281] or potassium persulfate (KPS) [282,283], with gelation often accelerated by and catalysts and/or accelerators such as tetramethylethylenediamine (TEMED) [284] to enable gelation at room temperature without the need for additional energy input. Alternatively, high-energy UV light [67,285,286] or oxidation [287,288] can induce radicals without the presence of a catalyst, with UV photopolymerization in which the initiator is only initiated through the shining of long wave (365 nm) or short wave (254 nm) UV light [284] being particularly widely used. Microwave [289] irradiation has also been used *in vivo* since prolonged exposure to UV induces tissue necrosis and given its ability to successfully generate radicals at room or physiological temperature. However, some of these methods (microwave, UV, gamma) require specific equipment that can pose safety risks during the gelation process, depending on the intended application.

While direct radical crosslinking of starch and other carbohydrates is possible (e.g. using gamma irradiation to generate radicals by hydrogen abstraction from the starch backbone), carbohydrates are more commonly crosslinked via FRP following acrylation/methacrylation of the carbohydrate to introduce unsaturated polymerizable functional groups on the polymer. Hyaluronic acid [290], starch [291], and chitosan [292] have all been demonstrated to enable the fabrication of both homopolymer gels and blends crosslinked by FRP, using either all (meth)acrylated polymer precursors or a mixture of such polymers with monomers to create more advanced materials (i.e., methacrylated chitosan + PNIPAM hydrogels [293]).

1.4.3 Crosslinking via reactive mixing

Another crosslinking method to create hydrogels requires one or more moieties that can react with another chemically distinct moiety spontaneously upon mixing to form a covalent crosslink (often referred to as *in situ* or mixing-induced gelation). Common bioconjugate chemistries often applied in this context include Michael-type additions, disulfides, hydrazones, oximes, Diels-Alder cycloaddition, alkyne-azide "click" chemistry (strain-promoted and otherwise), and imines [262]. Of particular interest to this thesis are, imine linkages, a type of Schiff base possessing the general structure of $R_2C{=}NR_0$ (where R_0 is not H) that has been widely used to fabricate degradable hydrogels in biomedical applications [117,294]. Imine covalent bonds form readily (seconds to minutes) between amines and aldehydes/ketones but are highly reversible in water, with the rate of crosslink hydrolysis related to the concentration of the precursor polymers and/or the number of crosslinks formed between the precursor polymer chains. One of the major benefits of using imines herein is that they have quicker degradation times in neutral solutions compared to other hydrolysable crosslinks, such as hydrazones, which tend to degrade at faster rates only in more acidic microenvironments. Degradation can be further tuned by incorporating hydrophobic groups near the reactive imine precursors to affect water imbibition and thus the hydrolytic half-life of the imine bond [295,296], using sodium cyanoborohydride to reduce the imine and create secondary amine linkages

to form a non-degradable crosslink (reductive amination) [297], or by using double network strategies to induce quicker gelation [298].

1.4.4 Crosslinking via physical interactions

A variety of physical forces or interactions can also be applied to form hydrogels or manipulate the interactions between nanoparticle building blocks for NNHs. Hydrophobic interactions are driven by the maximization of the entropy of water by minimizing the contact between the hydrophobic moiety and the aqueous environment. This method has been applied to create carbohydrate-based physical hydrogels [299,300] by introducing hydrophobic groups on the carbohydrate backbone in a number of ways [301,302]; alternately, a low concentration of such groups will promote aggregation/self association to viscosify a precursor polymer solution without inducing bulk gelation or a stand-alone elastic network [303]. Electrostatic interactions between cationic, anionic, and/or zwitterionic precursor polymers can also induce gelation or, like with hydrophobic interactions, weaker interactions depending on the charge density of the polymers and the salt concentration in the surrounding solution [304] [305].

1.5 Probing Hydrogel Morphologies

When conducting studies involving either nanocomposite (NCs) or nanoparticle network hydrogels (NNHs), it is imperative that the internal morphology of the gel is characterized by some means to determine how the nanoparticles are distributed (i.e. homogeneously or heterogeneously) and what type(s) of nano-domains they form. Such network structure considerations have a direct relationship with the functionality of the entire network for its intended purpose. The mesh size, crosslink density, and mass distributions in hydrogels can be probed using techniques like light scattering [306], X-ray scattering [307], and turbidity measurements [308] for example. Additionally, the internal porosity can be characterized if the size and distribution of the pores makes a profound impact on the functionality of the gel, as it does in the case of both controlled release and tissue engineering. Methods such as fluorescence recovery after photobleaching (FRAP) [309], pulsed field gradient (PFG) NMR [310], modified electron microscopy methods (i.e. cryo, high vacuum, and environmental scanning) [311], or molecular probe diffusion experiments [312] are most commonly used for this purpose. However, a once "niche" field of research known as small angle neutron scattering (SANS) has started to be applied more frequently within materials science and engineering since it can allow researchers to assess crosslink density, mass distributions, and internal porosity simultaneously within both soft and hard materials at the nanoscale level.

Small angle neutron scattering (SANS) is a particularly powerful tool for assessing hydrogel morphology now being broadly used to gain more information within the hydrogel and soft material scientific communities [313], **Figure 1.10**. The method involves exposing a sample to a collimated beam of neutrons from a cold neutron source (uranium) and using the resulting scattering profile to understand how the neutrons interact with the internal structure of hydrogels and/or particles [314,315]. The SANS method is similar to light or X-ray scattering, but neutrons interact with the nucleus while

X-rays interact with electron clouds. If an X-ray and a neutron both have the same de Broglie wavelength of 0.15 nm for example, the neutron possesses 36 meV of energy, while the X-ray will have 8.2 keV of energy - nearly 200,000x higher [316]. As such, neutrons are much better at preserving sensitive samples like hydrogels. Furthermore, since neutrons scatter off nuclei (which have dimensions 10^4-10^6 times smaller than their wavelength while X-rays interact with the entire cross-section of the atom (similar in size to the X-ray wavelength), neutrons have significantly better penetration depth/efficacy and thus allow for quantification of higher length scale feature sizes in the angstroms to near micron size range [317].

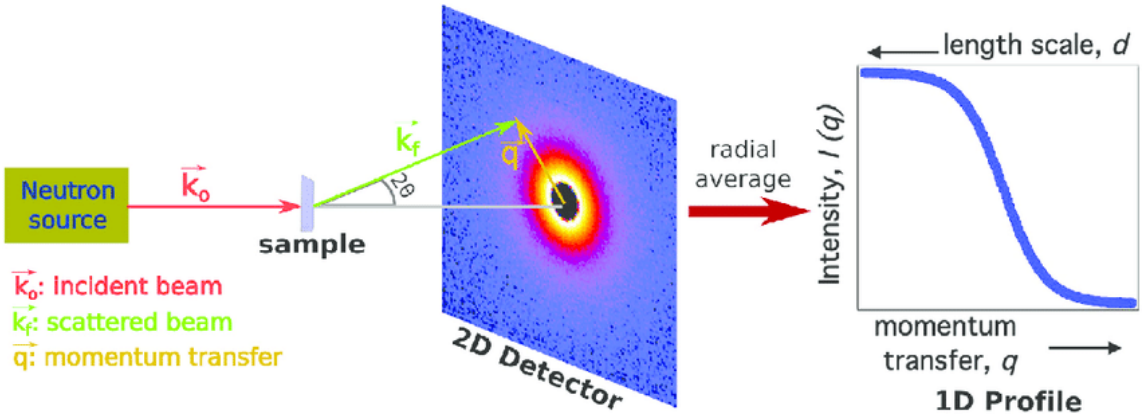

Figure 1.10: Schematic of a small-angle neutron scattering experiment showing the irradiation/scattering (left) and the representative data gleaned (right). Image reproduced with permission from Elsevier under the Creative Commons CC-BY license [318].

Our research group has extensively applied SANS to investigate the internal morphology of pre-formed hydrogels and microgel particles to gain more insight into their properties [64,246,248,285]. However, emerging techniques in the literature attempt to use SANS not only to track the final morphology of a material but also as a method to track the kinetics of different phenomena (i.e. gelation or network formation) in real-time [319,320]. While the relative number of papers on this is small compared to other *in situ* gelation/aggregation characterization methods, there are reports of the use of SANS in this context for associative polymers [321], sticky microgels [322], proteins [323], ionic liquids [324], and nanoparticles in the presence of a polymer [304], typically by tracking increases in the intensity of neutron scattering due to new crosslinks or structures formed using acquisition times that are fast on the timescale of the gelation/structure evolution process being tracked. This linkage between structure and gelation kinetics is particularly informative with NNH hydrogels, as such measurements would enable real-time tracking of changes in nanoparticle clustering and/or nanoparticle dimensions during the gelation process. Specifically, such knowledge would improve our understanding of the role of the nanoparticle in the network formation process as well as how (or if) network formation alters the internal structures nanoparticle building blocks of NNHs.

1.6 Objectives

The goal of this thesis project is to chemically modify SNPs and then use these functionalized SNPs to design, characterize, and apply starch-based nanoparticle network hydrogels (NNHs) in several applications related to bioactive delivery, tissue scaffold/biomaterial engineering, and environmental plant/soil studies [68,325–328]. It is proposed that completion of this multidisciplinary project will yield sustainable stimuli-responsive hydrogels made from SNPs, which are expected to offer economic and societal benefits to Canada within the next ten years and significantly add to the scientific literature. As previously described, while there have been many descriptions of the synthesis and use of starch nanoparticles in the literature, the unique properties of starch nanoparticles as nanoparticle network hydrogel building blocks (i.e. their degradability, hygroscopicity, tunable chemistry, and - for our SNP source - small size) have not previously been explored despite the interesting potential impacts of these parameters on the performance of the resulting NNHs.

More specifically, the work described herein can be broken down into six unique projects (**Chapters 2-6** herein), each attempting to answer a different research question with respect to the formation of NNHs based on SNPs. **Chapters 2 and 3** describe the key physical properties and explore the kinetics of network fabrication in SNP-based NNHs, while **Chapter 4** demonstrates the potential utility of SNP-based NNHs in biomedical applications and **Chapter 5** explores the utility of SNP-based NNHs in agricultural applications.

Chapter 2 covers the development of the first reported hydrogels made from only SNP building blocks, without the need for a long chain crosslinker or another polymer for support. More specifically, we report the first colloidal nanoparticle network hydrogel (NNH) (described in **Section 1.2.3.2**) using covalent crosslinking via free radical photopolymerization (FRP) as previously described. By functionalizing the SNPs with methacrylic anhydride, a terminal vinyl group was tethered to the NP surface at varying degrees of substitution (DS) to create gels with varying crosslinking densities. By comparing SNP-based gels to those made from conventional soluble starch (SS), we were able to establish a reliable way to crosslink SNPs can create NNHs with stronger mechanics, low cell-adhesive properties, and minimal cytotoxicity to NIH 3T3 fibroblasts.

Chapter 3 expands on the photopolymerizable colloidal gel work from **Chapter 2** by exploring the kinetics of photogelation of SNPs with or without charge relative to linear soluble starch using the new technique of very small angle neutron scattering (vSANS) that allows for rapid collection of SANS data. The vSANS and dynamic hybrid rheology (DHR) data suggest that the presence of charge promotes more particle-particle repulsion before gelation, leading to quicker gelation times (less Brownian motion). In general, differences in the network formation rate and structure were inferred by noting the differences in the scattering angle range related to the formation of new C-C bonds after photopolymerization.

Chapter 4 describes another biomedical application of SNP-based hydrogels based on imine crosslinking chemistry between SNPs modified with aldehyde groups and carboxymethyl chitosan in order to safely deliver a novel antipsychotic peptide to the brain of schizophrenic rats. Results showed that the in situ-gelling and degradable bulk nanoparticle network hydrogels enabled intranasal delivery via injection or spray, high nasal mucosal retention, and functional controlled release of an antipsychotic peptide drug (PAOPA). PAOPA-loaded SNP-CMCh hydrogels were shown to alleviate negative symptoms associated with schizophrenia (i.e. decreased social interaction time) for up to 72 hours in an induced-schizophrenia rat model at a lower drug dosage (0.5 mg/kg) compared to conventional PAOPA administration via the intraperitoneal route, which requires twice the PAOPA concentration to provide a therapeutic effect persisting for only a few hours. This chapter thereby shows the versatility of the SNP building blocks to be used with a wide range of chemistries, depending on the needs of the final application.

Chapter 5 describes the fabrication of hydrophobized SNPs via chemical modification with either succinic (SA) or octenyl succinic anhydride (OSA), applying information we learned about the loading properties of SNPs in Chapter 5 and the interfacial properties of SNPs in Chapters 3 and 4 to create SNPs with very different surfaces compared to their starting forms. Hydrophobization of the SNPs allow for enhanced particle-particle interactions to potentially form a gel (if desired), create higher affinity delivery vehicles for hydrophobic bioactives in agriculture, or to allow for better attachment to plant leaf surfaces for foliar drug delivery. The native neutral surface charge and small size of the SNPs are demonstrated to enable modified SNPs to be highly effective but safe penetrants for plant-based bioactive delivery.

Overall, the work described in this thesis aims to leverage the unique properties and adaptable chemistry of SNPs to fabricate new functional hydrogels with translational potential in biomedical and agricultural applications due to the high scalability of the reactive extrusion-based SNP production as well as the inexpensive nature of the crosslinking and modification approaches described herein (many of which may be possible to perform simultaneous to the reactive extrusion-based method of SNP fabrication).

Chapter 2: UV Photopolymerized Starch Nanoparticle (SNP) Network Hydrogels for Biomedical Applications

Preface

Chapter two and its corresponding appendix/supporting information section are reproduced from the initial publication in *Carbohydrate Polymers* describing the development of UV photopolymerized SNP-based hydrogels designed for application in biomedical applications. Methacrylic anhydride was used to impart vinyl groups onto the surface of the SNPs so when exposed to long wave (365 nm) UV light, a nanoparticle network hydrogel (NNH) could form. Modified and native SNPs were first characterized for various physical (molecular weight and particle size distributions) and chemical properties (degree of methacrylic substitution). The resulting nanoparticle network hydrogels made from these modified SNPs were then characterized for their swelling/degradability, mechanical properties, cytotoxicity levels, and internal gel morphology. This chapter largely serves as the initial steppingstone for which all of the other chapters were arrived from since this is the first description of an all-starch nanoparticle network hydrogel in the scientific literature. More tunable and advanced cross linkages were further studied in response to the promising results gleaned in this study. The main goal of this chapter was to determine if starch nanoparticle network hydrogels would have any biomedical utility to begin with before beginning more advanced or targeted delivery studies.

Michael J. Majcher[1] (email: majcherm@mcmaster.ca), Carter L. McInnis[1] (email: carter.l.mcinnis@gmail.com), Sebastian Himbert[2] (email: himberts@mcmaster.ca), Richard J. Alsop[2] (email: alsoprj@mcmaster.ca), Dennis Kinio[3] (email: dkinio@ecosynthetix.onmicrosoft.com), Markus Bleuel[4] (email: markus.bleuel@nist.gov), Maikel C. Rheinstädter[2] (email:rheinsm@mcmaster.ca), Niels M.B. Smeets[3] (email: NSmeets@walkerind.com), Todd Hoare[1*] (email: hoaretr@mcmaster.ca)
[1]Department of Chemical Engineering, McMaster University, 1280 Main Street West, Hamilton, ON L8S 4L8, Canada
[2]Department of Physics and Astronomy, McMaster University, 1280 Main Street West, Hamilton, ON L8S 4L8, Canada
[3]EcoSynthetix Inc., 3365 Mainway, Burlington, ON L7M 1A6, Canada
[4]NIST Center for Neutron Research, National Institute of Standards and Technology, Gaithersburg, Maryland 20899-6100, United States

In Majcher, M.J., et al., "Photopolymerized Starch Nanoparticle (SNP) Network Hydrogels", *Carbohydrate Polymers*, **2020**, 236, 115998, doi: https://doi.org/10.1016/j.carbpol.2020.115998.

Abstract
Starch is an attractive biomaterial given its low cost and high protein repellency, but its use in forming functional hydrogels is limited by its high viscosity and crystallinity. Herein, we demonstrate the use of fully amorphous starch nanoparticles (SNPs) as functional hydrogel building blocks that overcome these challenges. Methacrylation of SNPs enables hydrogel formation via photopolymerization, with the low viscosity of SNPs enabling facile preparation of pre-gel suspensions of up to 35 wt% SNPs relative to <10 wt% with linear starch. Small angle neutron scattering indicates a significantly different microstructure in SNP-based hydrogels compared to linear starch-based hydrogels due to the balance between inter- and intra-particle crosslinks, consistent with SNPs forming denser and stiffer hydrogels. Functionalized SNPs are highly cytocompatible at degree of substitution values <0.25 and, once gelled, can effectively repel cell adhesion. The physicochemical versatility and biological functionality of SNP-based hydrogels offer potential in various applications.

2.1 Introduction

The use of starch as a hydrogel building block has attracted growing interest due to its low cost, renewability, and ready availability [31,329]. For biomedical applications, the innate enzymatic degradability of starch into glucose [330,331] coupled with its highly hygroscopic nature [332] offer advantages for enabling clearance while maintaining high water contents and thus minimal protein adsorption/cell adhesion. While multiple starch-based hydrogels have been reported [31], the high viscosity, high degree of crystallinity that can impede water binding and reduce the reactivity of hydroxyl groups for functionalization [333], and large batch-to-batch and source-to-source variability of starch [8] all pose challenges to its practical use for hydrogel fabrication.

As an alternative to using linear starch as a hydrogel building block, starch nanoparticles (SNPs) offer multiple beneficial properties. In general, nanoparticles may be covalently or physically associated with another hydrogel, physically encapsulated another bulk hydrogel matrix, or (if they are themselves gels) comprise the hydrogel matrix without any additional materials [79]. The incorporation of nanoparticles into hydrogels has been demonstrated to (1) increase the density and, by extension, alter the mechanics of the gel network, (2) control the diffusion and/or partitioning and thus release of a payload; (3) introduce differential degradability into the hydrogel; and/or (4) produce useful optical properties [93,334]. Both starch nanoparticles [335,336] and starch nanocrystals [337,338] have been explored as potential nanoparticle fillers in this context to create nanocomposite hydrogels both via simple physical incorporation [122,339] (s well as chemical grafting [118,340]; in a few cases, multi-functional SNPs have been used as crosslinkers to form hydrogels [116] or networks with other nanoparticles [341]. Significantly fewer reports of all-nanoparticle hydrogels in which nanoparticles are directly crosslinked together to form the hydrogel network have been published, with network formation having been achieved via double layer repulsion of dense nanoparticle suspensions [342,343], photopolymerization [344], click chemistry [345], and temperature-induced gelation [346]. However, aside from the chiral nematic self-gelation of cellulose nanocrystals that forms gels that are inherently unstable to dilution [172], to our knowledge no sustainable nanoparticle network hydrogel composed of solely nanoscale building blocks has yet been reported.

Effective formation of an SNP-based hydrogel is dependent on the formation of amorphous and reproducible SNPs. Traditional methods for fabricating SNPs include the precipitation of amorphous starch granules [119,347], complex formation and enzymatic hydrolysis [348], microfluidization-based homogenization [50], and ultrasound treatment [349–351]. However, all these methods result in highly variable particle size distributions and morphologies. Newer strategies offer other challenges; for example the surfactant-regulated self-assembly of size-controlled SNPs upon enzymatic hydrolysis [352] results in narrowly dispersed 15-35 nm SNPs but offers limited scalability [353] while chemical extraction of phytoglycogen nanoparticles naturally existing in certain corn varieties creates highly monodisperse nanoparticles but is resource-intensive and results in dendritic rather than gel-like nanoparticles [57,354]. A more scalable strategy involves a

process in which starch is gelatinized, "regenerated" via a secondary process, and then further cross-linked to form a nanoparticle [6,353]. Reactive co-extrusion is one such process, by which native starch granules (~ 30 μm) are plasticized and subsequently crosslinked within a twin screw extruder to yield fully amorphous 20-50 nm SNPs [52,355,356]. The extremely high specific surface area of these SNPs, coupled with the potential for high-density surface functionalization of the fully amorphous nanoparticles, makes such SNPs attractive building blocks for hydrogels. Specifically, we hypothesize that using reactive co-extrusion processed and functionalized starch nanoparticles as building blocks for hydrogel formation will facilitate the formation of denser and stiffer hydrogels than can be achieved with linear starch. In particular, the potential to leverage both intra-particle and inter-particle crosslinking to regulate hydrogel properties, coupled with the ease of functionalization of the fully amorphous SNPs, will enable the design of highly tunable biopolymer hydrogels for biomedical applications.

Herein, we apply SNPs fabricated via reactive extrusion and subsequently methacrylated via a highly scalable chemistry to fabricate SNP-based nanoparticle network hydrogels via photopolymerization. SNP-based hydrogels can be prepared at ~4-fold higher mass concentrations relative to linear starch-based hydrogels while also exhibiting enhanced mechanics, low cytotoxicity, and high cell repulsion. In addition, the internally crosslinked structure of the 20-50 nm SNP building blocks is shown to substantially alter the internal morphology of the resulting hydrogel without negatively impacting (or, in some cases, improving) the biological properties of the hydrogels.

2.2 Experimental Section

2.1.1 Materials

Experimental grade starch nanoparticles (SNPs) and experimental grade cold water-soluble linear starch (SS) (both waxy starches with 100% amylopectin) were provided by EcoSynthetix Inc. (Burlington, ON). Methacrylic anhydride (MAAn, 94%), Irgacure 2959 photoinitiator (98%), bovine serum albumin (BSA) (≥ 98%), fluorescein isothiocyanate isomer I (FITC) (≥ 97.5%), and resazurin sodium salt (80%) were all obtained from Sigma Aldrich (Oakville, ON) and used as received. 3T3 Mus musculus mouse fibroblast cells were obtained from ATCC Cedarlane Laboratories (Burlington, ON) and cultured in Dulbecco's modified Eagle's medium (DMEM) supplemented with 10% fetal bovine serum (FBS) and 1% penicillin streptomycin (PS) (all from ThermoFisher). Trypsin-EDTA and calcein AM/ethidium homodimer live/dead assay kits were obtained from Invitrogen. For all experiments, Millipore Milli-Q grade distilled deionized water (MQW, 18.2 MΩ cm resistivity) was used.

2.2.2 Synthesis of Methacrylated Starch

SNPs were functionalized with methacrylate groups using a method adapted from literature [357]. Briefly, a 25 w/v% dispersion of 50 g dry weight of SNPs and 0.7 g of sodium carbonate in MQW was created using an IKA homogenizer operating at 12,000 rpm. Subsequently, a predetermined amount of MAAn to target degree of substitution (DS) values of 0.25 (11.44 mL MAAn), 0.10 (4.56 mL MAAn), 0.050 (2.29 mL MAAn),

and 0.015 (0.69 mL) was added dropwise over a period of 60 min while the reaction temperature and pH were held at 25 °C and 10.4 respectively, the latter through the addition of 1 M sodium hydroxide (NaOH) as required. The reaction was run for an additional 30 min, after which the pH was neutralized to pH 7 using 1 M hydrochloric acid (HCl) and the product was dialyzed against MQW over 6 x 6h dialysis cycles using a 3.5-5 kDa molecular weight cut-off membrane. The same procedure was followed to methacrylate the cold water-soluble linear starch control (SS) at the same DS values, but the w/v% of the SS was lowered to 7.5 w/v% to compensate for the higher viscosity and molecular weight of SS versus SNPs. **Supplementary Information Figure S2.2** shows a detailed mechanism of the esterification reaction performed using MAAn.

2.2.3 Chemical Characterization of Functionalized Starch

The degree of substitution (DS) of methacrylate groups on both modified SNP and SS samples was analyzed using ^{1}H nuclear magnetic resonance (Bruker AVANCE 600 Hz 1H-NMR) by comparing the intensities of the vinylic protons (δ = 5.8 and 6.2 ppm) with that of the anomeric α-carbon present on each functional unit of the glucose backbone (δ = 5.4 ppm); see the representative ^{1}H-NMR spectra in **Supplementary Information Figure S2.3 (a, b)** and data summary in **Supplementary Information Table S2.1**. A comparison between the theoretical/targeted DS and the experimental/actual DS is also provided in **Supplementary Information Figure S4**.

2.2.4 Physical Characterization of Starch Hydrogel Precursors

The hydrodynamic radius, refractive index, and molecular weight distribution of unmodified and methacrylated SNPs and SS were analyzed using a Viscotek GPCmax and Triple Detection Array 305 (Malvern) using an Aquagel PAA-200 series column (PolyAnalytik). All samples were run at room temperature at 3-5 w/v% using dimethyl sulfoxide (DMSO) containing 0.05 M lithium bromide as the solvent and pullulan as the calibration standard. The particle size of SNPs before and after functionalization was analyzed using three methods: (1) Dynamic light scattering (DLS) was run at a particle concentration of 0.1 wt% (count rate 150-200 kcps) in a 1 mM sodium chloride solution following water bath sonication for 5-10 min at room temperature prior to analysis to reduce aggregation. The reported average particle sizes/error bars represent the averages/standard deviations of four independent measurements (Supporting Information **Figure S2.5(a, b) and Table S2.2**); (2) Nanoparticle tracking analysis (NTA, NanoSight LM10) was used to measure the number particle size distribution. All samples were run at a concentration of 100 µg/mL in MQW and sonicated for 5-10 min prior to testing as described for DLS measurements to ensure good SNP dispersibility (**Supporting Information Figure S2.6**); (3) Transmission electron microscopy (TEM) was performed using a JEOL 1200EX TEMSCAM instrument to assess particle size and structure. In order to prevent film formation of SNPs on the TEM grid, a low contrast poly(methyl methacrylate) (PMMA) latex (particle size = 300 nm) was used as an imaging aid by aliquoting 0.5 wt% SNPs with 0.1 wt% PMMA latex dispersions on a standard carbon/Formvar TEM grid and drying overnight prior to measurement. Average particle

size results are reported based on the average of the sizes reported from ImageJ analysis of 30-40 particles, with the error bar representing the standard deviation.

2.2.5 Formation of SNP and SS Hydrogels

To fabricate all-SNP nanoparticle network hydrogels, 35, 25, or 10 wt% dispersions of methacrylated SNPs were prepared in MQW following homogenization using an IKA overhead homogenizer operating at 10,000-12,000 rpm; the solids content of each "dry" SNP sample was confirmed using a CEM microwave dryer to ensure consistency in dry SNP contents between the prepared hydrogels. Subsequently, for every 1 mL of starch solution, 100 µL of a 1.5 w/w% Irgacure 2959 solution in DMSO was added to the pre-gel dispersion, yielding a final concentration of 0.15 wt% of Irgacure 2959. Following 5-10 minutes of vortexing, the samples were pipetted into a 12.7 mm diameter/4 mm thick silicone mold and then irradiated at a wavelength of 365 nm using a CureAll lamp (80 mW/cm^2 power) for 10 min., an irradiation time chosen based on a preliminary gelation kinetics experiments (see **Supplementary Information, Table S2.3**). **Figure 2.1** summarizes the full fabrication scheme used to generate the SNP hydrogels. Hydrogels based on SS precursors were prepared using the same protocol but using lower starch concentrations (10, 7.5 and 5 wt% SS) accounting for the high viscosity of the SS precursor polymers.

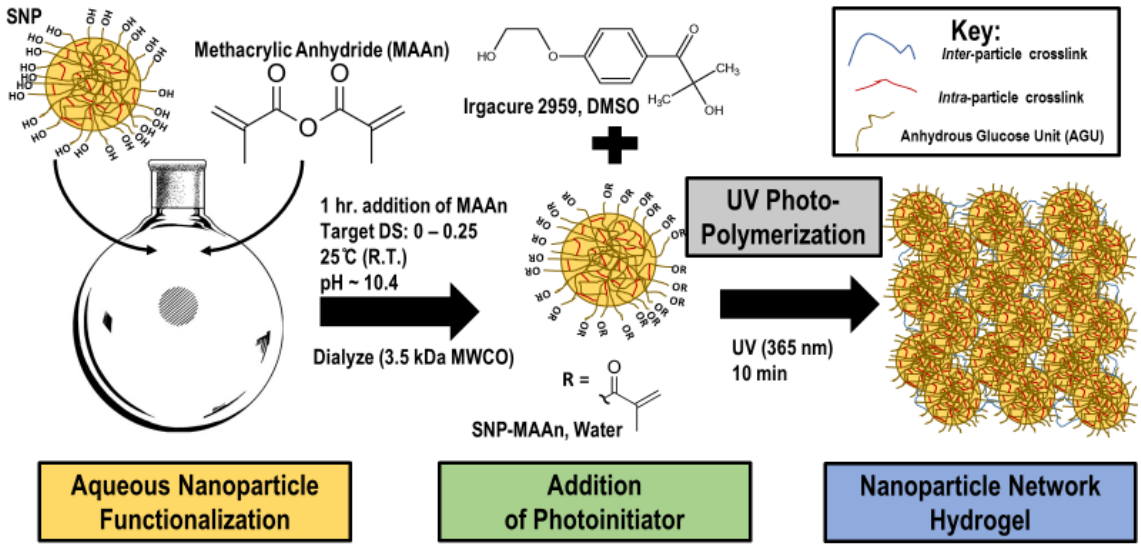

Figure 2.1 Experimental protocol for methacrylation and subsequent photogelation of SNP-based nanoparticle network hydrogels.

2.2.6 Hydrogel Characterization

Gravimetry was used to track both hydrogel swelling and degradation over time. Samples were prepared as described in section 2.5 and subsequently incubated in 10 mL of 10 mM PBS at 37 °C using cell culture inserts (0.4 µm pore size) inserted in 12-well plates. The equilibrium swelling ratio was defined as the point at which the rate of gel mass change

between two consecutive samples was statistically insignificant via a two-tailed t-test (α = 0.05). The swelling ratios reported were calculated by comparing the mass of the unswollen hydrogels directly after synthesis in their silicone molds to their equilibrated, fully swollen state. The mechanical properties of the hydrogels were assayed using the same hydrogel disks using a MACH-1 micromechanical tester (Biomomentum Inc., Laval, Canada). A strain sweep was performed spanning an amplitude of 0.1 deg to 2.154 deg at a frequency of 1 Hz to identify the linear viscoelastic range; following, a frequency sweep was performed using 1% strain over a frequency range of 0.1 Hz to 2.154 Hz to determine the storage (G') and loss (G") moduli. The raw data was analyzed using the sinusoidal analysis function on the MACH-1 analysis software.

2.2.7 Gel Microstructure

Both dispersions and gels of SNPs were analyzed using the NGB 30 m small angle neutron scattering (SANS) instrument at the NIST Center for Neutron Research (NCNR) in Gaithersburg, MD, USA. Gel samples were fabricated inside the NCNR's standard titanium sample holders equipped with two quartz windows (19 mm diameter, 2 mm path length) by photopolymerizing gels of the same compositions described above. For SNP dispersions, the "fuzzy sphere" model of Stieger et al. [358] with an additional square well potential to account for aggregation [359] (**Equations 1 & 2**) was used to fit the SANS data, allowing for extraction of the radius of the SNPs (*R*), the polydispersity of the SNPs, the width of "fuzzy" interface σ (although fitting was effective in each case when this value was manually set to 0 for all samples, suggesting that SNPs can be modeled as homogeneous spheres rather than fuzzy spheres), and the Ornstein-Zernike Lorentzian correlation length ξ (related to the mesh size of the internal gel network).

$$I(q) = \frac{scale}{V}(\Delta\rho)^2\langle A^2(q)\rangle S(q) + \frac{I_{lor}(0)}{1+\xi^2 q^2} + bkg \qquad \textbf{Eqn. 1}$$

$$A(q) = \frac{3[\sin(qR) - qR\cos(qr)]}{(qR)^3} exp\left(\frac{-(\sigma_{surf}q)^2}{2}\right) \qquad \textbf{Eqn. 2}$$

Note that the structure factor *S(q)* was set equal to 1 for all *q* in the case of diluted solutions.

SNP hydrogel data were fitted to the Porod model (**Equation 3**) that describes networks in the absence of static inhomogeneities [63,360]:

$$I(Q) = \frac{s_{porod}}{Q^n} + \frac{s_{oz}}{1+(Q\xi)^m} + bkg \qquad \textbf{Eqn. 3}$$

Here, s_{porod} and s_{oz} measure the scale of the Porod and Ornstein Zernike functions, *n* is the low-*q* Porod exponent describing clustering and swelling within a network [361], ξ is the correlation length of the network indicative of gel mesh size, *m* is the Lorentzian exponent quantifying polymer-solvent interactions, and bkg is the incoherent

background. All fits were performed using Igor Pro (Software Version 6.37) together with the SANS reduction and analysis macro provided by the NCNR.

2.2.8 *In Vitro* Cytotoxicity Assay and Leachate Test

The cytocompatibility of the SNP and SS precursor solutions used was assessed using a resazurin assay. NIH 3T3 Mus musculus fibroblasts were plated at a density of 10,000 cells per well in a 96-well plate and maintained in DMEM media supplemented with 10% FBS and 1% penicillin/streptomycin. Cells were cultured for 24 hours at 37 °C and 5% CO_2 in 1 mL of DMEM, after which SNP or SS samples (both unmodified and methacrylated) at concentrations ranging from 0.1-10 mg/mL were added and cells were incubated for an additional 24 h. A resazurin solution was added to each well give a final concentration of 10 μg/mL resazurin and incubated for 8 h, after which the entire supernatant was removed, loaded into a 96 well plate, and analyzed on a plate reader (Infinite M200 Pro, Tecan; λ_{ex} = 560 nm, λ_{em} = 590 nm). All results were normalized using media and hydrogel-only blanks. Error bars represent the standard deviation of the measured cell viability percentages (n=4 wells/sample).

To assess the potential cytotoxicity of any gel leachates, pre-formed hydrogel disks (6.35 mm diameter, 4 mm thickness) were incubated in 5 mL DMEM with 10% FBS and 1% Pen-Strep for 1, 3, 5, and 7 days at 37 ˚C under 500 rpm shaking. Following, the samples were filtered using a 0.45 μm filter (Acrodisc) and frozen for storage (-20˚C). When all leachate samples were collected, the samples were thawed and 50 μL was added into a 96 well plate containing 10,000 NIH 3T3 cells/well (n=6). Cytotoxicity was measured using the resazurin assay previously described.

2.2.9 *In Vitro* Cell Adhesion Assay

To assess the adhesion of cells to the hydrogels, 270 μL of each filtered polymer precursor solution was aliquoted into a 48-well plate. The precursors were photopolymerized at 365 nm for 10 min and left to sit for 1 h, after which they were swollen to equilibrium over 48 h following the addition of 600 μL of sterile 10 mM PBS to each well. The gels were washed with DMEM media, after which 10,000 NIH 3T3 cells in 600 μL media were plated in each well. The samples were incubated at 37°C and 5 % CO2 for 1, 3, 5, or 7 days, after which a LIVE/DEAD assay (2 mM calcein and 4 mM ethidium homodimer) was used to stain the cells. The samples were washed three times with sterile PBS to remove any weakly bound cells, after which the residual cells were imaged using excitation wavelengths of 525 nm (live) or 470 nm (dead) using an Olympus inverted microscope.

2.3 Results and Discussion

2.3.1 Characterization of Methacrylated SS and SNPs

Esterification of both soluble starch (SS) and SNPs with methacrylic anhydride introduces photopolymerizable methacrylate groups on starch. Degree of substitution (DS) values measured via ^{1}H NMR (**Supplementary Information Table S2.1**) were lower than those predicted by stoichiometry but scaled with the predicted DS values

(**Supplementary Information Figure S2.4**), with the linear starch yielding a slightly higher DS than SNPs for most DS values tested. These results are consistent with the increasing steric barriers to methacrylation of a crosslinked starch nanoparticle relative to fully solubilized starch. The methacrylation reaction does not significantly affect the hydrodynamic diameter of either SS or SNPs in solution, with GPC analysis showing similar retention profiles for both SS and SNPs before and after methacrylation (**Figure 2(a, b)**). Dynamic light scattering (DLS) analysis on SNPs confirms the independence of particle size on the DS value (**Table S2.2 and Table 2.1**). Intensity-averaged DLS measurements (**Supplementary Information Fig. S2.5**) indicate that SNPs have two sub-populations suggestive of minor aggregation in the sample independent of sample concentration: one centered at ~20 nm (20-40% of scattered intensity) the other centered at 170-190 nm (90-100% of scattered intensity). This result and interpretation are consistent with the NTA analysis (**Fig. 2.2c and Table 2.1**), which consistently reported sizes of ~180 nm for each SNP tested (note that the sizes of free SNPs are at or below the 30 nm lower limit of detection of NTA). Converting the intensity- weighted DLS results to number-weighted results by assuming a refractive index of 1.34 (between that of starch (1.40-1.44) and the water swelling the particles (1.30-1.33)), a single peak of freely non-aggregated SNPs appears with a size of ~20 nm independent of the DS of the SNP (**Table 2.1**). This smaller base particle size is also consistent with the TEM results (average sizes in **Fig. 2.2d** from images in **Fig. 2.2(e,f)**), which show single SNP particles oriented along the outside edge of the PMMA latex particles (size 300 ± 15 nm) added to prevent SNP film formation. Thus, independent of the methacrylation DS value, SNP samples consist of a dominant fraction of small (20-30 nm) nanoparticles.

Table 2.1: Mean and mode diameters of SNPs before and after various degrees of methacrylation as measured by dynamic light scattering (0.1 wt% SNP concentration) and nanoparticle tracking analysis (100 μg/mL SNP concentration). See **Supplementary Information Figure S2.5 and Table S2.3** for DLS sizing data at different dilutions.

Degree of Substitution	DLS Diameter (intensity-weighted) (nm)	DLS Diameter (number-weighted) (nm)	NTA Mean Diameter (nm)	NTA Mode Diameter (nm)
0	194 ± 8	21 ± 8	184 ± 41	178 ± 41
0.015	230 ± 30	14 ± 8	214 ± 68	202 ± 68
0.05	242 ± 8	21 ± 5	178 ± 48	161 ± 48
0.10	287 ± 14	17 ± 5	184 ± 58	171 ± 58
0.25	270 ± 9	19 ± 6	186 ± 55	161± 55

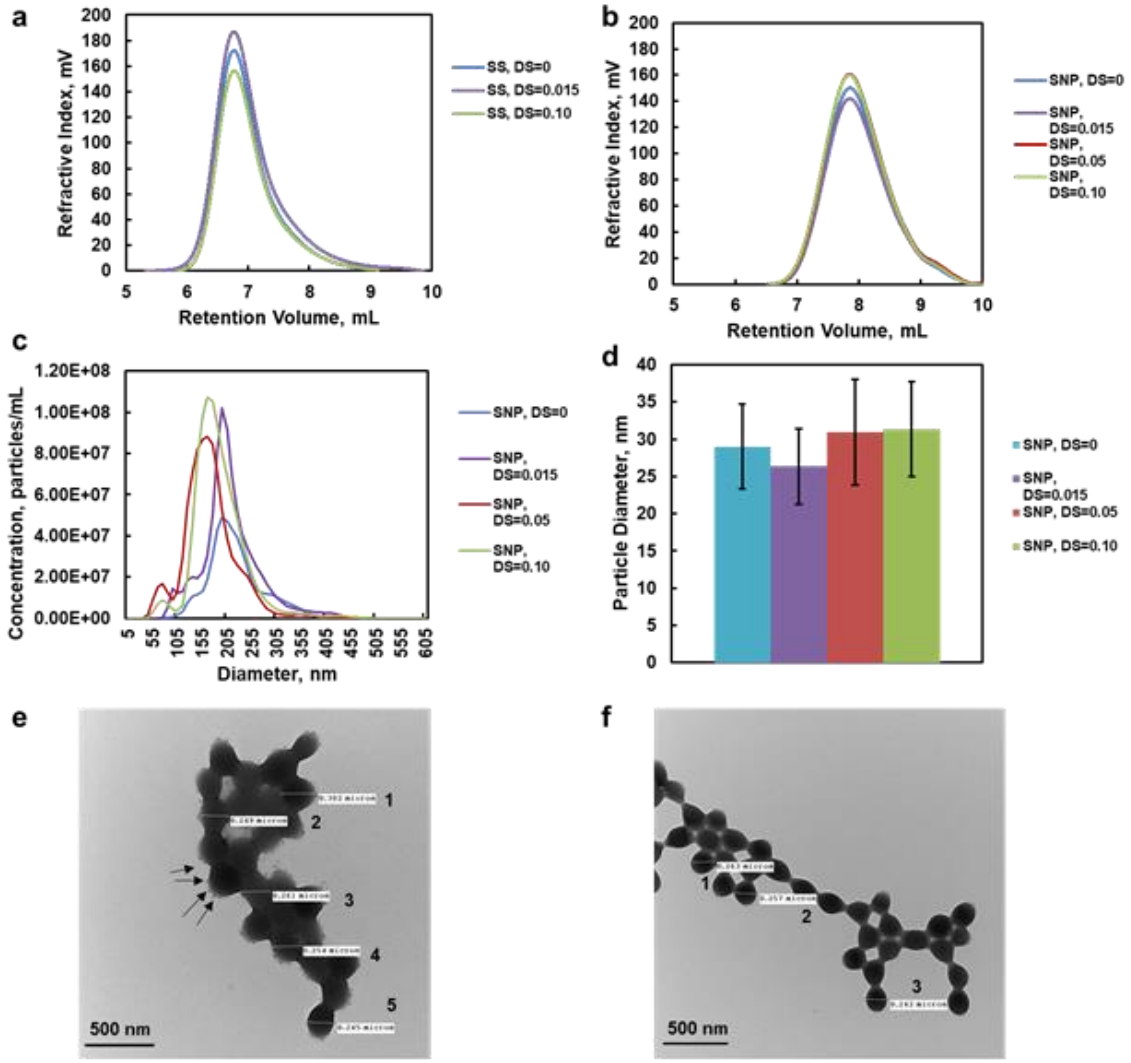

Figure 2.2 (a-f): Particle sizes of SNPs and SS before and after methacrylation: (a, b) GPC traces for (a) SS and (b) SNP samples before and after methacrylation with different target DS values; (c) NTA results as a function of the degree of substitution of SNPs; (d) average particle sizes from TEM image analysis software for SNPs before and after methacrylation (30-40 individual particles were sized for each formulation); (e, f) TEM images of SNPs in a PMMA latex (e) relative to the PMMA latex alone (f) (scale bar = 500 nm). The numbers in (e) and (f) correspond to individual PMMA particles sized for comparison to the SNP average sizes reported in panel (d).

2.3.2 Physical Characterization of Photopolymerized SS and SNP Hydrogels

Photoinitiation of the methacrylate groups grafted to the SNPs induces a typical free radical chain growth polymerization in suspension to crosslink SNPs together, with SNPs acting as multivalent macromonomers to form a bulk hydrogel. Note that the small size coupled with the high degree of internal hydration of the SNPs facilitates gelation compared to the use of a similar process with a "hard" nanoparticle, although a degree of

both intraparticle and interparticle crosslinking within each SNP is likely to occur as a result of the close proximity of C=C groups within the SNPs. SS, as a noncrosslinked linear polymer, has higher conformational mobility than SNPs and crosslinks through a more typical solution-based gelation mechanism. Despite these differences in crosslinking phenomena based on the type of starch used, photopolymerization of all methacrylated SS and SNP samples yielded hydrogels within 10 minutes of UV exposure.

Of particular note, the significantly lower viscosity of SNPs relative to SS allowed for achieving much higher SNP weight percentages (as high as 35 wt%) in the precursor polymer solutions than achievable with SS (<10 wt%). The elastic storage modulus (G') as a function of the initial polymer concentration and the degree of methacrylation is shown in **Figure 2.3** for hydrogels prepared using different SNP (**Fig. 2.3a**) or SS (**Fig. 2.3b**) precursors, while the loss modulus (G") is reported in **Fig. 2.3c and Fig. 2.3d**, respectively. In either case, G' increases with the precursor polymer concentration and/or the DS of methacrylate groups, consistent with gelation theory. At equivalent DS and mass concentrations (10 wt% polymer and DS = 0.25, the maximum concentration at which SS was soluble in water and the minimum concentration/DS at which SNPs could form a hydrogel), the G' of the SS-based hydrogels (G' ~ 1000 Pa) exhibited a modulus value double than that observed with SNP-based hydrogels (G' ~ 500 Pa), consistent with the linear SS hydrogels having more conformational mobility relative to the internally crosslinked SNPs at the same mass fraction. However, the significantly higher concentrations achievable with SNP-based hydrogels enabled the formation of much stiffer hydrogels using SNPs as the building block, with G' values up to ~6500 Pa achieved for 35 wt% SNP (DS 0.10) hydrogels; this is ~6-fold higher than the highest modulus achievable with SS. Similar trends were observed at the equilibrium swollen state (**Supplementary Information Fig. S2.7**), although the absolute storage modulus values were reduced due to the influx of water into the network. Thus, by using SNPs as a hydrogel building block, significantly denser and stronger hydrogels can be fabricated without introducing processability/solubility complications.

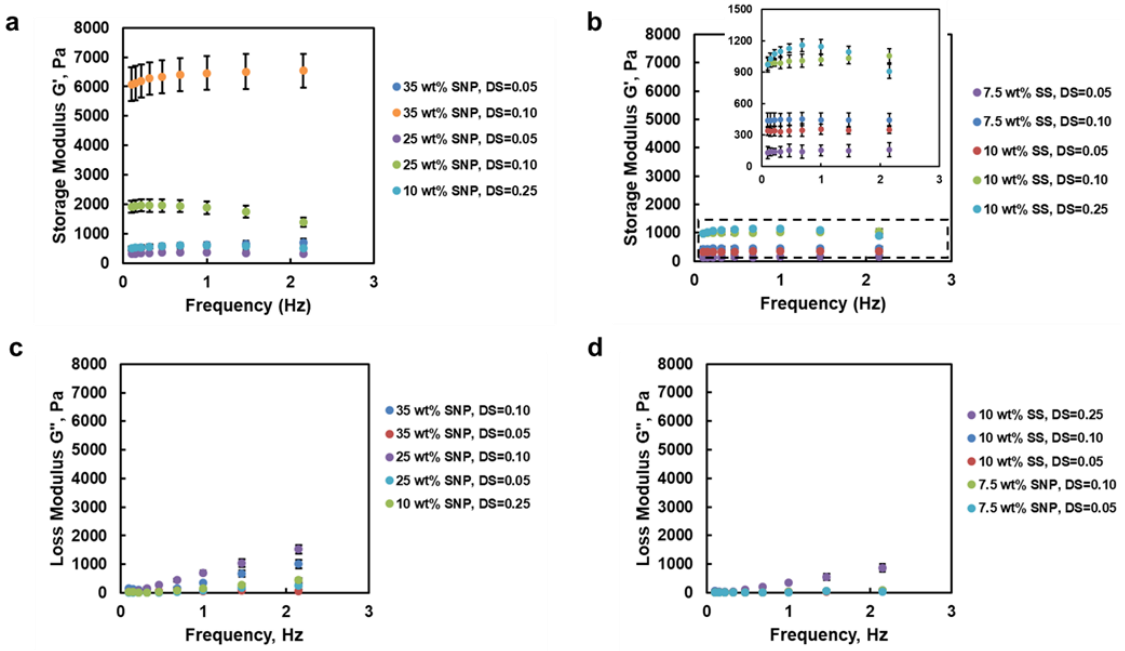

Figure 2.3 (a-d): Shear storage modulus (G') as a function of strain frequency for hydrogels prepared with (a) SNP building blocks and (b) SS building blocks at various concentrations and DS values (insert of (b) is a zoom-in between moduli of 0-1500 Pa to more clearly show differences between the weaker SS hydrogel mechanics with the same x and y axis information). Also shown is the shear loss modulus (G") for the same SNP (c) and SS (d) samples.

Figure 2.4(a-f) show the equilibrium volumetric swelling ratios of SS and SNP-based hydrogels prepared at various DS values and mass concentrations (see Supplementary Information, Fig. S8 for the corresponding swelling kinetics data). For both SS and SNP-based hydrogels, increasing either the DS or the mass concentration of the precursor units results in a reduction of the equilibrium degree of swelling, consistent with the mechanical testing results (**Fig. 2.3**) and the typical link between increasing crosslink density and reducing swelling. However, clear differences were observed between the SS and SNP-based hydrogel series. At an equivalent 0.25 DS/10 wt% mass concentration, the equilibrium swelling degree of SNP-based hydrogels was slightly higher than that achieved with SS-based hydrogels, consistent with the weaker mechanics of the SNP-based hydrogel at this DS/concentration value due to the internal SNP crosslinks restricting inter-particle crosslinking (**Fig. 2.3a**). However, the higher mass concentrations achievable with SNP hydrogels allow for significant reductions in the equilibrium degrees of swelling that are achievable, with the highest concentration/DS SNP-based hydrogel that could be fabricated swelling less than half that of the highest concentration/DS SS-based hydrogel that could be fabricated (**Fig. 2.4**). This result is attributable to both the higher wt% of the SNP hydrogels (introducing more photopolymerizable crosslinking points in the same hydrogel volume at equivalent DS

values) and the pre-existing internal crosslinks within the SNPs themselves that act as an additional elastic driving force for limiting swelling. On this basis, using SNPs can maintain the beneficial properties of starch as a hydrogel building block but achieve both stiffer and lower swelling hydrogels than possible with conventional starch.

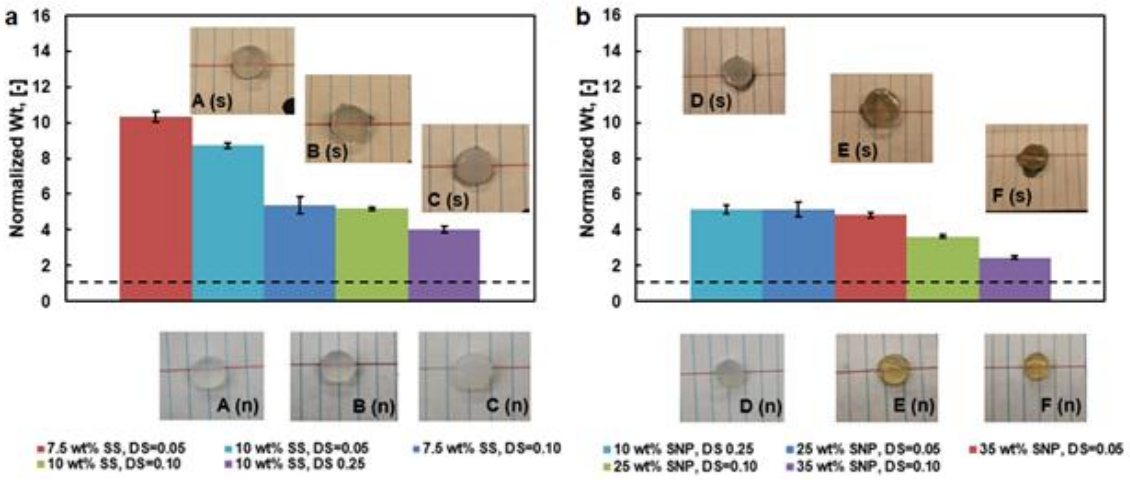

Figure 2.4: Equilibrium swelling ratios (relative to the dry state) for hydrogels prepared with SNP building blocks (a, left) and hydrogels prepared with SS building blocks (b, right). Photographs of selected hydrogel formulations are included below in the neat state (n) and above in the equilibrium swollen state (s) for the following: A. 10 wt% SS at DS 0.05 (lt. blue), B. 10 wt% SS at DS 0.10 (green), C. 10 wt% SS at DS 0.25 (purple), D. 10 wt% SNP at DS 0.25 (lt. blue), E. 35 wt% SNP at DS 0.05 (red), and F. 35 wt% SNP at DS 0.05 (purple). Note: the dotted line represents the starting weight (pre-swelling) as a value of 1.0

2.3.3 Small Angle Neutron Scattering

Small angle neutron scattering (SANS) was performed to compare the internal morphology of the SNPs before and after methacrylation. **Supplementary Information Table S2.4** shows the key fitting results for single SNPs before and after methacrylation; for raw SANS data and best-fit lines, see **Supplementary Information Fig. S2.9**. The SNP diameter was determined to be ~160-170 nm independent of DS, fully consistent with the results obtained from DLS and NTA (**Table 2.1**). In addition, neither the particle scattering length density (related to the water content of the SNP) nor the correlation length (related to the internal distance between inhomogeneities/crosslinks in the sample) significantly change before and after methacrylation. This analysis further confirms that methacrylation has no significant impact on the SNP structure, allowing us to relate all observed property changes to changes in the SNP interparticle crosslink density imparted by the different degrees of methacrylation/starch concentrations.

Figure 2.5 shows representative SANS curves and fits for an SNP-based hydrogel relative to an SS-based hydrogel, while **Table 2.2** shows a summary of the key SANS

parameters for the SNP nanoparticle networks; all collected SANS graphs are available in **Supplementary Information Figures S2.9-S2.15** and the full set of corresponding best-fit parameters are presented in **Table S2.5**.

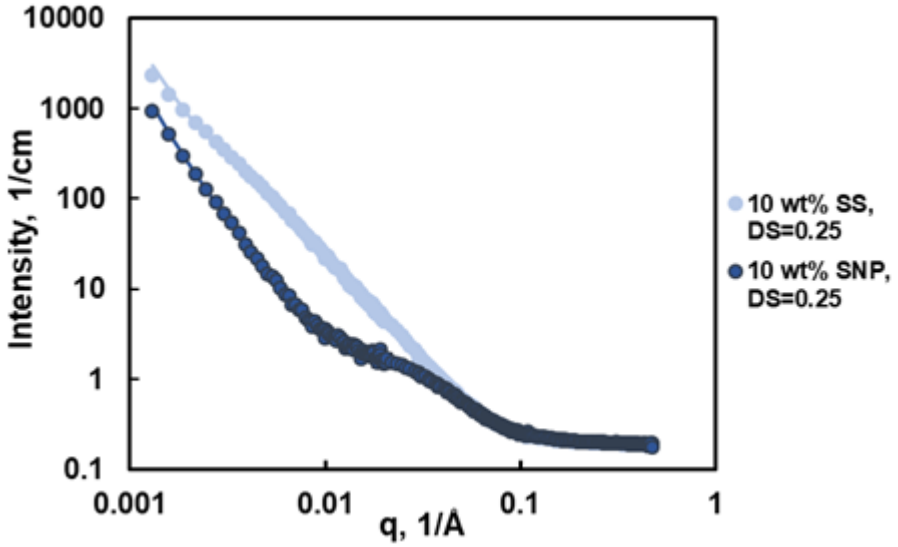

Figure 2.5: Representative SANS curves for 10 wt%/DS 0.25 hydrogels based on (a) SNPs (lighter blue) and (b) SS (darker blue).

Table 2.2: Key SANS parameters for photopolymerized hydrogels prepared with soluble starch (SS) compared with starch nanoparticles (SNPs)

Parameter	**10 wt% SS, DS=0.10**	**10 wt% SNP, DS=0.10**	**25 wt% SNP, DS=0.10**	**25 wt% SNP, DS=0.05**	**25 wt% SNP, DS=0.015**	**35 wt% SNP, DS=0.10**
Porod Exponent	2.74 ± 0.01	2.54 ± 0.05	2.42 ± 0.04	2.38 ± 0.03	2.82 ± 0.01	2.68 ± 0.09
Lorentzian Exponent	2.55 ± 0.01	2.51 ± 0.01	2.69 ± 0.02	2.77 ± 0.03	3.27 ± 0.04	2.71 ± 0.02
Lorentzian Screening Length (nm)	18.8 ± 0.5	13.1 ± 0.2	9.2 ± 0.2	8.8 ± 0.2	2.41 ± 0.02	16.4 ± 3
Lorentzian Scale	166 ± 3	65 ± 3	14.3 ± 0.7	11.8 ± 0.7	0.43 ± 0.01	87 ± 5

Qualitatively (**Fig. 2.5**), SS and SNP-based hydrogels show similar curve shapes in the high q region (consistent with similarities in the starch polymer chain structures) but significant deviations in curve shapes at the low q region indicative of the different length scales of crosslinking between individual chains/particles in each sample. Based on the best-fit parameters (**Table 2.2**), SS hydrogels correspondingly have significantly lower

Porod exponents (corresponding to more Gaussian, swollen chains), significantly higher Lorentzian screening lengths (indicating larger gel mesh sizes), and much larger Lorentzian scales (indicating a significantly more fluid network structure) than SNP-based hydrogels. All these observations are consistent with replacing a soluble linear starch with a smaller but internally crosslinked SNP as the hydrogel building block. Within the SNP-only hydrogels, increasing the wt% of SNPs used to prepare the hydrogel results in a relatively unchanged Porod exponent (suggesting minimal changes to the fractal nature and thus internal swelling of the SNP building blocks themselves) but a marked decrease in both the Lorentzian screening length (i.e. internal mesh size) and Lorentzian scale (i.e. the relative contribution of the fluid-like inhomogeneities to the overall scattering observed), both consistent with the creation of denser and more crosslinked hydrogel networks. Similarly, as the DS is increased at a single wt% of SNPs (25 wt%), the Porod exponent again remains relatively unchanged while decreases are again observed in both the Lorentzian screening length and the Lorentzian scale, consistent with the production of more crosslinked SNP-based hydrogels as a result of the higher degree of SNP methacrylation. Thus, the SANS results suggest that the degree of inter-particle crosslinking is substantially changed when either the SNP concentration or degree of methacrylation are changed (as evidenced by the trends in each of the Lorentzian/fluid-like fluctuation terms) but the internal structure/swelling of the SNP does not appreciably change (as evidenced by the relatively constant Porod exponent). Note that the constant Porod exponent also suggests that the small SNP aggregate fraction consistently observed in suspension (**Fig. 2.2**) does not introduce significant heterogeneities in the photocrosslinked hydrogels.

2.3.4 *In Vitro* Cell Studies

To assess the cytotoxicity of SNPs alone as well as the effect of methacrylation on the cytotoxicity of SS and SNPs, a resazurin assay was performed using 3T3 mouse fibroblasts (**Figure 2.6**). Neither SS nor SNPs exhibited significant cytotoxicity at any concentration tested prior to methacrylation. High cytocompatibility (>80% relative to the cell-only control) was also maintained for DS=0.05 modified SS and SNPs as well as DS=0.10 modified SS across the full range of concentrations tested. However, moderate toxicity was noted for DS=0.10 SNPs at the highest concentration tested (10 mg/mL) while significant cytotoxicity was observed for DS=0.25 SS and SNPs at concentrations of 0.5 mg/mL and above. This observation is most likely related to the reactivity of free methacrylates to cells via Michael addition reactions with cell-bound proteins [362] and/or to cellular glutathione [363]. While the rapid photogelation achieved will consume most of these free methacrylate groups, these results suggest limiting the DS to 0.10 or less in any practical biomedical application.

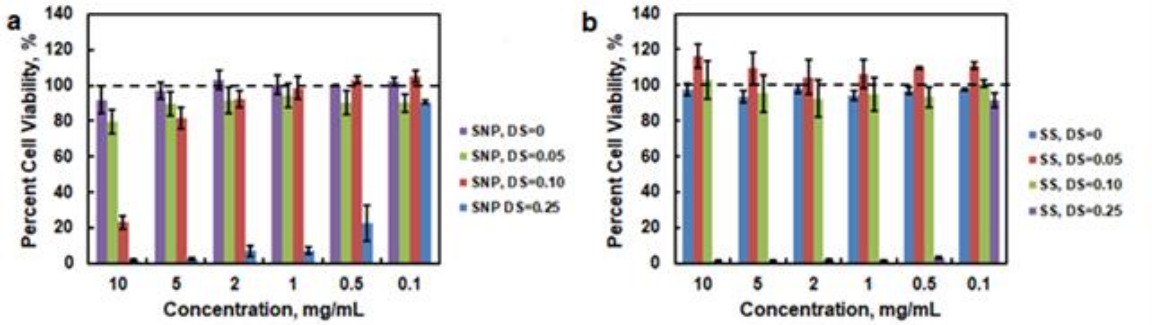

Figure 2.6: In vitro cell viability of 3T3 mouse fibroblasts based on the resazurin assay for (a) SNPs and (b) SS over a range of DS values.

To assess cell interactions with SNP and SS-based hydrogels, we performed two assays: (1) aqualitative assessment of cell adhesion to the hydrogels based on LIVE/DEAD staining of residual adhered cells following washing (**Figure 2.7**) and (2) a leachate study to assess the potential cytotoxicity of the hydrogels to cells over time (**Figure 2.8**). Together, these studies permit a full assessment of the anti-fouling properties of the hydrogels while controlling for potential complications due to cell death rather than inherent anti-fouling properties. Both SS and SNP hydrogels showed minimal adhered and viable cells at all DS values following three washes in 10 mM PBS after five days of cell incubation, a time over which the cells become confluent on the tissue culture polystyrene (TCPS) controls (**Fig. 2.7**). Correspondingly, the leachates from the gels exhibited no significant cytotoxicity (**Fig. 2.8**) aside from the DS 0.25 samples already noted as being cytotoxic (**Fig. 2.6**). Combined, these results suggest that the lack of cell adhesion is an inherent property of the DS 0.05 and DS 0.10 samples. Slightly more cells adhered to the SNP samples (attributable to the lower water concentrations in these materials, **Fig. 2.4**) and to DS 0.10 samples (higher crosslink density/stiffer substrate but still no cytotoxic leachates); however, overall, all the SS and SNP materials tested are non-adherent to even strongly adherent fibroblast cells. Note that the toxicity observed at higher DS values further emphasizes the benefits of using SNP building blocks that allow for accessing stiffer gels at lower degrees of methacrylation (**Fig.2.3**) that will not induce any cytotoxicity.

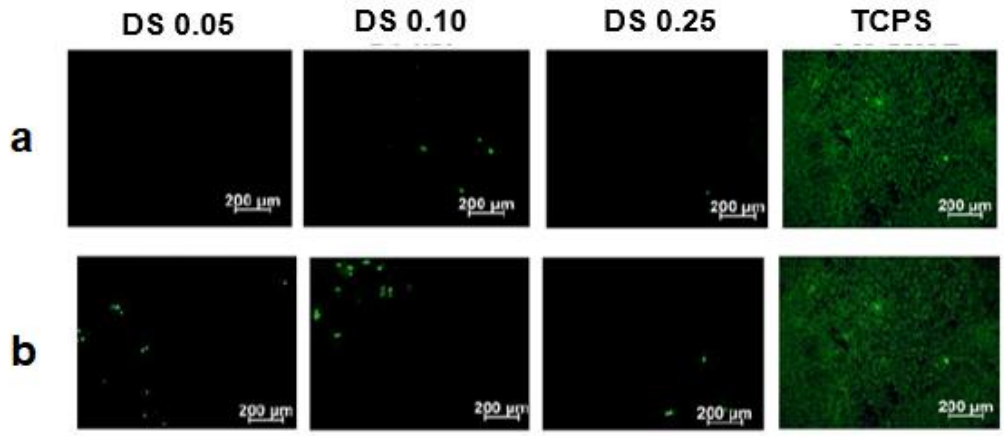

Figure 2.7: 3T3 mouse fibroblast adhesion to hydrogels prepared from (a) SNP and (b) SS building blocks with different degrees of substitution (DS) relative to a tissue culture polystyrene control after 5 days of incubation (LIVE/DEAD staining).

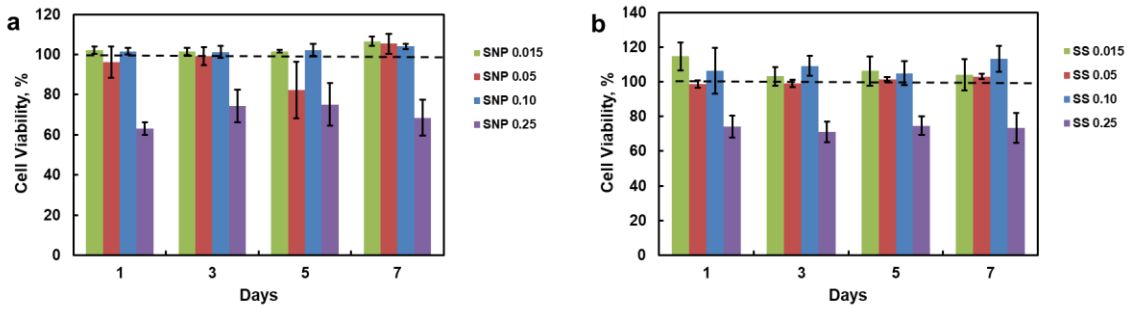

Figure 2.8: Cell viability (via the resazurin assay) of 3T3 fibroblasts after 24 h of incubation with leachate samples from hydrogels made of (a) SS or (b) SNP building blocks soaked in DMEM media for different periods of time.

2.4 Conclusions & Acknowledgments

Starch nanoparticles fabricated via reactive co-extrusion are demonstrated to be a relevant and useful starting material for the design of hydrogel systems based on their neutral surface charge, their surface rich in hydroxyl groups for subsequent modification (here, methacrylation to enable photopolymerization), their small size (< 50 nm), their low cost, and their generally safe degradation products (glucose). Relative to linear starch hydrogels prepared at the same degree of methacrylation, hydrogels fabricated from SNP precursors can achieve at least five-fold higher shear moduli while demonstrating at least two-fold lower swelling ratios. This result was attributed to the dual intraparticle/interparticle crosslinking structure of the SNP-based hydrogels, as confirmed and elucidated via small angle neutron scattering analysis. Furthermore, provided the DS is limited to 0.10 or lower, SNP-based hydrogels exhibited high cytocompatibility and

very low cell adhesion over a 7 day period, with SNP building blocks enabling access to stiffer gels that are inaccessible using soluble starch building blocks without inducing cytotoxicity. On this basis, SNP-based hydrogels are attractive options for fabricating stiffer but still highly cytocompatible and anti-biofouling hydrogels based on natural and degradable polymer precursors.

2.5 Acknowledgements

The authors would also like to acknowledge Marcia Reid for her help with TEM and Dr. Boualem Hammouda for his help with acquiring the 30 m SANS data. The Natural Sciences and Engineering Research Council of Canada (NSERC, Strategic Project Grant 463327-14) is gratefully acknowledged for funding this work. This work utilized facilities supported in part by the National Science Foundation under Agreement No. DMR-0944772. We acknowledge the support of the National Institute of Standards and Technology, US Department of Commerce, in providing the neutron facilities used in this work. Use of facilities provided by McMaster's Biointerfaces Institute and EcoSynthetix Inc. is also gratefully acknowledged.

Appendix 2S: Supporting Information to Chapter 2

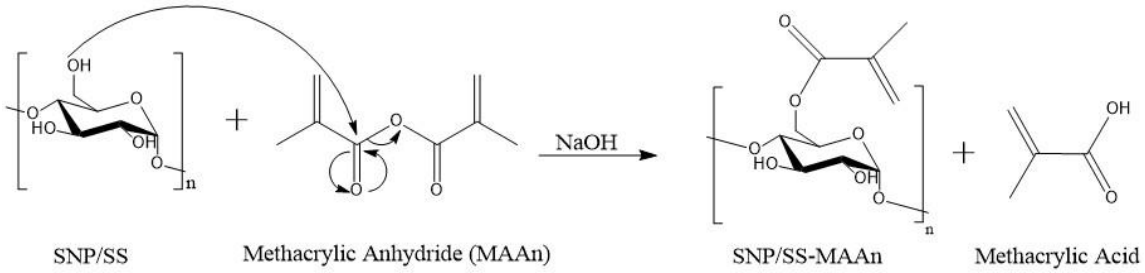

Figure S2.1: Mechanism for the esterification reaction of starch (SNP or SS) and methacrylic anhydride (MAAn) in basic aqueous conditions (pH ~ 10.4). The residual methacrylic acid left over from the reaction is removed via dialysis in distilled deionized water.

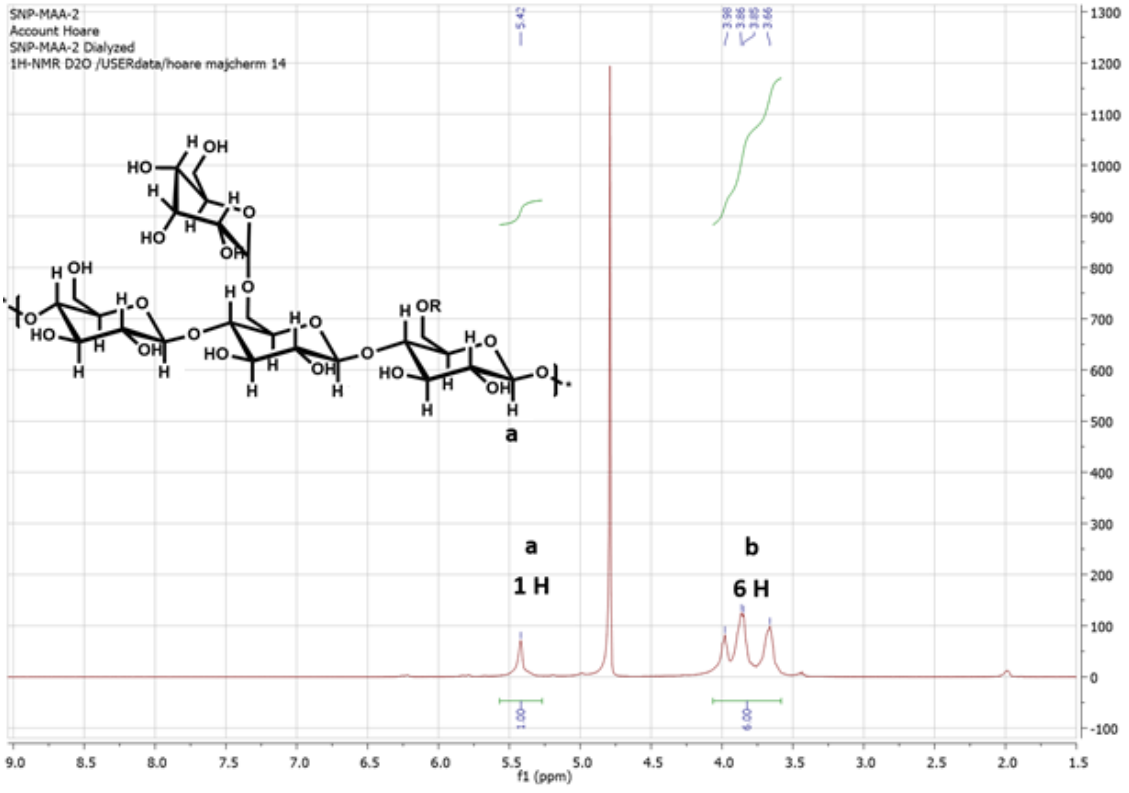

Figure S2.2(a): A representative ^{1}H-NMR (solvent DMSO-d_6) of unfunctionalized starch nanoparticles (SNPs). The peak subscripts represent (a) the anomeric proton and (b) the other six hydroxyl groups present on the starch backbone. Upon integration, a 1:6

ratio of the intensities of the anomeric carbon peak (Ha) and the protons from the 6 hydroxyl groups on the glucose backbone, confirming that the starch structure is still intact following methacrylation.

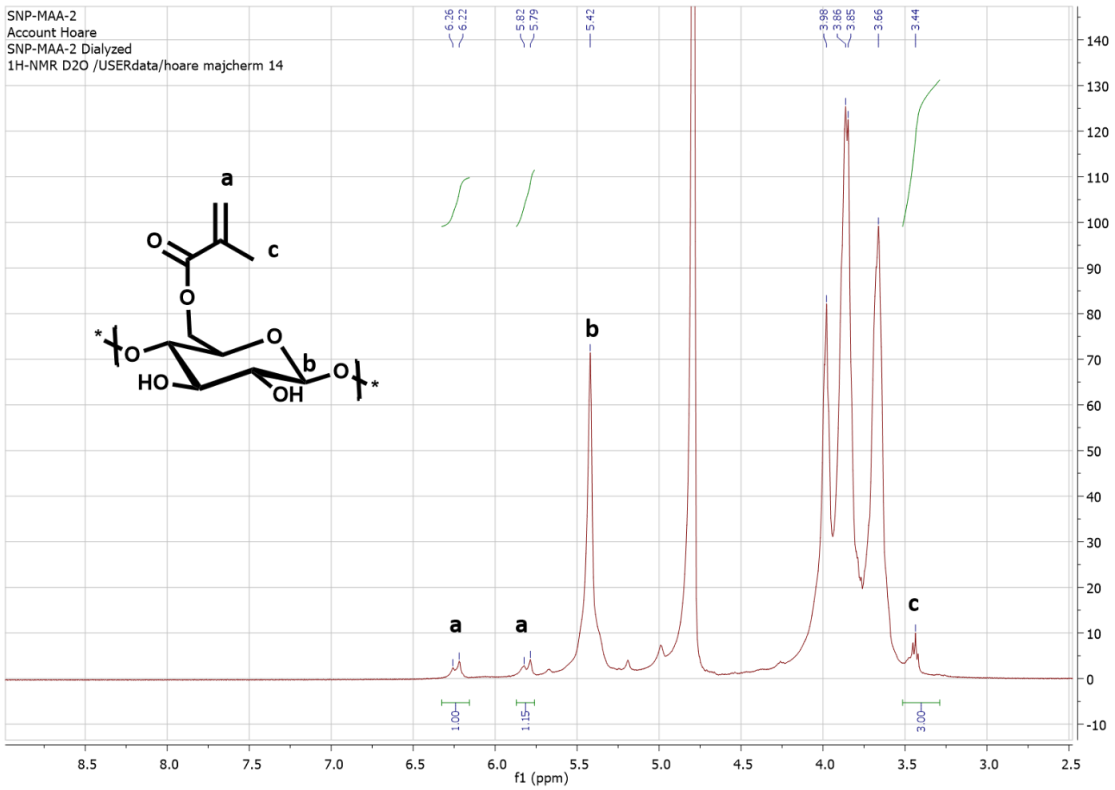

Figure S2.2(b): A representative ^{1}H-NMR of methacrylated starch nanoparticles (SNP-MAAn) after treatment with methacrylic anhydride (MAAn). The peak subscripts represent (a) the two protons coming from the vinyl peak of the methacrylate group, primarily at the C6 position ($I_{5.8}$ and $I_{6.2}$), (b) the anomeric proton ($I_{5.4}$), and (c) the three methyl protons adjacent to the vinyl group in the methacrylic functionality, ($I_{3.4}$). The DS is calculated using the equation $DS=((I_{5.8}+I_{6.2})/2)/I_{5.4}$

While the methacrylic group can in theory graft at the C2, C3, or C6 positions of starch (Hedin, Östlund, & Nydén, 2010), all NMR data is consistent with the C6-preferred reactivity of methacrylic anhydride given the consistent chemical shift observed for the methyl group of the grafted methacrylate moiety [357]. A more detailed explanation of the ^{1}H-NMR data acquired from similar spectra to those shown **in Figure S2.2(a & b)** is provided in **Table S2.1** below to show how the degree of substitution) can be tuned by controlling of the amount of MAAn introduced into the system.

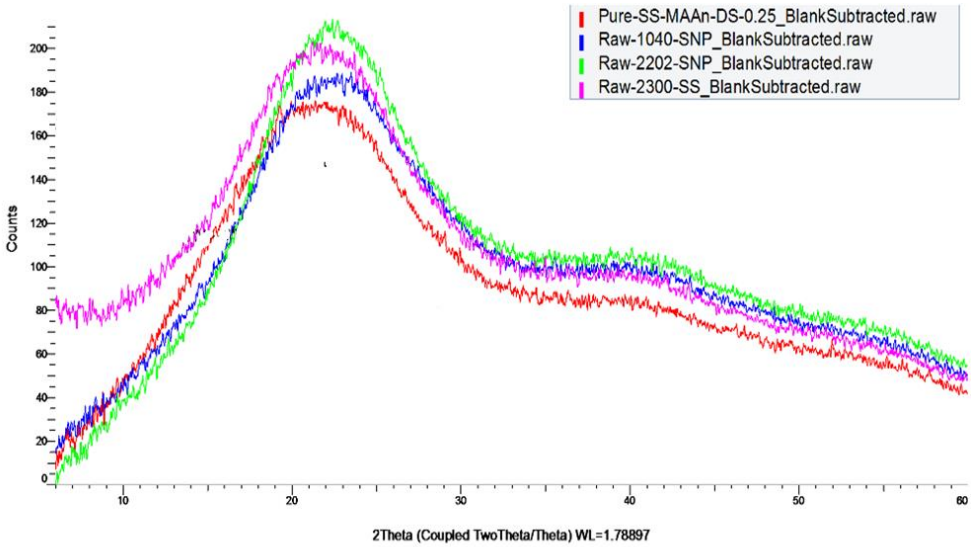

Figure S2.3: XRD data of selected SS and SNP samples showing that the samples are largely amorphous post-fabrication in the reactive extruder.

Samples were analyzed using a Bruke D8 DISCOVER with DAVINCI Design with a Co sealed tube (wavelength = 1.79026A). The instrument settings used are as follows: 35 kV and 45 mA power settings, parallel focus Goebel Mirror, Micro Slit (1 mm), Short collimator (0.5 mm), Vertical D8 goniometer, Chi cradle with phi rotation on an X/Y/Z translation stage, Laser-Video sample alignment, and a Vantec 500 (MiKroGap TM technology) area detector. The experiment parameters are as follows: 2θ (fixed θ = 8 deg), number of frames: 3, frame exposure: 900s/frame, range collected: 6-60 deg, and detector distance: 20 cm. All 2D frames were collected with DIFFRAC Measurement Centre Version 6.5 software and integrated to 1D using DIFFRAC.EVA Version 4.2.

Table S2.1: Summary of the experimental degree of substitution (DS) values calculated for the methacrylated soluble and particulate starch samples from ^{1}H NMR data.

Sample	I (δ=5.8)	I (δ=6.2)	I (δ=5.4)	Exp. DS
SNP DS=0.015	1.640	1.000	206.070	**0.006**
SNP DS=0.05	1.490	1.000	125.700	**0.010**
SNP DS=0.10	1.350	1.000	15.700	**0.075**
SNP DS=0.25	6.950	1.000	1.090	**0.150**
SNP DS=0.50	4.090	1.000	1.030	**0.248**
SS DS=0.015	0.970	1.000	39.470	**0.025**
SS DS=0.05	1.320	1.000	37.930	**0.031**
SS DS=0.10	1.340	1.000	12.890	**0.091**
SS DS=0.25	7.650	1.000	1.120	**0.139**
SS DS=0.50	3.920	1.000	1.130	**0.272**

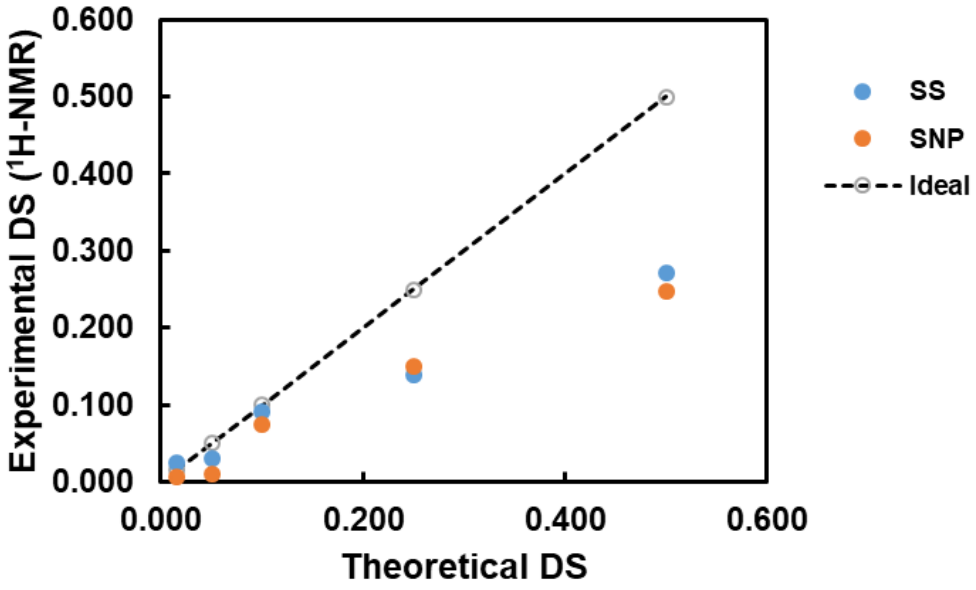

Figure S2.4: Comparison of the experimental versus theoretical degree of substitution (DS) from ^{1}H-NMR for both SS and SNPs (see Table S1 for tabulated data). The dotted line represents stoichiometric functionalization.

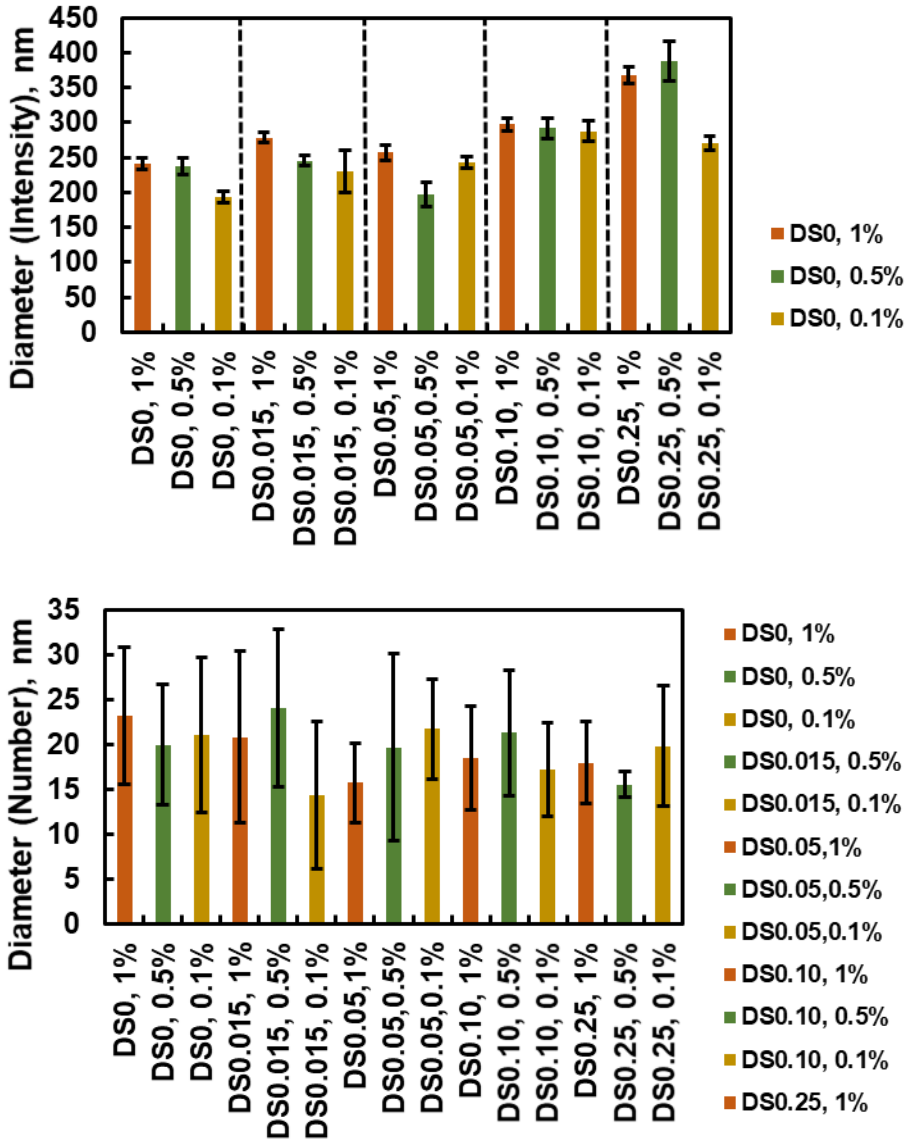

Figure S2.5 (a, b): DLS results on the methacrylated SNPs in 1 mM NaCl with DS values ranging from 0 to 0.25 at concentrations of 1, 0.5, and 0.1 wt% based on (a) the intensity-weighted average particle diameter or (b) the number-weighted average particle diameter (assuming RI = 1.4 for particle). The data suggest that esterification does not significantly alter particle size in the process and that altering the wt% during the DLS experiment has little effect on the resulting particle size within the range tested.

Table S2.2: Summary of particle size distribution (PSD) data for the functionalized SNP building blocks via DLS using different weigh percentages. No significant change in the measured diameters were observed, confirming that the data presented is characteristic of the SNPs themselves.

wt%	Particle Code	Diameter by Intensity, nm	Diameter by Number, nm
0.1	DS 0	194 ± 8	21 ± 8
	DS 0.015	230 ± 30	14 ± 8
	DS 0.05	242 ± 8	21± 5
	DS 0.10	287 ± 14	17 ± 5
	DS 0.25	270 ± 9	19 ± 6
0.5	DS 0	237 ± 11	19 ± 6
	DS 0.015	245 ± 8	24 ± 8
	DS 0.05	196 ± 17	19 ± 10
	DS 0.10	291 ± 15	21 ± 6
	DS 0.25	387 ± 27	15 ± 1
1	DS 0	241 ± 8	23 ± 7
	DS 0.015	278 ± 8	20 ± 9
	DS 0.05	256 ± 11	15 ± 4
	DS 0.10	297 ± 9	18 ± 5
	DS 0.25	367 ± 11	18 ± 4

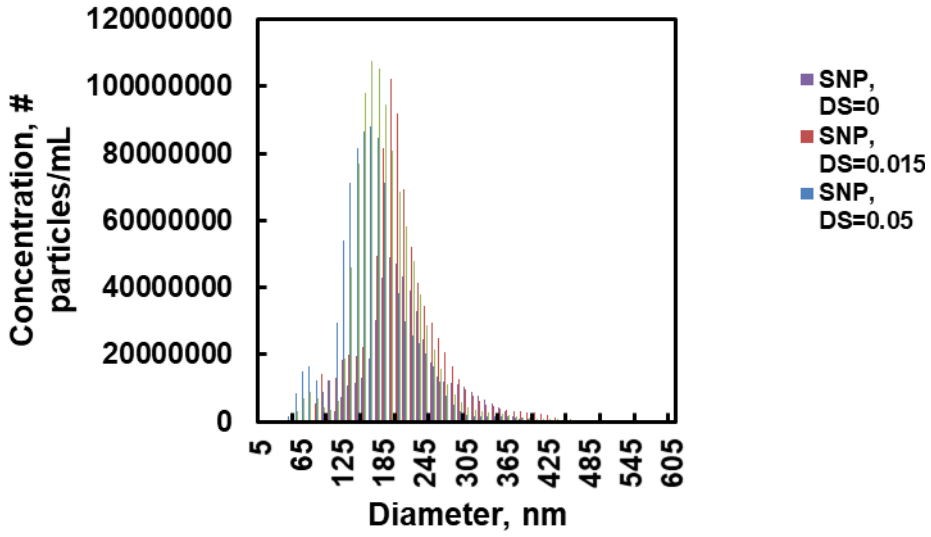

Figure S2.6: Representative nanoparticle tracking analysis (NTA) curves showing the concentration (particles/mL) vs. particle diameter (binned) of SNPs with different DS values.

Table S2.3: Gelation kinetics (using vial inversion testing) following UV photopolymerization of SS and SNP hydrogels. Lower degrees of substitution showed modest decreases in gelation kinetics, while decreases in weight percent resulted in a more significant increase in gelation time, particularly at very low weight percentages. These trends were observed for both SNP and SS based network hydrogels, supporting the increased presence of reactive methacrylate groups on the starch surface to participate in polymerization. SNP-based hydrogels also showed much longer gelation times compared to SS-based hydrogels consistent with the increased steric hindrance to crosslinking particles relative to soluble polymers.

SNP				**SS**			
	35 wt%	**25 wt%**	**10 wt%**		**10 wt%**	**7.5 wt%**	**5 wt%**
DS = 0.015 (low)	120 s	180 s	300 s	**DS = 0.015 (low)**	60 s	60 s	210 s
DS = 0.10 (high)	90 s	120 s	270 s	**DS = 0.10 (high)**	30 s	60 s	60 s

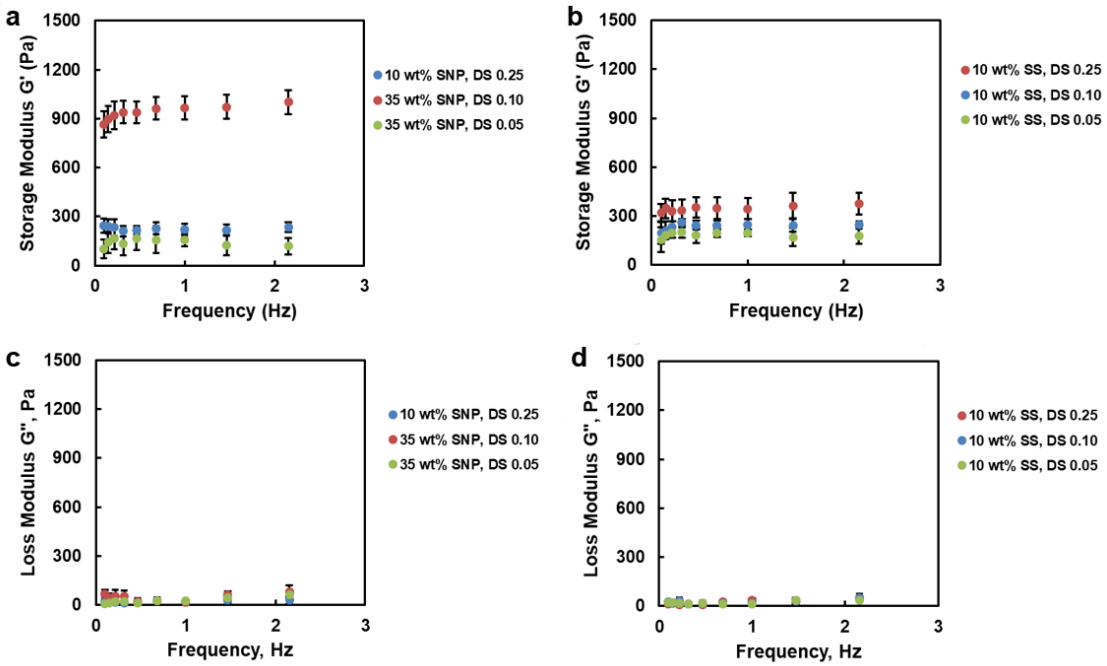

Figure S2.7: Storage (a, b) and loss (c, d) modulus data for selected hydrogel formulations at their swollen equilibrium state (after 3 days of incubation in 10 mM PBS at 37 ˚C). (a, c) SNP-based hydrogels; (b, d) SS-based hydrogels

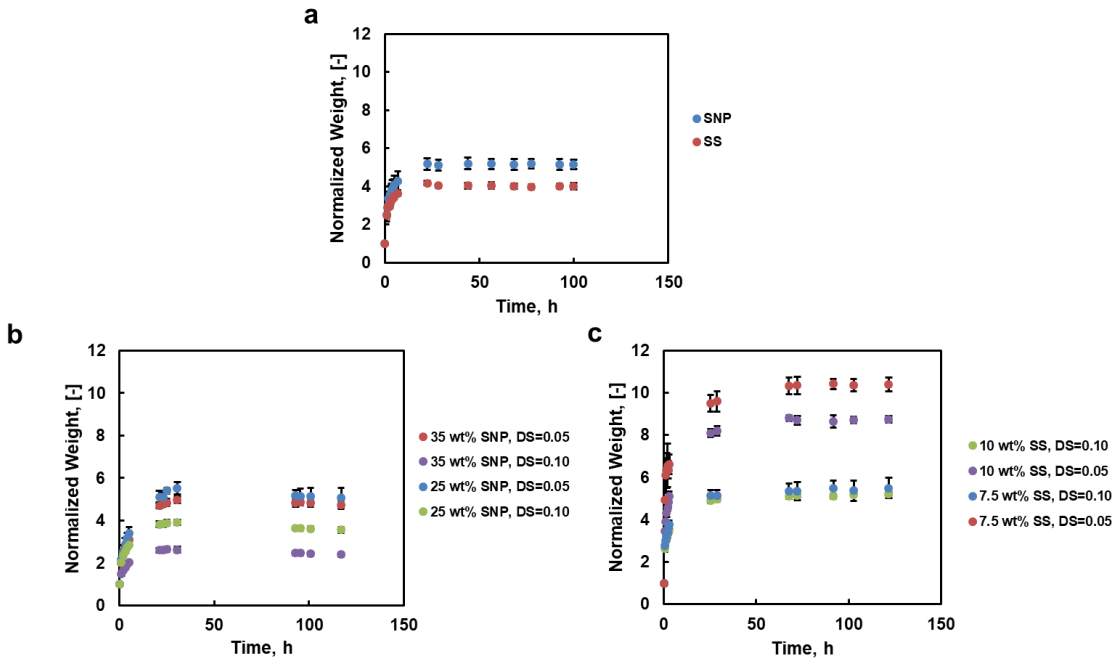

Figure S2.8: Swelling kinetics and equilibrium degrees of swelling (relative to the unswollen, "wet" hydrogels after fabrication) for hydrogels prepared with (a) SS and SNP building blocks at equivalent 10 wt%/DS 0.25 conditions; (b) SNP building blocks at different wt% and DS values (c) SS building blocks at different wt% and DS values.

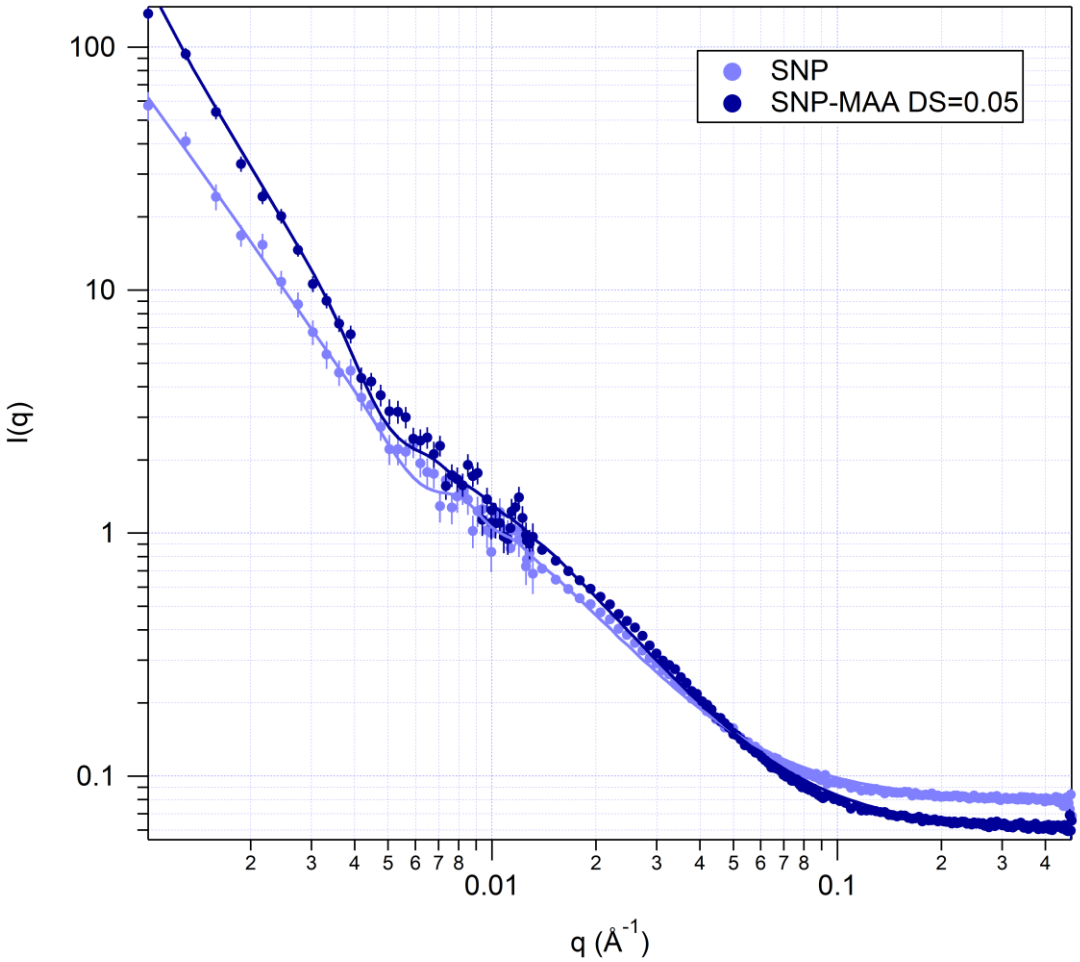

Figure S2.9: 30 m SANS scattering profiles of colloidal dispersions of SNPs before (light blue) and after (dark blue) methacrylation (DS = 0.05). While the background and low *q* scales are slightly altered before and after modification, both curves have the same general shape. This corroborates the NTA, DLS, TEM, and GPC results that the SNP size/structure is not substantially altered due to methacrylation.

Table S2.4. Key SANS parameters for unmodified and methacrylated SNPs in colloidal dispersions showing the independence of SNP structure on methacrylation

Parameter	***SNP***	***SNP-MAA DS=0.05***
Radius (nm)	703 ± 16	696 ± 13
Polydispersity	0.24 ± 0.02	0.4 ± 0.01
Particle Scattering Length Density (x 10^{-6} Å^{-2})	6.26	6.24
Correlation Length (nm)	106 ± 1.1	102.1 ± 0.9

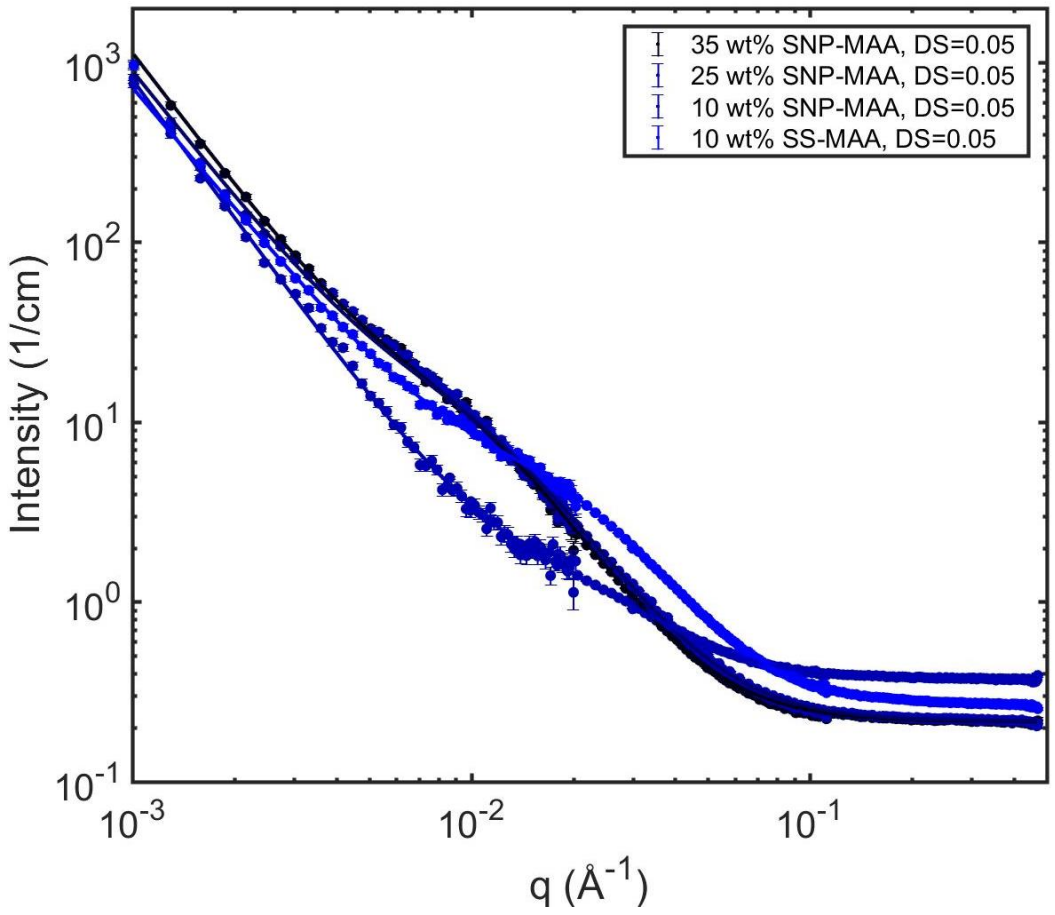

Figure S2.10: 30 m SANS scattering profiles of DS 0.05 SNP and SS-based hydrogels prepared at different starch concentrations. See **Table S2.5** for the corresponding fitting parameters.

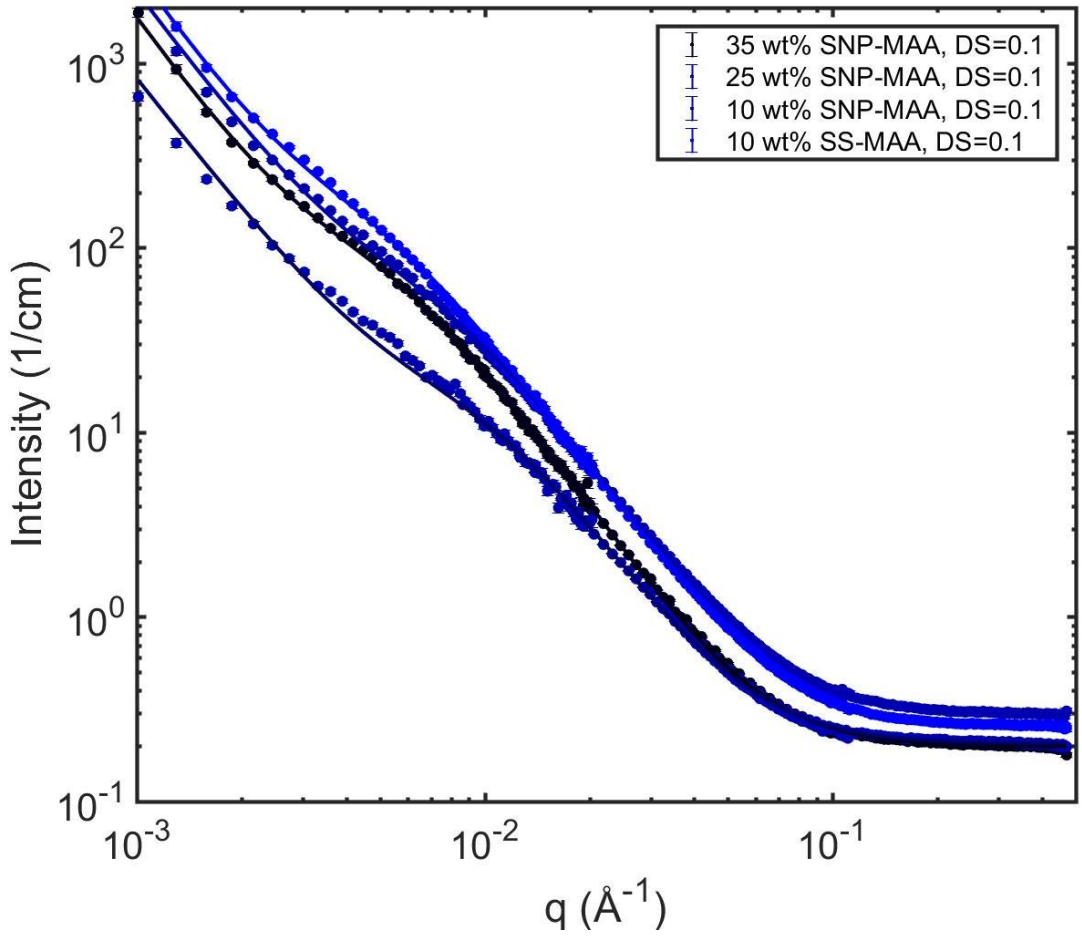

Figure S2.11: 30 m SANS scattering profiles of DS 0.10 SNP and SS-based hydrogels prepared at different starch concentrations. See **Table S2.6** for the corresponding fitting parameters

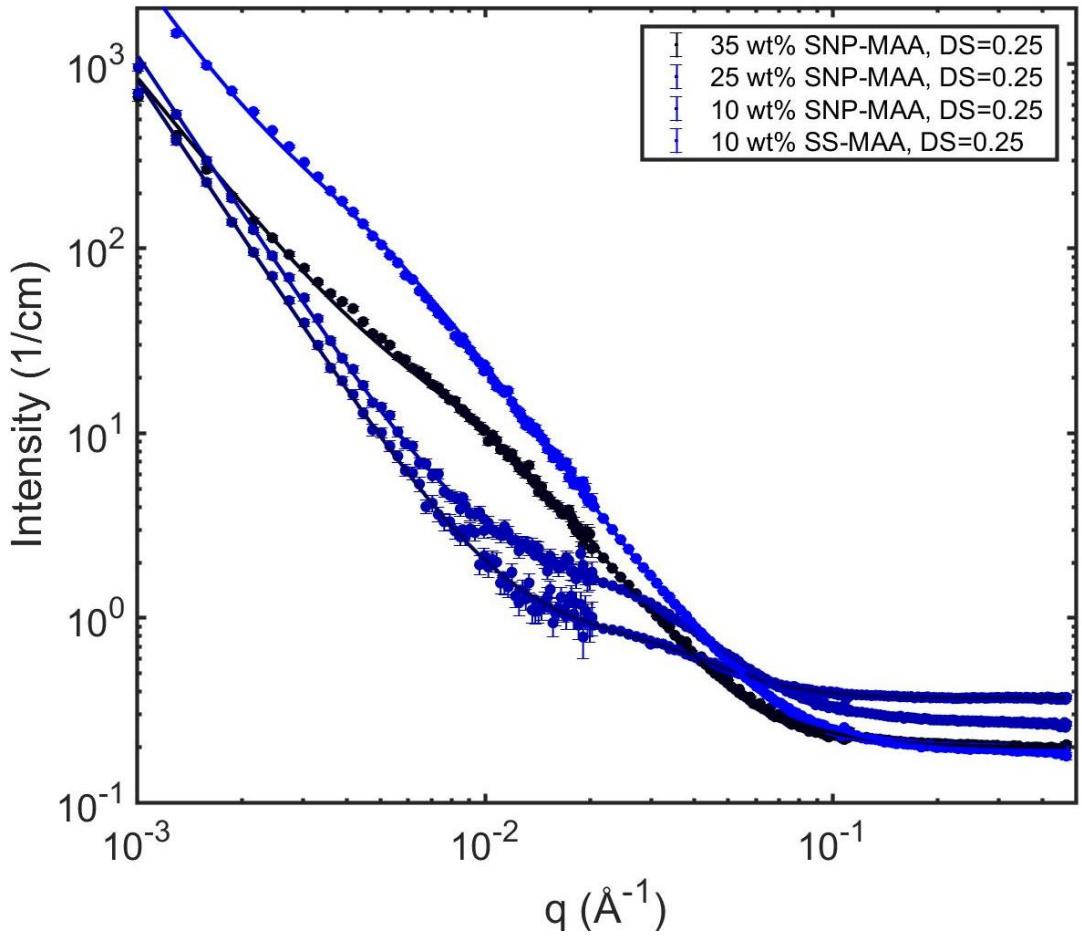

Figure S2.12: 30 m SANS scattering profiles of DS 0.25 SNP and SS-based hydrogels prepared at different starch concentrations. See **Table S2.5** for the corresponding fitting parameters.

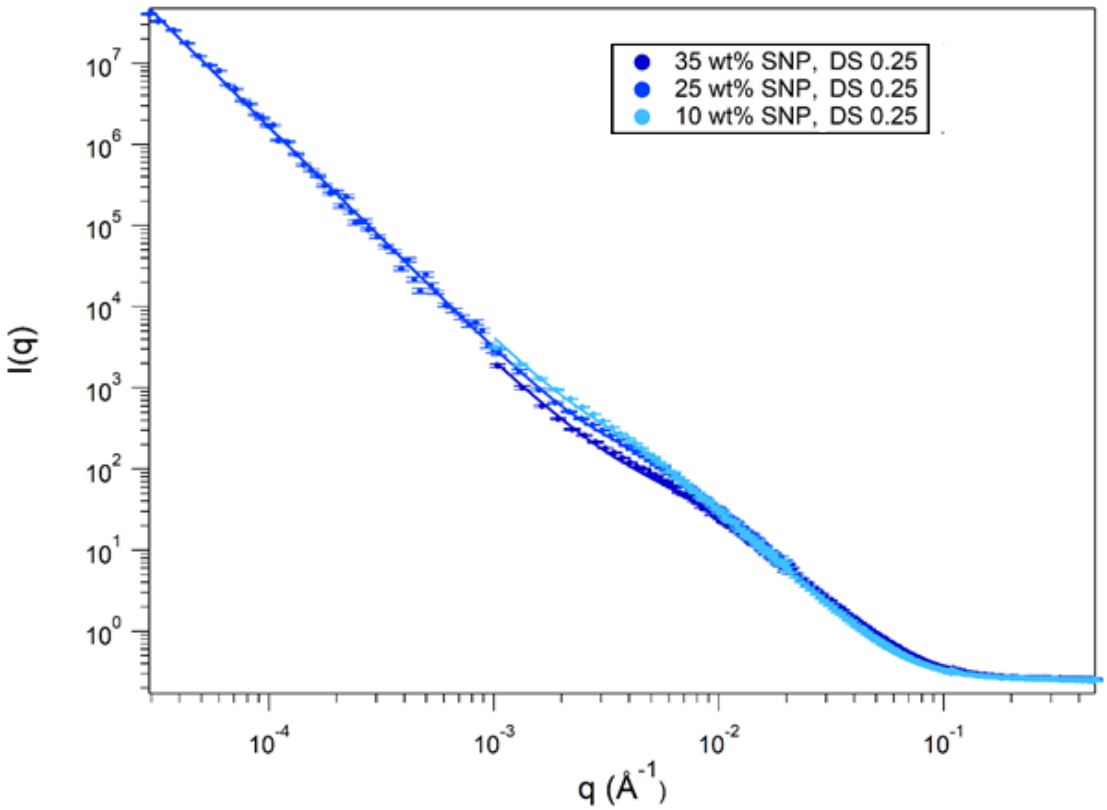

Figure S2.13: Starch hydrogel (SNP only) SANS curves showing the effect of changing wt% (10-35 wt%) while keeping the DS the same at DS = 0.25. See **Table S5** for the corresponding fitting parameters.

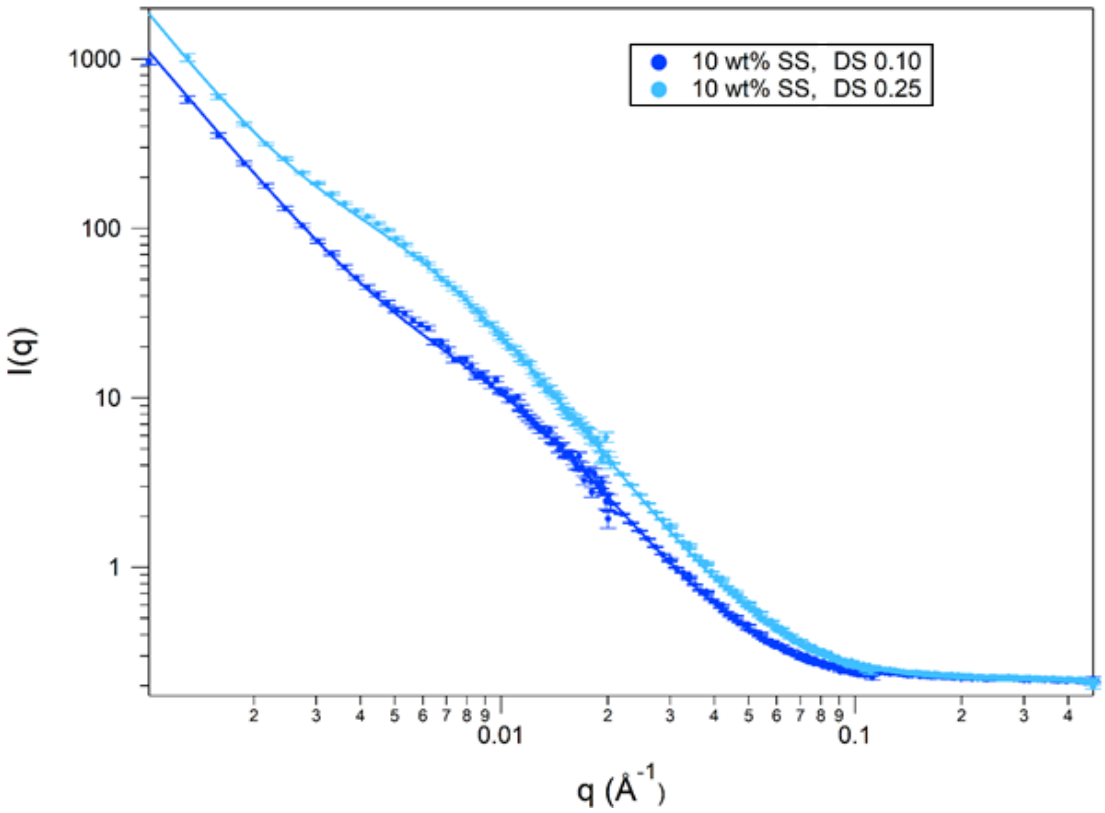

Figure S2.14: Starch hydrogel (SS only) SANS curves showing the effect of changing DS (0.10 and 0.25) while keeping the starch concentration constant at 10 wt%. See **Table S2.5** for the corresponding fitting parameters.

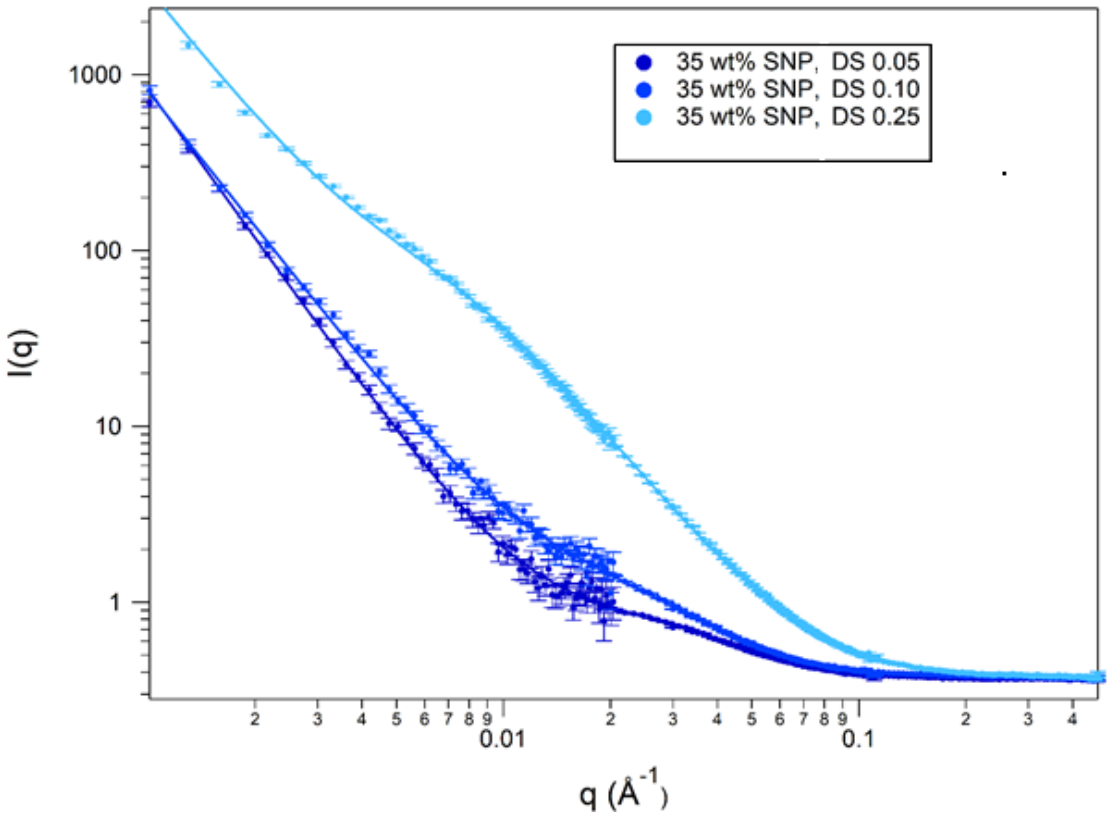

Figure S2.15: Starch hydrogel (SNP only) SANS curves showing the effect of changing DS (0.05-0.25) while keeping the starch concentration constant at 10 wt%. See **Table S2.5** for the corresponding fitting parameters.

Table S2.5: Key SANS parameters for photopolymerized hydrogels prepared with soluble starch (SS) compared with starch nanoparticles (SNPs), related to the curve fittings found in **Figures S2.10-S15**.

Parameter	***35 wt% SNP, DS=0.05***	***35 wt% SNP, DS=0.10***	***35 wt% SNP, DS=0.25***	***25 wt% SNP, DS=0.05***	***25 wt% SNP, DS=0.1***	***25 wt% SNP, DS=0.25***
Porod Exponent	2.49 ± 0.03	2.64 ± 0.09	2.34 ± 0.03	2.38 ± 0.03	2.42 ± 0.04	2.68 ± 0.09
Lorentzian Exponent	2.82 ± 0.03	2.72 ± 0.01	2.76 ± 0.03	2.77 ± 0.03	2.69 ± 0.02	2.71 ± 0.02
Lorentzian Screening Length (nm)	9.58 ± 0.2	162.3 ± 0.3	9.64 ± 0.25	8.86 ± 0.19	9.23 ± 0.16	1.64 ± 0.3
Lorentzian Scale	12.6 ± 0.8	84.9 ± 5.4	11.8 ± 0.9	11.5 ± 0.7	14.3 ± 0.7	87.0 ± 5.0

Parameter	***10 wt% SNP, DS=0.05***	***10 wt% SNP, DS=0.10***	***10 wt% SNP, DS=0.25***	***10 wt% SS, DS=0.05***	***10 wt% SS, DS=0.1***	***10 wt% SS, DS=0.25***
Porod Exponent	2.56 ± 0.02	2.54 ± 0.04	2.83 ± 0.01	2.25 ± 0.02	2.74 ± 0.01	2.76 ± 0.07
Lorentzian Exponent	2.77 ± 0.03	2.51 ± 0.01	2.96 ± 0.01	2.97 ± 0.17	2.55 ± 0.01	2.55 ± 0.01
Lorentzian Screening Length (nm)	3.45 ± 0.05	13.1 ± 0.2	2.93 ± 0.02	4.41 ± 0.04	18.8 ± 0.1	24.3 ± 0.4
Lorentzian Scale	0.93 ± 0.03	65.0 ± 3.3	1.4 ± 0.01	4.74 ± 0.11	165.8 ± 3.1	195.7 ± 14.2

Chapter 3: Investigating the Kinetics and Structure of Network Formation in Charged UV-Photopolymerizable Starch Nanoparticle (SNP) Network Hydrogels via Very Small Angle Neutron Scattering (vSANS) and Dynamic Hybrid Rheology (DHR)

Preface: This chapter describes an in-depth characterization of the internal morphology of UV photopolymerizable SNP hydrogels. Along with characterizing the neutral SNP-based hydrogels described in **Chapter 2**, charges were also introduced to the SNPs to see the effect of cationic (+) and anionic (-) charges in addition to the effect of starch type (branched soluble polymer vs. nanoparticle) on both the kinetic evolution and final architecture of the starch-based hydrogels using very small angle neutron scattering (vSANS) coupled with dynamic hybrid rheology (DHR) to understand the mechanics and viscosity changes that occur in tandem with network formation. This chapter will be submitted for publication concurrently with the thesis to *Macromolecules*. This work provides key insight into the effect of electrostatic forces on the kinetics and mechanics of nanoparticle network formation in nanoparticle network hydrogels (NNHs) for potential biomedical applications.

Authors: [1]Michael J. Majcher, [2]Sebastian Himbert, [1]Francesco Vito, [1]Matthew A. Campea, [1]Ridhdhi Dave, [3]Grethe Vetergaard Jensen, [2]Maikel C. Rheinstadter, [1]Niels Smeets, and [1]Todd Hoare

Affiliations: [1]Department of Chemical Engineering and [2]Department of Physics & Astronomy, McMaster University, 1280 Main St W., Hamilton, ON, Canada, [3]NIST Center for Neutron Research, National Institute of Standards and Technology, Gaithersburg, MD 20899-6100, United States

Abstract:
While photopolymerization has been broadly used to fabricate hydrogels using a range of different monomeric or polymeric building blocks, the kinetics of the structural evolution of such hydrogels during the photopolymerization process and how this relates to overall hydrogel performance is not well-understood. Herein, using methacrylated soluble (branched) starch and starch nanoparticles as the hydrogel building blocks, time-resolved very small angle neutron scattering (vSANS) and dynamic hybrid rheology (DHR) experiments are used in tandem to track the kinetics of structural changes during photopolymerization. In particular, by fabricating hydrogels by altering the concentration, charge (cationic (+), anionic (-), or neutral (0)), and morphology (soluble branched starch, starch nanoparticles, or combinations thereof) of the methacrylated starch building blocks, significant differences in the network evolution kinetics were observed by tracking the gelation time (t_{gel}) from DHR and the time constant of structural evolution ($1/\tau$) and best fit parameters of the fluid scale and correlation length from very small angle neutron scattering, SNPs were found to enable the fabrication of much denser hydrogels than soluble starch but took longer to gel due to the reduced conformational mobility of the polymerizable methacrylate groups on the SNPs; increasing the precursor starch concentration decreases the gelation time but results in lower changes in the fluid

scale. Alternately, the addition of charge (cationic or anionic) increases the bulk gelation time while significantly reducing the observed changes in the fluid scale and correlation length, suggesting less covalent crosslinking and inherent SNP deformation during photogelation. The fluid exponent of the vSANS fit increases during crosslinking with cationic SNPs, suggesting SNP deswelling/reduced hydration as the gel is formed to accommodate for charge-charge repulsion between the close-packed SNPs in the hydrogel; in contrast, the fluid exponent decreases during the crosslinking of neutral SNPs in which such repulsive interactions do not exist. The close-range interparticle charge-charge repulsion in hydrogels formed from charged SNPs also results in significantly stiffer hydrogels on the bulk scale as well as a significantly increased starting viscosity of the starting materials. The gelation kinetics insight gained from the combination of DHR (bulk) and vSANS (microstructure) measurements enables decoupling of the bulk and microstructural evolution during photogelation, providing key insight into the structural evolution of complex hydrogels during the photopolymerization process that can inform the design of new photopolymerizable hydrogels with targeted comprehensive properties.

3.1 Introduction

Hydrogels have attracted interest for a variety of biomedical applications such as drug delivery, tissue engineering, and cell encapsulation [364] The high water content and controllable porosity of hydrogels makes these materials of significant interest for use as surface coatings [365] with low non-specific protein adsorption and suppressed biofouling [128] (key to the proper function of biosensors) [366,367], biomedical implants/devices with low inflammatory responses [111,154,368–370], and various bioseparations-based applications [128,371,372]. The underlying micro- and/or nano-structure of the hydrogel determines the efficacy of the hydrogel in each targeted application, whether related to the diffusivity of drugs, cells, or nutrients through the gel (drug delivery/tissue engineering) or the contact angle/degree of hydration of the gel (anti-fouling). In this context, understanding the porosity and the nature of any inhomogeneities within the gel, as well as how to control such features as a function of the physical morphology and/or chemistry of the hydrogel building blocks, is critical to rationally engineer gels with targeted release kinetics, degradation times, and adsorption properties.

Most conventional hydrogels are fabricated by crosslinking linear polymers or polymerizing monomers and crosslinkers together *in situ* [61,262]. Depending on the nature of the building blocks used (e.g. their relative reaction rates, their propensity to phase separate, etc.), nano/microscale domains may form that significantly influence hydrogel properties [373,374]. Alternatively, more recent work has investigated the formation of hydrogels from specific building blocks in which well-defined and pre-crosslinked nano/microgels are subjected to a secondary crosslinking reaction to form a nano/microgel network hydrogel. The mechanical, diffusional, and sorption properties of such hydrogels are influenced by both the size and crosslink density within (*intra*-) the nano/micro-scale building blocks as well as the degree and type of crosslinks between

(*inter*-) those building blocks, providing multiple levers for controlling hydrogel properties as discussed in our recent review [105].

Our recent experimental focus in this area lies in using starch nanoparticles (SNPs) as building blocks for fabricating nanoparticle network hydrogels. SNPs are extremely small relative to other nanogel building blocks (20-50 nm on average), are based on a natural, highly cell-compatible and hydrolytically degradable material, and are available inexpensively at commercial scales, making SNP-based hydrogels relevant to both high value and commodity (e.g. agriculture or bioremediation) applications. Hydrogels can be formed via facile methacrylation of the SNPs and subsequent thermal or photopolymerization, with photopolymerization using long wave (365 nm) or short wave (264 nm) UV light found to be particularly useful for facile hydrogel formation [285] (**Figure 3.1**). SNPs can be crosslinked directly to themselves or by using methacrylated soluble (branched) starch (SS) as a crosslinking agent, offering the potential to form different network morphologies with identical chemistries**.** Correlating the morphologies of these materials with their properties, in terms of understanding both the final gel properties achieved as well as the structural evolution of such hydrogels as they are formed, is critical for rationally designing hydrogels for targeted applications.

While a variety of methods including dynamic [375] and static light scattering [376,377], X-ray scattering [378,379], turbidity/cloud point measurements [380,381], and advanced electron microscopy methods has been used for investigating the internal morphology of hydrogels, small angle neutron scattering (SANS) is particularly useful given that both the pore size and the dimensions of typical gel inhomogeneities lie in the accessible SANS length scale (1-200 nm) [382–385]. SANS is particularly useful for characterizing nanoparticle network hydrogels given that the mesh size of the nano/microgel, the mesh size between the nano/microgels, and the absolute size of the nano/microgels used all lie within the accessible SANS length scale (unlike with other methods) [386]. SANS studies on pre-formed nano/microgel network hydrogels at an equilibrium swelling state have been reported both by our group and others [257,301,387]. Specific to SNPs and soluble starch, our previous SANS results and suggested that SS hydrogels have significantly lower Porod exponents (corresponding to more Gaussian, swollen chains), significantly higher Lorentzian screening lengths or fluid correlation length as referred to herein (indicating larger gel mesh sizes), and much larger Lorentzian scales (indicating a significantly more fluid network structure) than SNP-based hydrogels. Furthermore, for SNP-only hydrogels, the degree of *inter*-particle crosslinking was observed to substantially change when either the SNP concentration or the degree of methacrylation were changed (as evidenced by the trends in each of the Lorentzian/fluid-like fluctuation terms) but the internal structure/swelling of each individual SNP building block did not appreciably change (as evidenced by the relatively constant Porod exponent) [285]. However, the dynamics of the gel formation process, and the structural implications of the different building blocks used on those dynamics, remain unexplored.

The structural evolution of the hydrogel during gelation has been tracked previously by SANS for other systems containing associative polymers [321], sticky microgels [322], proteins [323], ionic liquids [324], thermoresponsive polymers [388], colloidal nanoparticles [389], and shear-induced gelation [390], typically using the observed increases in scattering intensity (Porod scattering) over time as a proxy to the rate of the formation of new crosslinks. However, to the best of our knowledge, using SANS to directly track the kinetics of network structural evolution during photopolymerization (for any relevant hydrogel formulation, not just NNHs) has not been reported, in large part due to technical limitations with performing photopolymerization in the neutron beam line and subsequently acquiring relevant kinetic data on the timescale of a typical photopolymerization (often seconds-to-minutes). In this context, very small angle neutron scattering angle (vSANS) offers unique benefits. Built in 2017 and operated by the Center for High Resolution Neutron Scattering (CHRNS) at the National Institute of Standards and Technology (NIST) in Gaithersburg, MD, USA, the vSANS instrument is larger (45 m) than other neutron scattering machines and contains triple detection technology that allows for simultaneous data collection across a q-range of 0.002 to 10 nm^{-1} (size regime of 1 nm to 2000 nm), bridging the q ranges of SANS and USANS while allowing for significantly faster overall data collection (on a timescale suitable for photopolymerization) than is possible in other instruments in which sequential detector length data collection is required [391].

Herein, we apply the vSANS technique to track the kinetics and structural evolution of the network morphology in hydrogels prepared by photopolymerizing methacrylated soluble starch and/or methacrylated starch nanoparticle building blocks. Specifically, we explore the evolution of the nanostructure of photopolymerizable starch-based hydrogels depending on the concentration of the precursor building blocks, the morphology of the precursor building block (i.e. using either a SNP or soluble branched starch) as well as the interactions between those building blocks, which we manipulate by functionalizing both types of starch building blocks with cationic or anionic charges [108,305]. More specifically, by assessing differences in network evolution in hydrogels prepared with different SNP or SS concentrations, different building block morphologies (e.g. soluble starch only, SNPs only, and combinations of SNPs and soluble starch) as well as varying types of charged building blocks (considering in particular repulsive electrostatic interactions between the SNP building blocks, as is typically used to form colloidal crystals of nanogels) [392], we aim to correlate the physical nature of the building blocks with the structural evolution of the hydrogel during crosslinking. Furthermore, by combining dynamic hybrid rheology in which photocrosslinking is conducted directly on the rheometer, the bulk property evolution of the hydrogel over time can be matched with the microstructural evolution identified by vSANS, providing a comprehensive understanding of the network evolution during the photocrosslinking process on multiple length scales.

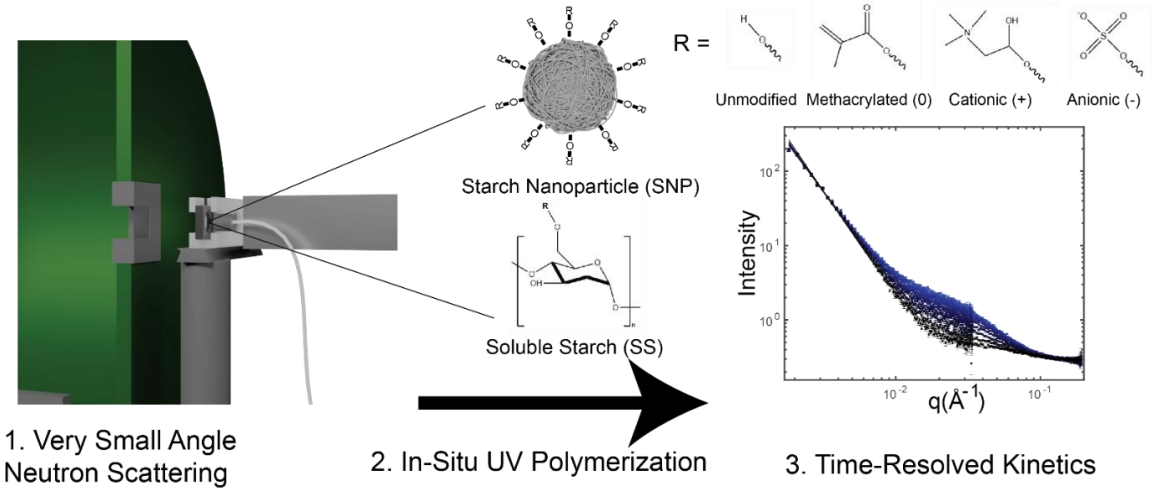

Figure 3.1: A schematic of the use of very small angle neutron scattering (vSANS) to acquire time-resolved gelation kinetics data for the *in situ* UV photopolymerization and bulk network formation of hydrogels based on methacrylated soluble (branched) starch (SS) and starch nanoparticle (SNP) building blocks with different charges.

3.2. Materials & Methods

3.2.1 Materials

Commercial grade cationic (quaternary ammonium, charge density 0.34 meq/g) starch nanoparticles, experimental grade *EcoSphere* starch nanoparticles and neutral cold water soluble starch (SS) samples were donated by *EcoSynthetix Inc.* (Burlington, Ontario, Canada). Pyridine (ACS reagent grade, ≥ 99%), 1,3-propane sultone (≥ 99%), methacrylic anhydride (contains 2,000 ppm topanol A as an inhibitor, 94%), mono-chloroacetic acid (ACS reagent grade, ≥ 99%), and dimethylaminopropylamine (99%) were obtained from Sigma-Aldrich. Sulfuric acid (16 M), methanol (reagent grade), and dimethylsulfoxide (DMSO) were obtained from Fisher Scientific. For all other "wet" steps, Milli-Q deionized water (MQW) with a conductivity between 17 and 18 mΩ was used. For purification of the precursor materials, 3.5-5 kDa cellulose ester dialysis tubing (SpectrumPor) and 0.45 um PTFE filters (VWR) were used.

3.2.2 Starch Chemical Modification

3.2.2.1 Cationic Functionalization

Experimental grade cationic starch nanoparticles with a charge density of 0.34 meq/g were generously gifted from *EcoSynthetix Inc.* for use in this experiment. The substitution of the positive charge was performed by a modified reactive co-extrusion process [393].

3.2.2.2 Anionic Functionalization

To match the charge density of the commercially-supplied cationic SNPs, a protocol for fabricating sulfated (anionic) SNPs was adapted from a previously published method [394]. Pyridinium-methyl-sulfate (Py-Me-S) reagent was first made by adding pure

sulfuric acid (95 mL) dropwise to methanol (175 mL) in an ice bath, stirring overnight (~16 h), adding 144 mL of pyridine (1 mol equivalent to sulfuric acid) to the reaction mixture, stirring at 4 °C overnight, washing with toluene three times, and drying the product *in vacuo*. The Py-Me-S reagent was then used to sulfate 20 g batches of SNP or SS using varying molar ratios of Py-Me-S to starch (see **Supporting Information, Table S3.1**); to match the charge density of the commercial cationic SNP, a 2.5:1 molar ratio of Py-Me-S to starch was found to be optimal when the reaction was performed at 60 °C for 3 hours in DMSO.

3.2.2.3 Methacrylation of Starch Precursors

Cationic, anionic, and neutral SNPs and neutral SS samples were subsequently functionalized with methacrylate groups using a previously published protocol [285] . After each modification to the starch chemical structure, samples were purified using 6 different 6 h cycles of dialysis (3.5-5 kDa MWCO) in MQW and lyophilized to form a white fluffy product. Once pure (either after charge addition of while in their native state), Methacrylic anhydride (MAAn, 4.56 mL) was used to functionalize 54.3 g of fully dispersed SNPs or dissolved SS in sodium hydroxide (pH 10.4) via a transesterification reaction with C6 hydroxyl groups on the starch backbone, targeting a degree of substitution (DS) of 0.10. Post-methacrylation, all particles were purified again using other regimen of 6 different 6 h cycles of dialysis (3.5-5 kDa MWCO) in MQW and lyophilized to form the final product. The degree of methacrylation was assessed via proton nuclear magnetic resonance (NMR) experiments in deuterated DMSO, with the degree of methacrylation calculated using a protocol established in a previous report from the authors on neutral methacrylated SNPs for NNH production via photopolymerization [285].

3.2.3 Characterization of Methacrylated Starch Nanoparticles (SNP) and Soluble Starch (SS)

3.2.3.1 Elemental Analysis (EA)

Elemental analysis was conducted using an Elementar Unicube using dried SS or SNP samples (2 mg) loaded into 4 x 4 x 11 mm tin boats. Samples were loaded onto an autosampling carousel and run using a combustion tube operating at 900 ˚C and a reduction tube operating at 799 ˚C. The samples were standardized using a sulfadimidine standard.

3.2.3.2 Dynamic Light Scattering (DLS) and Electrophoretic Mobility

SNP particle size was assessed by dispersing the nanoparticles in MilliQ water (MQW) at a concentration of 10 mg/mL (1 w/v%), vortexing the sample at 1600 rpm for 1 minute, and placing the samples into a low-power bath sonicator for 5-10 min to fully redisperse the SNPs. Vortexed samples were filtered with a 0.45 μm PTFE syringe filter to remove any large aggregates. Particle size was measured on a NanoBrook 90Plus PALS (Brookhaven, Long Island, NY, USA; temperature = 25°C), using the refractive index of starch (RI = 1.34) to calculate number average diameters as required [395]. Electrophoretic mobility measurements were performed by dispersing the SNPs in a 10

mM NaCl solution at a concentration of 10 mg/mL, vortexing, and filtering as described for DLS.

3.2.3.3 Polyelectrolye Titration

To determine the amount of charge per gram of material (meq/g) on the functionalized SNPs, a particle charge detector (BTG Mutek) was used, using poly(diallyldimethylammonium chloride) (PDADMAC, 0.001M) as the cationic titrant and poly(vinyl sulfate) (PVSK, 0.001M) as the anionic titrant consistent with reported methods [396,397]. The sample was suspended in MQW at concentrations of 10-30 mg/mL in a total volume of 10 mL, after which the oppositely charged titrant was added incrementally to the sample using the auto-titrator feature until the effective surface charge was 0 mV (indicating that all the charged groups have been titrated).

3.2.4 Fabrication of Starch Hydrogels

3.2.4.1 Homogenous Gels

Samples of SS and SNPs, the latter with or without charge functionalization, were suspended at various wt% in MQW, after which 0.15 v/v% 1-[4-(2-hydroxyethoxy)-phenyl]-2-hydroxy-2-methyl-1-propane-1-one (Irgacure 2959) solution was added. The solutions were then be placed into silicone molds of whatever size/shape desired (12.7 mm diameter, 4 mm thick for mechanical testing) and photopolymerized using a UV crosslinking oven (Cure All, 80 mW/cm^2) for a total of 10 minutes. To minimize evaporation of water during photocrosslinking, a cooling air jet was applied to control the surrounding temperature. Following irradiation, the hydrogels were parafilmed and left overnight in a crystal dish containing a 200 mL beaker of water (to prevent evaporation/drying) prior to characterization. Comparisons of hydrogels based on neutral SNP or neutral SS gels will be used to gain insights to the effect of starch type on network formation, while comparisons of hydrogels formed based on cationic, anionic, or neutral SNPs will be used to assess the effect of surface charges on gel properties.

3.2.4.2 Heterogenous Gels (Mixtures)

To assess the network structure evolution as a function of the morphology of the precursor polymers, mixtures containing 2:1, 1:1, and 1:2 ratios of methacrylated SS:SNP were created by dissolving/suspending required masses of each starch in MQW to achieve a final overall concentration of 10 wt%. These samples were then photocrosslinked as described above to create heterogenous hydrogels. For all gels, the theoretical degree of substitution of methacrylate groups was 0.10, the final wt% of Irgacure was 0.15 w/v%, and the UV irradiation time was 10 minutes.

3.2.5 Dynamic Hybrid Rheology Measurements

The rheological properties of the photocrosslinked starch hydrogels described above were assessed using a dynamic hybrid rheometer (Discovery HR-2, TA Instruments) maintained at 37 ˚C with a bottom quartz plate/in-line UV light. For each gel/formulation, three different rheological experiments were performed one after the other on the same initial sample (200 μL total volume): (1) viscosity versus shear rate

sweeps of the gel precursor solutions; (2) oscillatory sweeps during *in situ* UV irradiation to measure the gelation time (t_{gel}) [398]; and (3) oscillatory sweeps after gelation to assess the mechanics of the fully-formed network (via the plateaus in the G' and G" profiles as a function of oscillation frequency).

3.2.5.1 "Flow" Tests for Shear-Induced Viscosity Profiles

To assess the viscosity of the precursor starch solutions/suspensions, a "flow" test (viscosity vs. shear rate) was performed using a 20 mm aluminum top plate, a 20 mm quartz bottom plate, a 0.5 mm (500 um) parallel plate gap, shear rates from 0.1 to 100 s^{-1}, 5 points per decade, an average sampling time of 30 s, and an equilibration time of 5 s.

3.2.5.2 Oscillation Tests for Gelation Time and Post-Gelation Mechanics

Directly after performing the viscosity flow tests on the precursor solutions, the UV accessory was used to determine the gelation time (t_{gel}), defined as the time at which the storage modulus (G') and loss modulus (G") intersect. A "fast oscillation sweep" experiment was performed by applying a 1% strain at a frequency of 1 Hz for 30 s, after which a UV light (80 mW/cm^2, 365 nm wavelength) was used to *in situ* photocrosslink the precursor starch solutions/suspensions on the rheology platform through a quartz window for a total of 10 min (600 s) [399]; the storage modulus (G') and loss modulus (G") were measured every 30 seconds over the entire 10 minute irradiation window. Following gelation, the sample was left for 10 minutes to ensure that the crosslinking was complete, after which a strain sweep was first conducted to confirm operation within the linear viscoelastic region (LVE) followed by a frequency sweep (at 1% strain) from 0.1 to 100 rad/s to measure G' and G" for the final hydrogel.

3.2.6 Very Small Angle Neutron Scattering (vSANS)

3.2.6.1 Experimental Procedure

Very small angle neutron scattering (vSANS) measurements were performed on neutron guide B3 at the NIST Center for Neutron Research (NCNR) in Gaithersburg, MD, USA. The instrument setup is shown in **Figure 3.2**. All gel precursor solutions were prepared using starch nanoparticle concentrations of 10-35 wt% and soluble starch concentrations of 5-10 wt% (consistent with the gelation work performed above) using D_2O as the solvent. Precursor solutions/suspensions were loaded into NCNR's custom-made titanium sample chamber with quartz windows on either side (diameter 19 mm and path length 2 mm). The chamber was then placed in a temperature-controlled rack in front of a 45 m long evacuated tube enclosing a set of three detectors at positions 4.12 m, 19.12 m and 23.02 m from the sample; at the time of the experiment, only the two high-q detectors were available with an accessible q-range between $2x10^{-3}$ to 1 A^{-1}. The instrument was operated in its white beam configuration to maximize the neutron flux, resulting in a non-Gaussian wavelength spread of 40%; to compensate, the model was smeared accordingly as further described in **Section 3.3.3**.

A Prizmatix Ultra High Power Light Guide Coupled UV LED (UHP-F-5-365, 365 nm) was mounted parallel to the neutron guide such that the light illuminates the sample two

slots next to its position in the neutron beam. Hereafter, the sample position used for the SANS measurement will be referred as SANS slot and the position for the UV exposure as UV slot. The entire sample stage was covered with a black plastic dividing wall to prevent ambient light from accessing the sample. Each sample was measured using to the following protocol: (1) Take one SANS measurement; (2) Move the sample to the UV slot; (3) Expose the sample to UV light for 3 seconds; (4) Move the sample to the SANS slot; (5) Take one SANS measurement; (6) Move the sample back to UV slot and re-expose to UV light for 3 s; (7) Repeat 10 times to collect a set of 11 measurements for each sample tracking the structural evolution in the hydrogel during step-wise UV exposure (total power 6 W, 5 mm LLG core). Note that the Prizmatix UV light guide has a much higher power (up to 70 W/cm^2) than the UV light used for the rheology work (80 mW/cm^2) in order to achieve a maximum run time of 10 minutes per sample with 10 measurements for the kinetic profile, resulting in a total exposure time of 30 s ; as such, while the scaled kinetics of the structural evolution are expected to be comparable, the gelation timescales for the two methods are not directly comparable.

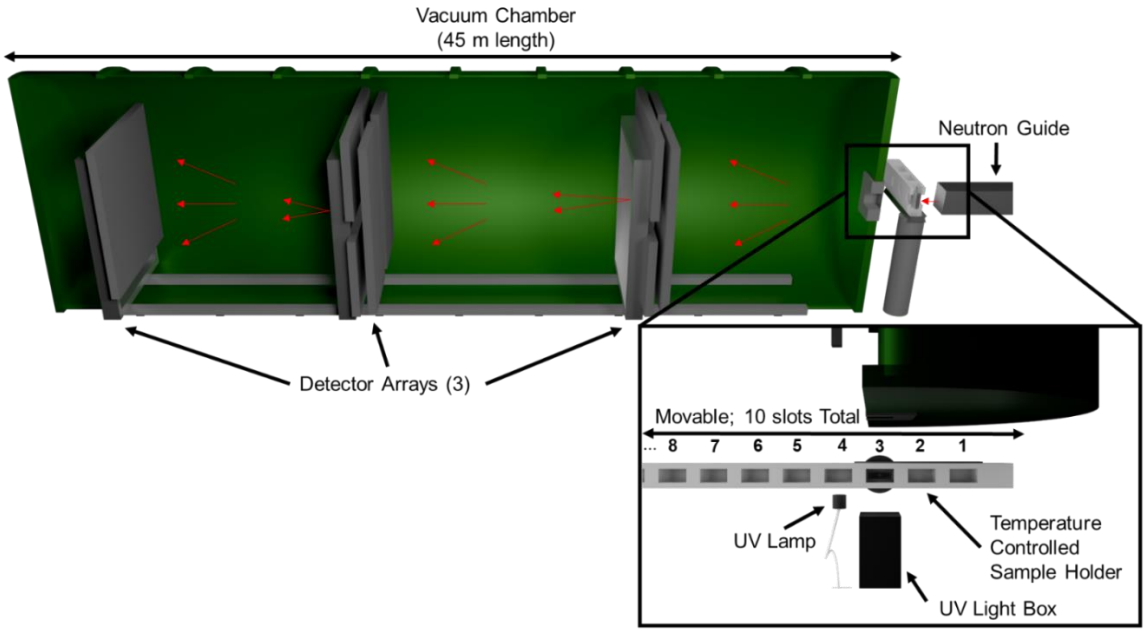

Figure 3.2: Schematic of the vSANS experimental setup. The instrument consists of a 45 m long vacuum tube enclosing a set of three detectors. The sample is loaded into custom-made titanium/quartz sample holders and placed in temperature-controlled rack fitting up to 9 samples at a time. The UV lamp was placed two slots next to the neutron guide. The sample rack was covered with black plastic dividing wall for the duration of the experiment to minimize the effect of ambient light.

Previous injectable hydrogel work on materials with similar or lower mass fractions achieved high signal:noise scattering profiles using measurement times of ~30 minutes per sample (~12 min. at 13 m, ~15 min. at 13 m (with lens), ~3 min. at 4 m, and ~1 min at

1 m [385]. While the lower *q* value data collection is not possible on the timescale of photocrosslinking (10-30 minutes), the key network evolution effects can be assessed using only the higher *q* data that can be collected in 3-4 minutes per sample.

3.2.6.2 Fitting Parameters & Modelling

Scattering profiles were fit using Shibayama's approach of combining an Ornstein-Zernicke scattering term with a Lorentzian term to account for the presence of domains (here, the denser SNPs relative to the less dense inter-SNP region) as well as the dynamics of the gel network (**Equation 3.1**) [333]:

$$I(Q) = \frac{s_{porod}}{Q^n} + \frac{s_{oz}}{1+(Q\xi)^m} + b \quad \textbf{Eqn. 3.1}$$

The equation above was developed by Hammouda and co-workers at NIST to anlyze the scattering spectra of polymer solutions and hydrogels using the I(q) scattering intensity and the scattering vector (q). In **Eqn. 3.1**, s_{porod} and s_{oz} measure the scale/weightings of the Porod and Ornstein-Zernike Lorentzian functions respectively, *n* is the Porod exponent describing clustering and swelling within a network (dominating the low-*q* regime of the SANS profile) [360,361], ξ is the correlation length of the hydrogel network, *m* is the Lorentzian exponent corresponding to polymer-solvent interactions (dominating the high *q* regime of the SANS profile), and *b* denotes the *q*-independent background resulting from incoherent neutron scattering [63,383].

Using the instrument in its white beam configuration has the consequence of measuring a spectrum that is convoluted with the beam's own wavelength distribution, correction for which was performed by convoluting **Eqn. 1** with the white beam spectrum provided by NIST. The model parameters were determined for each sample respectively and plotted against the UV exposure time to assess the structural evolution in the hydrogels over the time course of photocrosslinking. Exposure time-dependent trends observed with the correlation length ξ and the scale s_{oz} of the Ornstein-Zernike Lorentzian were fit using a stretched exponential function (**Eqn. 3.2**):

$$\xi(t) = e^{-\left(\frac{1}{\tau}t\right)^{\beta}} \quad \textbf{Eqn. 3.2} \qquad\qquad \boldsymbol{s_{oz}}(t) = e^{-\left(\frac{1}{\tau}t\right)^{\beta}} \quad \textbf{Eqn. 3.3}$$

Here, τ is the time constant of the dynamic processes (i.e. the photocrosslinking reaction) and β denotes the stretch that models relaxation processes in glass-like liquids (β=1 denotes an isotropic relaxation, while $0 < \beta$<1 is indicative of anisotropic relaxation and an anomalous diffusion process [401–403]). Work by de Gennes [404] supports the idea that the correlation length ($\xi(t)$) in homogeneous gels should be equal to or less than size of the average mesh and should not differ significantly from the correlation length of a polymer solution at the same concentration [405].

Fits were performed using MATLAB and the spec1d library provided by the Institute Laue-Langevin, Grenoble, France by computing the least-square fit for a given function and dataset using the Levenberg-Marquardt minimization algorithm [406,407].

3.3. Results & Discussion

3.3.1 Characterization of Starch Precursors

Dynamic light scattering (DLS) was used to determine the particle size of the starch nanoparticles before and after chemical modification. All modified SNPs have intensity-based particle sizes varying between 130-260 nm but a number-based particle size consistently lying in the range of 19-28 nm (**Table 3.1 (column a)**). These results are consistent with previous work [285] and suggest that SNP suspensions consist of very small nanogel-based gel building blocks that undergo a minimal degree of self-aggregation when suspended in water. Electrophoretic mobility measurements on the SNPs (**Table 3.1 (column b**)) show that the neutral (base) SNP has a net zero surface charge while the anionic SNPs have an electrophoretic mobility of -0.79×10^{-8} m^2/Vs and the cationic SNPs show an electrophoretic mobility of $+0.45 \times 10^{-8}$ m^2/Vs, confirming the success of the functionalization protocols for introducing negative and positive charges on the respective SNPs. Polyelectrolyte charge titration (using anionic PVSK as the titrant for the cationic SNPs and cationic PDADMAC as the titrant for the anionic SNPs) further confirms these results (**Table 3.1 (column c)**), with the charge density of both cationic and anionic SNPs lying in the range of |0.35-0.41| meq/g at the optimal (-)SNP recipe identified to match the charge density of the industrially-sourced (+)SNP sample (see **Supplementary Information Table S3.1** for details on this optimization process). Elemental analysis further confirms this result, with cationic-functionalized SNPs showing an increase in %N from 0.16 atom% to 0.42 atom% (**Supplementary Information, Figure S3.1a**) while the %S increases in a systematic manner as the ratio of pyridium methyl sulfate to starch is increased from 1:0.05 (0.07 atom% S) to 1:10 (5.1 atom% S) (**Supplementary Information, Figure S3.1b**). Subsequent methacrylation of the starch precursors resulted in no significant changes in either the number-average diameter or the electrophoretic mobility ($p>0.05$ in all pair-wise comparisons versus the non-methacrylated precursor material), with the degree of methacrylation based on NMR analysis being 0.10±0.01 for all SNPs (0.09-0.11, **Table 3.1 (column (e)**) and SS (0.10).

Note that the anionic (sulfated) SNPs showed a higher absolute electrophoretic mobility value (**Table 3.1**) and a higher S mol% (**Fig. S3.2**) than the cationic SNPs despite the very similar polyelectrolyte charge titration results observed for the anionic and cationic samples. We hypothesize that the sulfation chemistry may be more effective at internally functionalizing the SNPs in addition surface functionalization; note that electrophoretic mobility measurements in soft nanoparticles like SNPs also measure some internally-contained charges. However, we believe the comparison of the effect of charge on gelation best conducted by matching the surface charge density as measured by the polyelectrolyte charge titration data, for which the charge density of the cationic and anionic SNPs match, rather than the electrophoretic mobility values. As such, all

precursor starches have essentially the same degree of methacrylation (0.10 ± 0.01) and all charged SNPs have equivalent surface charge densities (~|0.40| meq/g), allowing direct comparisons to be made between the hydrogels formed from the different precursors.

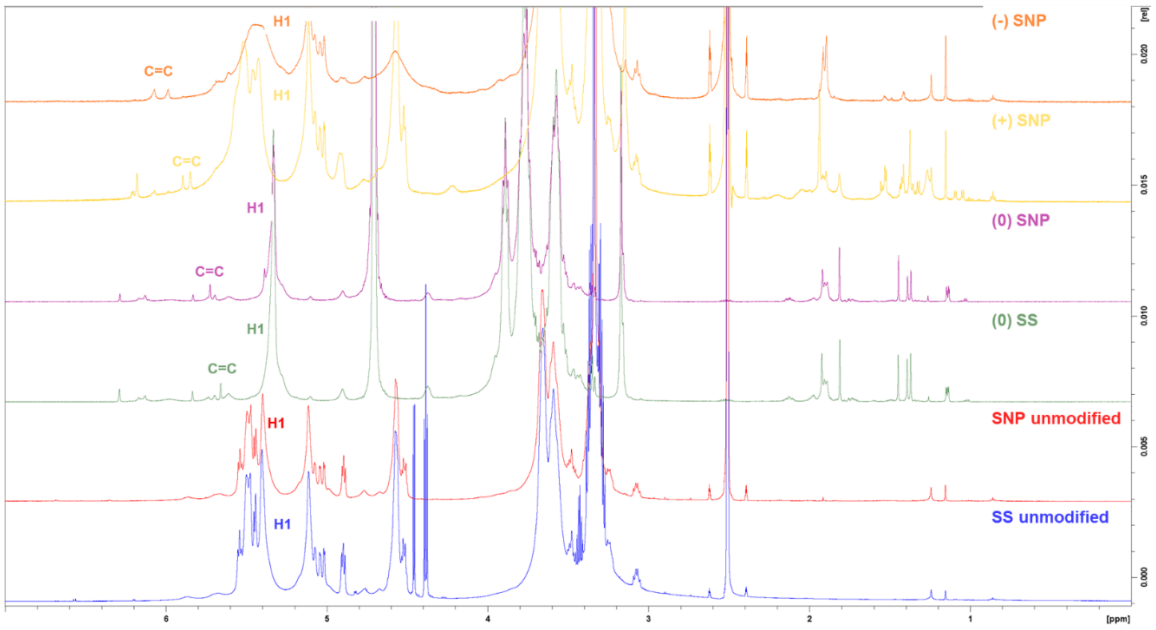

Figure 3.3: ^{1}H NMR spectra of methacrylated neutral and charged soluble starch (SS) and starch nanoparticles (SNP) relative to the non-methacrylated precursor polymers. The area under the doublets, indicative of a methacrylic group (I = 6.2 ppm, C=C), were compared to the anomeric carbon (I = 5.4 ppm, 1H) intensity to calculate the degree of substitution (DS) [285].

Table 3.1: Effective diameter (by intensity or number weighting), electrophoretic mobility, and surface charge density of native and functionalized starch nanoparticle (SNPs) used for hydrogel fabrication.

Starch Type	Effective Diameter by Intensity (nm)[a]	Effective Diameter by Number (nm)[a]	Electrophoretic Mobility ($\times 10^{-8}$ m^2/Vs)[b]	Surface Charge Density (meq/g)[c]	Degree of Functional (Charged) Group Substitution	Degree of Methacrylation[e]
(0) SNP	132 ± 2	28 ± 2	+0.03 ± 0.15	0.00	-	0.10
(-) SNP	175 ± 13	25 ± 7	-0.79 ± 0.06	-0.41	0.12	0.09
(+)SNP	264 ± 14	19 ± 12	+0.45 ± 0.05	+0.35	0.05	0.11

[a] from dynamic light scattering; [b] from phase analysis light scattering zeta potential measurements; [c] from polyelectrolyte charge titration; [d] from elemental analysis for charged SNPs; [e] from ^{1}H NMR.

3.3.2 Rheology

3.3.2.1 Pre-Gelation Viscosity

To assess the impacts of the concentration, morphology, and charge of the starch gel precursors on the initial viscosities of the pre-gel solutions/suspensions, viscosity versus shear rate tests were performed (**Figure 3.3**); the shear-thinning viscosity data for each sample extracted only at shear rates of 0.1, 1, 10, and 100 1/s is available in **Supporting Information Figure S3.4 (a-e)** to enable more direct comparisons between the samples. Note that the concentration ranges tested (25-35 wt% for SNPs, 7.5-10 wt% for SS) were chosen based on the upper range of the solubility of the SS as well as the concentration of the more compact SNPs previously identified to form hydrogels rather than simply viscous solutions following photocrosslinking [285].

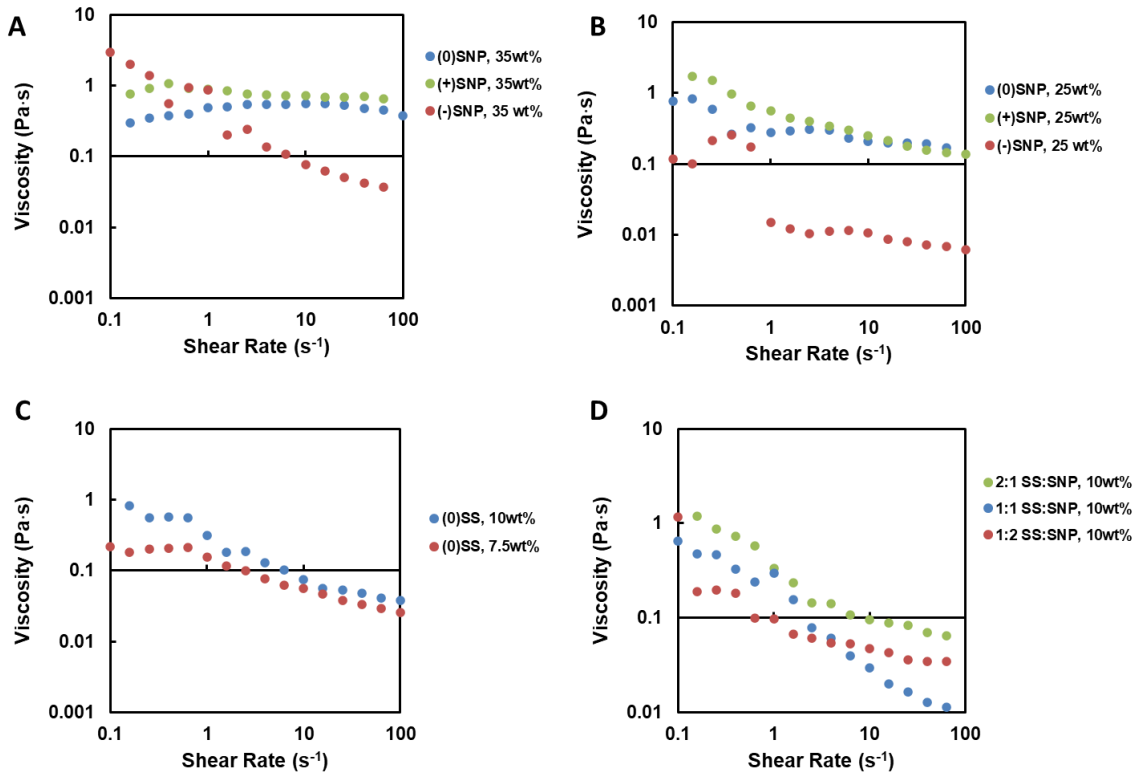

Figure 3.4 (a-d). Viscosity versus shear rate flow sweeps to determine the relationship between shear and viscosity for (A) 35 wt% homogenous gels (SNP building blocks); (B) 25 wt% homogenous gels (SNP building blocks); (C) SS-based homogenous gels at different concentrations (10 and 7.5 wt%); and (D) 10 wt% heterogenous gels (mixtures of SS and SNP building blocks).

The SS-only and SNP-SS mixture gel precursor solutions are shear thinning across all weight percentages tested, consistent with other waxy starch studies [408]. However, SNP-only samples show consistently lower viscosities and significantly less shear thinning behaviour than SS samples, with the 35wt% (0)SNP and (+)SNP precursors in particular exhibiting essentially no significant shear thinning over the shear rate range studied. This result is consistent with the higher molecular weight, degree of hydration, and potential for intermolecular entanglements observed with the branched soluble SS compared to the crosslinked compact SNPs. Correspondingly, increasing the concentration of either SS or SNPs (comparing **Figs. 3.3a** and **3.3b** for SNPs or **Fig. 3.3c** for SS) also results in increased viscosities. Introducing a cationic or anionic charge increases the precursor suspension viscosity at low shear, consistent with electrostatic repulsion between the precursor materials in solution; however, the charged SNPs also shear thin more than the neutral SNPs as the shear forces can better compete with the electrostatic repulsive forces present, particularly for the (-)SNP samples that appear to be similarly shear thinning to the SS samples. With respect to the mixtures of SS and SNPs (**Fig. 3.3d**), the more branched SS is included in the system, the higher the observed viscosity at low shear rates and the more shear thinning the sample at higher shear rates, consistent with increased chain entanglement as more of the branched soluble SS is added to the less conformationally-mobile SNPs in the precursor starch mixture. As such, both the charge and the morphology of the starch precursor(s) used significantly alter the interparticle/interchain interactions in solution prior to gelation, interactions we expect will be reflected in the structures and properties of the resulting hydrogels formed.

3.3.2.2 In Situ Gelation Kinetics

To assess the effects of starch concentration, morphology, and charge on the photocrosslinking of the methacrylated starches to form hydrogels, an *in situ* photocrosslinking experiment was conducted using the UV accessory on the rheometer to determine the time of gelation (t_{gel}). The time of gelation (t_{gel}) was defined at the time point corresponding to the inflection point in the G' and G" plots vs. time; note that this metric was chosen instead of the more conventional G'/G" = 1 convention since some of the precursor polymer samples (particularly higher concentration SS samples) were already highly viscous and showed G'/G">1 even before photocrosslinking, making that metric incompatible with our system (**Supplementary Information, Figure S3.3**). The resulting gelation times measured for each sample are shown in **Figure 3.4**.

Table 3.2: Gelation time (t_{gel}) for methacrylated starch photogelation as a function of starch concentration, morphology (SS or SNP), and charge.

Sample	Gel Type	wt%	t_{gel}, s
(0)SNP	Homogeneous	35	32
(0)SNP	Homogeneous	25	56
(+)SNP	Homogeneous	35	46
(+)SNP	Homogeneous	25	88
(-)SNP	Homogeneous	35	50
(-)SNP	Homogeneous	25	99
(0)SS	Homogeneous	10	20
(0)SS	Homogeneous	7.5	39
2:1 SS:SNP	Heterogeneous	10	41
1:1 SS:SNP	Heterogeneous	10	57
1:2 SS:SNP	Heterogeneous	10	92

In all cases, increasing the concentration of any SS or SNP precursor accelerates gelation while functionalizing the SNPs with charge significantly slows gelation, with (+) SNP and (-) SNP both observed to gel slower than the neutral SNPs at both concentrations tested. This trend is consistent with the interparticle (repulsive) particle interactions in the pre-gel suspension restricting the proximity of the polymerizable methacrylate groups on the SNPs and thus slowing photocrosslinking. However, the morphology of the starting material has a more complicated effect on gelation time. For the mixtures of SS and SNP (all at 10 wt%), the 1:1 SS:SNP ratio hydrogel gels the slowest among the ratios tested, while the 2:1 SS:SNP hydrogel gels particularly quickly (indeed, slightly faster than the SS-only hydrogel at the same concentration of 10 wt%); note that a 10 wt% SNP-only hydrogel cannot gel whatsoever even at extended irradiation times due to the compactness of the SNPs and is thus not included in this comparison set. We hypothesize this result is an effect of the combined effects of more SNPs providing enhanced mechanical strength based on the internally crosslinked structure of the SNP (a dominant effect at the 1:2 SS:SNP ratio) and more SS providing more effective interparticle crosslinking given that the methacrylate groups are less sterically hindered to polymerization than they are on the more rigid SNPs (a dominant effect at the 2:1 SS:SNP ratio).

3.3.2.3 Post-Gelation Mechanical Properties

Following gelation, a full frequency sweep was conducted to assess the mechanical properties of the resulting hydrogels, the results of which are shown in **Figure 3.5 (a-e)** below.

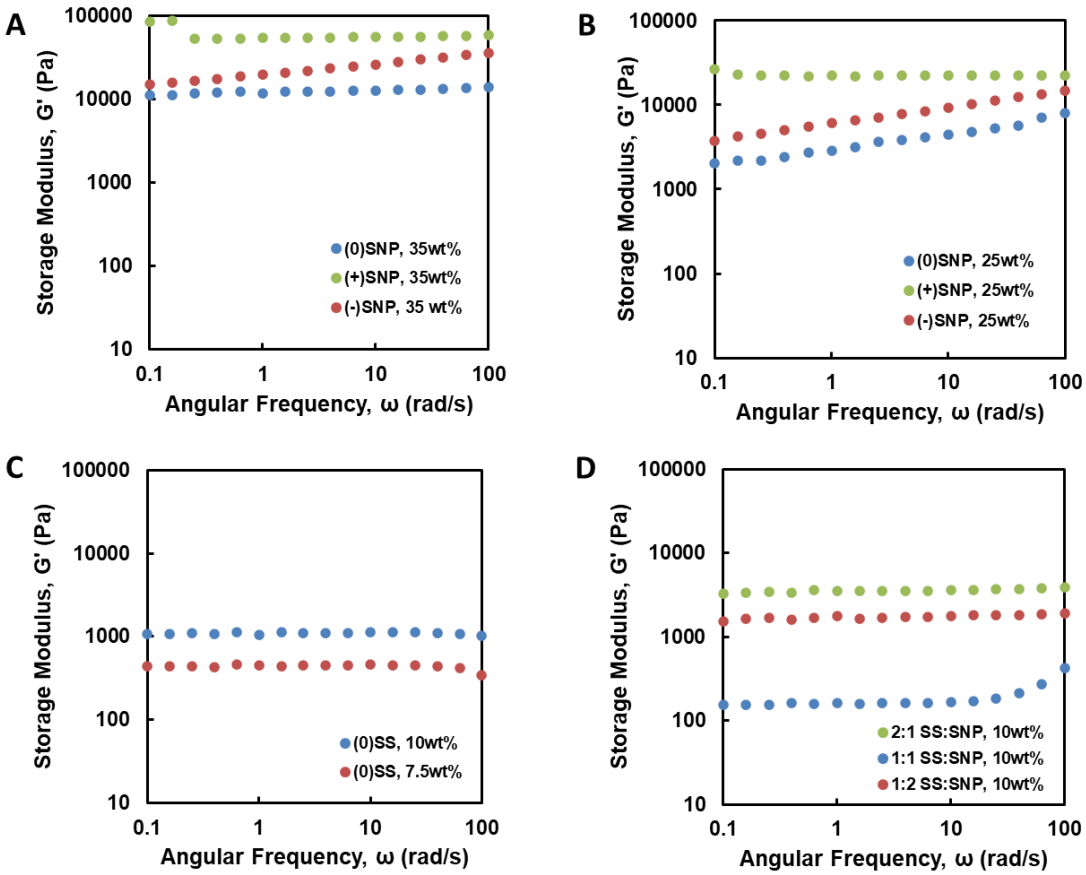

Figure 3.5 (a-e): Post-gelation mechanical properties for SS and/or SNP-based hydrogel systems fabricated at concentrations of (A) 35 wt% (SNP only); (B) 25 wt% (SNP only); (C) 10 and 7.5wt% (SS only); (D) 10% (mixed SS/SNP).

The use of SNPs results in the formation of significantly stiffer hydrogels, consistent with the much higher concentration of starch that can be used to prepare the hydrogels as a result of the nanoparticle rather than soluble/branched structure of the starting material coupled with the already internally crosslinked internal structure of the SNPs. Charged SNP-based hydrogels are consistently stiffer than their neutral counterparts at the same weight fraction, suggesting that repulsive interactions between the charged SNPs enhance the mechanics of the resulting hydrogel. In terms of the morphology of the building blocks, the same trends observed in gelation time are observed in the storage modulus of the final gels, with the balance between the increased inherent elasticity of the SNPs and the reduced steric hindrance to crosslinking with SS resulting in the lack of a clear trend in the modulus of the mixed SS/SNP hydrogels, similar to the gelation time trend observed (**Figure. 3.4**); hydrogels prepared with an excess of SS (higher entanglement) or an excess of SNPs (higher building block stiffness) have higher moduli than the 1:1 SS:SNP precursor mixture.

3.3.3 Very Small Angle Neutron Scattering

To track the structural evolution of the hydrogels during photopolymerization as a function of the charge and morphology of the starting materials, the unique combination of the high neutron flux and the simultaneous measurement of a wide *q*-range offered by the very small angle neutron scattering (vSANS) instrument is leveraged to probe the intermediate gel nanostructures in real time during the photopolymerization process. **Figure 3.6** shows a representative sample (for the 35 wt% neutral SNP gel) of the kinetic data acquired.

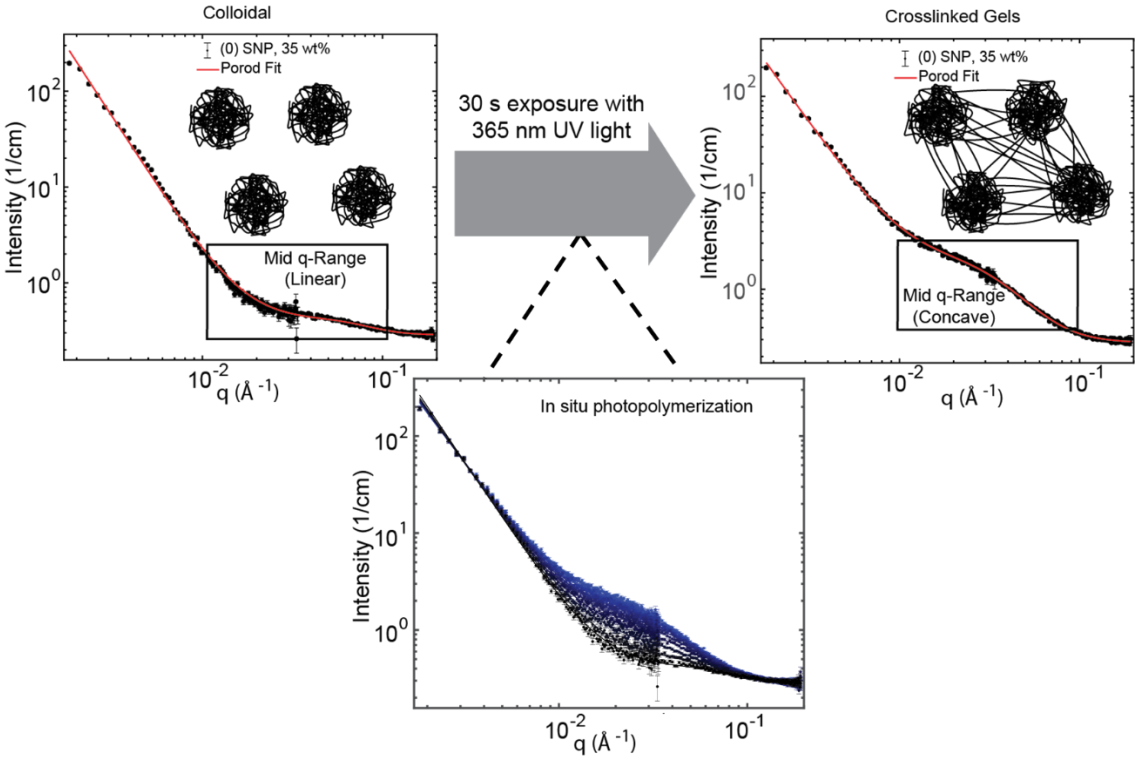

Figure 3.6: Schematic showing the evolution of network formation from concentrated SNP colloids to crosslinked SNP gels over a 30 s exposure time to 365 nm light.

The nonlinear least squares fit of the data enables the extraction of five fitting parameters. The two scale parameters (i.e. the Porod scale s_p and the fluid scale s_{oz}) correspond to the relative weightings of the Porod and Ornstein-Zernike functions required to fit the data, with the Porod term dominating at low *q* and the Lorentzian term dominating at high *q*. Given that the key differences in the SANS curves (**Figure 3.6**) were observed in the mid to high *q* range, the fluid scale s_{oz} is particularly relevant to this analysis, consistent with the Lorentzian term corresponding to the dynamics of the hydrogel network; more specifically, changes in the fluid scale can be used to track changes from more fluid-like systems (low fluid scale) to those less fluid-like/more solid-like (high fluid scale), consistent with the progression of gelation. The two exponents (i.e. the Porod exponent *n*

and the Lorentzian exponent *m*) also give key insight into the physics of the system. Porod exponents of *n*~2 indicate that the system is made up of Gaussian, swollen chains while a value of 3 or higher indicates that there is a clustering of mass within the system, the latter consistent with denser SNPs crosslinked together into a network by less dense crosslinking domains. A Lorentzian exponent $m \leq 2$ indicates that the polymer chains are behaving as through they are in a good solvent, while $m > 2$ indicates reduced polymer-solvent interactions, the latter consistent with polymer crosslinking and/or deswelling induced for any reason within the hydrogel network. Finally, the correlation length Ɛ gives insight into the changing distance between inhomogeneities in the system over time based on the changing position of the Lorentzian term over the course of the experiment, herein indicative of changes in the interparticle spacing between the denser SNP domains as crosslinking progresses.

Given that the DHR measurements presented above track the evolution of gelation on the bulk scale, we selected the fluid scale as the most appropriate parameter to track from the vSANS analysis since it provides a microscale representation of gelation that can be correlated to the bulk DHR measurements (indeed, the fluid scale and rheology both follow Maxwell's theory of viscoelastic behaviour). The kinetic trends in the fluid scale (**Figures 3.7 – 3.9 (a,b)** below) were thus extracted from each *in situ* photopolymerization experiment. The evolution of the correlation length follows similar general trends is shown in **Supporting Information Figures S3.5, S3.8, and S3.10** for comparison. A full summary of the fitting parameters used to fit the scattering data for all samples tested can also be found in the **Supporting Information Tables S3.2 – S3.12**. In the following sections, the trends in all best-fit vSANS parameters are analyzed as a function of time for each of the three key variables considered: (1) the concentration of the precursor starch, (2) the charge of the SNP precursor, and (3) the morphology of the starting material(s), with additional insight into the internal dynamics of the different hydrogels added as relevant based on trends observed in the other fitting parameters.

3.3.1.1 Effect of Starch Precursor Concentration

In theory, if a polymer (SS) or nanoparticle (SNP) have the same degree of substitution of methacrylate groups (DS = 0.10 for both herein, **Table 1**), a higher wt% of polymer should result in a faster gelation time if the irradiation time/power is kept constant. **Figure 3.7a** (for SNPs) and **Figure 3.8a** (for SS) show the evolution of the fluid scale over the 30 s duration of UV photoirradation and the corresponding exponential best fits, while **Figure 3.7b** (for SNPs) and **Figure 3.8b** (for SS) show the corresponding gelation rate as defined by the inverse of the exponential best-fit time constant ($1/\tau$); note that a larger value for $1/\tau$ indicates a slower gelation time and a longer t_{gel}. See **Figure S3.5 (a,b)** (for SNPs) or **Figure S3.6 (a,b)** (for SS) for the corresponding figures comparing the evolution of the fluid correlation length.

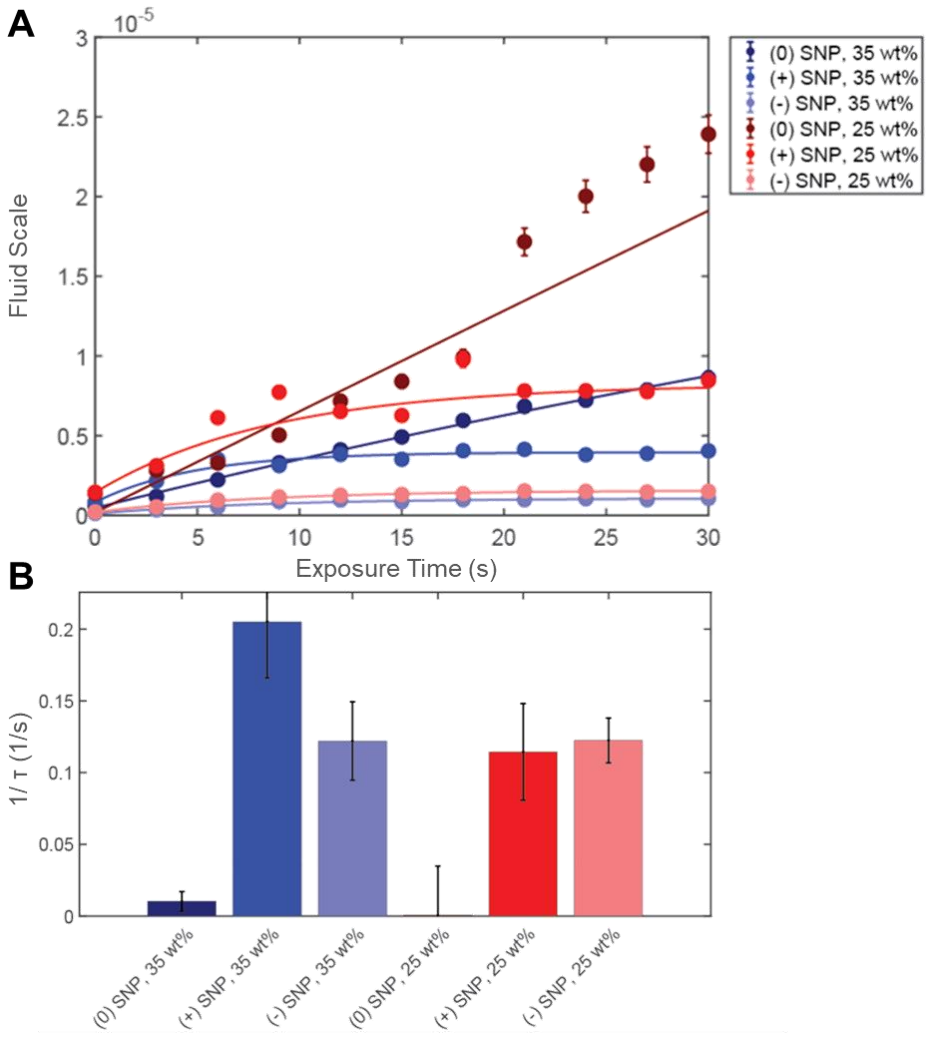

Figure 3.7 (a, b): Measured changes in the a. fluid scale over 30 s UV exposure and b. 1/ τ for all homogenous SNP hydrogels formed *in situ* in the beamline

Based on a comparison of the y-axis ranges in **Figure 3.7a** (SNP gels, maximum y-value 1×10^{-5}) and **Figure 3.8a** (SS gels, maximum y-value 7×10^{-5}), SS samples scatter significantly more than the SNP gels despite the much lower mass concentration of starch present in SS-based hydrogels. This result is consistent with our previous work that indicated a significant molecular weight difference between SS (~5,000,000 g/mol) and SNPs (~250,000-500,000 g/mol, both based on linear pullulan standards) [285,409]. In terms of kinetics, nearly linear correlations were observed between the fluid scale and the gelation time for the (0)SNP gels at both concentrations tested (**Figure 3.7a**) and no significant characteristic timescale (i.e. very slow dynamics) was observed related to the exponential fit of the kinetics data, with zero lying within the experimental error of each 1/τ value measured (**Figure 3.8a**). The slope of the correlation for (0)SNP 35 wt% is

roughly half of that observed for (0)SNP 25 wt%, the latter in which fluid scale is still increasing (i.e. gelation is continuing) even at the 30 s mark. We rationalize that this result is related to the lower conformational mobility of higher concentration SNP suspensions, such that fewer crosslinks need to form to lock in the solid-like gel structure. By comparing the percentage changes in the Porod exponent (*n*) and the fluid/Lorentzian exponent (*m*) for 35 wt% (**Figure S3.6**) and for 25 wt% (**Figure S3.7**) homogenous SNP hydrogels, additional insight can be gained into the effect of photocrosslinking on the internal structure of the uncharged SNP homogeneous gels. The Porod exponent remains just below 3 for both (0) SNP gels tested during the whole photopolymerization process, suggesting that the SNPs remain distinct nanoparticles (and as such localized mass scattering units) over the whole crosslinking process; however, the fluid exponents decrease by ~40% for (0)SNP, 35wt% and ~32% for (0)SNP, 25 wt% over the duration of photocrosslinking, suggesting that crosslinking improves the solubilization of the polymer chains comprising the SNPs. We hypothesize this observation is related to the pulling on individual starch chains as polymerization proceeds that can compete with the internal crosslinking within the SNPs, thereby extending the starch chains within the SNPs into solution and away from the denser SNP domain. This interpretation is also supported by the continual increases in the fluid correlation length observed during photopolymerization (**Figure S3.5**), an observation consistent with the interface of the SNPs becoming more hydrated to increase the distance between the dense polymer-rich domains remaining inside each SNP.

The same general trend can be seen for the SS samples in **Figure 3.8a**, with the fluid scale of the lower concentration (0)SS-7.5 wt% gel increasing faster than the (0)SS-10 wt% gel (albeit with slightly less differentiation between the samples since the difference in wt% between the two SS gels tested is smaller than that used for the SNP gels). The total change in the fluid scale is also much larger and the kinetics in the fluid scale development more clearly exponential for SS-based hydrogels; this result is consistent with the higher degree of chain entropy in the SS-based starting materials, which enables both faster gelation due to the higher conformational mobility of the methacrylate groups and a larger change in the solid-like properties of the system given the absence of intraparticle crosslinking prior to gelation.

Of note, these results directly relate to the bulk gelation kinetics data from the DHR experiments (**Table 3.2),** in which (0)SNP 35wt% (32 s) was observed to gel faster than (0)SNP 25wt% (56 s) and (0)SS 10 wt% (20 s) gels faster than (0)SS 7.5 wt% (39 s). Thus, although the absolute magnitudes of the gelation times vary based on the different light source powers observed, bulk rheological data and microscopic structural parameter tracking via vSANS result in similar trends. Interestingly, however, despite the (0)SNP 35 wt% gel forming faster than the (0)SS 7.5 wt% gel based on bulk gelation measurements, the (0)SS 7.5 wt% gel achieves a plateau in the fluid scale after ~20 s while the fluid scale in the (0)SNP 35 wt% gel keeps increasing in a near-linear fashion over the full 30 s irradiation period. This result implies that the SNP-based gels undergo

significantly more internal rearrangement following the observation of macroscopic gelation relative to SS-based gels.

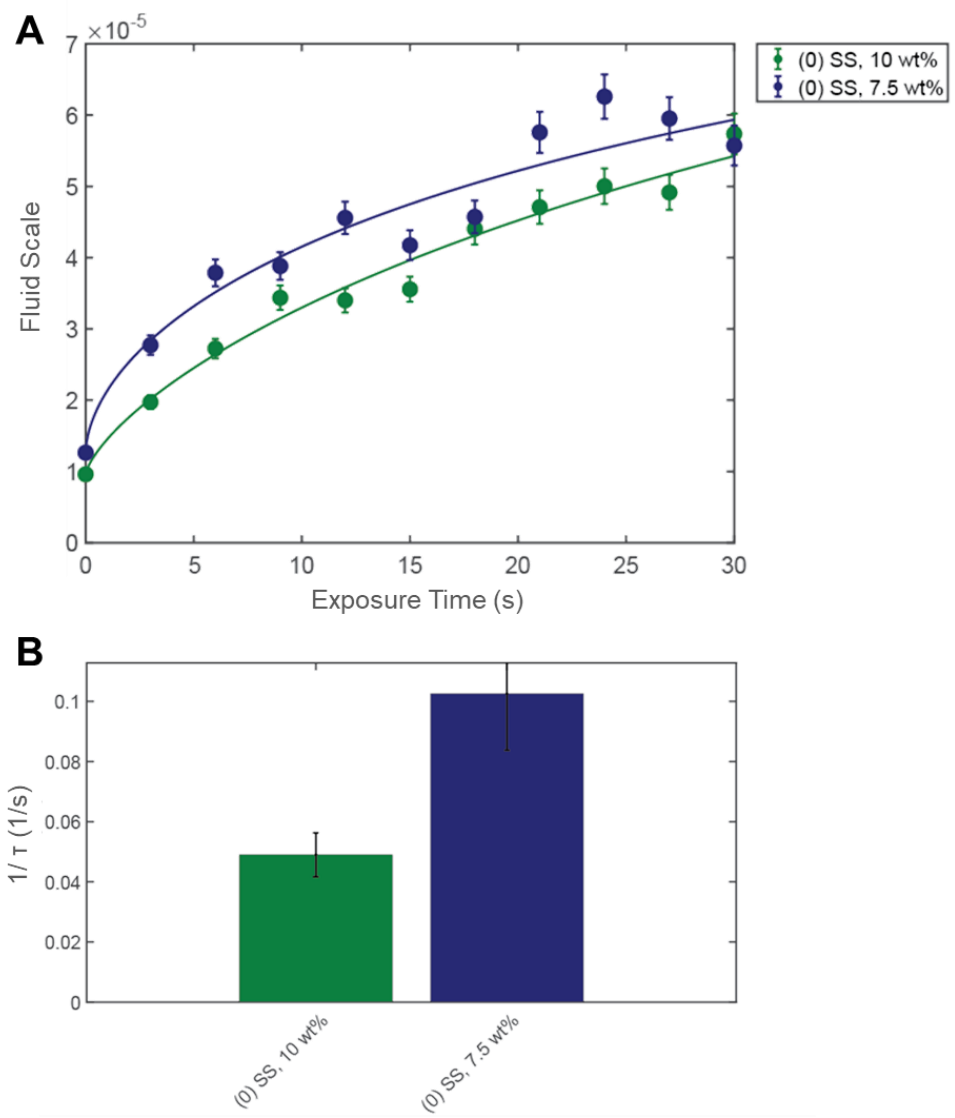

Figure 3.8 (a, b): Measured changes in the a. fluid scale over 30 s of UV exposure and b. 1/ τ for all homogenous SS hydrogels formed *in situ* in the beamline

The Porod and fluid exponent trends are also consistent with this interpretation (**Figure S3.9**), with the Porod exponent showing a significant decrease (15-18% depending on SS concentration) while the fluid exponent remains essentially unchanged during photopolymerization. We interpret this result as crosslinking having a minimal effect on the local chain hydration with SS-based hydrogels but reducing the degree of mass clustering as semi-collapsed starch chains are stretched by the crosslinking process. The concurrent significant increase observed in the correlation length is also consistent with

fewer mass-clustered domains being observed as the crosslinking proceeds, unlike in the SNP-based gels in which the internally crosslinked SNP retains the presence of locally higher mass concentration domains throughout photopolymerization.

3.3.1.2 Effect of Charge

As with the neutral (0)SNP-based hydrogels, hydrogels prepared with (-)SNP and (+)SNP also showed lower changes in fluid scale over the gelation time if the concentration of the SNP building block is increased However, while the fluid scale of the (0)SNP gels remained relatively linear as a function of time over the duration of the vSANS experiment, hydrogels formed by using (+)SNP and (-)SNP-based show very different fluid scale trends over time (**Figure 3.7a**). Both anionic and cationic SNP gels undergo only a small increase in fluid scale in the first 10-12 s of irradiation followed by a plateau over the rest of the experiment. Comparing the effect of charge, at each concentration tested, (0)SNP shows the largest overall change in fluid scale (**Figure 3.7a**), lowest characteristic timescale ($1/\tau = 0.01\pm0.01$ s^{-1} at 35% and 0.00 ± 0.03 s^{-1} at 25 wt%) (**Figure 3.7b**), and shortest bulk gelation time (32 s at 35 wt% and 56 s at 25 wt%) (**Table 3.2**) while (+)SNP shows intermediate overall changes in fluid scale (**Figure 3.7a**), characteristic timescale ($1/\tau = 0.21\pm0.04$ s^{-1} at 35 wt% and 0.11 ± 0.03 s^{-1} at 25 wt%) (**Figure 3.7b**), and bulk gelation time (46 s at 35 wt% and 88 s at 25 wt%) (**Table 3.2**) and (-)SNP shows the smallest overall change in fluid scale (**Figure 3.7a**), highest characteristic timescale ($1/\tau = 0.12\pm0.03$ s^{-1} at 35 wt% and 0.12 ± 0.02 s^{-1} at 25 wt%) (**Figure 3.7b**), and slowest bulk gelation time (50 s at 35% and 99 s at 25 %) (**Table 3.2**).

We hypothesize that the significantly lower changes in fluid scale observed for the charged SNP-based hydrogels are related to the high interparticle repulsion present between the charged SNPs due to charge-charge interactions, which both limits the closeness of approach of the SNPs to facilitate covalent crosslinking while also providing a colloidal crystal-like electrostatic gelation effect when the SNPs are brought sufficiently close together by the formation of covalent crosslinks. Thus, while the fluid scale results suggest that significantly less covalent photogelation occurs in the charged SNP-based hydrogels, the inherent high degree of internal electrostatic repulsion between the SNPs accounts for the much higher elastic modulus values observed for both (-)SNP and (+)SNP-based hydrogels (**Figure 3.5 (a, b**)). Interestingly, the correlation length (**Figure S3.5**) also changes significantly less for the charged SNP precursor gels over the photoirradiation period, suggesting significantly less changes in the spacing between SNPs structure during photogelation relative to the uncharged precursor nanoparticles; this observation is again consistent with reduced covalent crosslinking and more charge-charge repulsion influencing the network structure of these charged SNP hydrogels.

Analysis of the Porod and Fluid/Lorentzian exponent trends during photopolymerization for 35 wt% (**Figure S3.6**) and for 25 wt% (**Figure S3.7**) homogenous SNP hydrogels with charge give further insight into the SNP responses to photocrosslinking. For (+)SNP, the initial fluid exponent is significantly lower than that observed with (0)SNPs, consistent with the increase in charge-induced swelling (and thus chain hydration) in the

SNPs; however, upon photocrosslinking, the fluid exponent increases as crosslinking proceeds. We attribute the initial large increase in the fluid exponent to bringing the charged SNPs closer together during crosslinking, inducing some transient deswelling in the SNPs to try to maximize the interparticle distance and reduce interparticle repulsion. Interestingly, the same fluid scale trend is not observed with (-)SNP hydrogels, although the fluid scale values are consistently higher over the whole photopolymerization process for those hydrogels such that the stiffer internal structure of the (-)SNP may resist the deswelling induced in the (+)SNPs. As with the (0)SNPs, the Porod exponent for (-)SNPs remains essentially unchanged during photopolymerization consistent with the maintenance of independent SNP structures in the network. The reason for the slight (25-27%) decrease observed in the Porod exponent of the (+)SNP gels is less clear but may be related to the significantly smaller initial size or (+)SNPs and the higher propensity for nanoclustering of (+)SNPs in suspension compared to (-)SNPs and (0)SNPs (**Table 3.1**).

3.3.1.3 Effect of Starch Morphology

To assess the impact of mixing starch morphologies within a single hydrogel, **Figure 3.9 (a,b)** shows the measured changes in the fluid scale (**Figure 3.9a**) and the value of $1/\tau$ (**Figure 3.9b**) for heterogeneous starch hydrogels fabricated by varying the ratios of SS and SNP precursors used to form the hydrogel (10 wt% total concentration in all cases); see **Figure S3.7 (a,b)** for the corresponding correlation length data. The evolution of the fluid scale is very similar for the 2:1 SS:SNP, 10 wt% and 1:1 SS:SNP, 10 wt% hydrogels, with both gels showing near-linear increases in the fluid scale and virtually no measurable exponential time constant over the entire duration of the 30 s UV exposure period (consistent with the (0)SNP data, **Figure 3.7a**); the total change in the fluid scale (~5 units) is also large and consistent with the (0)SS data collected at the same concentration (**Figure 3.8a**). Hence, replacing a fraction of the SS with SNP slows down gelation due to the replacement of the larger/more conformationally mobile SS with SNPs (consistent with the bulk gelation data in **Table 3.2**) and results in a significantly weaker hydrogel (**Figure 3.5**) but ultimately achieves a similar fluid scale on the microscale. While the 1:2 SS:SNP, 10 wt% hydrogel has an even slower gelation time (**Table 3.2**, as expected by replacing more of the SS with SNPs), the fluid scale trend is completely different in that only a very small increase in the fluid scale was observed over the first 5-7 s of the experiment after which the fluid scale plateaus. In this case, the fluid scale trend is very similar in terms of both shape and magnitude to that observed with the charged SNP hydrogels (**Figure 3.7**). Correspondingly, the 1:2 SS:SNP hydrogel is significantly stiffer than the 1:1 SS:SNP hydrogel (**Figure 3.5**). This result suggests that a minor fraction of soluble branched SS may act as both a covalent macromolecular crosslinker as well as a functional steric stabilizer for the major SNP fraction, resulting in the formation of a hydrogel with a lower covalent crosslink density but higher internal interparticle repulsion to induce the higher observed modulus values.

The changes in the Porod and fluid/Lorentzian exponents for heterogenous SS:SNP hydrogels also show intermediate values compared to those observed for homogeneous SNP and SS-based hydrogels (**Figure S3.11**). The Porod exponent decreased by 6% (2:1

SS:SNP, 10 wt%), 5% (1:1 SS:SNP, 10 wt%), and 14% (1:2 SS:SNP, 10 wt%) respectively, while the fluid exponent decreased by 3%, 0%, and 7% for those same heterogeneous SS:SNP hydrogels during the photocrosslinking process. These small changes are all consistent with the effects of SNPs (fixed Porod exponent, reducing fluid exponent over time during homogeneous gel formation) and SS (reducing Porod exponent and fixed fluid exponent over time during homogeneous gel formation) effectively competing to govern the overall hydrogel properties.

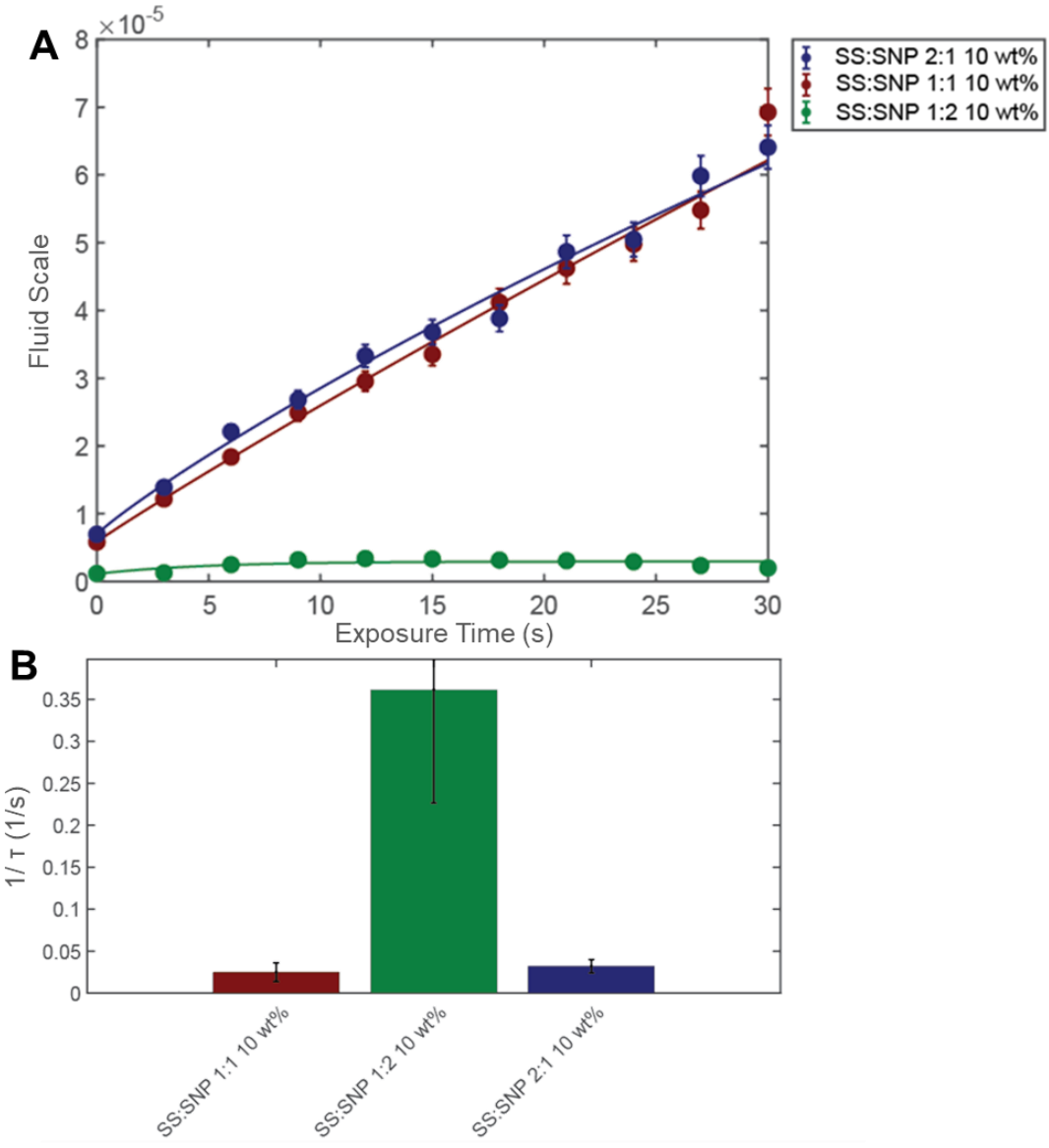

Figure 3.9 (a, b): Measured changes in the a. fluid scale over 30 s UV exposure and b. 1/ τ for all heterogenous SS/SNP hydrogels formed *in situ* in the beamline

To our knowledge, this is the first report on the characterization time-resolved gelation kinetics using SANS, a measurement that is uniquely enabled by the vSANS instrument at NIST. Coupling these measurements with *in situ* photorheometry allows for insight on the full kinetic picture of the photogelation process on both the microscale (vSANS) and macroscale (rheometry). While clear correlations were observed between the bulk and microscale data in many systems (e.g. with regard to the effect of concentration on the hydrogel properties), the differences observed between the mechanics of the hydrogel and the evolution of the fluid scale were strikingly different depending on the charge and morphology of the starch building blocks. We hypothesize that the correlation of the fluid scale to the liquid-to-solid transition enables discrimination between the formation of new crosslinks and initial differences in the interparticle interactions in the precursor gel suspension that are otherwise challenging to discriminate using different techniques. These differences demonstrate the benefit of simultaneously tracking microscale and macroscale changes over time to gain insight into gelation processes. We believe this approach is particularly valuable for gaining a better fundamental understanding of crosslinking in nanoparticle network hydrogels in which an already internally crosslinked microgel particle is used as one of the building blocks and the distinction between the intraparticle and interparticle crosslinking via bulk hydrogel measurements is otherwise challenging to explicitly identify. The morphological insights gained around how individual SNPs in the network respond to the photogelation process (via tracking of the Porod and Lorentzian exponents) add additional insight into the internal morphologies of the resulting hydrogels, with crosslinking observed to induce swelling, deswelling, or no changes in the solvation of the constituent starch depending on the morphology of the starch building blocks and whether or not strong repulsive forces exist between constituent SNP building blocks. Such insight is only possible using SANS given that the length scales analyzed are not accessible using other techniques.

3.4. Conclusion

Through tracking the kinetics of the microscale (very small neutron scattering) and macroscale (dynamic hybrid rheology) properties of the photopolymerization of methacrylated soluble (branched) starch and/or starch nanoparticles with varying charges over the time course of photogelation, key physical insights into the structure-property relationships in such hydrogels can be achieved. In particular, this strategy enabled the elucidation of three key differences in the bulk versus microscale trends observed: (1) the fluid scale of neutral SNP-based hydrogels continues to increase over time well past the time at which macroscopic gelation was observed, suggesting significant reconformations within the SNP building blocks to drive higher interparticle crosslinking over time in such systems; (2) hydrogels formed based on charged starch nanoparticles exhibited stiffer mechanics but much smaller changes in the fluid scale as function of time relative to neutral starch nanoparticle-based hydrogels, suggesting that interparticle repulsion is playing a key role in maintaining the bulk rheological properties of these hydrogels; and (3) hydrogels prepared with mixtures of soluble branched starch and starch nanoparticles exhibited highly decoupled changes between the fluid scale and the mechanics depending

on whether the soluble starch (higher hydrodynamic diameter, higher conformational mobility) or the starch nanoparticles (smaller hydrodynamic diameter, smaller conformational mobility) represented the major fraction, with the 1:1 ratio unexpectedly resulting in the weakest hydrogel. In addition, cationic SNPs appear to deswell to some degree during photocrosslinking to compensate for the close charge-charge repulsion between SNPs in the constrained gel volume while neutral SNPs slightly swell upon crosslinking as the interparticle crosslinks counteract the swelling restrictions imposed by the intraparticle crosslinks. Moving forward, the general approach demonstrated herein can be applied to better understand the role of the charge, morphology and/or size of other types of building blocks for photocrosslinked hydrogels, allowing for the more rational design of hydrogels with targeted comprehensive properties for various applications.

3.5 Notes

Disclaimer

Certain commercial equipment, instruments, or materials are identified in this paper to foster understanding. Such identification does not imply recommendation or endorsement by the National Institute of Standards and Technology, nor does it imply that the materials or equipment identified are necessarily the best available for the purpose.

Funding sources

The Natural Sciences and Engineering Research Council of Canada (NSERC, Strategic Project Grant 463327-14) is gratefully acknowledged for funding this work. This work utilized facilities supported in part by the National Science Foundation under Agreement No. DMR-0944772. We acknowledge the support of the National Institute of Standards and Technology, US Department of Commerce, in providing the neutron facilities used in this work. Use of facilities provided by McMaster's Biointerfaces Institute and *EcoSynthetix Inc*. is also gratefully acknowledged.

3.6 Acknowledgements

The authors would like to acknowledge Markus Blueul, Kenneth A. Rubinson, and Juscelino Leao at the National Institute of Standards and Technology for their assistance in setting up the custom vSANS equipment used to irradiate the samples next to the beamline during our experiment. The authors would also like to thank McMaster University's NMR facility for assistance in acquiring the reported NMR data. Lastly, Dr. Jean Duhamel is acknowledged for his useful discussions on the analysis of the vSANS data

We acknowledge the support of the National Institute of Standards and Technology, U.S. Department of Commerce, in providing the neutron research facilities used in this work. Access to NGA-NSE and the NGB30-SANS was provided by the Center for High Resolution Neutron Scattering, a partnership between the National Institute of Standards and Technology and the National Science Foundation under Agreement No. DMR-2010792.

Appendix 3S: Supporting Information to Chapter 3

Title: Investigating the Kinetics and Structure of Network Formation in Charged UV-Photopolymerizable Starch Nanoparticle (SNP) Network Hydrogels via Very Small Angle Neutron Scattering (vSANS) and Dynamic Hybrid Rheology

Authors: [1]Michael J. Majcher, [1]Sebastian Himbert, [1]Francesco Vito, [1]Matthew A. Campea, [1]Ridhdhi Dave, [2]Grethe Vetergaard Jensen, [1]Maikel C. Rheinstadter, [3]Niels Smeets, and [1]Todd Hoare

Affiliations: [1]Departments of Chemical Engineering and Physics/Astronomy, McMaster University, 1280 Main St W., Hamilton, ON, Canada, [2]NIST Center for Neutron Research, National Institute of Standards and Technology, Gaithersburg, MD 20899-6100, United States, [3]EcoSynthetix Inc., 3365 Mainway, Burlington, ON L7M 1A6, Canada

Keywords: starch nanoparticle, neutron scattering, nanoparticle network, hydrogel, UV photopolymerization, kinetics, free radical polymerization

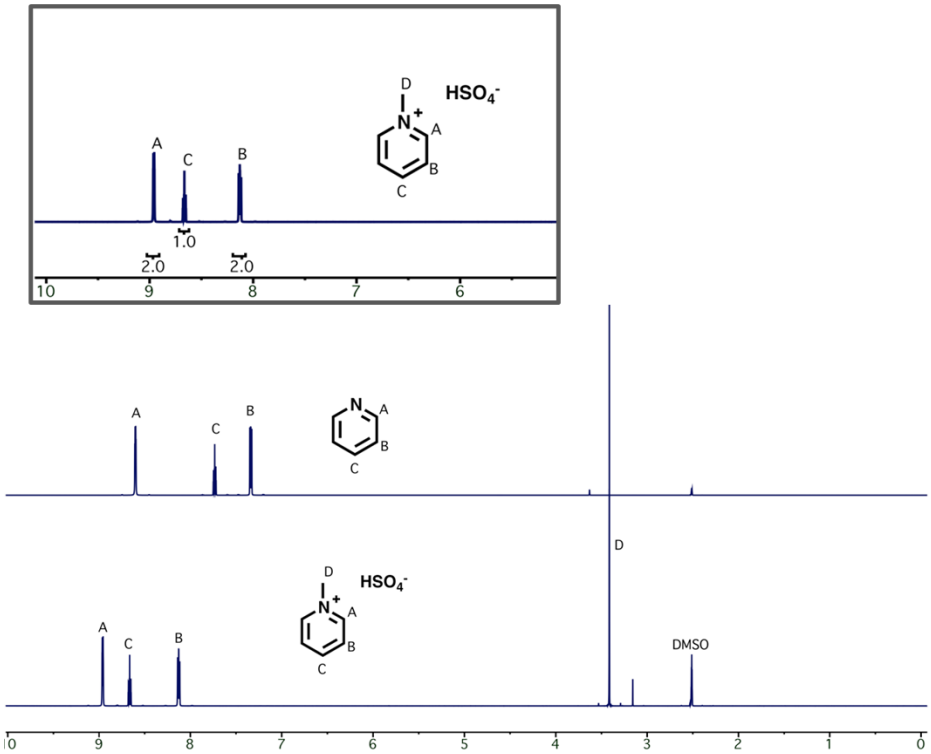

Figure S3.1: Confirmation of the structure of synthesized pyridinium methyl sulfate (Py-Me-S). The [1]H-NMR indicates a pure sample of correct structure with a small amount of residual DMSO, which is used as the solvent for the functionalization reaction.

Table S3.1: Charge titration results from various anionic-modified SNPs designed to match the charge density of the provided cationic SNP sample using poly(DADMAC) as the positively charged titrant/polyelectrolyte. Note that the "SNP-SO_4-5-d" sample was chosen for the subsequent work in the manuscript given that the absolute surface charge measured matches with that of the commercially-acquired (+)SNP, allowing direct comparisons between the cationic and anionic SNP-based hydrogels.

Sample	**Mass Starch, g**	**Mass Py-Me-S, g**	**Ratio Starch: Py-Me-S**	**Volume of DMSO, mL**	**Mass of Crushed Ice, g**	**Concentration (g/L)**	**Charge (meq/g)**	**Titrant**
SNP-SO_4-1-d	1	0.1	1:0.1	30	30	2.5	-0.02	POLY-DADMAC
SNP-SO_4-2-d	1	1	1:1	30	30	2.5	-0.16	POLY-DADMAC
SNP-SO_4-3-d	1	10	1:10	30	30	0.3	-0.85	POLY-DADMAC
SNP-SO_4-4-d	0.5	0.25	1:0.5	15	15	1	-0.22	POLY-DADMAC
SNP-SO_4-5-d	0.5	1.25	1:2.5	15	15	0.25	-0.41	POLY-DADMAC
SNP-SO_4-6-d	0.5	2.5	1:5	15	15	0.2	-0.94	POLY-DADMAC
SNP-SO_4-7-d	0.5	3.75	1:7.5	15	15	0.2	-2.28	POLY-DADMAC

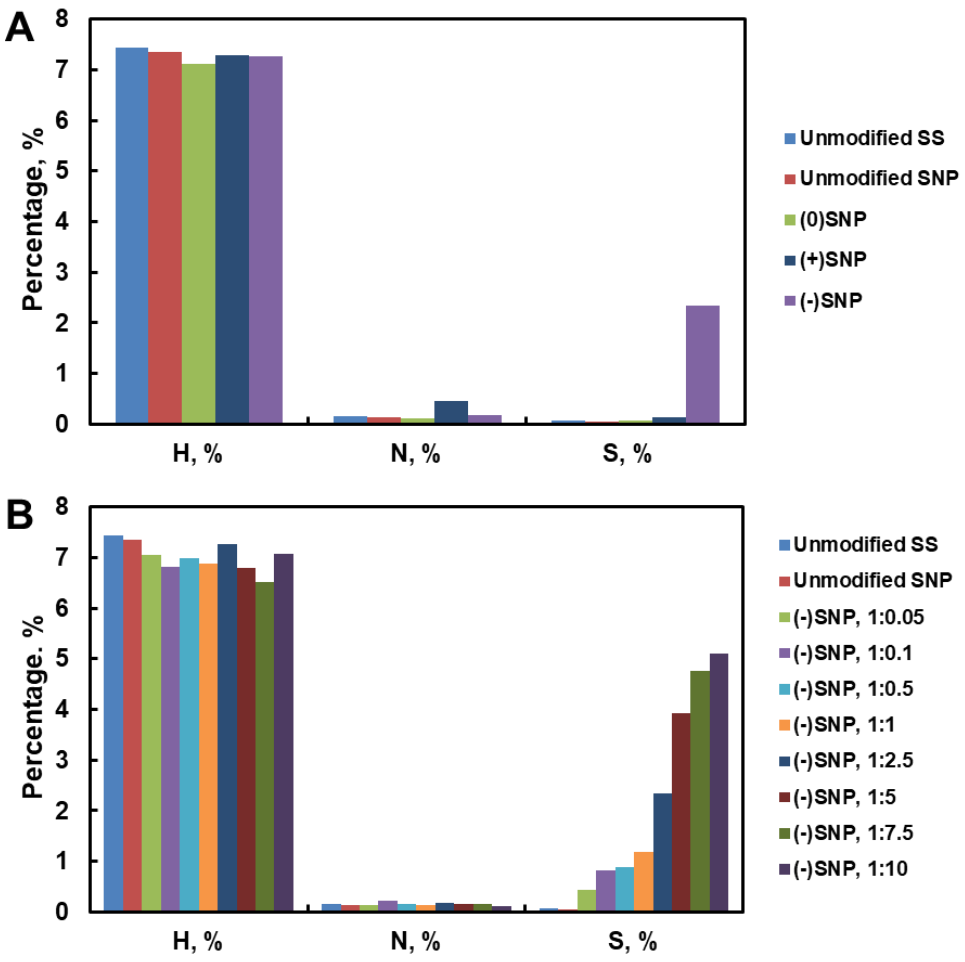

Figure S3.2 (a,b): Elemental analysis results for a CHNS scan of cationic (a) or anionic (b) modified starch particles. To view the differences in nitrogen and sulfur, the carbon peak was omitted (C was in the range of 50-55 mol% for all samples).

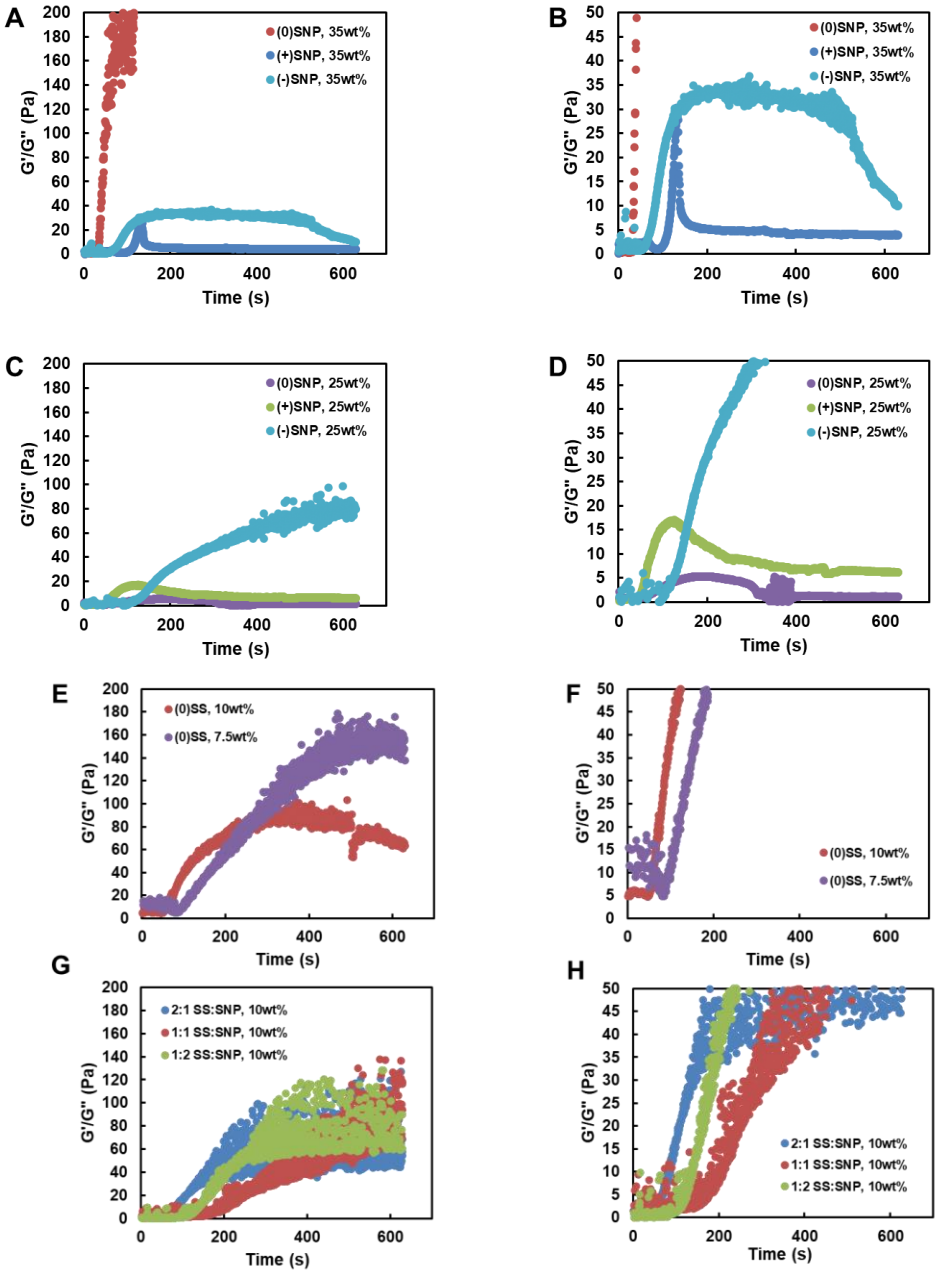

Figure S3.3 (a-h): G'/G" (storage modulus to loss modulus) ratio as a function of time over the duration of UV exposure for: (a, b) 35 wt% homogenous SNP gels over the full modulus range (a) or zoomed in (b); (c, d) 25 wt% homogenous SNP gels at over the full modulus range (c) or zoomed in (d); (e, f) 10 and 7.5 wt% SS homogenous gels over the full modulus range (e) or zoomed in (f); and (g, h) 10 wt% heterogeneous SS:SNP gels over the full modulus range (g) or zoomed in (h). The bulk gelation time was measured based on the point at which the best-fit line of the G'/G" data yields a major inflection point, which represents the point at which the elasticity of the gel significantly changes relative to that of the initial precursor solution/suspension.

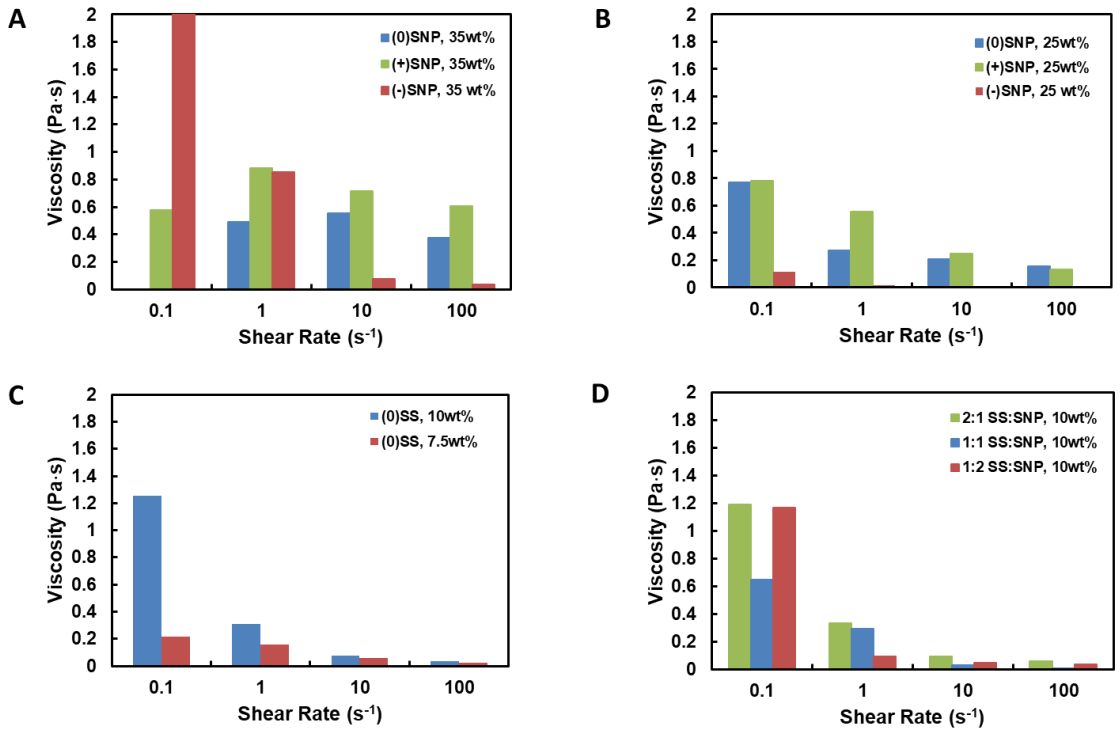

Figure S3.4 (a-d): Rheological flow sweeps described in a decade format for easier comparison between samples: (a) 35 wt% SNP (homogenous); (b) 25 wt% SNP (homogeneous); (c) 10 wt% SS (homogenous); (d) 7.5 wt% SS (homogeneous); and (e) 10% (heterogenous). Notice that the x axis range is the same for all graphs, but the y-axis of panels c and d are more extended than those in panels a, b, and e due to differences in starting sample viscosity due to the starch type used.

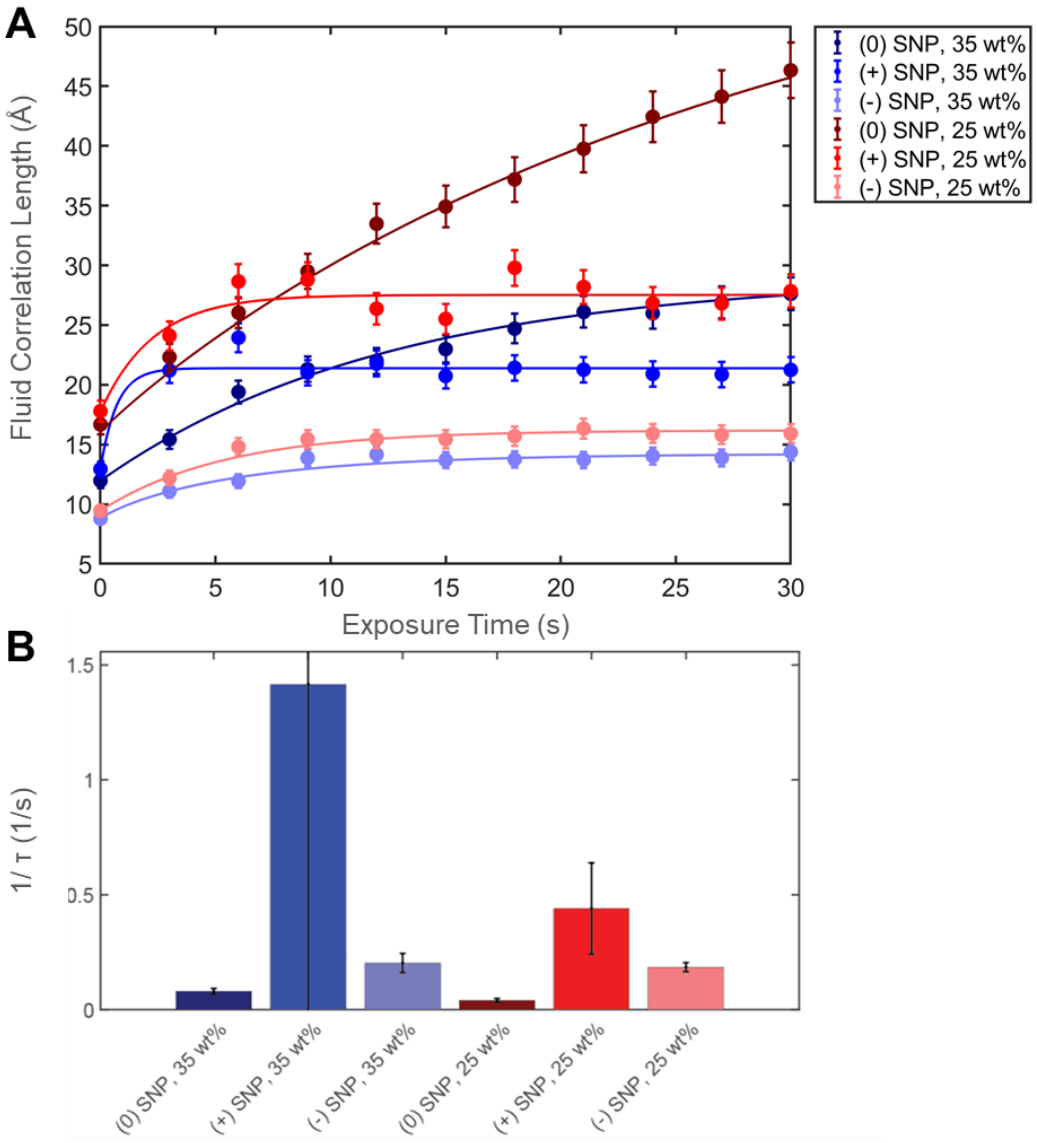

Figure S3.5: Measured changes in (a) the fluid correlation length over 30 s UV exposure and (b) the time constant of the exponential best-fit line (1/ τ) for all homogenous SNP hydrogels formed *in situ* in the beamline; see **Figure 3.7 (a,b)** for the corresponding data on the fluid scale.

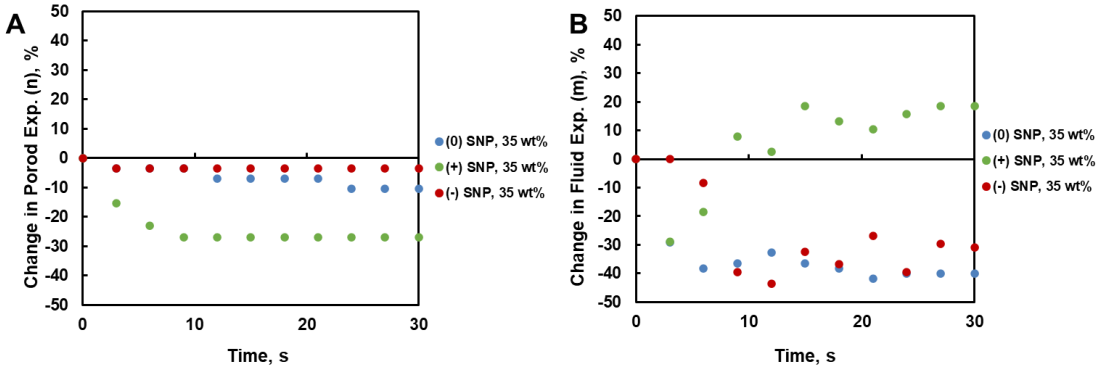

Figure S3.6 (a,b): Percentage changes in (a) the Porod exponent and (b) the fluid (Lorentzian) exponent over 30 s of UV irradiation for 35 wt% homogenous SNP hydrogels

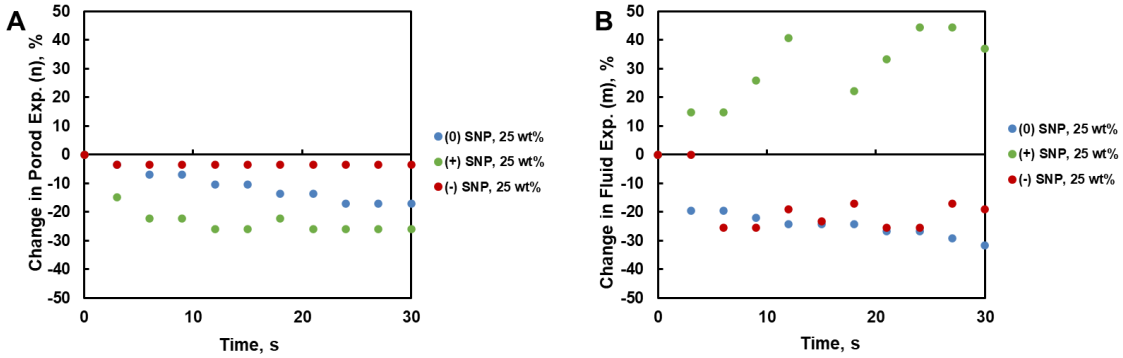

Figure S3.7 (a,b): Percentage changes in (a) the Porod exponent and (b) the fluid (Lorentzian) exponent over 30 s of UV irradiation for 25 wt% homogenous SNP hydrogels

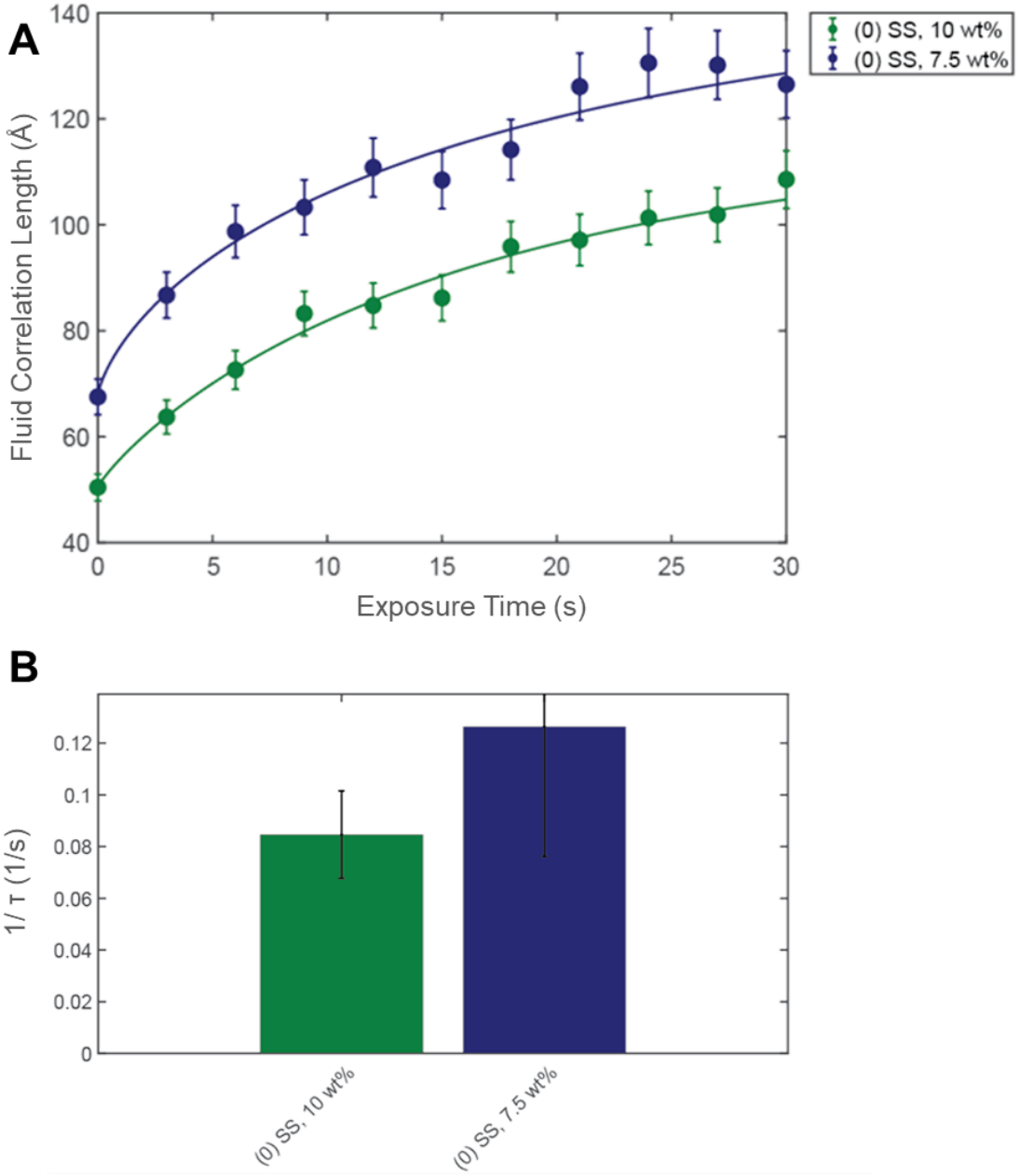

Figure S3.8: Measured changes in (a) the fluid correlation length over 30 s UV exposure and (b) the time constant of the exponential best-fit line (1/ τ) for all homogenous SS hydrogels formed *in situ* in the beamline; see **Figure 3.8 (a,b)** for the corresponding data on the fluid scale.

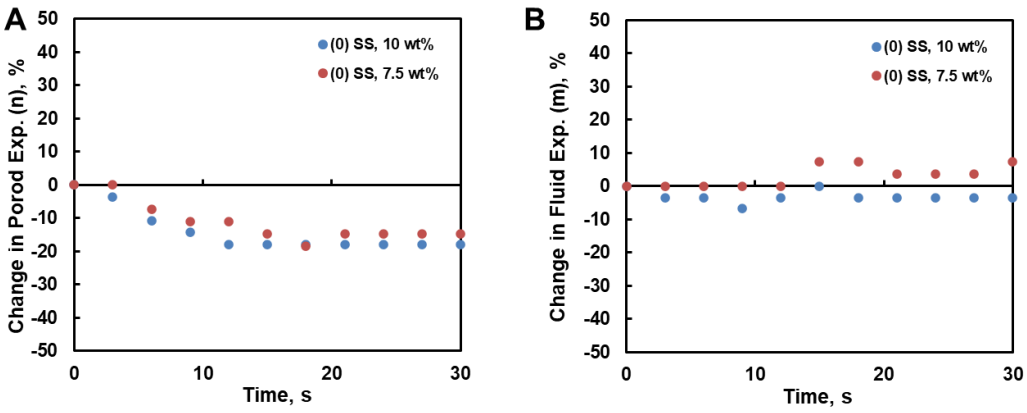

Figure S3.9 (a,b): Percentage changes in (a) the Porod exponent and (b) the fluid (Lorentzian) exponent over 30 s of UV irradiation for homogeneous SS hydrogels.

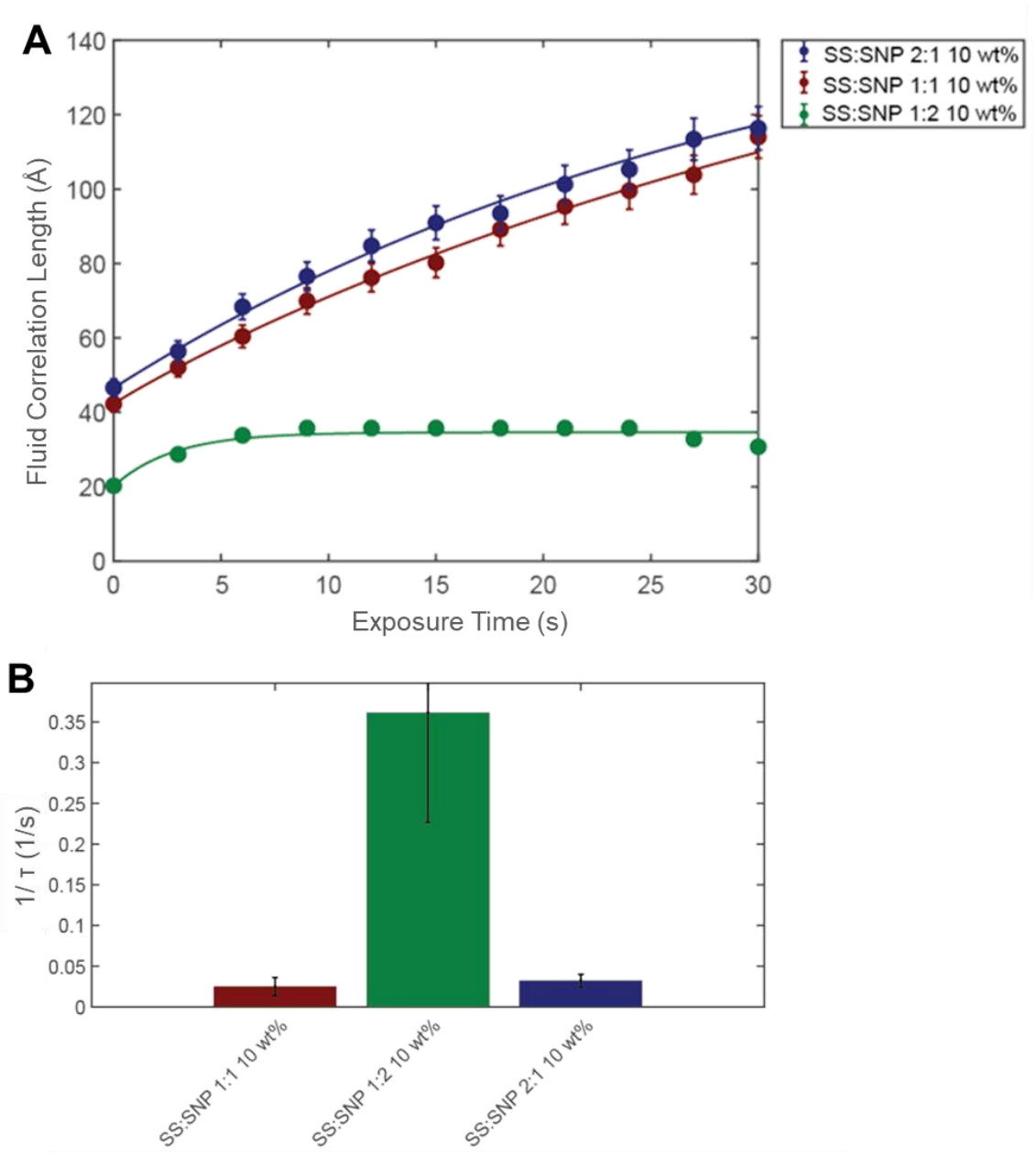

Figure S3.10: Measured changes in (a) the fluid correlation length over 30 s UV exposure and (b) the time constant of the exponential best-fit line ($1/\tau$) for all heterogeneous SS:SNP hydrogels formed *in situ* in the beamline; see **Figure 3.9 (a,b)** for the corresponding data on the fluid scale.

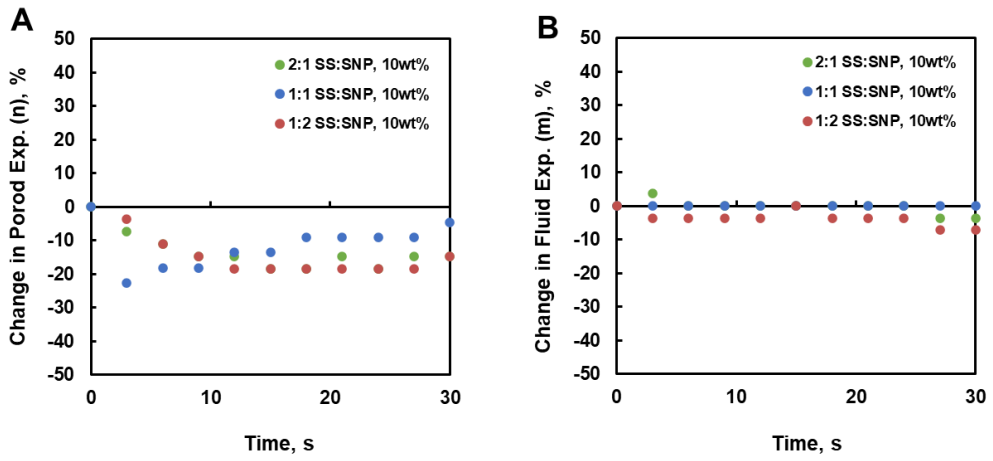

Figure S3.11 (a,b): Percentage changes in (a) the Porod exponent and (b) the fluid (Lorentzian) exponent over 30 s of UV irradiation for heterogenous hydrogels.

Table S3.2: (0)SNP, 35wt% raw vSANS best fit parameters.

Exposure Time (s)	Porod Scale	Porod Exponent	Fluid Scale	Fluid Correlation Length	Fluid Exponent
0	1.4e-06 ± 7.3e-09	-2.9e+00 ± 9.1e-15	6.1e-07 ± 1.9e-08	1.2e+01 ± 3.5e-16	5.5e+00 ± 7.5e-16
3	1.4e-06 ± 5.7e-09	-2.8e+00 ± 1.7e-14	1.2e-06 ± 2.1e-08	1.5e+01 ± 1.2e-15	3.9e+00 ± 2.2e-15
6	1.4e-06 ± 5.3e-09	-2.8e+00 ± 3.6e-14	2.2e-06 ± 2.9e-08	1.9e+01 ± 3.4e-15	3.4e+00 ± 3.9e-15
9	1.4e-06 ± 4.8e-09	-2.8e+00 ± 4.9e-14	3.3e-06 ± 3.1e-08	2.1e+01 ± 5.6e-15	3.5e+00 ± 3.5e-15
12	1.4e-06 ± 4.5e-09	-2.7e+00 ± 5.3e-14	4.1e-06 ± 3.3e-08	2.2e+01 ± 7.6e-15	3.7e+00 ± 2.4e-15
15	1.4e-06 ± 4.9e-09	-2.7e+00 ± 7.8e-14	4.9e-06 ± 3.9e-08	2.3e+01 ± 1.1e-14	3.5e+00 ± 1.8e-15
18	1.4e-06 ± 4.7e-09	-2.7e+00 ± 9.2e-14	6.0e-06 ± 4.1e-08	2.5e+01 ± 1.3e-14	3.4e+00 ± 8.1e-16
21	1.4e-06 ± 4.5e-09	-2.7e+00 ± 1.1e-13	6.8e-06 ± 4.3e-08	2.6e+01 ± 1.5e-14	3.2e+00 ± 4.8e-15
24	1.4e-06 ± 4.5e-09	-2.6e+00 ± 1.2e-13	7.2e-06 ± 4.5e-08	2.6e+01 ± 1.7e-14	3.3e+00 ± 5.8e-15
27	1.4e-06 ± 4.5e-09	-2.6e+00 ± 1.4e-13	7.9e-06 ± 4.8e-08	2.7e+01 ± 1.9e-14	3.3e+00 ± 1.1e-14
30	1.4e-06 ± 4.9e-09	-2.6e+00 ± 1.7e-13	8.6e-06 ± 5.5e-08	2.8e+01 ± 2.4e-14	3.3e+00 ± 1.4e-14

Table S3.3: (0)SNP, 25wt% raw vSANS best fit parameters.

Exposure Time (s)	Porod Scale	Porod Exponent	Fluid Scale	Fluid Correlation Length	Fluid Exponent
0	1.2e-06 ± 4.6e-09	-2.9e+00 ± 1.2e-14	1.3e-06 ± 1.9e-08	1.6e+01 ± 1.2e-15	4.1e+00 ± 1.6e-15
3	1.1e-06 ± 3.9e-09	-2.8e+00 ± 2.7e-14	2.5e-06 ± 2.4e-08	2.1e+01 ± 3.2e-15	3.3e+00 ± 2.7e-15
6	7.3e-07 ± 2.4e-09	-2.7e+00 ± 2.4e-14	3.1e-06 ± 2.1e-08	2.5e+01 ± 3.4e-15	3.3e+00 ± 3.4e-16
9	7.3e-07 ± 2.2e-09	-2.7e+00 ± 4.7e-14	4.8e-06 ± 2.5e-08	2.9e+01 ± 5.9e-15	3.2e+00 ± 5.2e-15
12	7.1e-07 ± 2.2e-09	-2.6e+00 ± 7.2e-14	6.8e-06 ± 3.2e-08	3.3e+01 ± 9.8e-15	3.1e+00 ± 1.7e-14
15	7.1e-07 ± 2.1e-09	-2.6e+00 ± 1.1e-13	8.2e-06 ± 3.7e-08	3.5e+01 ± 1.3e-14	3.1e+00 ± 2.8e-14
18	7.1e-07 ± 2.1e-09	-2.5e+00 ± 1.5e-13	9.9e-06 ± 4.1e-08	3.7e+01 ± 1.7e-14	3.1e+00 ± 4.5e-14
21	1.1e-06 ± 2.9e-09	-2.5e+00 ± 5.0e-13	1.8e-05 ± 7.1e-08	4.0e+01 ± 4.9e-14	3.0e+00 ± 1.7e-13
24	1.1e-06 ± 2.9e-09	-2.4e+00 ± 6.3e-13	2.0e-05 ± 7.8e-08	4.2e+01 ± 6.0e-14	3.0e+00 ± 2.4e-13
27	1.1e-06 ± 3.2e-09	-2.4e+00 ± 8.6e-13	2.2e-05 ± 9.4e-08	4.4e+01 ± 7.8e-14	2.9e+00 ± 3.4e-13
30	1.1e-06 ± 3.1e-09	-2.4e+00 ± 1.0e-12	2.6e-05 ± 1.0e-07	4.8e+01 ± 9.2e-14	2.8e+00 ± 5.3e-13

Table S3.4: (+)SNP, 35wt% raw vSANS best fit parameters.

Exposure Time (s)	Porod Scale	Porod Exponent	Fluid Scale	Fluid Correlation Length	Fluid Exponent
0	1.5e-06 ± 5.6e-09	-2.6e+00 ± 1.2e-14	8.2e-07 ± 1.7e-08	1.3e+01 ± 4.3e-16	3.8e+00 ± 1.7e-15
3	1.4e-06 ± 5.5e-09	-2.2e+00 ± 1.0e-13	2.2e-06 ± 3.4e-08	2.1e+01 ± 3.7e-15	2.7e+00 ± 6.0e-15
6	1.4e-06 ± 4.9e-09	-2.0e+00 ± 3.0e-13	3.5e-06 ± 4.8e-08	2.4e+01 ± 1.0e-14	3.1e+00 ± 1.3e-15
9	1.3e-06 ± 5.2e-09	-1.9e+00 ± 3.2e-13	3.1e-06 ± 4.8e-08	2.1e+01 ± 1.2e-14	4.1e+00 ± 7.9e-16
12	1.3e-06 ± 5.3e-09	-1.9e+00 ± 3.7e-13	3.8e-06 ± 5.3e-08	2.2e+01 ± 1.6e-14	3.9e+00 ± 1.1e-15
15	1.3e-06 ± 4.8e-09	-1.9e+00 ± 3.1e-13	3.5e-06 ± 4.6e-08	2.1e+01 ± 1.3e-14	4.5e+00 ± 3.2e-16
18	1.4e-06 ± 4.8e-09	-1.9e+00 ± 3.5e-13	4.1e-06 ± 4.9e-08	2.1e+01 ± 1.6e-14	4.3e+00 ± 1.1e-15
21	1.3e-06 ± 5.1e-09	-1.9e+00 ± 3.6e-13	4.1e-06 ± 5.0e-08	2.1e+01 ± 1.7e-14	4.2e+00 ± 8.0e-16
24	1.3e-06 ± 5.4e-09	-1.9e+00 ± 4.3e-13	3.8e-06 ± 5.8e-08	2.1e+01 ± 1.9e-14	4.4e+00 ± 1.7e-15
27	1.3e-06 ± 4.5e-09	-1.9e+00 ± 3.2e-13	3.9e-06 ± 4.4e-08	2.1e+01 ± 1.5e-14	4.5e+00 ± 2.9e-16
30	1.3e-06 ± 4.7e-09	-1.9e+00 ± 3.7e-13	4.0e-06 ± 5.0e-08	2.1e+01 ± 1.7e-14	4.5e+00 ± 6.0e-16

Table S3.5: (+)SNP, 25wt% raw vSANS best fit parameters.

Exposure Time (s)	Porod Scale	Porod Exponent	Fluid Scale	Fluid Correlation Length	Fluid Exponent
0	1.2e-06 ± 6.3e-09	-2.7e+00 ± 3.0e-14	1.5e-06 ± 2.8e-08	1.8e+01 ± 1.6e-15	2.7e+00 ± 6.3e-15
3	1.2e-06 ± 5.0e-09	-2.3e+00 ± 1.4e-13	3.1e-06 ± 4.5e-08	2.4e+01 ± 7.2e-15	3.1e+00 ± 0.0e+00
6	1.1e-06 ± 5.2e-09	-2.1e+00 ± 5.2e-13	6.1e-06 ± 7.4e-08	2.9e+01 ± 2.4e-14	3.1e+00 ± 1.9e-14
9	1.1e-06 ± 5.4e-09	-2.1e+00 ± 7.1e-13	7.7e-06 ± 9.1e-08	2.9e+01 ± 3.8e-14	3.4e+00 ± 3.5e-14
12	1.1e-06 ± 4.7e-09	-2.0e+00 ± 6.3e-13	6.5e-06 ± 7.4e-08	2.6e+01 ± 2.9e-14	3.8e+00 ± 1.4e-14
15	1.1e-06 ± 4.6e-09	-2.0e+00 ± 6.3e-13	6.3e-06 ± 7.3e-08	2.6e+01 ± 2.9e-14	4.1e+00 ± 1.1e-14
18	1.1e-06 ± 6.0e-09	-2.1e+00 ± 8.4e-13	9.8e-06 ± 1.0e-07	3.0e+01 ± 4.8e-14	3.3e+00 ± 3.5e-14
21	1.1e-06 ± 5.4e-09	-2.0e+00 ± 8.9e-13	7.8e-06 ± 9.1e-08	2.8e+01 ± 4.1e-14	3.6e+00 ± 2.6e-14
24	1.1e-06 ± 5.1e-09	-2.0e+00 ± 7.7e-13	7.8e-06 ± 8.6e-08	2.7e+01 ± 3.9e-14	3.9e+00 ± 1.7e-14
27	1.1e-06 ± 5.2e-09	-2.0e+00 ± 8.4e-13	7.8e-06 ± 9.1e-08	2.7e+01 ± 4.2e-14	3.9e+00 ± 2.2e-14
30	1.1e-06 ± 5.2e-09	-2.0e+00 ± 9.3e-13	8.5e-06 ± 9.3e-08	2.8e+01 ± 4.4e-14	3.7e+00 ± 2.8e-14

Table S3.6: (-)SNP, 35wt% raw vSANS best fit parameters.

Exposure Time (s)	Porod Scale	Porod Exponent	Fluid Scale	Fluid Correlation Length	Fluid Exponent
0	1.3e-06 ± 7.6e-09	-2.9e+00 ± 5.7e-15	1.2e-07 ± 1.3e-08	8.8e+00 ± 1.7e-16	1.7e+04 ± 1.2e-23
3	1.3e-06 ± 5.6e-09	-2.8e+00 ± 9.2e-15	3.5e-07 ± 1.4e-08	1.1e+01 ± 1.3e-16	7.1e+00 ± 1.9e-16
6	1.3e-06 ± 5.6e-09	-2.8e+00 ± 1.2e-14	5.2e-07 ± 1.5e-08	1.2e+01 ± 3.3e-16	6.5e+00 ± 3.5e-16
9	1.3e-06 ± 5.5e-09	-2.8e+00 ± 2.2e-14	8.6e-07 ± 1.9e-08	1.4e+01 ± 8.1e-16	4.3e+00 ± 1.4e-15
12	1.3e-06 ± 5.4e-09	-2.8e+00 ± 2.3e-14	9.6e-07 ± 1.9e-08	1.4e+01 ± 9.2e-16	4.0e+00 ± 1.7e-15
15	1.3e-06 ± 5.2e-09	-2.8e+00 ± 1.9e-14	8.6e-07 ± 1.8e-08	1.4e+01 ± 8.2e-16	4.8e+00 ± 1.0e-15
18	1.3e-06 ± 5.6e-09	-2.8e+00 ± 2.2e-14	9.7e-07 ± 1.9e-08	1.4e+01 ± 9.7e-16	4.5e+00 ± 1.4e-15
21	1.3e-06 ± 4.7e-09	-2.8e+00 ± 1.7e-14	9.7e-07 ± 1.6e-08	1.4e+01 ± 9.5e-16	5.2e+00 ± 8.8e-16
24	1.3e-06 ± 5.8e-09	-2.8e+00 ± 2.5e-14	1.0e-06 ± 2.0e-08	1.4e+01 ± 1.1e-15	4.3e+00 ± 1.7e-15
27	1.3e-06 ± 4.8e-09	-2.8e+00 ± 1.9e-14	9.8e-07 ± 1.7e-08	1.4e+01 ± 9.2e-16	5.0e+00 ± 9.8e-16
30	1.3e-06 ± 5.1e-09	-2.8e+00 ± 2.2e-14	1.1e-06 ± 1.9e-08	1.4e+01 ± 1.2e-15	4.9e+00 ± 1.1e-15

Table S3.7: (-)SNP, 25wt% raw vSANS best fit parameters.

Exposure Time (s)	Porod Scale	Porod Exponent	Fluid Scale	Fluid Correlation Length	Fluid Exponent
0	9.6e-07 ± 4.6e-09	-2.9e+00 ± 2.7e-15	2.1e-07 ± 8.9e-09	9.4e+00 ± 9.1e-17	1.4e+01 ± 1.7e-17
3	9.4e-07 ± 3.7e-09	-2.8e+00 ± 6.8e-15	5.3e-07 ± 1.0e-08	1.2e+01 ± 2.1e-16	4.7e+00 ± 4.8e-16
6	9.1e-07 ± 3.4e-09	-2.8e+00 ± 1.2e-14	9.6e-07 ± 1.3e-08	1.5e+01 ± 6.3e-16	3.5e+00 ± 1.5e-15
9	9.1e-07 ± 3.5e-09	-2.8e+00 ± 1.4e-14	1.2e-06 ± 1.4e-08	1.5e+01 ± 8.9e-16	3.5e+00 ± 1.8e-15
12	9.1e-07 ± 3.4e-09	-2.8e+00 ± 1.4e-14	1.3e-06 ± 1.4e-08	1.5e+01 ± 1.0e-15	3.8e+00 ± 1.6e-15
15	9.0e-07 ± 3.4e-09	-2.8e+00 ± 1.4e-14	1.3e-06 ± 1.4e-08	1.5e+01 ± 1.1e-15	3.6e+00 ± 1.8e-15
18	9.2e-07 ± 3.1e-09	-2.8e+00 ± 1.3e-14	1.4e-06 ± 1.3e-08	1.6e+01 ± 1.1e-15	3.9e+00 ± 1.5e-15
21	9.0e-07 ± 3.0e-09	-2.8e+00 ± 1.4e-14	1.5e-06 ± 1.3e-08	1.6e+01 ± 1.2e-15	3.5e+00 ± 1.9e-15
24	8.9e-07 ± 3.4e-09	-2.8e+00 ± 1.5e-14	1.5e-06 ± 1.5e-08	1.6e+01 ± 1.2e-15	3.5e+00 ± 2.2e-15
27	9.2e-07 ± 3.3e-09	-2.8e+00 ± 1.4e-14	1.5e-06 ± 1.4e-08	1.6e+01 ± 1.3e-15	3.9e+00 ± 1.6e-15
30	9.2e-07 ± 3.1e-09	-2.8e+00 ± 1.4e-14	1.5e-06 ± 1.4e-08	1.6e+01 ± 1.3e-15	3.8e+00 ± 1.6e-15

Table S3.8: (0)SS, 10wt% raw vSANS best fit parameters.

Exposure Time (s)	Porod Scale	Porod Exponent	Fluid Scale	Fluid Correlation Length	Fluid Exponent
0	9.0e-07 ± 2.7e-09	-2.8e+00 ± 2.3e-13	9.6e-06 ± 6.6e-08	5.0e+01 ± 1.9e-14	2.9e+00 ± 9.3e-14
3	8.8e-07 ± 2.3e-09	-2.7e+00 ± 6.2e-13	2.0e-05 ± 9.6e-08	6.4e+01 ± 5.1e-14	2.8e+00 ± 4.7e-13
6	8.7e-07 ± 2.3e-09	-2.5e+00 ± 2.0e-12	2.7e-05 ± 1.4e-07	7.3e+01 ± 1.0e-13	2.8e+00 ± 1.3e-12
9	8.6e-07 ± 2.4e-09	-2.4e+00 ± 5.0e-12	3.4e-05 ± 2.2e-07	8.3e+01 ± 1.9e-13	2.7e+00 ± 3.2e-12
12	8.6e-07 ± 2.4e-09	-2.3e+00 ± 8.4e-12	3.4e-05 ± 2.5e-07	8.5e+01 ± 2.2e-13	2.8e+00 ± 3.6e-12
15	8.6e-07 ± 2.3e-09	-2.3e+00 ± 1.1e-11	3.6e-05 ± 2.8e-07	8.6e+01 ± 2.6e-13	2.9e+00 ± 4.2e-12
18	8.6e-07 ± 2.4e-09	-2.3e+00 ± 1.6e-11	4.4e-05 ± 3.4e-07	9.6e+01 ± 3.7e-13	2.8e+00 ± 7.3e-12
21	8.6e-07 ± 2.4e-09	-2.3e+00 ± 1.6e-11	4.7e-05 ± 3.2e-07	9.7e+01 ± 3.5e-13	2.8e+00 ± 7.1e-12
24	8.6e-07 ± 2.2e-09	-2.3e+00 ± 2.2e-11	5.0e-05 ± 3.8e-07	1.0e+02 ± 4.6e-13	2.8e+00 ± 1.0e-11
27	8.5e-07 ± 2.5e-09	-2.3e+00 ± 2.9e-11	4.9e-05 ± 4.4e-07	1.0e+02 ± 5.0e-13	2.8e+00 ± 1.0e-11
30	8.6e-07 ± 2.4e-09	-2.3e+00 ± 3.4e-11	5.7e-05 ± 4.8e-07	1.1e+02 ± 6.1e-13	2.8e+00 ± 1.5e-11

Table S3.9: (0)SS, 7.5wt% raw vSANS best fit parameters.

Exposure Time (s)	Porod Scale	Porod Exponent	Fluid Scale	Fluid Correlation Length	Fluid Exponent
0	8.3e-07 ± 2.5e-09	-2.7e+00 ± 5.0e-13	1.3e-05 ± 9.7e-08	6.8e+01 ± 3.1e-14	2.7e+00 ± 3.0e-13
3	8.2e-07 ± 2.3e-09	-2.7e+00 ± 1.7e-12	2.8e-05 ± 1.6e-07	8.7e+01 ± 9.3e-14	2.7e+00 ± 1.6e-12
6	8.2e-07 ± 2.2e-09	-2.5e+00 ± 5.0e-12	3.8e-05 ± 2.3e-07	9.9e+01 ± 1.8e-13	2.7e+00 ± 4.0e-12
9	8.1e-07 ± 2.3e-09	-2.4e+00 ± 1.1e-11	3.9e-05 ± 3.1e-07	1.0e+02 ± 2.6e-13	2.7e+00 ± 6.0e-12
12	8.1e-07 ± 2.4e-09	-2.4e+00 ± 1.8e-11	4.6e-05 ± 3.8e-07	1.1e+02 ± 3.7e-13	2.7e+00 ± 9.5e-12
15	8.1e-07 ± 2.2e-09	-2.3e+00 ± 2.4e-11	4.2e-05 ± 4.3e-07	1.1e+02 ± 4.2e-13	2.9e+00 ± 8.6e-12
18	8.1e-07 ± 2.2e-09	-2.2e+00 ± 3.6e-11	4.6e-05 ± 5.2e-07	1.1e+02 ± 5.5e-13	2.9e+00 ± 1.1e-11
21	8.0e-07 ± 2.4e-09	-2.3e+00 ± 4.7e-11	5.8e-05 ± 5.9e-07	1.3e+02 ± 6.6e-13	2.8e+00 ± 2.0e-11
24	8.0e-07 ± 2.4e-09	-2.3e+00 ± 6.1e-11	6.3e-05 ± 7.0e-07	1.3e+02 ± 8.7e-13	2.8e+00 ± 2.8e-11
27	8.0e-07 ± 2.4e-09	-2.3e+00 ± 6.2e-11	6.0e-05 ± 7.0e-07	1.3e+02 ± 8.5e-13	2.8e+00 ± 2.7e-11
30	8.0e-07 ± 2.5e-09	-2.3e+00 ± 6.6e-11	5.6e-05 ± 7.5e-07	1.3e+02 ± 8.9e-13	2.9e+00 ± 2.4e-11

Table S3.10: 2:1 SS:SNP, 10wt% raw vSANS best fit parameters.

Exposure Time (s)	Porod Scale	Porod Exponent	Fluid Scale	Fluid Correlation Length	Fluid Exponent
0	8.7e-07 ± 2.6e-09	-2.7e+00 ± 1.7e-13	7.0e-06 ± 5.4e-08	4.7e+01 ± 1.2e-14	2.7e+00 ± 5.9e-14
3	8.5e-07 ± 2.3e-09	-2.5e+00 ± 5.0e-13	1.4e-05 ± 7.7e-08	5.6e+01 ± 3.2e-14	2.8e+00 ± 2.3e-13
6	8.4e-07 ± 2.5e-09	-2.4e+00 ± 1.7e-12	2.2e-05 ± 1.3e-07	6.8e+01 ± 7.6e-14	2.7e+00 ± 8.6e-13
9	8.3e-07 ± 2.4e-09	-2.3e+00 ± 4.2e-12	2.7e-05 ± 1.8e-07	7.7e+01 ± 1.3e-13	2.7e+00 ± 1.9e-12
12	8.3e-07 ± 2.6e-09	-2.3e+00 ± 7.7e-12	3.3e-05 ± 2.4e-07	8.5e+01 ± 2.0e-13	2.7e+00 ± 3.6e-12
15	8.2e-07 ± 2.4e-09	-2.2e+00 ± 1.3e-11	3.7e-05 ± 3.0e-07	9.1e+01 ± 2.7e-13	2.7e+00 ± 5.3e-12
18	8.2e-07 ± 2.6e-09	-2.2e+00 ± 1.7e-11	3.9e-05 ± 3.0e-07	9.3e+01 ± 2.6e-13	2.7e+00 ± 5.0e-12
21	8.2e-07 ± 2.6e-09	-2.3e+00 ± 2.3e-11	4.9e-05 ± 4.3e-07	1.0e+02 ± 5.0e-13	2.7e+00 ± 1.3e-11
24	8.2e-07 ± 2.5e-09	-2.2e+00 ± 3.1e-11	5.0e-05 ± 4.8e-07	1.1e+02 ± 5.6e-13	2.7e+00 ± 1.5e-11
27	8.1e-07 ± 2.4e-09	-2.3e+00 ± 3.5e-11	6.0e-05 ± 4.8e-07	1.1e+02 ± 6.0e-13	2.6e+00 ± 1.9e-11
30	8.2e-07 ± 2.6e-09	-2.3e+00 ± 4.1e-11	6.4e-05 ± 5.2e-07	1.2e+02 ± 6.8e-13	2.6e+00 ± 2.2e-11

Table S3.11: 1:1 SS:SNP, 10wt% raw vSANS best fit parameters.

Exposure Time (s)	Porod Scale	Porod Exponent	Fluid Scale	Fluid Correlation Length	Fluid Exponent
0	8.9e-07 ± 2.4e-09	-2.7e+00 ± 1.2e-13	5.8e-06 ± 4.3e-08	4.2e+01 ± 8.9e-15	2.8e+00 ± 3.2e-14
3	8.8e-07 ± 2.5e-09	-2.6e+00 ± 3.4e-13	1.2e-05 ± 7.0e-08	5.2e+01 ± 2.6e-14	2.7e+00 ± 1.6e-13
6	8.6e-07 ± 2.5e-09	-2.4e+00 ± 1.1e-12	1.8e-05 ± 1.1e-07	6.0e+01 ± 5.9e-14	2.7e+00 ± 5.3e-13
9	8.5e-07 ± 2.7e-09	-2.3e+00 ± 3.2e-12	2.5e-05 ± 1.7e-07	7.0e+01 ± 1.2e-13	2.7e+00 ± 1.5e-12
12	8.4e-07 ± 2.4e-09	-2.2e+00 ± 5.4e-12	3.0e-05 ± 2.1e-07	7.6e+01 ± 1.7e-13	2.7e+00 ± 2.4e-12
15	8.5e-07 ± 2.5e-09	-2.2e+00 ± 8.5e-12	3.4e-05 ± 2.5e-07	8.0e+01 ± 2.3e-13	2.8e+00 ± 3.4e-12
18	8.3e-07 ± 2.7e-09	-2.2e+00 ± 1.4e-11	4.1e-05 ± 3.3e-07	8.9e+01 ± 3.5e-13	2.7e+00 ± 7.0e-12
21	8.3e-07 ± 2.7e-09	-2.2e+00 ± 2.0e-11	4.6e-05 ± 3.9e-07	9.5e+01 ± 4.4e-13	2.7e+00 ± 9.9e-12
24	8.3e-07 ± 2.8e-09	-2.2e+00 ± 2.8e-11	5.0e-05 ± 4.7e-07	1.0e+02 ± 5.6e-13	2.7e+00 ± 1.3e-11
27	8.3e-07 ± 2.8e-09	-2.2e+00 ± 3.4e-11	5.5e-05 ± 5.1e-07	1.0e+02 ± 6.3e-13	2.6e+00 ± 1.6e-11
30	8.3e-07 ± 2.8e-09	-2.3e+00 ± 4.3e-11	6.9e-05 ± 6.0e-07	1.1e+02 ± 8.8e-13	2.6e+00 ± 2.9e-11

Table S3.12: 1:2 SS:SNP, 10wt% raw vSANS best fit parameters.

Exposure Time (s)	Porod Scale	Porod Exponent	Fluid Scale	Fluid Correlation Length	Fluid Exponent
0	9.3e-07 ± 5.4e-09	-2.2e+00 ± 5.6e-14	1.2e-06 ± 3.9e-08	2.0e+01 ± 5.9e-15	1.2e+04 ± 0.0e+00
3	7.6e-07 ± 6.6e-09	-1.7e+00 ± 3.9e-13	1.3e-06 ± 1.0e-07	2.9e+01 ± 2.6e-15	1.2e+04 ± 0.0e+00
6	7.1e-07 ± 5.6e-09	-1.8e+00 ± 5.3e-13	2.5e-06 ± 1.2e-07	3.4e+01 ± 1.4e-14	1.2e+04 ± 0.0e+00
9	7.0e-07 ± 5.0e-09	-1.8e+00 ± 7.6e-13	3.2e-06 ± 1.2e-07	3.6e+01 ± 1.6e-14	1.2e+04 ± 0.0e+00
12	7.0e-07 ± 5.0e-09	-1.9e+00 ± 9.2e-13	3.4e-06 ± 1.3e-07	3.6e+01 ± 3.9e-14	1.2e+04 ± 0.0e+00
15	7.1e-07 ± 4.8e-09	-1.9e+00 ± 1.1e-12	3.3e-06 ± 1.2e-07	3.6e+01 ± 3.0e-14	1.2e+04 ± 0.0e+00
18	7.1e-07 ± 5.2e-09	-2.0e+00 ± 1.2e-12	3.1e-06 ± 1.4e-07	3.6e+01 ± 2.4e-14	1.2e+04 ± 0.0e+00
21	7.1e-07 ± 5.4e-09	-2.0e+00 ± 1.4e-12	3.1e-06 ± 1.4e-07	3.6e+01 ± 3.8e-14	1.2e+04 ± 0.0e+00
24	7.0e-07 ± 6.0e-09	-2.0e+00 ± 1.6e-12	2.9e-06 ± 1.6e-07	3.6e+01 ± 1.9e-14	1.2e+04 ± 0.0e+00
27	7.1e-07 ± 6.2e-09	-2.0e+00 ± 1.5e-12	2.3e-06 ± 1.4e-07	3.3e+01 ± 4.1e-15	1.2e+04 ± 0.0e+00
30	7.1e-07 ± 6.3e-09	-2.1e+00 ± 1.3e-12	2.0e-06 ± 1.4e-07	3.1e+01 ± 2.1e-15	1.2e+04 ± 0.0e+00

Chapter 4: In Situ-Gelling Starch Nanoparticle (SNP) and O-Carboxymethyl Chitosan Plum Pudding Hydrogels for the Intranasal Delivery of Antipsychotic Peptides

Preface

Chapter four describes the design of SNP and O-carboxymethyl chitosan hydrogels for the purpose of aiding in peptide delivery to the brain using schizophrenic Sprague-Dawley rats. By introducing aldehyde groups onto the surface of the SNPs using sodium periodate, the starch can form imine bonds via the amine groups on chitosan. The formed imine bonds are much more transient than the covalent cross-linkages formed using free radical polymerization (FRP) in **Chapters 2 and 3** previously described. The hydrolysis of the imine bonds allows for the production of stable plum pudding nanocomposite hydrogels that degrade/erode predicably as a factor of the crosslinking density (or mass content of precursors) to achieve biologically relevant release profiles. When loaded with the anti-schizophrenic peptide PAOPA, the hydrogels were observed to reduce the negative social interaction symptoms of schizophrenia in knocked down (diclonzipine-treated) Sprague Dawley adult male rats for up to 72 h compared to controls. This chapter was published in the *Journal of Controlled Release* (JCR) in February 2021. Additionally, a reduced version of the data along with the work of others was submitted as a provisional patent in May 2020 that was converted to a PCT patent application in May 2021.

Majcher, M.J.; Babar, A.; Lofts, A.; Li, X.; Campea, M.A.; Hoare, T. "In Situ Gelling Polysaccharide-Based Nanoparticle Hydrogel Compositions, and Methods of Use Thereof". U.S. Patent Application No. 17/323659, filed May 18, 2021.

Majcher, M.J.; Babar, A.; Leung, A.; Li, X.; Smeets, N.M.B.; Mishra, R.K.; and Hoare, T.R., "In Situ-Gelling Starch Nanoparticle (SNP)/O-Carboxymethyl Chitosan (CMCh) Nanoparticle Network Hydrogels for the Intranasal Delivery of an Antipsychotic Peptide", *Journal of Controlled Release*, 2021, 330 , pp. 738-752, doi: https://doi.org/10.1016/j.jconrel.2020.12.050

Author Names and Affiliations: [1]Michael J. Majcher (email: majcherm@mcmaster)‡, [2]Ali Babar (email: babara2@mcmaster.ca)‡, [1]Ashlyn Leung (email: leunga10@mcmaster.ca), [1]Xiaoyun Li (email: xiaoyunli1990@gmail.com) , [2,3]Ram K. Mishra (email: mishrar@mcmaster.ca), [4]Niels M.B. Smeets (email: NSmeets@walkerind.com), [1]Todd Hoare (email: hoaretr@mcmaster.ca)*
[1]Department of Chemical Engineering, McMaster University, 1280 Main Street West, Hamilton, ON L8S 4L8, Canada
[2]School of Biomedical Engineering, McMaster University, 1280 Main Street West, Hamilton, ON L8S 4L8, Canada
[3]Department of Psychiatry and Behavioural Neurosciences, McMaster University, 1280 Main Street West, Hamilton, ON L8S 4L8, Canada
[4]EcoSynthetix, 3365 Mainway, Burlington, ON L7M 1A6, Canada

Abstract
Existing oral or injectable antipsychotic drug delivery strategies typically demonstrate low bioavailability to targeted brain regions, incentivizing the development of alternative delivery strategies. Delivery via the nasal cavity circumvents multiple barriers for reaching the brain but requires drug delivery vehicles with very specific properties to be effective. Herein, we report in situ-gelling and degradable bulk nanoparticle network hydrogels consisting of oxidized starch nanoparticles (SNPs) and carboxymethyl chitosan (CMCh) that enable intranasal delivery via spray, high nasal mucosal retention, and functional controlled release of the peptide drug PAOPA, a positive allosteric modulator of dopamine D2 receptor. PAOPA-loaded SNP-CMCh hydrogels can alleviate negative symptoms like behavioural abnormalities associated with schizophrenia (i.e. decreased social interaction time) for up to 72 hours in an MK-801-induced pre-clinical rat model of schizophrenia at a low drug dosage (0.5 mg/kg); in comparison, conventional PAOPA administration via the intraperitoneal route requires twice the PAOPA dose to achieve a therapeutic effect that persists for only a few hours. This strategy offers potential for substantially decreasing re-administration frequencies and overall drug doses (and thus side-effects) of a range of potential antipsychotic drugs via a minimally-invasive administration route.

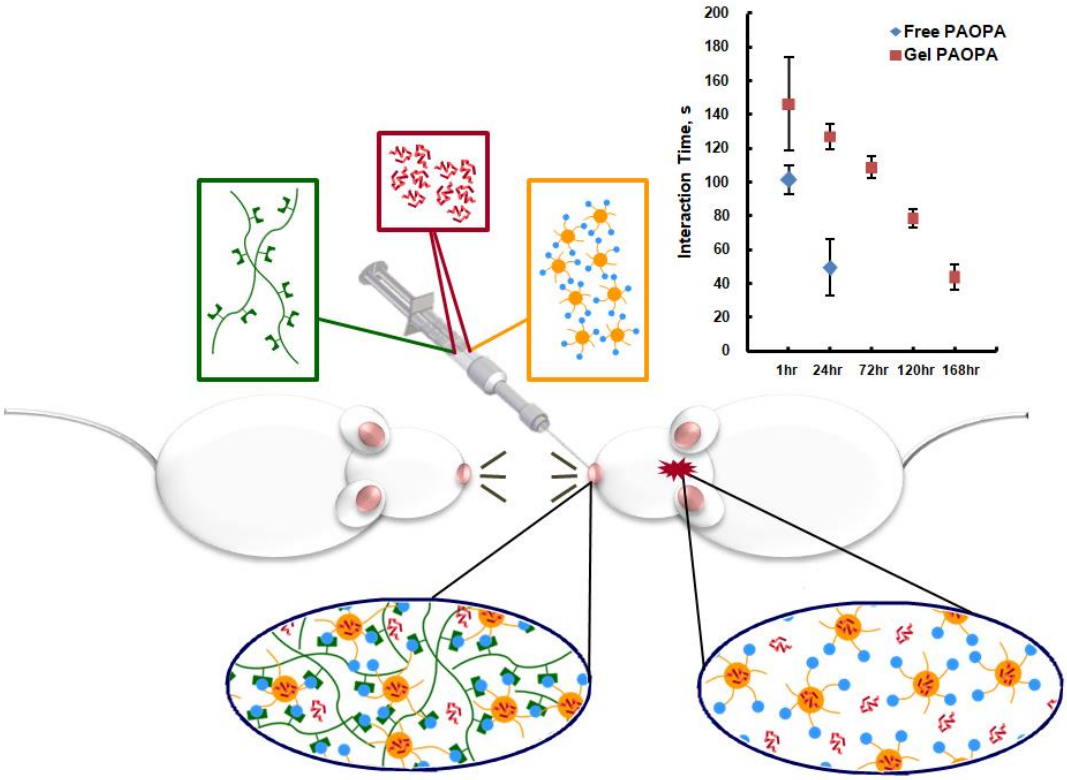

Graphical Abstract: A unique hydrogel formulation was created CMCh (green), aldehyde-modified starch nanoparticles (SNP-CHO, yellow), and PAOPA (red) which can gel in situ (< 10 min) and can be sprayed or pipetted into rat nasal cavities. Once loaded, the observed the effects on animal behavior were observed by first inducing schizophrenia using MK-80 and then observing changes to animal social interaction patterns due to the PAOPA released from the bulk gel, which remained for 3-4 days in total for the experimental samples compared to healthy controls (blue).

4.1 Introduction

Schizophrenia is a serious mental illness that is difficult to properly diagnose and treat given its large range of symptoms including positive, negative, and cognitive abnormalities. Schizophrenia affects ~1% of the worldwide population but is the fifth leading cause of years lost due to disability [410]. Current schizophrenia treatment typically consists of some combination of psychosocial interventions [411], antipsychotic/adjunctive medications [412,413], and experimental/somatic therapies (e.g electro-convulsive therapy or deep brain stimulation) [414]. Given the lack of progressive deterioration or amelioration of the disease that is typically observed [415]) and the complex patient population involved (i.e. ~26% of schizophrenics take more than one antipsychotic and 74% take concomitant medications [416]), the effective long-term delivery of antipsychotic medications in this context presents clear challenges. Such challenges are exacerbated by the frequent strong adverse side-effects of many antipsychotic medications, including but not limited to weight gain, metabolic changes, and sexual dysfunction; the development of extrapyramidal side-effects coupled with the already compromised mental state of schizophrenic patients make patients less likely to adhere to their drug regimen, further exacerbating the disease [417]. Thus, there is a clear need to develop improved delivery systems for antipsychotic drugs that minimize side-effects while also reducing the current requirement for daily (or multiple times daily) administration.

Intranasal (IN) administration of drugs targeting the brain is increasingly attracting interest for minimizing the side-effects of drug therapies. Relative to oral or intraperitoneal (IP) delivery, IN delivery facilitates a more direct and less invasive pathway to the brain through the olfactory and/or trigeminal nerves. Utilizing this pathway avoids the dual challenges of first-pass hepatic metabolism that sequesters/degrades a large amount of oral or IP-delivered drug and the blood-brain barrier (BBB) that limits the transport of circulating drugs to the brain [418]; furthermore, IN delivery avoids microbial metabolism and degradation within the gut [419]. However, the nose-to-brain delivery of free drug suffers from high clearance rates compares to other routes of administration due to the high turn-over rate of the nasal and olfactory epithelial layer (hours to days) along with the secretion of mucin and flow of CSF over the olfactory bulb that can promote convective drug clearance *in vivo* [420]. Collectively, these advantages typically result in IN delivery enabling effective therapies using lower amounts of drug, reducing the occurrence of the highly undesirable off-target side-effects [225].

While the very fast onset of activity of antipsychotic drugs delivered IN is clinically beneficial [421], drug delivered IN is also typically cleared faster than following oral or IP administration; furthermore, many conventional antipsychotic drugs are poorly soluble in non-acidic aqueous solutions, complicating their practical safe delivery into the nose. As such, developing controlled release vehicles for prolonged antipsychotic drug release following IN administration is an emerging area of interest. A wide variety of IN delivery vehicles already exist, including nasal sprays/drops, suspensions, emulsions, liposomal

formulations, and powders [226]. However, few delivery solutions currently exist for the emerging class of antipsychotic peptide drugs including zicronapine (a D1, D2, and serotonin 5-HT2A receptor antagonist) [422], brexpiprazol (a partial serotonin 5-HT1A agonist) [423,424], RP-5063 (a partial D1 agonist) [425] and bitopertin (a non-competitive N-methyl-D-aspartate (NMDA) agonist) [426,427]; our group has specific interest in PAOPA (3(R)-[(2(S)-pyrrolidinylcarbonyl)amino]-2-oxo-1-pyrrolidineacetamide), a potent dopamine D2 allosteric modulator that shows effective alleviation of schizophrenia-like phenotypes (e.g. social interaction and locomotor function) in pre-clinical animal models [428–434]. Such peptides have enabled high symptom alleviation with reduced side-effects compared to conventional antipsychotic drugs when administered via IP injection, which is inconvenient and invasive for a regular therapeutic; however, oral administrations are generally ineffective given the high rate of peptide degradation in the digestive tract [419], making IN delivery the only clear non-invasive alternative.

Previously reported intranasal peptide [420,435,436] and antipsychotic [225,437] delivery vehicles include various nano/micro carriers externally decorated [438] or internally loaded [420] with the peptide of interest or cells/biologics [439] or cells/biologics [438] that express the peptide of interest, depending on the polymer structure, peptide of interest, and region of targeting/specificity within the brain . The addition of absorption [439] or penetration [440,441] enhancers, cell signaling molecules [442], and/or different mucoadhesives to enhance retention in the nose [443] have also all been explored to improve the efficacy of IN delivery. However, many of these formulations are expensive to manufacture and may have limited practical utility in the clinic and/or require extensive chemical modification of complex carriers to function. As such, a controlled intranasal delivery strategy for PAOPA (which could also be extended to other peptide drugs) based on an inexpensive and tissue-compatible vehicle would offer an attractive alternative for exploiting the improved properties of peptide-based antipsychotic drugs while simplifying administration for patients. Such a formulation would ideally be: (1) sprayable to enable facile administration; (2) mucoadhesive and/or in situ-gelling to promote immobilization of the formulation (and thus the drug) to the mucus layer upon administration; (3) transportable (ideally via active transport mechanisms) across the nasal epithelium and subsequently to the olfactory and/or trigeminal nerve(s); and (4) slow releasing to facilitate extended efficacy following a single dose, reducing the need for frequent re-administrations that can reduce compliance in schizophrenic patient populations.

Herein, we describe a sprayable in situ-gelling hydrogel for the intranasal delivery of the antipsychotic peptide PAOPA based on mixing carboxymethyl chitosan (CMCh, a water-soluble and mucoadhesive polymer [444]) and oxidized starch nanoparticles (SNPs, highly penetrative 20-50 nm nanoparticles that are easy to modify due to their hydroxyl-rich surfaces). Larger starch nano/microparticles have been reported to be effective drug carriers within the nasal cavity [445–449]; however, the very small size (20-50 nm, typically predictive of high biological transport through barriers such as the nasal

epithelium) [450] and highly amorphous nature of the extrusion-derived SNPs used in this work (facilitating improved chemical functionalizability) offer unique advantages to our SNPs in the context of IN delivery. By mixing lightly oxidized SNPs (SNP-CHOs) with CMCh upon delivery to the nose, rapidly forming but highly hydrolytically labile (hours-days) Schiff base crosslinks can be formed between the primary amine groups in CMCh and the aldehyde groups generated via SNP oxidation to enable rapid in situ gelation in the nose following spray-based administration, high persistence in the IN cavity (aided by the established mucoadhesivity of CMCh [451]) and tunable degradation to release free SNP-CHOs to transport through the nasal epithelium and into the brain (**Figure 4.1**). PAOPA or other peptides can be loaded into the gel by simple dissolution, with the aldehyde-functionalized SNP-CHO likely to load most of the peptides via the same Schiff base interactions used to facilitate gelation and thus actively transport them into the brain upon gel dissolution. Such a strategy for fabricating degradable bulk gels with tunable properties for IN-controlled release of therapeutics for both schizophrenia and other brain disorders is anticipated to lower required drug doses and ultimately improve clinical outcomes in treating mental illness.

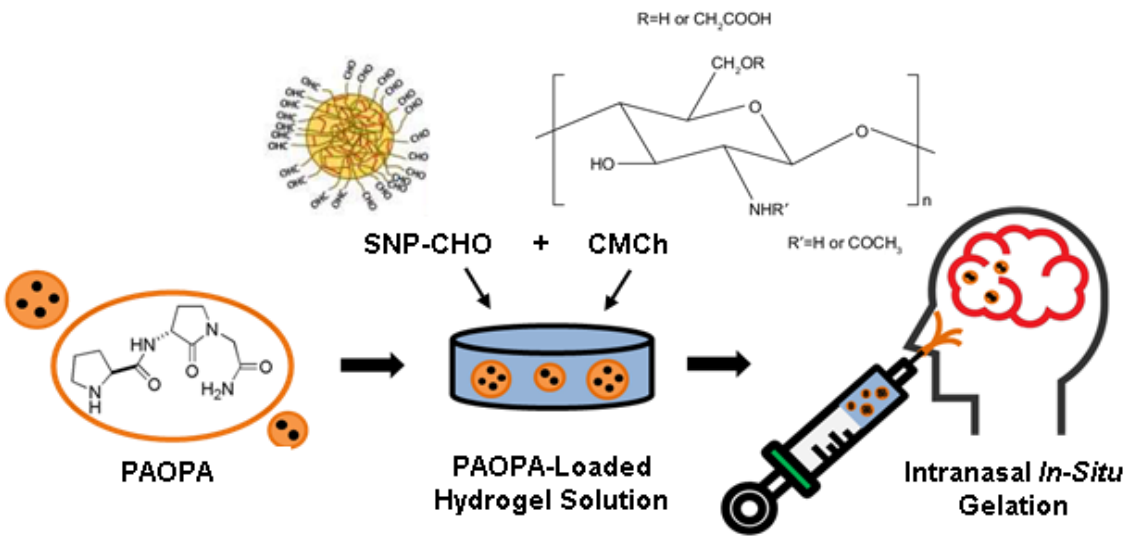

Figure 4.1: Schematic diagram of the IN delivery strategy to administer PAOPA to the brain using *in situ*-gelling SNP-CHO/CMCh hydrogels.

4.2 Experimental Section

4.2.1 Materials

Experimental grade starch nanoparticles (SNPs) were supplied by EcoSynthetix Inc. (Burlington, ON, Canada) and used as received. O-carboxymethyl chitosan (CMCh with ≥ 80% DS, 10-1000 mpa*s viscosity, from Bonding Chemical, Katy, TX, USA), sodium periodate (NaIO4, 99% from AK Scientific, California, USA), and ethylene glycol (99.8% anhydrous reagent grade, MilliporeSigma, Oakville, ON, Canada) were all used as received. PAOPA ((3R)-2-oxo-3-[[(2S)-2-pyrrolidinylcarbonyl]amino]-1-

pyrrolidineacetamide] (≥ 98%) was purchased from Tocris Bioscience (Oakville, ON, Canada). (+)-MK-801 ((+)-5-methyl-10,11-dihydro-5H-dibenzo [a,d]cyclohepten-5,10-imine maleate salt) was purchased from Sigma-Aldrich (Oakville, ON, Canada). SHSY-5Y human neuroblastoma cells were obtained from American Type Culture Collection (ATCC). Dulbecco's Modified Eagle Medium: Nutrient Mixture (DMEM:F12) media supplemented with heat inactivated bovine serum (10% v/v), L-glutamine (1% v/v), and penicillin streptomycin (1% v/v) was obtained from Thermo Fisher Scientific [Burlington, ON, Canada]. A resazurin in vitro toxicology assay kit was obtained from Sigma-Aldrich (Oakvile, ON, Canada). The Sylgard 184 elastomer kit used for the lap shear mucoadhesion measurements was purchased from Dow Corning.

For all experiments, Millipore Milli-Q grade distilled de-ionized water (MQW, 18.2 MΩ/cm resistivity) was used. Phosphate buffered saline (PBS) was prepared by dissolving PBS tablets (MilliporeSigma, Oakville, ON, Canada) at a concentration of 200 mL/tablet in MQW to achieve the desired concentrations (0.01 M phosphate buffer, 0.0027 M potassium chloride and 0.137 M sodium chloride, pH 7.4, at 25 °C) The pH of the buffer was confirmed using a pH probe. Artificial cerebrospinal fluid (aCSF) was prepared by sequentially dissolving 701 mg (120 mM) NaCl, 36 mg (4.8 mM) KCl, 16 mg (1.2 mM) KH2PO4, 30 mg (1.2 mM) $MgSO_4$, 37 mg (25 mM) $NaHCO_3$, 211 mg (2.5 mM) $CaCl_2$, and 180 mg (10 mM) D-glucose in 100mL of MQW.

4.2.2 Synthesis of Aldehyde Functionalization of Starch Nanoparticles (SNP-CHO)

Sodium periodate oxidation was used to introduce dialdehydes on the anhydrous glucose unit (AGU) repeat units of SNPs [452]. 10 g of dry SNPs (as confirmed via a % solids measurement using a CEM microwave drier) was dispersed in 400 mL MQW via mechanical agitation (stir bar), and the pH was adjusted to pH 7. A second solution was then made in which molar equivalents of 0.25 (3.3 g $NaIO_4$ per 10.64 g SNP), 0.5 (6.61 g $NaIO_4$ per 10.64 g SNP), 1 (13.25 g $NaIO_4$ per 10.64 g SNP), or 2 (26.525 g NaIO4 per 10.64 g SNP) moles sodium periodate to moles of anhydrous glucose units in the SNPs was dissolved in 100 mL of MQW and subsequently added to the SNP dispersion. The mixture was allowed to react at room temperature for 18 h, after which the reaction was stopped by adding an equimolar amount of ethylene glycol to quench residual sodium periodate and stirring overnight. The final product was dialyzed using a 3.5 kDa MWCO membrane for 6 cycles (6 hours each) against MQW, lyophilized, and stored at room temperature in the dark as a dry powder. The samples were denoted as "SNP-CHO-x", where x denotes the molar equivalent of sodium periodate added for the oxidation reaction.

4.2.3 Characterization of SNP-CHO

^{1}H nuclear magnetic resonance spectra before and after SNP oxidation were acquired using a Bruker AVANCE 600 Hz 1H-NMR instrument and deuterium oxide (D2O) as the solvent. The collected spectra were plotted and analyzed in TopSpin (academic version 4.0.9, Bruker). SNP hydrodynamic radius distributions were assessed via gel permeation chromatography (GPC) using a Viscotek GPCmax and Triple Detection Array 305 (Malvern, Worcestershire, UK) and an Aquagel PAA-200 series column (PolyAnalytik)

run at 25 °C using 0.05 M lithium bromide in dimethyl sulfoxide (DMSO) as the elution solvent.

Hydrodynamic diameter was analyzed using a NanoPlus 90 dynamic light scattering (DLS) system (Brookhaven, Long Island, NY, USA). All samples were run at 1 w/v% in MQW and lightly sonicated (lowest setting) in a sonicator bath at room temperature for 15 min prior to analysis to reduce SNP aggregation without disturbing the nanoparticle structure. For each sample, 6 data points were collected (with 3 individual measurements per data point) with acquisition times of 5 min; the particle size represents the number average of these measurements, while the uncertainty represents the standard error of the replicate measurements. Number average hydrodynamic diameters were estimated based on the refractive index of starch (~1.34) [395]. The size and morphology of the SNPs before and after functionalization was tracked with transmission electron microscopy (TEM) using a JEOL 1200EX TEMSCAM instrument. To reduce the likelihood of film formation by SNPs during drying on the TEM grid, a low contrast poly(methyl methacrylate) latex with a particle size of 100 nm was made via semi-batch emulsion polymerization [453] and used to separate the SNPs upon drying. Samples were dried on a standard copper grid at concentrations of 5 mg/mL and imaged using an acceleration voltage of 80 kV.

4.2.4 Formation and Delivery of SNP-CHO/CMCh Hydrogels

CMCh was dissolved in MQW at 2, 4, or 6 w/v%, while SNP-CHO were dispersed in MQW at 35, 25, or 10 w/v% as described above. For degradation and mechanics testing, each component was placed into separate barrels of a double barrel syringe (2.5 mL L-series, Medmix, Switzerland) and a 16 gauge needle was attached to the mixing end of the syringe. The gels were expelled into 400 µL silicone rubber molds (diameter 6.35 mm) for kinetics of degradation measurements and 600 µL silicone rubber molds (diameter 12.7 mm) for micromechanical testing. Gelation was allowed to proceed for 16 hours to ensure equilibrium crosslink formation. Alternately, for the assessment of spray-based delivery, LMA MAD nasal intranasal mucosal atomization devices (Equipment Medical Rive Nord, Montreal, QC, Canada) were attached to the end of the double barrel syringe. Spray efficacy was tested by spraying the contents of the syringe on a vertical sheet of paper from distances of 5, 10 and 15 cm, with the upper limit selected based on the distance between the nostril and the nasopharynx (the posterior of the nasal cavity) [454–456]. Blue and yellow food coloring was used to visualize the spray field, which was subsequently imaged and analyzed (using ImageJ) for total surface area deposition measurement.

4.2.5 Kinetics of Gelation via Inversion Testing

The stock SNP-CHO and CMCh solutions were well mixed using a standard heavy-duty vortex mixer (VWR) at ~500 rpm for up to 5 minutes beforehand to ensure even mixing. In a 1.5 mL Eppendorf centrifuge tube, 100 µL of CMCh (2-6 wt%) and SNP-CHO (5-35 wt%) were added consecutively using a micropipette, using separate tips for each solution to prevent contamination and premature gelation before the timer begins. The vial was

inverted/agitated by hand every 5 seconds, with the gelation time (t_{gel}) recorded as the time at which no flow was observed within 2 seconds after sample inversion. All gel combinations were run in quadruplicate (n=4).

4.2.6 Kinetics of Degradation by Gravimetric Analysis

Hydrogel disks were fabricated in silicone molds (4 mm thick, 6.35 mm diameter) using the double barrel syringe delivery strategy described in **Section 4.2.4** and allowed to equilibrate overnight prior to testing. The formed gels were then loaded into pre-weighed transwell inserts to allow for free diffusion of water and immersed fully in 10 mM PBS (0.01 M phosphate buffer, pH 7.4, at 25 °C) inside individual wells of a 6-well plate. At predetermined time intervals (every half hour for the first hour, every hour for the next 4 hours and then twice a day for two weeks), the transwell inserts were removed, excess water was wicked away using a Kimwipe, the sample mass was weighed, and the inserts were returned to the tray. All gel combinations were run in quadruplicate (n=4).

4.2.7 Micromechanical Properties

Hydrogels were fabricated in silicone molds (4 mm thick, 12.7 mm diameter) using the double barrel syringe-based loading procedure described in **Section 4.2.4** and equilibrated overnight in a humidity-controlled chamber prior to testing. The mechanical properties of the hydrogel were assessed using a MACH-1 Micromechanical Analyzer (Biomomentum, Inc., Laval, QC Canada). For all small angle oscillatory measurements, a strain sweep was performed from 0.1° to 2.154° at a frequency of 1 Hz to determine the linear viscoelastic region (LVE). After the LVE was determined, a frequency sweep was performed from 0.1 Hz to 2.154 Hz within this linear viscoelastic regime (0.45 – 1.44°) to determine the storage modulus (G') and loss modulus (G") of the hydrogels. The raw data were analyzed using the sinusoidal analysis function on the MACH-1 analysis software. All gels were run in quadruplicate (n=4), with error bars representing the standard deviation of the data.

4.2.8 *In Vitro* Mucoadhesion Assay

Mucoadhesion of the nanoparticle network bulk hydrogels was assessed using a lap shear device configuration of the MACH-1 micromechanical tester [53]. Images of the lap shear device and sample holder (**Figure S4.1, a-f**) and overall experimental set up (**Figure S4.2, a-d**) are provided in the **Supplementary Information**). Sylgard 184 PDMS substrates (thickness of 2 mm) were created on a 22 mm × 22 mm (glass cover slip) and cured, first overnight at room temperature followed by an additional 24 h at 50°C. The surface of the PDMS was then functionalized with mucous via simple adsorption of a prepared 2 wt% bovine mucin solution and drying under ambient conditions. The resulting mucin-PDMS wafers were attached with double-sided adhesive to a metal support (plate) equipped with mounting holes enabling attachment to the mechanical tester. Removable corner brackets were then tightly fitted to contain the precursor polymer between the lower and upper PDMS wafers. Following, an anchoring plate was mounted with screws to hold the assembly together, at which point a solution of pre-mixed SNP-CHO and CMCh hydrogel precursors of targeted concentrations (total

volume 1 mL) was injected and allowed to crosslink in situ between the two PDMS surfaces. Following gelation, the retaining walls were removed and threaded rods with pin and nut connections were used to attach the plastic support plates to the base and Z-motion stage of the mechanical tester to perform the lap shear test using five small-amplitude stress relaxation cycles with 0.1 mm steps at a rate of 0.05 mm/s. After each cycle (10 s total), the sequence resets back to the starting position with a fixed relaxation time of 1 s and relaxation rate of 0.1 gf/mm. The work of adhesion was subsequently calculated by integrating the area under the force vs. distance curves, while the slope of the force vs. position (z-axis) graph between the relaxation steps defined the shear modulus. n=4 samples were tested per sample, with error bars representing sample standard deviation.

4.2.9 *In Vitro* Cytotoxicity Assay

SH SY5Y human neuroblastoma cells (broadly used to model neurons) were cultured in DMEM:F12 media to ~70% confluency. Following trypsin addition and centrifugation, 50 µL of a 200,000 cells/mL cell suspension (corresponding to 10,000 cells/well) was plated in a 96 well plate and incubated for 24 hours. Polymer and SNP solutions were prepared in sterile 10 mM PBS followed by filtration through a 0.45 µm Acrodisc filter and 30 minutes of UV exposure to ensure sterility, after which they were added to the cell wells at concentrations between 0.1-10 mg/mL. After 24 hours of incubation, 50 µL of resazurin dye in sterile PBS was added to each well (final resazurin concentration per well = 10 µg/mL). The cells were returned to the incubator for between 4-12 h (as necessary to develop differentiable colours between the different wells), after which the plates were read using an Infinite 200 Pro (Tecan) plate reader using excitation and emission wavelengths of 560 nm and 590 nm, respectively. Background fluorescence was corrected by subtracting the fluorescence of blank wells (correcting for the effects of media, resazurin, and polymer) from the experimental wells. The ratio of fluorescence between the positive controls and the experimental samples once blanked yielded the relative cell viability. All samples were run in quadruplicate (n=4); error bars represent standard deviations.

4.2.10 Drug Stability

SNPs and CMCh were suspended/dissolved in an aCSF solution containing 1.66 mg/mL PAOPA and left to equilibrate for 24 hours, after which hydrogels were prepared as described in **Section 4.2.4** to physically entrap PAOPA in the gel. Following overnight equilibration, the hydrogels were loaded into cell inserts and incubated in 10 mL of PBS inside a 6 well plate at 37 ˚C and 100 rpm. At defined time points, the supernatant was sampled and the PAOPA drug stability was assessed via gradient high performance liquid chromatography (HPLC, Waters, Milford, MA, USA) using a Waters 1525 binary pump, a Waters 2707 autosampler, a C-18 column (5 µm, 150 mm × 4.6 mm), and a Waters 2489 UV/visible detector (λ = 215 nm for PAOPA) operating at ambient temperature and a flow rate of 1.0 mL/min. To elute PAOPA, a gradient mobile phase of 70% water/30% acetonitrile held constant for 5 minutes, gradually switching to 30% water/70% acetonitrile over the next 7 minutes, and then holding the composition constant for the

next 5 minutes was used, after which the mobile phase was reverted to 70% water/30% acetonitrile and held constant for 15 minutes to recover the baseline.

4.2.11 *In Vivo* Animal Studies

4.2.11.1 Animals

Age-matched male Sprague-Dawley rats (250-300 g, Charles River Canada, St. Constant, QC, Canada) received care that complied with protocols approved by the Animal Research Ethics Board at McMaster University and the guidelines of the Canadian Council on Animal Care. Animals were housed individually in standard cages on a reverse 12 h light cycle. Upon arrival, animals were habituated to their holding room for 1 week, followed by a week of handling (touching and petting for 5 minutes each, every other day) prior to any testing. Animals were housed in a room maintained at 22°C and 50% humidity and access to food and water *ad libitum*.

4.2.11.2 Intranasal Administration

PAOPA (with or without hydrogel formulation) was dissolved in aCSF at a concentration that would result in a 0.5 mg/kg dosage delivered to each animal, a dosage selected based on an initial screen of free PAOPA concentrations delivered IN ranging from 0.1-1 mg/kg. Animals were anaesthetized using isoflurane, and 30 μL of solution was pipetted into each nasal cavity, with a 1 minute break between each pair of nostrils to allow for deposition within the cavity. For controls, animals received either no solution, aCSF alone, or free PAOPA in aCSF directly. For experimental gel groups, precursor solutions of SNP-CHO and CMCh dissolved in aCSF (either with or without PAOPA) were mixed immediately prior to IN administration. Following a 30 minute wait time, MK-801 was administered at 0.3 mg/kg via IP injection; the MK-801 model was selected over others [457,458] due to its simple administration (IP injection) and successful use in previous work [431]. Six experimental groups were tested at different PAOPA and gel concentrations (n=4 per experimental group): (A) no drug, no gel, no MK-801 (blank control); (B) drug, no gel, no MK-801 (drug-only control); (C) gel, no drug, no MK-801 (material-only control); (D) no drug, no gel, MK-801 (negative behavioural control); (E) drug, no gel, MK-801 (drug-induced symptom alleviation); (F) drug, gel, MK-801 (formulation-induced symptom alleviation). All behavioural tests were conducted 30 minutes following MK-801 administration.

4.2.11.3 Social Interaction Testing

The lack of social interaction reflects negative symptoms of schizophrenia in humans and is routinely used in pre-clinical models for testing effectiveness of anti-schizophrenia drugs. Rats were assessed for social interaction with and without MK-801 and drug/formulation administration following published methods [459,460]. Animals were habituated alone in the social interaction arena, a black Plexiglass open box (100 cm x 100 cm x 40 cm) placed on black Plexiglass floor, prior to testing. On the day of testing, two unfamiliar (i.e. no prior social interaction) rats were placed in opposite corners of the social interaction arena. A ceiling-mounted video camera was placed above the arena to track interactions during a 5 minute tracking time during which the experimenter was

absent from the room, with half of the room lights remaining switched on during the testing period. Total time spent in interaction was recorded for each rat and further divided into active interaction (sniffing, following, crawling over/under, grooming, and any aggressive behavior) or passive interaction (close proximity). Recordings were analyzed by three independent blinded observers, with the interaction times assessed by each observer averaged. No animal pairing was repeated (i.e. each rat pair represented a novel social interaction), and the arena was thoroughly cleaned using 75% ethanol between each social interaction recording.

4.2.11.4 Biodistribution

To determine the transport and residence time of the gel formulation, SNP-CHO were fluorescently tagged (F-SNP-CHO) with AlexaFluor Hydrazide 657 by adding 1 mg of AlexaFluor to 700 mg of SNPs in aCSF and stirring at room temperature for 1 h. Following, sodium cyanoborohydride (2× molar excess to the amount of aldehyde groups) was added to the solution and the flask was allowed to stir overnight to reduce the hydrazone bond. The particles were then dialyzed against MQW (6 × 6 hour cycles, 3500 molecular weight cut-off membrane) and lyophilized. Following, F-SNP-CHO was re-dispersed in a 35 wt% dispersion aCSF, mixed with 2 or 4 wt% CMCh, and administered into a rat's nose using the method described in **Section 4.2.11.2.** At t = 24 hrs (1 day) or t = 72 hrs (3 days), the animals were sacrificed and the cerebellum, olfactory bulb, liver, lung, kidney, spleen, and nasal tissue were removed. The tissues were washed using saline and then frozen in an aluminum foil-wrapped container. Following, the tissue samples were homogenized in saline, and the fluorescence of the resulting mixtures was analyzed using an Infinite 200 Pro plate reader (λ_{ex} = 633 nm, λ_{em} = 683 nm). Concentrations of F-SNP-CHO in each organ were estimated based on a standard curve.

4.2.11.5 Statistical Analysis

For all comparisons tested, a one-way analysis of variance (ANOVA) with an alpha value of 0.05 along with a Tukey's post-hoc test (SAS) was used to determine specific groups with statistical differences.

4.3 Results and Discussion

4.3.1 Characterization of SNP-CHO

Confirmation of the oxidation of the C2 and C3 cis-diols on the AGU backbone was achieved using ^{1}H-NMR via the appearance of a new aldehyde peak at ~9.1 ppm relative to the precursor SNPs (**Supplementary Information Figure S4.3**). The experimental DS of aldehyde functionalization was estimated based on the intensity of the -CHO peak at ~9 ppm relative to the anomeric glucose proton intensity at ~5.4 ppm, as described in a previous report [291]. Triple detection gel permeation chromatography of SNPs prepared at various degrees of substitution indicates a progressive shift to longer retention times (corresponding to smaller particle sizes) as higher sodium periodate concentrations are used (**Fig. 4.2A**), consistent with the starch degradation via this oxidation reaction [452]. However, a particularly significant shift (corresponding to substantial degradation) was observed for the SNP-CHO-2 mol sample, suggesting that a maximum of 1 mol sodium

periodate per mole of anhydrous glucose units should be used preserve the nanoparticle structure of native SNPs. Dynamic light scattering analysis of SNP-CHO-0.25 indicated a tri-modal distribution with peaks at ~40nm, ~100nm and ~350nm (the latter attributable to aggregation of SNPs in water) based on intensity but a single population centered at ~45 nm when assessed by number (**Fig. 4.2C**); transmission electron microscopy confirmed the average size of the SNP-CHO-0.25 particles (**Fig. 4.2B**) as being between 20-40 nm and the shape to be largely spherical, with any observed shape deformation likely attributable to the drying of a soft gel-like nanoparticle in the presence of the hard anti-film forming PMMA latex (visible as the lighter larger particles in the background of the TEM image). Collectively, these results show that sodium periodate oxidation can successfully produce aldehyde-functionalized SNPs with different aldehyde contents while preserving the small but well-defined nanoparticle morphology of native SNPs hypothesized to be useful for penetration through the nasal epithelium and transport of drug into the brain.

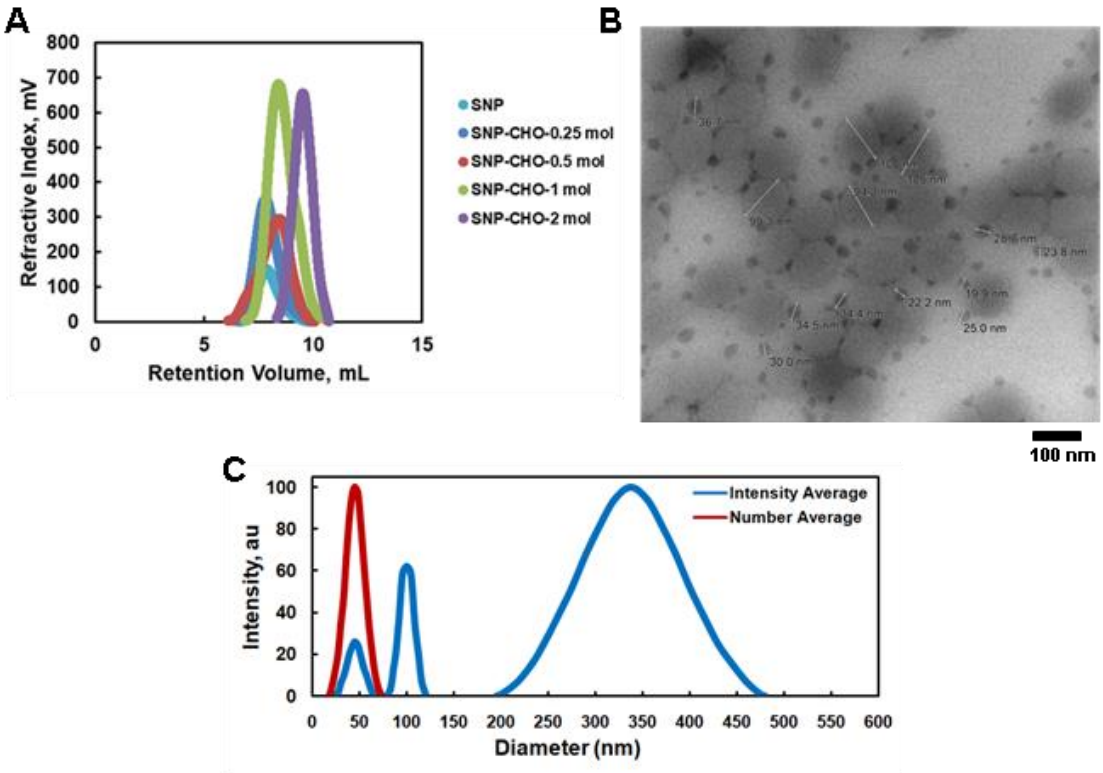

Figure 4.2 (a-c): Characterization of oxidized starch nanoparticles (SNP-CHO): (A) gel permeation chromatography analysis of the relative hydrodynamic diameter of SNP-CHO prepared at different degrees of oxidation; (B) representative transmission electron microscopy image of SNP-CHO-0.25 in the presence of background PMMA nanoparticles used to prevent SNP-CHO film formation during drying (100 nm scale bar); (C) intensity average (blue) and number average (red) particle size distribution of SNP-CHO-0.25 via dynamic light scattering.

4.3.2 Physical Characterization of CMCh/SNP-CHO Hydrogels

The gelation times observed following mixing of various concentrations of O-carboxymethyl chitosan (2-6 wt%, the upper limit corresponding to the highest wt% at which CMCh remained an injectable solution) with various concentrations and degrees of oxidation of SNP-CHO are shown in **Figure 4.3 (a-c)**. Note that the y-axis scales and the SNP concentrations tested for each degree of oxidation of SNP tested are significantly different, corresponding to the different concentrations of SNP required to make gels in each case.

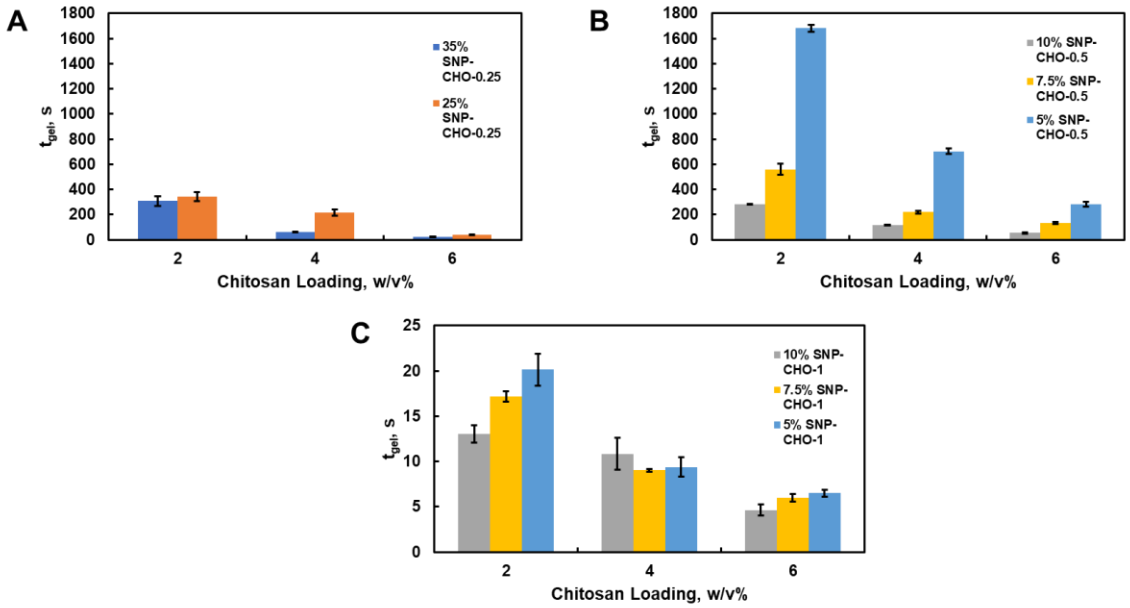

Figure 4.3 (a-c): Gelation times (via vial inversion) for CMCh/SNP-CHO hydrogels prepared using various CMCh and SNP-CHO concentrations: (A) SNP-CHO-0.25-based hydrogels; (B) SNP-CHO-0.5-based hydrogels; (C) SNP-CHO-1-based hydrogels.

Overall, as the weight/volume percent (w/v%) of SNP-CHO or chitosan used to fabricate the hydrogel increased, gelation time decreased; correspondingly, increasing the functionality of SNP-CHO resulted in decreased gelation times. This result is consistent with the proposed Schiff base-induced crosslinking mechanism, by which the presence of more aldehyde and/or amine groups should result in more crosslinking and thus faster gel formation. Hydrogels prepared with SNP-CHO-0.25 required at least 25 mol% SNPs to fabricate gels, while increasing the degree of oxidation of the SNPs (SNP-CHO-0.5 or SNP-CHO-1) resulted in gel formation within the <10 minute timeframe for SNP concentrations as low as 5 wt%; gels based on SNP-CHO-1 gelled consistently in <20 s. Given the practical considerations around performing in situ gelation in the nose, for which gelation times on the order of a few minutes are anticipated to be ideal to enable facile injection/spray but still promote good retention of the gel on the nasal mucosa

(assuming that gelation rates should be faster than the transitional and respiratory epithelium turnover rate of ~10 minutes in a rat [461] or up to ~20 minutes in humans [462]), formulations based on SNP-CHO-0.25 and SNP-CHO-0.5 appear to be most promising; the very high potential SNP loadings achievable using SNP-CHO-0.25, which gels at an appropriate time for intranasal delivery using up to 35 wt% SNP-CHO, may be particularly useful from a drug delivery perspective if released SNPs can transport through the nasal epithelium into the brain.

To assess the hydrolytic stability of the resulting labile Schiff base crosslinked hydrogels, the mass of the gels was tracked over time to gravimetrically assess the swelling and ultimate degradation of the hydrogel (**Figure 4.4**). Note that the lifetime of the gel *in vivo* is expected to be somewhat different based on the less fully hydrated conditions in the nasal cavity coupled with the presence of enzymes and esterases in the mucosa and interstitial fluids; however, the comparisons in Fig. 4 do provide effective relative comparisons of gel swelling and stability

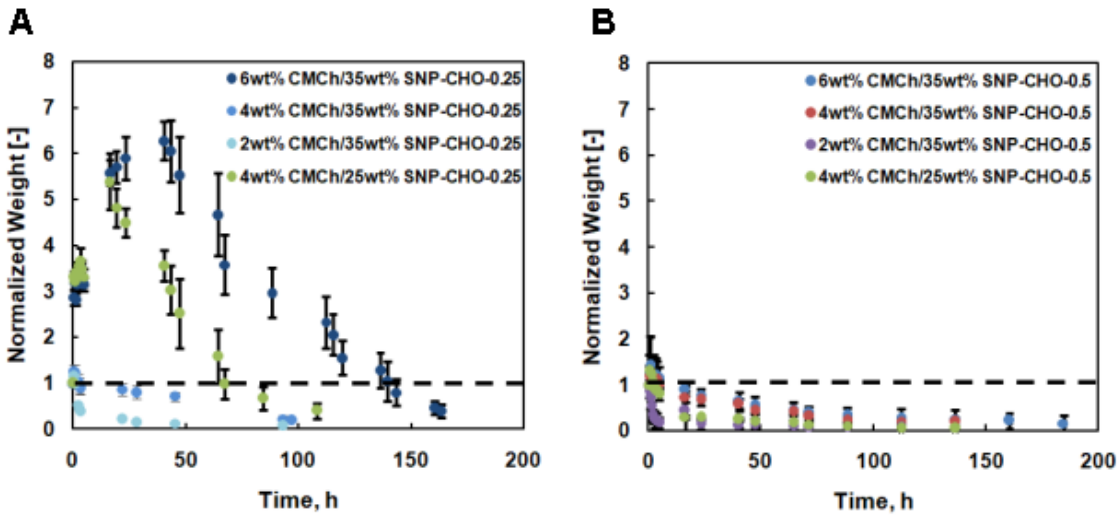

Figure 4.4(a,b): Gravimetric *in vitro* swelling/degradation profiles in 10 mM PBS at 37 ˚C for CMCh/SNP-CHO hydrogels based on (A) SNP-CHO-0.25 and (B) SNP-CHO-0.5.

Hydrogels with higher CMCh contents and lower SNP contents exhibited substantial swelling upon incubation in PBS, with the 6 wt% CMCh/35 wt% SNP-CHO-0.25 hydrogel in particular swelling to 6.5× its original mass prior to the onset of mass loss due to degradation. In contrast, all hydrogels prepared with SNP-CHO-0.5 and hydrogels prepared with SNP-CHO-0.25 but with higher SNP contents/lower CMCh contents (i.e. 4 wt% CMCh/35 wt% SNP-CHO-0.25 and 2 wt% CMCh/35 wt% SNP-CHO-0.25) exhibited only minimal swelling prior to degradation. Lower (ideally near zero) swelling hydrogels would be preferred for nasal administration to ensure a thin film and/or a thin array or droplets are deposited on the nasal mucosa as opposed to a thicker gel layer that may impair breathing. Hydrogels were observed to fully degrade in as little as 4 days (100 h) in PBS, with

hydrogels prepared with SNP-CHO-0.25 showing predictably faster degradation times compared to more highly aldehyde-functionalized SNP-CHO-0.5 hydrogels. These degradation times are on the same order of magnitude as the turnover time of olfactory mucous (several days) [461] and are thus appropriate for nasal usage.

The shear storage moduli of the fabricated hydrogels are shown in **Figure 4.5 (a-c)**.

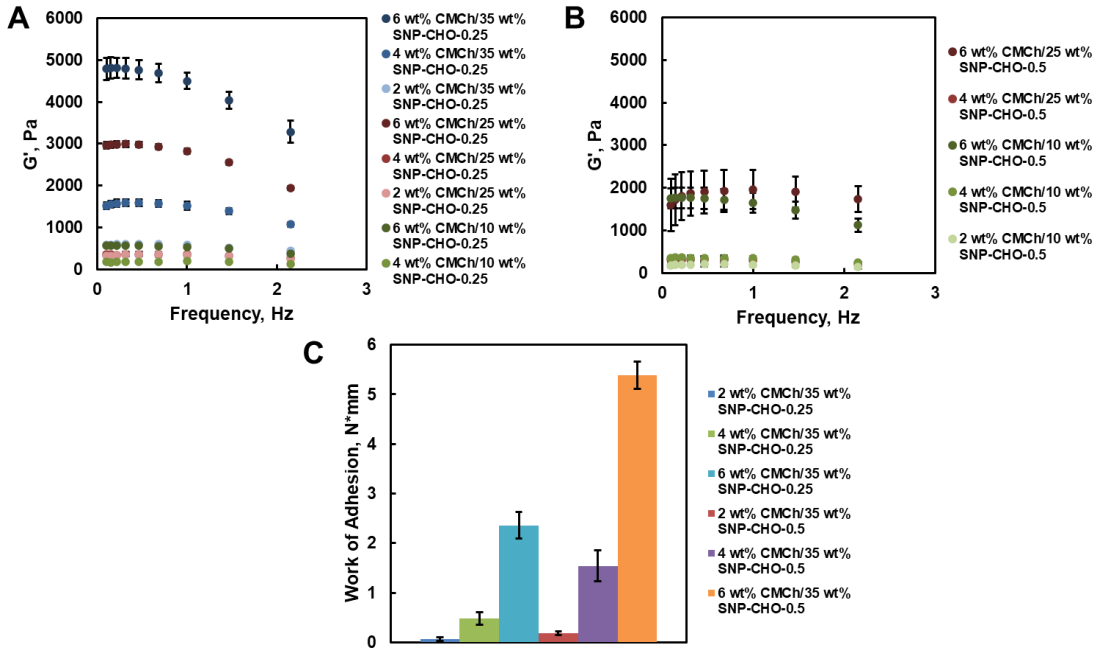

Figure 4.5 (a-c): Mechanical properties of CMCh/SNP-CHO hydrogels. (A, B) Shear storage modulus (G') as a function of frequency for CMCh/SNP-CHO hydrogels prepared with (A) SNP-CHO-0.25; (B) SNP-CHO-0.5; (C) Work of mucoadhesion for selected CMCh/SNP-CHO hydrogels with relevant gelation/degradation properties for IN delivery

Consistent with theory, increasing the concentration of CMCh or concentration and/or degree of functionalization of SNP-CHO resulted in the formation of stiffer hydrogels. Most hydrogels showed G' values of 2 kPa or less except for gels prepared with 6 wt% CMCh and higher SNP-CHO loadings. Relative to the very low shear storage modulus of the nasal mucosa (~30 Pa) [463], all hydrogels tested are stiffer but within 1-2 orders of magnitude of modulus; coupled with the tunable gelation time that allows for a much lower modulus material to transiently exist in the nose following spray administration, we anticipate that interpenetration and thus adhesion between the native mucous and the gel will still occur. This hypothesis tested by measuring the work of adhesion of hydrogel formulations that exhibit relevant gelation/degradation properties for IN delivery to mucous-coated PDMS, the results of which are shown in **Fig. 4.5C** (see **Supplementary Information, Figure S4.4(a-f)** for raw mucoadhesion data). For both SNP-CHO DS

values tested, increasing the concentration of mucoadhesive CMCh increases the work of adhesion between the hydrogel and the mucin-coated Sylgard membranes, with higher DS SNP hydrogels exhibiting higher works of adhesion at the same CMCh loading consistent with the presence of a higher number of aldehyde groups that can form Schiff bases with the enzyme/protein components of the mucous layer. Taking these physical characterization results together, formulations consisting of 2 or 4 wt% CMCh mixed with 10-35 wt% of SNP-CHO-0.25 or SNP-CHO-0.5 would result in hydrogels that are mucoadhesive, form in less than 10 minutes, and degrade in a week or less, properties that are amenable for IN administration.

4.3.3 *In Vitro* Cytotoxicity

The cytotoxicity of CMCh and SNP-CHO gel precursor materials suitable for IN hydrogels to SH-SY5Y neuroblastoma cells was assessed using a resazurin assay, the results of which are shown in **Figure 4.6** below. For CMCh and SNP-CHO-0.25, all concentrations tested within the concentration range of 0.1 to 10 mg/mL yielded cell viability measurements of >90%, suggesting high cytocompatibility. For SNP-CHO-0.5, cell viability remains high at concentrations of 0.1 – 1 mg/mL but then declines at concentrations >2 mg/mL sample, with concentrations >5 mg/mL yielding high cytotoxicity. While the concentrations of SNPs used in vivo are much higher than those tested here (35 wt%), based on the degradation studies it is unlikely the local concentration would at any point exceed the cytotoxic threshold observed for SNP-CHO-0.5; however, such risk can be entirely mitigated by using SNP-CHO-0.25.

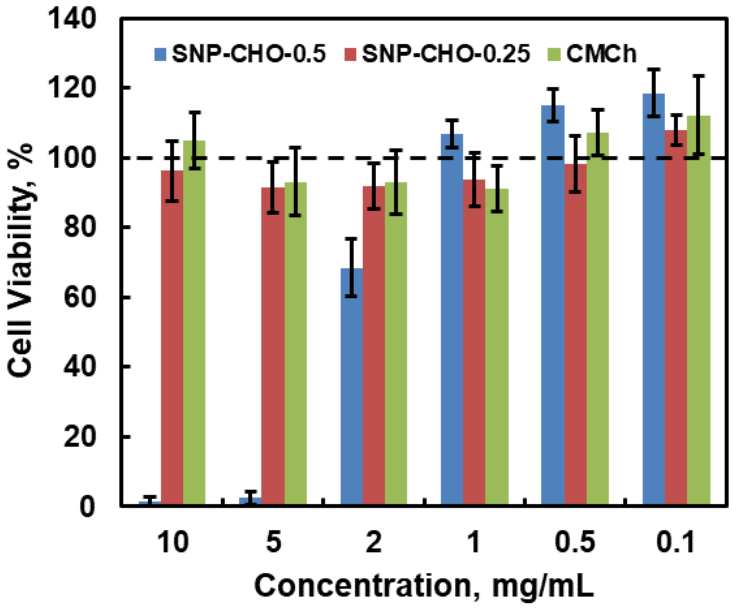

Figure 4.6: Cell viability resazurin assay for SNO-CHO-0.25 (red), SNP-CHO-0.5 (blue), and CMCh (green) with SH-SY5Y neuroblastoma cells.

4.3.4 *In Vitro* PAOPA Stability

To assess the stability of PAOPA loaded inside the hydrogels, in vitro stability experiments were conducted. SNP-CHO can form Schiff bases with the primary amine in PAOPA (Scheme 1), suggesting potential benefits for using hydrogels containing SNP-CHO for both stabilizing PAOPA in storage and prolonging its release. HPLC characterization of PAOPA over a 7-day storage period indicated that with the retention time of the drug (corresponding to its chemical stability) showed only slight shifts when hydrogels were prepared with either SNP-CHO-0.5 or SNP-CHO-0.25 but significantly shifted when PAOPA was dissolved directly in aCSF solution (**Supplementary Information, Figure S4.5**). This result suggests that Schiff base formation between SNP-CHO and PAOPA helps to stabilize the peptide drug against oxidative degradation, thus offering potential to improve the bioavailability of PAOPA in vivo.

4.3.5 Nebulization/Aerosolization Testing

Based on the results presented, the 4 wt% CMCh/35 wt% SNP-CHO-0.25 and 2 wt% CMCh/35 wt% SNP-CHO-0.25 hydrogels were selected for in vivo studies given that they facilitate the highest possible loading of SNPs (beneficial for PAOPA loading, stabilization, and in vivo transport), offer suitable gelation times for intranasal delivery, and exhibit no significant cytotoxicity of either component at any relevant concentration. To confirm the ease of spray-based administration of the selected optimal formulations for intranasal delivery, the potential of the formulations to be nebulized was assessed using an intranasal mucosal atomization device. **Figure 4.7 (a,b)** shows the average spray areas achieved as a function of the spray distance for the two lead hydrogel formulations to a vertically-mounted paper substrate, with the maximum tested 15 cm spray distance corresponding to the maximum typical distance between the human nostril and nasopharynx [461].

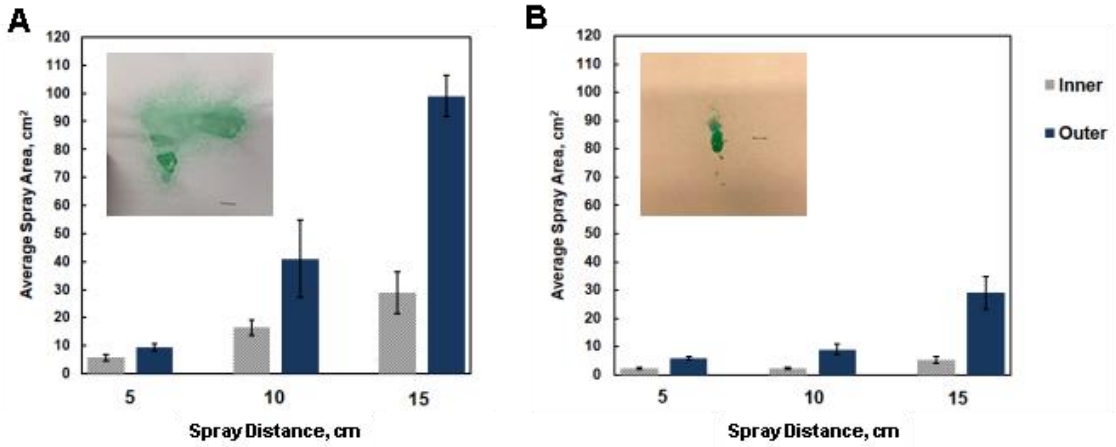

Figure 4.7 (a,b): Spray pattern of a nebulized hydrogel at a various spray distances for (A) 2 wt% CMCh/35 wt% SNO-SNP-0.25 and (B) 4 wt% CMCh/35 wt% SNP-CHO-0.25, comparing the inner (hatched bar) area corresponding to the focused spray area in which most droplets are deposited and the outer (solid) spray area corresponding to the maximum diameter impacted by the atomization. Inset pictures represent characteristic images of spray patterns from the 15 cm distance best modeling the human nasal cavity (food coloring is added for visualization).

In both cases, an inner (thicker) and outer (thinner) layer was observed, with the former representing the focus of the spray and the latter representing the total impacted surface following spray. At a spray distance of 5 cm, the inner and outer profiles were relatively close, covering 6-10 cm^2; these areas diverged at larger distances, with inner areas of ~30 cm^2 and outer areas of up to ~100 cm2 observed at a 15 cm spray distance for 2 wt% CMC/35 wt% SNP-CHO-0.25 (**Fig. 4.7A**). These areas are consistent with the surface area of the human intranasal cavity (~80-160 cm^2) [455,456,461], suggesting the potential for effective spray-based delivery of this formulation. The higher viscosity of the 4 wt% CMCh/35 wt% SNP-CHO-0.25 formulation resulted in smaller overall spray distances and less uniform nebulization (**Fig. 4.7B**), although the formulation could still be delivered via the nebulizer.

4.3.6 *In Vivo* Behavioural Studies

Schizophrenia-like behavioral abnormalities were induced in Sprague-Dawley rats via IP injection of MK-801, which has been demonstrated to induce several positive and negative symptoms of schizophrenia such as increased locomotor activity, social withdrawal, and disrupted cognitive functioning including deficits in attentional set-shifting [464–466]. Social interaction withdrawal was specifically chosen as the tracking variable given that it can be quantitatively measured by video tracking [467]. Given that there are no previous reports of IN delivery of PAOPA, the solution-based IN dose required to effectively alleviate MK-801-induced schizophrenic-like symptoms was first assessed to determine optimal dosing. Animals were dosed IN with 0.1, 0.25, 0.5, and 1 mg/kg PAOPA and tested for total social interaction time, the results of which are shown

in **Supporting Information Table S4.1**. Dosing 0.1 mg/kg PAOPA does not significantly increase social interaction time versus the aCSF-only IN administration; however, substantial increases in social interaction time were achieved with PAOPA doses as low as 0.25 mg/kg. Further increasing the dose to 1 mg/kg PAOPA (the concentration administered to observe drug efficacy via the IP route), a substantial decrease in total interaction time far below the aCSF control was observed. We hypothesize that the higher efficacy of IN versus IP delivery of PAOPA results over-dosing at the 1 mg/kg concentration that subsequently leads to PAOPA receptor internalization, ultimately intensifying rather than alleviating schizophrenia-like symptoms. On this basis, 0.5 mg/kg was used as the PAOPA loading for the gel formulations to ensure that over-dosing is avoided while controlled release of physiologically-relevant drug doses was maintained for as long as possible.

PAOPA-loaded hydrogels with appropriate controls were then administered IN, with changes in total social interaction time for various treatment groups shown in **Figure 4.8 (a-d)**. In the absence of MK-801 (panel A), groups treated with PAOPA only (0.5 mg/kg) or unloaded hydrogel formulations (2 wt% CMCh/35 wt% SNP-CHO-0.25 or 4 wt% CMCh/35 wt% SNP-CHO-0.25) showed neither increased nor decreased total interaction times relative to the negative control rat that received no treatment. The PAOPA result is consistent with the literature, in which IP delivery of PAOPA even at a higher concentration (1 mg/kg) did not affect social interaction time [431]. When MK-801 was administered to induce schizophrenia-like symptoms (panel B), injection with aCSF only resulted in significant decreases in total interaction times ($F(5,19) = 38.85$, $p<0.00001$; post hoc, $^*p<0.01$). Administration of PAOPA (0.5 mg/kg) at an acute time point 30 minutes before MK-801 challenge demonstrated the expected attenuation of social interaction deficits when assessed 30 minutes post-MK-801 administration ($F(5,19) = 38.85$, $p<0.00001$; post hoc, $^{**}p<0.05$); however, when groups treated with PAOPA alone were challenged with MK-801 24 hours later without further drug administration, no residual benefit of PAOPA was observed ($F(5,19) = 38.85$, $p<0.00001$; post hoc, $^*p<0.01$ comparing 1 hr and 24 hr PAOPA-only treatments). This result indicates rapid clearance of free PAOPA and would mandate repeated (multiple times daily) administrations of PAOPA to achieve any continuous therapeutic benefit. In contrast, when the same 0.5 mg/kg dose of PAOPA was delivered in the 2 wt% CMCh/35 wt% SNP-CHO-0.25 hydrogel (panel C), full symptom alleviation relative to the negative controls (panel A) was observed for as long as 3 days post-administration, with significant decreases in social interaction time not observed until the 5 day time point (although some benefit was still retained even then in comparison to untreated controls) ($F(6,22) = 27.39$, $p<0.00001$; post hoc, $^*p<0.01$). The 4 wt% CMCh/35 wt% SNP-CHO-0.25 hydrogel (panel D) exhibits similar positive effects relative to the positive aCSF control over the same 5-day period but only achieves comparable social interaction times to negative control results at the 24 hour time point, with an apparent induction time at shorter time points and a tailing off of drug efficacy at longer time points ($F(6,23) = 35.49$, $p<0.00001$; post hoc, $^*p<0.01$ relative to untreated controls). We postulate that the higher viscosity, longer degradation time (**Fig. 4.4**, corresponding to slower release of the SNP-

CHO carriers from the hydrogel film), and less diffuse spray area (**Fig. 4.7**, corresponding to a thicker deposited layer and/or increased probability of sloughing off with mucosal turnover) collectively result in less effective PAOPA release from the 4 wt% CMCh/35 wt% SNP-CHO-0.25 hydrogels, resulting in sub-clinical doses being released at both shorter and longer release times. After 7 days (168 hours), no significant benefit is observed with either hydrogel, indicating full degradation of gels and/or depletion of PAOPA to a sub-clinical dose.

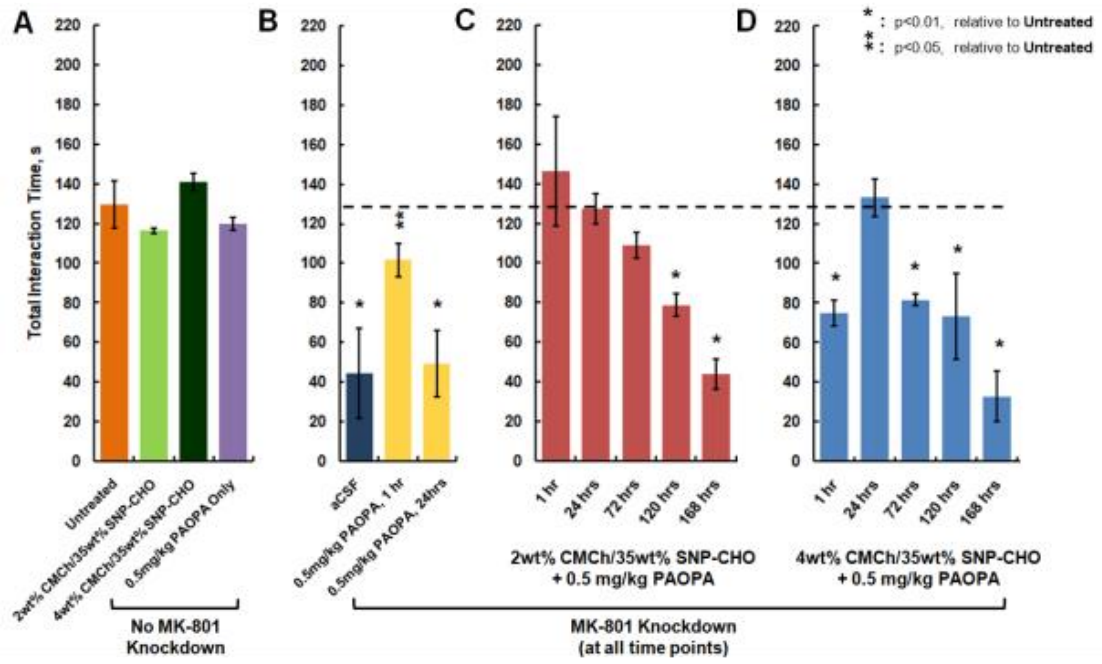

Figure 4.8 (a-d): Effect of CMCh/SNP-CHO hydrogels with or without 0.5 mg/kg PAOPA loading on reversing MK-801-induced social interaction schizophrenia symptoms in Sprague-Dawley rats. (A) Controls of untreated rats, 2 wt% CMCh/35 wt% SNP-CHO hydrogels alone, 4 wt% CMCh/35 wt% SNP-CHO hydrogels alone, and 0.5 mg/kg PAOPA without MK-801 knockdown indicate the hydrogels or drug alone do not alter rat behavior; (B) 0.5 mg/kg PAOPA in solution can reverse MK-801-induced schizophrenia social withdrawal (relative to the aCSF series) for short times but has no benefit after 24 hours; (C) 2 wt% CMCh/35 wt% SNP-CHO-0.25 hydrogel loaded with 0.5 mg/kg PAOPA can fully reverse MK-801-induced social deficits for at least 3 days, with positive effects persisting over 5 days; (D) 4 wt% CMCh/35 wt% SNP-CHO-0.25 hydrogel loaded with 0.5 mg/kg PAOPA can sustain some positive effects of PAOPA for up to 5 days but does not fully recover the control interaction times and has an induction time at shorter testing intervals. n=4 for all test groups; statistical comparisons at different confidence intervals are shown by different symbols on the graphs. The dashed line in B-D represents the average social interaction time from A in the absence of MK-801 model induction for easier comparison of social interaction recovery upon PAOPA treatment.

4.3.7 *In Vivo* Biodistribution Studies

To correlate the observed efficacy in prolonged PAOPA delivery to the brain to the distribution of the SNP-CHO-0.25 nanoparticles hypothesized to be the primary carriers of PAOPA, a biodistribution study was performed using AlexaFluor 647-labeled SNPs. The accumulation of SNP-derived fluorescence in major clearance organs, the nose, and the brain (separated assessed between the cerebellum, the olfactory bulb, and the remainder of the brain) at 1 day and 3 day observation times post-IN administration is shown in **Figure 4.9 (a,b)**. Note that the auto-fluorescence of the untreated tissues (**Supplementary Information Figure S4.6**) was subtracted from each of the F-SNP-CHO-0.25 results to ensure the fluorescence measured is attributable to the nanoparticles present rather than differential autofluorescence values between different tissues.

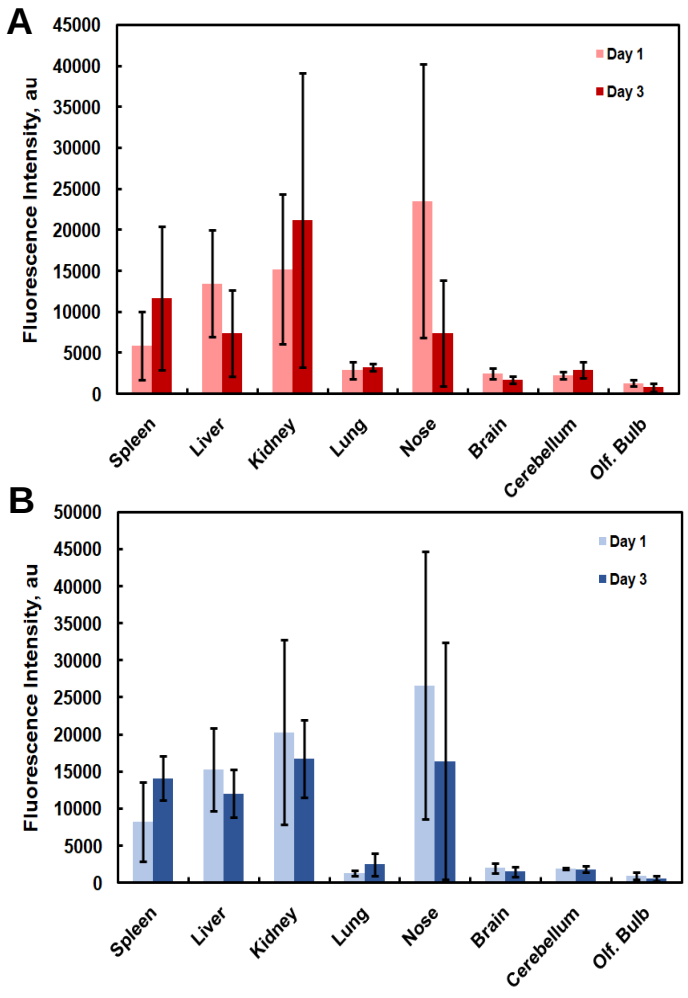

Figure 4.9 (A, B): Biodistribution of SNP-CHO-0.25 nanoparticles 1 day (light series) or 3 days (dark series) following IN administration for (A) 2 wt% CMCh/35 wt% SNP-CHO-0.25 hydrogels and (B) 4 wt% CMCh/35 wt% SNP-CHO-0.25 hydrogels

On day 1, for both the 2 wt% and 4 wt% CMCh/35 wt% SNP-CHO-0.25 gels, the largest fluorescence intensity was detected in the nose with significant but lower fractions detected in typical nanoparticle clearance organs (e.g. spleen, liver, and kidney) and very low fractions present in the lung. This result suggests relatively good retention of the administered formulation in the nasal cavity, accounting for the effective longer-term behavioral benefits observed with the gel delivery vehicles. Note that the larger error bars associated with the nose readings are associated with the very small volume of the nasal cavity collected, resulting in more animal-to-animal variation in tissue collection. While fluorescence in the different collected brain regions was lower than that observed in clearance organs, significant signals related to the presence of the SNPs throughout the brain are measured, clearly demonstrating effective transport of SNPs to the brain. On day 3, similar overall patterns in biodistribution were observed, with apparently lower SNP concentrations in the nose (although not statistically significant given the large error bars), similar SNP concentrations in most brain regions, and slightly higher concentrations in the major clearance organs. Thus, in situ gelling CMCh/SNP-CHO hydrogels are demonstrated to be both effectively retained in the nose over several days and enable the transport of SNPs into the brain, as desired for effective antipsychotic delivery.

Overall, this work demonstrates the benefits of using a hydrolytically-labile in situ-gelling hydrogel formulation based on nanoparticle building blocks for delivering PAOPA to the brain. We expect that similar benefits would be observed with other antipsychotic peptides, given that the same Schiff base interactions could be achieved between any amine-terminated peptide and the SNP-CHO building blocks. In principle, other nanoparticles could also be physically entrapped inside the in situ-forming hydrogel to enable the delivery of more conventional antipsychotic drugs loaded into hydrophobic nanocarriers; co-delivery of precise doses of combination therapies could be envisioned in the same manner by simply mixing different nanoparticle delivery vehicles. The components of the delivery vehicle are all carbohydrates with an established record of safe use in vivo [446,468,469], while the sprayability of the formulation (**Fig. 4.7**) enables the hydrogels to be administered clinically using existing delivery technologies. The longer-term efficacy of the hydrogel formulations (>3 days) relative to drug-only administrations (a few hours) also reduces the likelihood of patient non-compliance with schizophrenia therapy, a particular challenge with effectively managing schizophrenia symptoms.

4.4 Conclusions

Simple co-spraying of oxidized starch nanoparticles (SNP-CHO) and carboxymethyl chitosan (CMCh) enables the formation of hydrolytically-degradable nanocomposite network hydrogels that facilitate intranasal mucosal adherence and controlled release of an antipsychotic peptide (PAOPA). CMCh/SNP-CHO hydrogels loaded with 0.5 mg/kg PAOPA can enable full alleviation of induced schizophrenia symptoms in rats for up to 3 days (72 h), while biodistribution analysis indicated the presence of significant

concentrations of SNPs in the brain over the same time period. We fully expect that similar benefits could be achieved with other emerging antipsychotic peptides, offering the potential to enable effective and minimally-invasive schizophrenia therapy while significantly reducing the burden of repeated administration that currently limits patient adherence to schizophrenia treatment regimens.

Appendix 4S: Supporting Information to Chapter 4

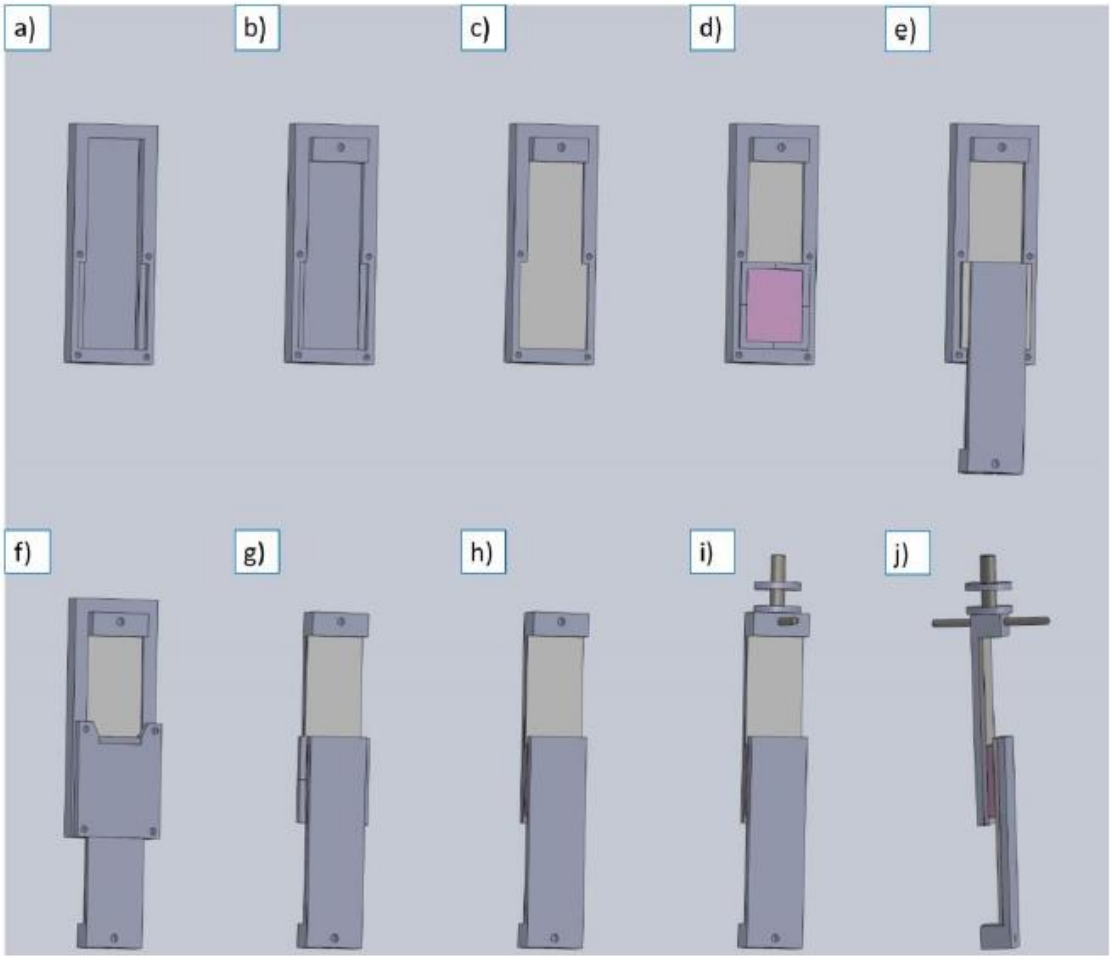

Figure S4.1 (a-j): Sample holder design kit consisting of: a) mold backplate, b) backplate with support for mucin-coated PDMS membranes, c) assembly in (b) with PDMS wafers inserted with tape, d) insertion of mold walls and polymer precursors solution (pink), e) second PDMS wafer added, f) top plate added to secure the second PDMS wafer (assembly screwed together until gelation occurs), g) removal of the back plate and top plate post-gelation, h) removal of mold walls post-gelation, i) insertion of mounting screw on top of assembly (same for bottom), and j) mounting of the test assembly to the instrument.

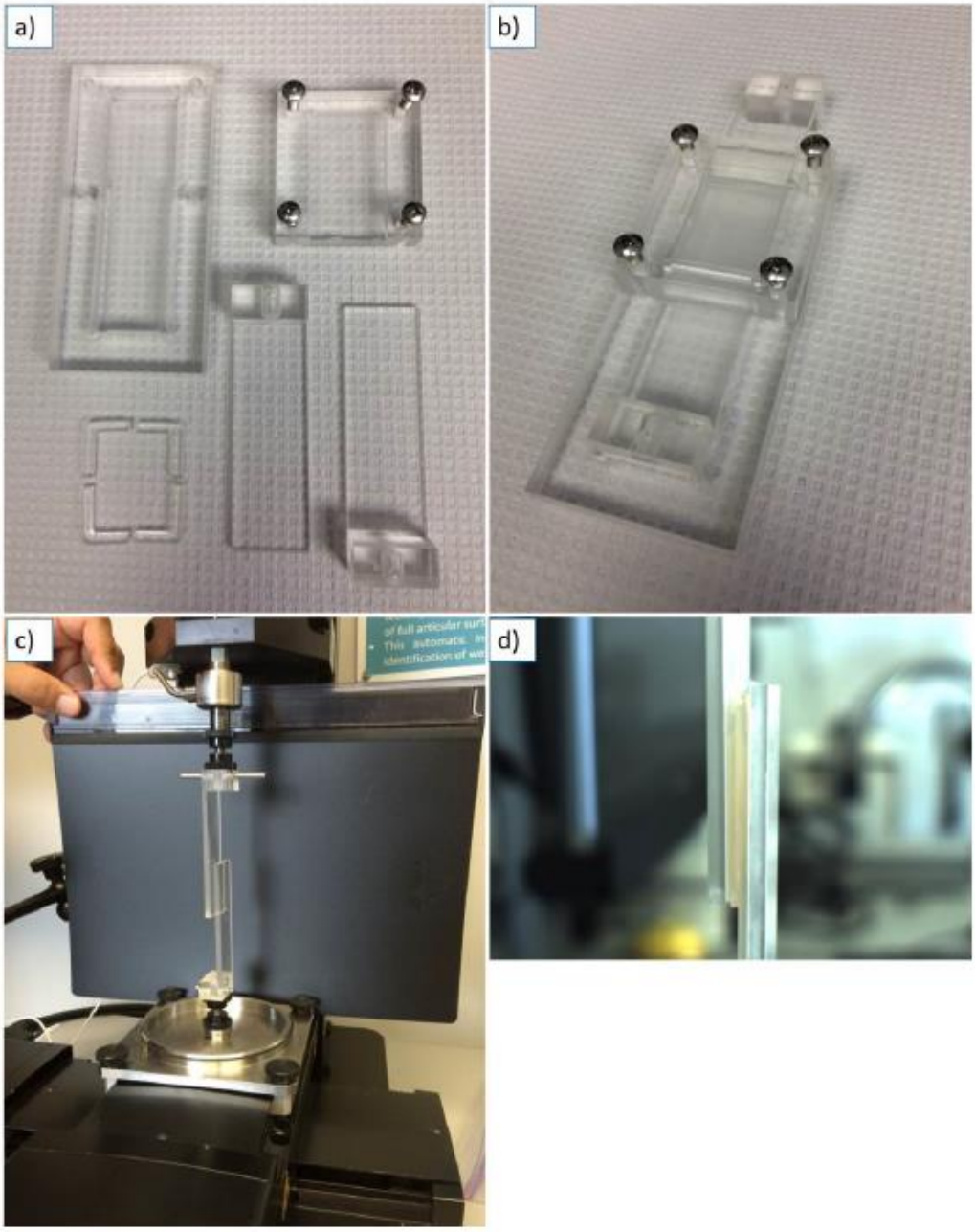

Figure S4.2 (a-d): The individual components (a) and assembled acrylic sample holder (b) to gel a sample *in situ* for mucoadhesion testing. The device is then removed and the mucin-modified silicone sheets connected by the gel are mounted onto the MACH-1 micromechanical tester to perform the lap shear test (c, d).

a

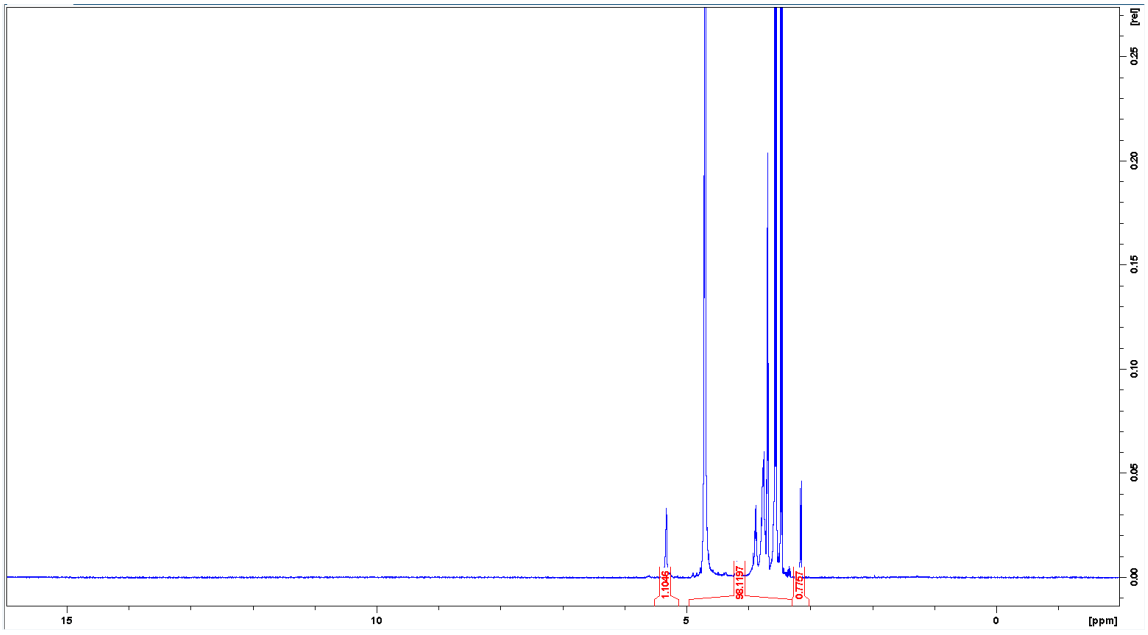
[rel]
0.25
0.20
0.15
0.10
0.05
0.00
1.1046
86.1197
0.7767
15
10
5
0
[ppm]

b

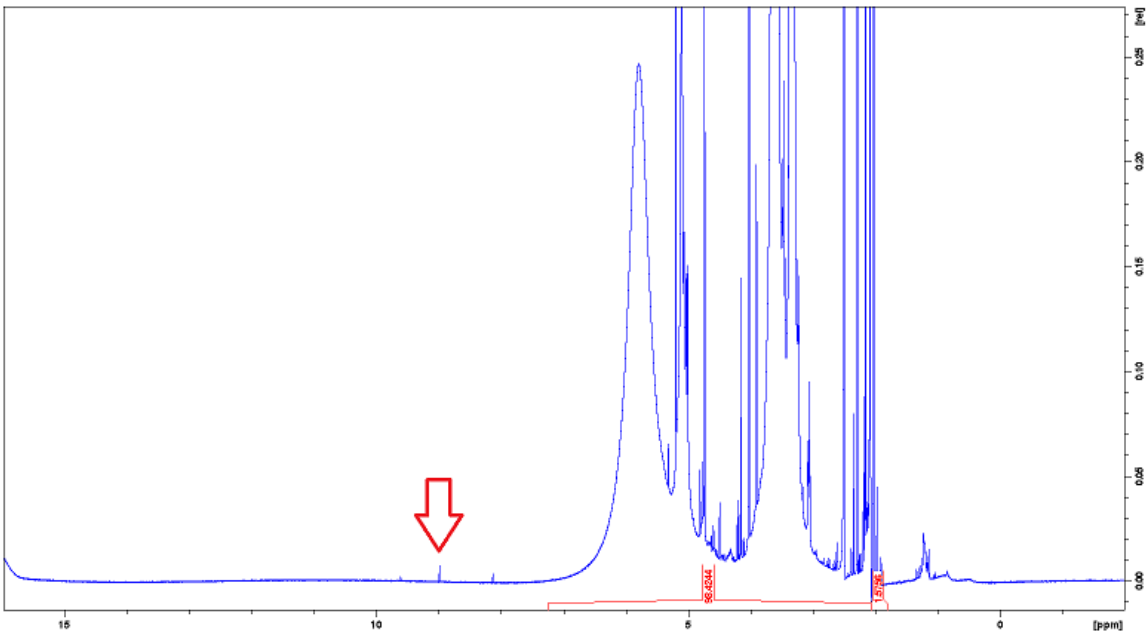
[rel]
0.25
0.20
0.15
0.10
0.05
0.00
86.4244
15
10
5
0
[ppm]

c

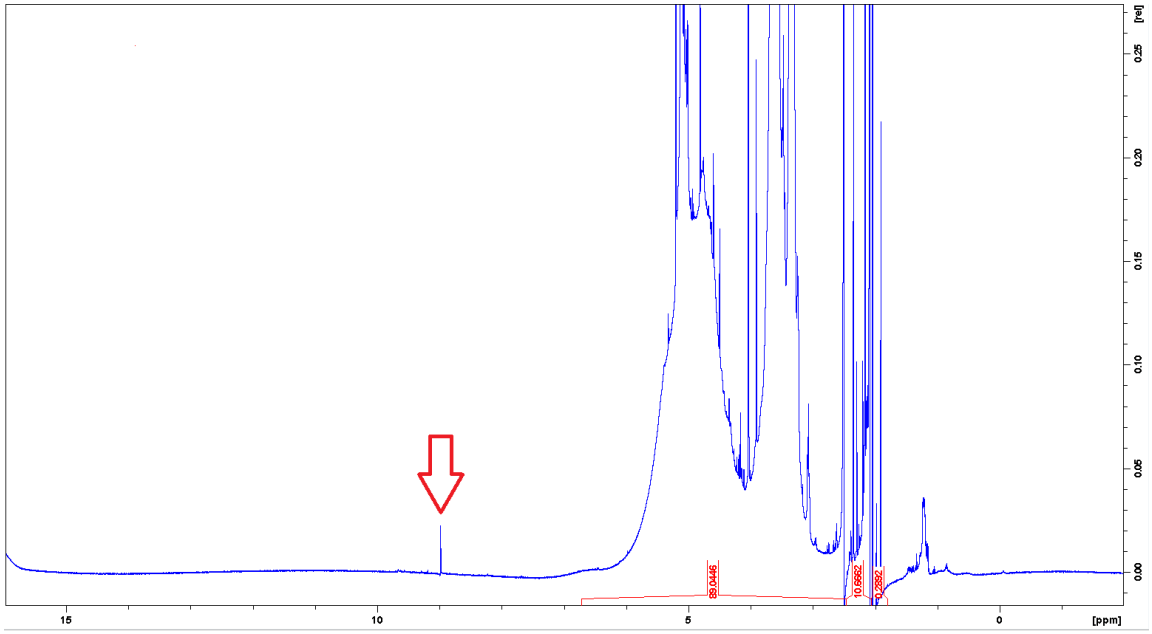

Figure S4.3 (a-c): ^{1}H-NMR data for (a) a raw, unmodified SNP, (b) SNP-CHO-0.25, and (c) SNP-CHO-0.5 showing the confirmation of the aldehyde functionality on the SNP surface. By comparing a native, unmodified SNP (a) to SNP-CHO (b, c), a clear peak at 9-9.1 ppm is observed due to the imparted functionality that is not normally present and increases at higher DS values, as indicated by the red arrows.

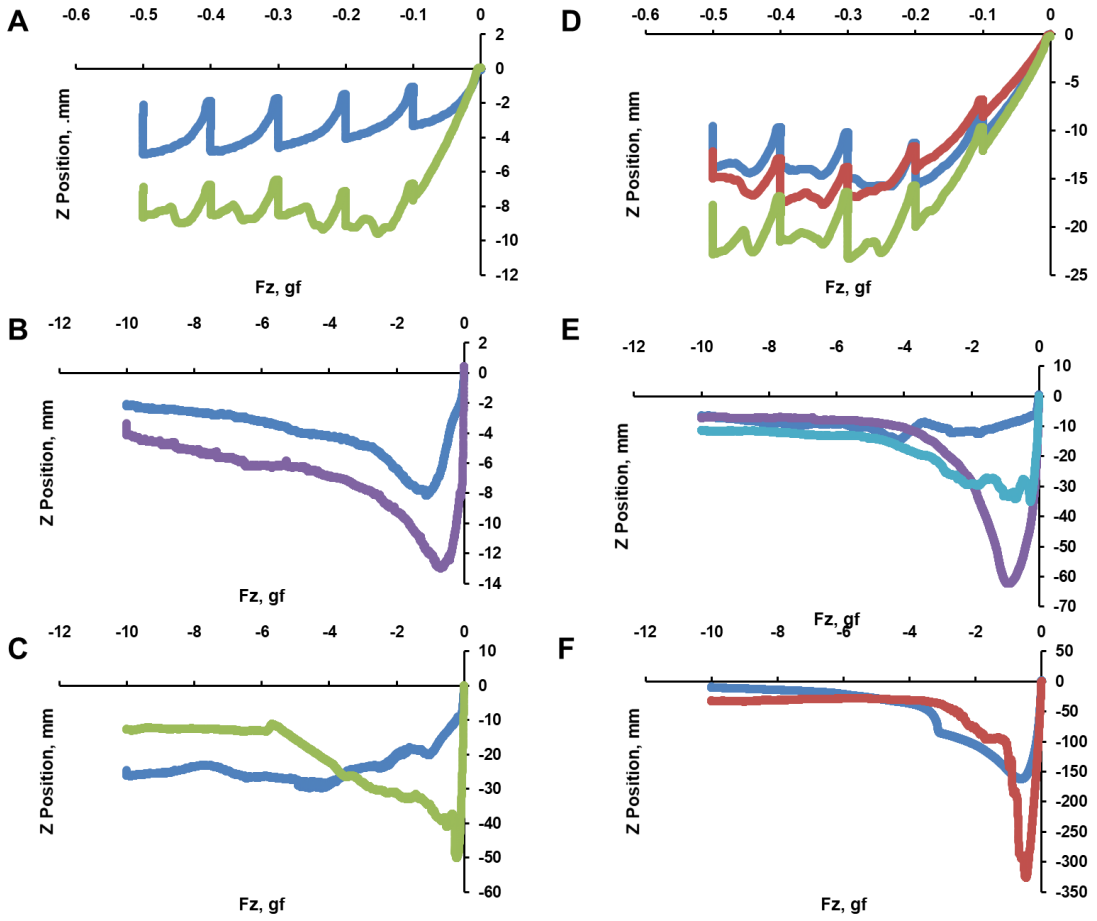

Figure S4.4 (a-f): Raw mucoadhesion data from small-amplitude stress relaxation experiments; the area under each curve was used to calculate the work of adhesion. Panels (a-c) represent the data for the 35 wt% SNP-CHO-0.25 mixed with 2 wt% (a), 4 wt% (b), and 6 wt% (c) CMCh. Panels (d-f) represent the data for the 35 wt% SNP-CHO-0.5 mixed with 2 wt% (d), 4 wt% (e), and 6 wt% (f) CMCh. For each formulation, selected replicates are shown to show the reproducibility of the mucoadhesion experiments. Note that the y-axis changes for each sample since the total distance moved will vary depending on the stress relaxation properties of each gel.

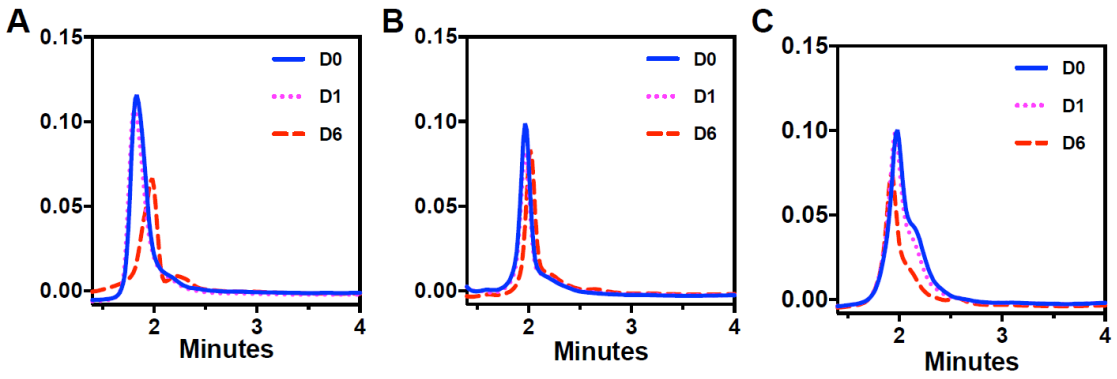

Figure S4.5 (a-c): HPLC chromatograms of free PAOPA prepared fresh (D0), after 1 day (D1), and after 6 days (D6) when loaded in (A) free solution in aCSF, (B) 2 wt% CMCh/35 wt% SNP-CHO-0.25 and (C) 2 wt% CMCh/35 wt% SNP-CHO-0.5 hydrogels.

Table S4.1: Total social interaction time following MK-801 knockdown of rats treated with various IN doses of PAOPA dissolved in aCSF

Experimental Group	Total Interaction Time (s)
aCSF only	44 ± 20
0.1 mg/kg PAOPA	60 ± 1
0.25 mg/kg PAOPA	87 ± 8
0.5 mg/kg PAOPA	90 ± 6
1 mg/kg PAOPA	0

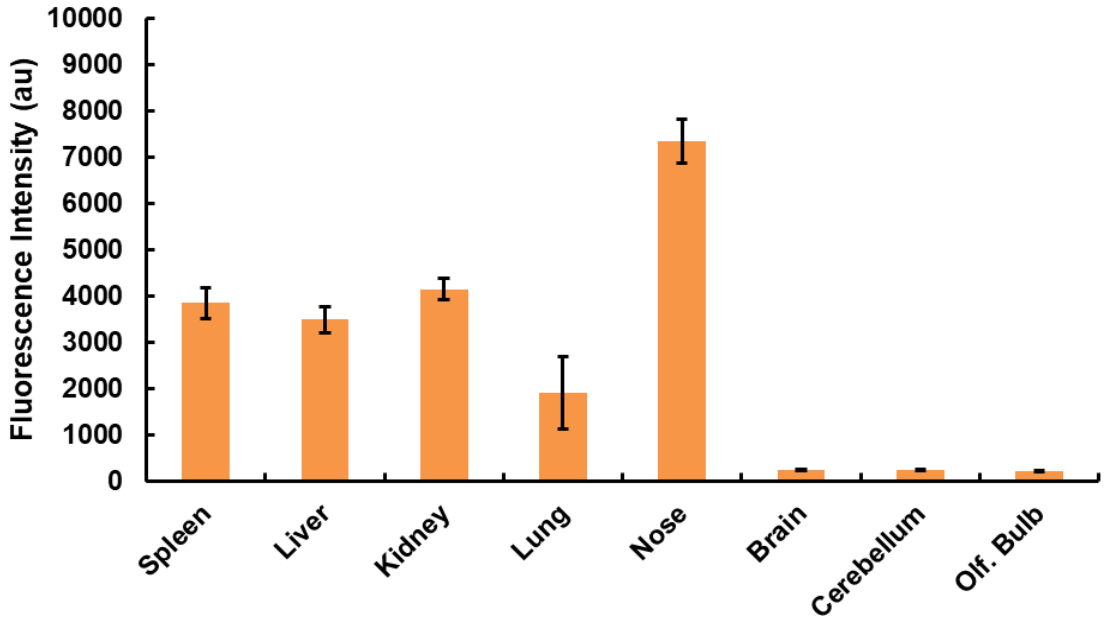

Figure S4.6: Baseline auto-fluorescence of target tissues for the *in vivo* biodistribution study. These fluorescence intensities were subtracted from the fluorescence intensities measured with F-SNP-CHO nanoparticles to produce the biodistribution data shown in **Fig. 4.9** in the main manuscript.

Chapter 5: Hydrophobized Starch Nanoparticles (SNPs) Engineered for Foliar Plant Delivery

Preface

This chapter describes a strategy to create nanoscale vehicles for the delivery of agricultural agents to plants. Building on previous chapters describing the chemical modification of SNPs to allow them to form stable crosslinks with SNPs containing the same functional group (**Chapter 2 and 3**) or with a chemically reactive reaction on another neighboring moiety (**Chapter 4**) to form stable nanoparticle network hydrogels (NNH), in this chapter the surface hydroxyl groups of the SNPs are replaced with hydrophobic moieties (octenyl succinic acid, OSAn and succinic anhydride, SAn) to make the surface of the NP more hydrophobic. Such modifications promote physical crosslinking (i.e., hydrophobic interactions) between the SNPs while enhancing the adhesion of the SNPs to stick to the naturally waxy leaves of *Arabsidopsis*, pumpkin, and watermelon plants. We intend to submit this to a peer-reviewed journal (*ACS Sustainable Chemistry and Engineering*) in winter 2022 after more targeted experiments are performed by Dr. Madeline Simpson during her post-doctoral research in the Hoare lab.

Abstract

Agrochemicals such as herbicides, pesticides, fungicides, growth factors, or antimicrobials are most commonly delivered through the plant's leaves (foliar) or through the roots. While both routes have inherent limitations, the foliar delivery method is the most favourable from an industrial standpoint given that it allows for efficient large-scale application over large areas. However, with the foliar route, key challenges around the effects of animals/pests, rain, poor ab/adsorption due to the leaf's waxy cuticular protective barriers, and the variable size constraints associated with plant transport must be addressed to enable effective delivery. To address this challenge, we have modified SNPs with hydrophobic groups using octenyl succinic acid (OSAn) and succinic anhydride (SAn), aiming to enhance the retention of the SNPs on a leaf's surface as well as the ability of the SNPs to cross the waxy barrier and enter the cells. Hydrophobization increased the contact angle of a sprayed watermelon and pumpkin leaves from less than 60˚ (unmodified) to upwards of 80˚ when modified (DS 0.25), while confocal fluorescence microscopy confirmed that the hydrophobized SNPs can both adhere to the leaf surface as well as penetrate into the leaves when sprayed due to their small size (25-50 nm), offering the potential to translocate within plants due to the small size and net neural surface charge of SNPs. To demonstrate the potential of the highly mobile SNPs for payload delivery, SNPs were passively loaded with humic acid, achieving encapsulation efficiencies of >55% for all formulations and sustained release for >200 hours under simulated *in vitro* conditions. As such, the use of hydrophobized SNPs has significant potential benefits for treating plant diseases that require the transport of an agrochemical inside the leaf.

5.1 Introduction

There is an increasing economic, environmental, and human health need to improve current agricultural practices to enhance the safety, bioavailability, and ultimately efficacy of pesticides, fungicides, herbicides, and plant growth promoters. The use of "green" chemistries has attracted particular interest in this regard [37,470], including the use of carbohydrate polymers such as starch for the design of bio-based drug/agrichemical carrier systems [471–473], soil conditioner/moisturizers [474,475], and other related products [476,477]. More recently, hydrogel nanotechnologies have been proposed not only for their favourable physiochemical properties but also for their ability to allow engineers to facilitate new targeting strategies or delivery approaches [223].

In this context, the role of agricultural delivery vehicles to promote the transport of plant bioactives into plant tissues is of particular interest. A classical strategy to penetrate plant tissues is through the root system via capillary action of the root hairs and projections through the soil rhizome [478]. However, soil-based delivery subjects formulations to multiple degradation stimuli including hydration, soil-based microbes, and other environmental factors like heat that can require more frequent re-application cycles [479]. Delivery through the leaves while they are transpiring (foliar route) [480] is also possible but also introduces additional challenges related to animals, rain effects [481], and poor ab/adsorption due to the waxy cuticular layer covering the apical sections of most leaves that act as a protective barrier against the entry of contaminants [482], with particularly notable size constraints observed for transport on both the cuticle and stromal sides of leaves [483,484]. This latter factor of poor ab/adsorption is particularly limiting when spray-based aerosol formulations are used [484]. Such formulations enable inexpensive administration of agrochemicals over large areas in a relatively short period of time [485]; however, if a formulation is poorly retained by the leaves, potential issues with spray-based administrations including downstream human/animal exposure or the loss of agrochemical due to water evaporation, volatilization, or animal interactions become even more problematic [483,484].

The emerging use of nanotechnology in agriculture has in recent years facilitated re-engineering of the way in which agrochemicals interact with natural photosynthetic processes of plants. Nanoparticles (NPs) of various types including nano-capsules, micelles, liposomes, nano-emulsions, and dendrimers [486] have been explored as delivery vehicles for plant bioactives. Soft nanoparticles offer particular advantages in terms of their potential to exploit the viscoelastic properties of such materials to change their conformation (as demonstrated in other processes [487,488]) and improve their potential to pass through small foliar and/or root-associated pores, significantly enhancing their potential to deliver bioactive agents into plants [489] and subsequently transport across cell-cell junctions or cellular/nuclear membranes inside the plant tissue [450]. Such transport properties are primarily dependent on the nanoparticle size and/or surface chemistry, although the potential of soft nanomaterials to deform to pass through smaller pores can also promote transport. A summary of these general size exclusion requirements for plant transport is shown in **Figure 5.1** [490].

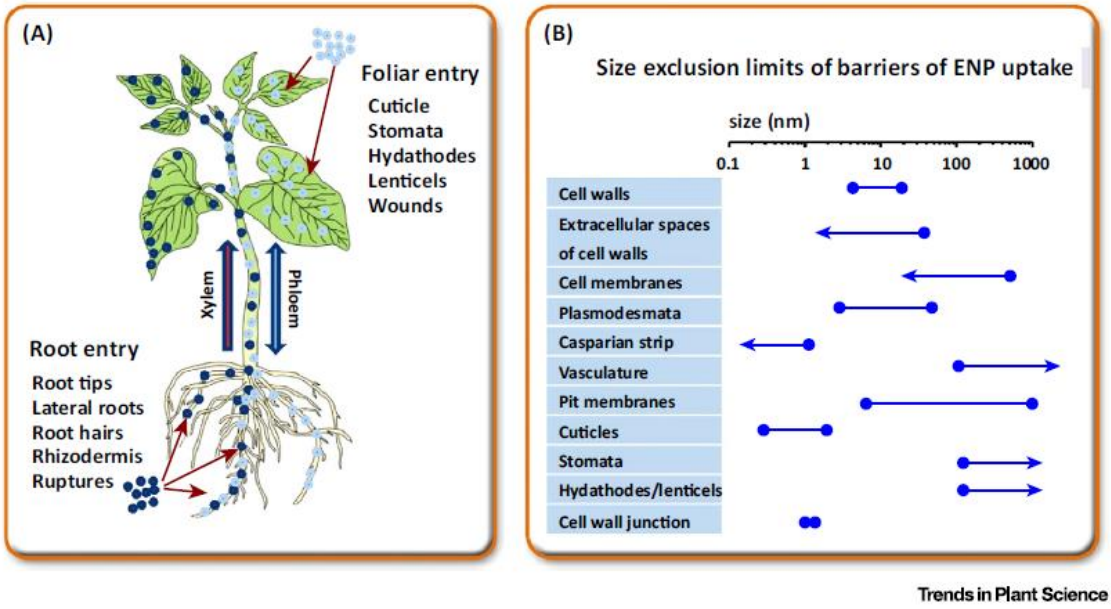

Figure 5.1: A summary of the foliar and root entry routes for plant-based agricultural delivery mechanisms (a) and a summary of the reported size ranges for particle size exclusion limits for internal barriers to nanoparticle translocation (b). Adapted from Wang et al (2016) [490].

An additional factor important for the uptake and more importantly translocation of nanoscale agrochemical delivery systems is the overall surface charge of the material. In general, the surface of most plant leaves bear a net negative charge [491], suggesting that cationic nanoparticles should result in enhanced surface retention following spray-based administration [492]; however, the anionic cell membranes within the plant tissue can also bind to cationic nanoparticles and significantly reduce their mobility [481] while enhancing off-site binding [493], depending on the plant type. Additionally, most soils are anionic due to their high concentrations of minerals and ions and can thus exhibit cationic exchange properties [494,495]. The effects of surface charge on key processes in nanoparticle-assisted agricultural delivery such as translocation, transformation, uptake, and phytotoxicity have been extensively studied [496,497]. Even though most prior studies describe the transport of hard metallic NPs rather than "soft" NPs [498], small surface-neutral nanoparticles appear to be most effective for mediating sufficient ab/adsorption and subsequent transport into leaves.

The starch nanoparticles described elsewhere in this thesis, produced on a commodity industry scale via a reactive extrusion process, are hypothesized to be small enough (25-50 nm) to pass through the leaf stomata (foliar) or root capillaries (soil) to penetrate into the plant as well internally throughout the plant through cell membranes and the extracellular spaces of cell walls. Additionally, the soft deformable gel-like nature of the SNPs coupled with their net neutral charge in water both offer the potential to improve

nanoparticle transport across biological barriers, while the use of starch as the material is highly favourable in terms of preserving plant and environmental compatibility of the delivery vehicle. However, one potential drawback of the use of native SNPs for plant delivery is their highly hydrophilic (-OH-rich) interface, resulting in potentially poor ab/adsorption to leaves following spray-based administration. To address this potential drawback, herein we hydrophobize the SNPs using two anhydrides with varying hydrocarbon chain lengths: succinic anhydride (SAn) [499] and octenyl succinic anhydride (OSAn) [447,500,501], the latter of which is most noted for its use in food applications [502] (**Supporting Information Figure S5.1**). Other hydrophobically modified starch nanoparticle systems created by grafting pyrene [503–505], imidazole [506], or cholesteryl groups [116] have been reported ; however, herein, we elected to use industrially relevant chemistry that is amenable with the reactive co-extrusion process used to create these SNPs to promote the potential scale-up of useful vehicle designs.

We hypothesize that these hydrophobized SNPs will (1) be able to penetrate into the leaves of plants when sprayed foliarly (size/charge effect); (2) be able to stick to the leaf surface following spray administration (hydrophobicity effect); (3) will translocate within the plants (size/charge effect); and (4) enable controlled release of a loaded cargo herein demonstrated using humic acid, a key soil component that aids in regulating internal plant cell metabolism and related photo-transformation processes [507] and boosting growth patterns [508] (hydrophobicity/internal particle morphology effect). Together, these properties are expected to enable effective transport of a targeted agrochemical into a plant and provide release of that agrochemical over a prolonged period to reduce the required frequency of bioactive agent administrations and thus the burden and cost of such administration to farmers.

5.2 Experimental Section

5.2.1 Materials

Commercial grade starch nanoparticles (SNP) and cold water soluble starch controls were donated by *EcoSynthetix Inc*. Succinic anhydride (SAn), octenyl succinic anhydride (OSAn), sodium carbonate, fluorescein isothiocyanate isomer I (FITC), dimethyl sulfoxide (DMSO, reagent grade), and humic acid (HA, MW 2000 – 5 million g/mol) were all obtained from Sigma Aldrich (Oakville, ON) and used as received. The watermelon and pumpkin seeds were acquired from McKenzie Seeds (Brandon, MB). The *Arabidopsis* plants for testing SNP penetration via confocal microscopy was generously donated by Dr. Wenzi Ckurshumova. Milli-Q water (MQW) was used for all *in vitro* experiments. The 4” plastic pots and Promix BX soil were both graciously provided by the McMaster University Department of Biology’s Greenhouse.

5.2.2 Functionalization of SNPs with anhydrides

To create a library of hydrophobized SNPs, succinic anhydride (SAn) and octenyl succinic anhydride (OSAn) were grafted to SNPs at targeted 0.10 and 0.25 degrees of substitution (DS) by modifying a previously reported protocol for SNP methacrylation [285] (see **Supporting Information Figure S5.2**). For each modification, 50 g of dry

starch (54.3 g of the SNP stock, accounting for 8-10% hygroscopic water absorption as measured using microwave-assisted gravimetry at ambient lab conditions) was dissolved in a 600 mL of a 50:50 MQW/DMSO mixture and manually agitated with a magnetic stirrer (500-1000 rpm) in a 1 L round bottom flask to ensure SNP dispersion. Following, 0.7 g sodium carbonate was added to create an alkaline environment, after which a pre-determined amount of OSAn or SAn was added to the flask. The amount of OSAn or SAn added depended on the degree of anhydride grafting targeted based on the code X-Y where X is the anhydride used and Y is the targeted degree of substitution (SAn-0.10 - 3.09 g SAn, 54.31 g SNP; SAn-0.25 - 7.72 g SAn, 54.29 g SNP; OSAn-0.10 - 6.49 g OSAn, 54.29 g SNP; and OSAn-0.25 - 16.22 g OSAn, 54.29 g SNP). The reaction vessel was allowed to stir at room temperature, maintaining the pH in the range 10<pH<11 or 8<pH<9 (depending on the protocol used) throughout the reaction period via the addition of 1 M NaOH. The reaction was stopped when no further pH changes were observed, typically 20-30 hours following anhydride addition depending on the targeted DS. The crude product was then neutralized using 1 M HCl, dialyzed (6 × 6 h cycles, 3.5 kDa MWCO, Spectrapor), and lyophilized for storage.

5.2.3 Physicochemical Characterization of Hydrophobized SNPs

5.2.3.1 Degree of substitution (DS)

The experimental degree of substitution of the anhydride on SNPs was assessed via a base-into-acid conductometric titration (Mandel Model PC-1104-00 titrator with a Model 4510 conductivity meter), exploiting the fact that one carboxylic acid group is generated for every anhydride grafted to the SNP (**Supporting Information Figure S5.2**). A mass of 50 mg of modified SNP was dispersed in a 50 mL solution of 3 mM KCl, the initial pH was lowered to ~2 using 1 M HCl, and the sample was titrated with 0.1 M NaOH. By comparing the moles of acid detected to the moles of the anhydrous glucose unit (AGU) added, the experimental degree of substitution can be calculated. See **Supporting Information Figure S5.3 (a-d)** for the raw data used for the calculations.

5.2.3.2 Particle size distribution and electrophoretic mobility

The particle size distribution of the SNPs was assessed before and after anhydride functionalization to assess whether the presence of the hydrophobic grafts altered the particle size or impacted SNP aggregation. A 1 w/w% suspension of each SNP in water was tested characterized using a Brookhaven Nano90Plus dynamic light scattering instrument. Each sample was placed in a 3510 Branson sonicating water bath on the lowest setting at room temperature (~22˚) for 5-10 minutes before analysis to ensure efficient SNP dissolution prior to measurement. A run consisted of ten individual measurements that are averaged, with two runs conducted for each sample/wt% combination. Intensity distributions were converted to number distributions using the refractive index of starch (1.34). To assess the electrophoretic mobility as a measurement of surface charge before and after chemical modification, a 1 wt% solution of SNPs was suspended in 5 mM NaCl (pH 7.1) and tested using the Nano90Plus instrument operating in phase analysis light scattering (PALS) mode.

5.2.3.3 Surface hydrophobicity

The imparted hydrophobicity resulting from the modification was confirmed using sessile drop contact angle measurements. Static contact angles were measured by the sessile drop method on glass microscope slides (Gold Line Microscope Slides, VWR). In a typical experiment, glass microscope sides were cleaned (Sparkleen detergent, Fisher Scientific), and a uniform section of watermelon and pumpkin plant leaves (cut with an Xacto blade into 1 mm x 1 mm sections) were adhered to the slide using double-sided tape. Each functionalized SNP formulation was sprayed (10 times of waxy side and 10 times on non-waxy side) at a concentration of 5 wt% in MQW onto the leaf surface (attached to the microscope slide) before being adhered to the microscope slide. The treated slides were washed three times with a deionized water spray to remove unbound nanoparticles. The water/air contact angle was determined by placing a water drop on the dry slides. Contact angle measurements were performed using a Krüss contact angle measuring instrument running Drop Shape Analysis (DSA) 1.80.0.2 software. Two batches of gels were tested, as outlined in **Supporting Information Figure S5.6.**

5.2.4 Synthesis of fluorescein-labeled SNPs (FITC-SNPs)

Native and hydrophobized starch nanoparticles were fluorescently tagged using an established protocol [369] by dissolving 50 mg of SNPs and 2 mg of FITC in a total volume of 100 mL of a sodium carbonate buffer (pH ~ 9.5) . The mixture was stirred at room temperature overnight, after which the SNPs were dialyzed (3.5-5 kDa MWCO) and lyophilized to form the final purified product. A calibration curve relating fluorescence to SNP concentration was collected by suspending the FITC-SNPs in PBS at a concentration of 2 mg/mL, generating a set of serial dilutions, and analyzing the fluorescence using a PerkinElmer 1420 Multilabel counter Victor3V plate reader (λ_{ex} = 485 nm, λ_{em} = 535 nm) (**Supporting Information Figure S5.4**).

5.2.5 Photodegradation of FITC-SNP

To assess the potential photobleaching/photodegradation of the FITC-SNPs due to ultraviolet (UV) irradiation in natural or simulated growing conditions [509,510], FITC-SNPs were dispersed in MQW at a concentration of 5 wt% and irradiated in 20 mL scintillation vials under natural greenhouse conditions or simulated sunlight (HELIOS® Daylight Uniform Source System, Labsphere) with an irradiance of 1000 mM/m^2 s to track photodegradation for up to 3 days, a time point anticipated to be much longer than the rate of evaporation or transpiration of either plant [511,512]. The samples were manually agitated each day to prevent sedimentation and aggregation. Changes in fluorescence intensity were tracked to determine the extent of photo-bleaching or degradation using a plate reader as described above (λ_{ex} = 485 nm, λ_{em} = 535 nm).

5.2.6 Loading and release of humic acid (HA)

To load humic acid into the SNP matrix, both passive diffusion and centrifugal loading were tested. For passive loading, the particles were soaked in a scintillation vial with 17 mL of 0.05wt% HA solution (8.5 mg HA total per sample) at a concentration of 5 wt% SNPs for a total of 24 h to allow for diffusive loading into the porous and swellable

particles. For centrifugal loading, a 5 wt% hydrophobized SNPs suspension in 17 mL of a 0.05% HA solution in MQW was centrifuged at 20,000 rpm for 15 minutes, with the concentration of (unloaded) HA in the supernatant measured via UV-vis spectroscopy (Cary 100) based on the difference in peak intensity at the wavelengths of 465 nm and 665 nm, following a previously published method [513]. The encapsulation efficiency (EE%) of HA into the SNPs (assuming all humic acid not present in the supernatant is loaded into the SNPs in the pellet) is calculated via **Equation 5.1**.

$$\mathrm{EE\%} = \frac{Total\ [HA] - [HA]\ in\ Supernatant}{Total\ [HA]} = \frac{[HA] in\ SNPs}{Total\ [HA]} \quad \textbf{Eqn. 5.1}$$

To assess the release kinetics of the loaded HA, Float-a-Lyzer experiments were conducted using low (3.5-5 kDa), medium (100 kDa), and high (1 million kDa) molecular weight cut-offs to enable an understanding of the relative release kinetics of different molecular weight fractions within the very broad 2000 – 500,000 g/mol cited molecular weight range of HA. HA-loaded SNPs were suspended into 0.1 M sodium pyrophosphate buffer and loaded into a 10 mL Float-a-Lyzer which is subsequently fully submerged in 17 mL of the same sodium pyrophosphate solution as the release medium. 2 mL samples were taken from the releasing medium and replaced with fresh buffer at each collection timepoint. Given the estimated weight-average molecular weight of SNPs of 250-500 kDa via gel permeation chromatography (GPC) [285], the 3.5-5 kDa membrane will track the release of low-MW HA, the 100 kDa membrane will enable tracking of primarily low/medium-MW HA release, and the 1 MDa membrane will allow passage of all HA fractions as well as the SNPs themselves. To confirm this latter point, iodine was used to determine the presence of starch in the release media by adding 50 μL of the 0.0125 M iodine stock solution to 3 mL of the unknown solution and tracking the colorimetric starch oxidation signal at 580 nm using UV-vis spectrophotometry [7], relating the colorimetric signal to the concentration of starch based on a starch-iodine calibration curve (**Supporting Information Figure S5.5**).

5.2.7 Plant Experiments

5.2.7.1 Growth Conditions

All samples were grown in the McMaster University's greenhouse (latitude: 43.2580, longitude: -79.9180) and no additional growing agents or fertilizers were used. To each 4" pot, ~50 g of dry soil (Promix BX) was added, maintaining sufficient room to account for hydrogel swelling and natural moisture drainage. The watermelon and pumpkin seeds were planted during the summer months (May – August) ~4 cm below the soil surface. The plants were watered every other day and allowed to grow for a total of four weeks (28 days) before conducting any spray tests to allow for the first leaf emergences to grow to maturity (true leaves). The plants were watered every other day until which point water is visibly draining from the bottom of each pot.

5.2.7.2 Adhesion to the Leaf Surface

FITC-SNPs were dispersed in MQW at a concentration of 5 wt% and loaded into a standard 10 mL spray bottle. To each plant, 10 sprays were administered to the cuticle side (top) and the stomata side (bottom) of the leaves (20 sprays total) and left to sit in the greenhouse overnight to allow for the suspension to dry on the leaf surface. At t=24 h, the leaves were cut from the live plant with trimming scissors, immediately after which eight 0.5" diameter circular cuts were made randomly in each leaf and placed in separate wells of a 48 well plate, four with the cuticle side up and four with the stomatal side up. Unsprayed leaves were also tested for background fluorescence, with the background subtracted from the measured fluorescence from the FITC-SNPs. Tests were performed using both *Citrullus lanatus* (watermelon) [514] and *Cucurbita pepo* (small sugar pumpkin) [515], both of which have larger stomata of sizes 5-8 μm.

5.2.7.3 Penetration into Plant Leaves

Leaves were sprayed with selected formulations in the same manner as previously described (20 sprays, 10 each side) and dried for 24 h. Following, randomly located sections were carefully extracted for the root hairs, stem (at various points), and leaves and placed into glass-bottomed 48 well plates for visualization (**Supporting Information Figure S5.7**). The samples were imaged using confocal microscopy (Nikon Eclipse Ti) to determine the extent of penetration/ uptake into the different plant tissues using the GFP/FITC (480/30 excitation filter) and the TRITC/Cy3 (540/25 excitation filter) long pass filter cubes. For the initial penetration tests using pumpkin and watermelon plants, only the FITC filter was used; for the *Arabidopsis* penetration test, both filters were used since the TRITC filter can show the choloroplasts and cellular material without significant photobleaching of FITC-SNPs.

5.3 Results and Discussion

5.3.1 Starch nanoparticle (SNP) characterization

Succinic anhydride (SAn) and octenyl succinic (OSAn) were grafted to SNPs to enhance the hydrophobicity of the SNPs, hypothesized to improve SNP adhesion to plants upon spray-based application. **Figure 5.2a** shows the comparison between the experimental degree of substitution (DS) value and the pH at which the reaction is run, as measured via conductometric titration of the residual carboxylic acid group that forms upon anhydride grafting. Performing the grafting reaction at pH 8-9 led to higher experimental DS values for both SAn and OSAn modification compared to when the grafting reaction was conducted at pH 10-11. This result is hypothesized to relate to the increased ionic strength of the suspension at higher pH values partially collapsing the nanogel-like SNPs and making the internal hydroxyl groups less accessible for anhydride grafting; pH 8-9 was thus used for all further modifications. **Figure 5.2b** shows a comparison between the theoretical (x-axis) and actual (y-axis) DS values, with stoichiometric grafting indicated by the green line. Both SAn and OSAn grafting achieves ~80% of theoretical substitution at a theoretical DS of 0.10; at the theoretical DS of 0.25, the OSAn modification maintained relatively high grafting efficiency (73% of theoretical) while the SAn grafting is less efficient (46% of theoretical). It is postulated that the lower functionalization

efficiency observed with succinic anhydride-modified particles compared to octenyl succinic anhydride-modified SNPs may be due to competing hydrolysis reactions occurring during the strong base into acid titration, with the smaller molecule (SAn) hydrolyzing faster to reduce graft yields; hydrophobic interactions between unbound octenyl succinic anhydride and bound octenyl succinic acid groups on the SNP surface may also drive the recruitment of unbound hydrophobic groups to the particle surface to promote more effective grafting. However, the results indicate that both SAn and OSAn can effectively functionalize SNPs with hydrophobic grafts, exploiting the (unusually) high chemical reactivity of the starch -OH groups in the reactive extrusion-processed SNPs.

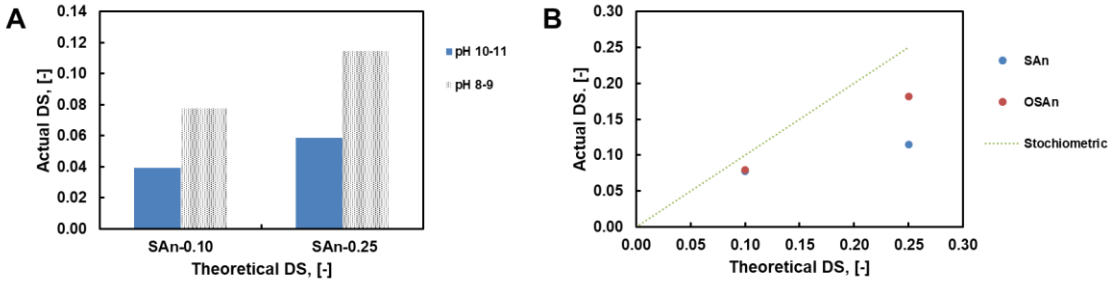

Figure 5.2: Degree of substitution of anhydride-modified SNPs: (A) Comparison of actual versus theoretical DS values for succinic anhydride-modified SNPs (SAn) functionalized at pH 10-11 (blue, solid) or pH 8-9 (green, textured); (B) Comparison of actual versus theoretical DS values for both succinic anhydride and octyl succinic anhydride-modified SNPs functionalized at pH 8-9; the green dotted line represents 100% grafting efficiency (denoted as "ideal").

To assess the change in hydrophobicity induced by anhydride grafting, the hydrophobized SNPs were sprayed on a leaf surface and the contact angle was measured (**Figure 5.3**). With the succinic anhydride modified starch nanoparticles, a notable increase in contact angle (CA) from 63.5˚ to 82.5˚ was observed when the DS was increased from 0.10 to 0.25, consistent with the introduction of more alkyl groups to the SNP. In comparison, the same treatment performed on the leaf controls by spraying MQW alone resulted in a contact angle of 57.4˚, indicating that even the lowest DS/least hydrophobically modified starch (SAn-0.10) was effective at enhancing the hydrophobicity of the SNPs. In comparison, using OSAn-modified starch resulted in even larger enhancements in contact angle at equivalent DS values (i.e. comparing SAn-0.10 and OSAn-0.10), as anticipated based on the longer alkyl chain present in this formulation. As such, the anhydride grafting strategy significantly enhances the hydrophobicity of the SNPs.

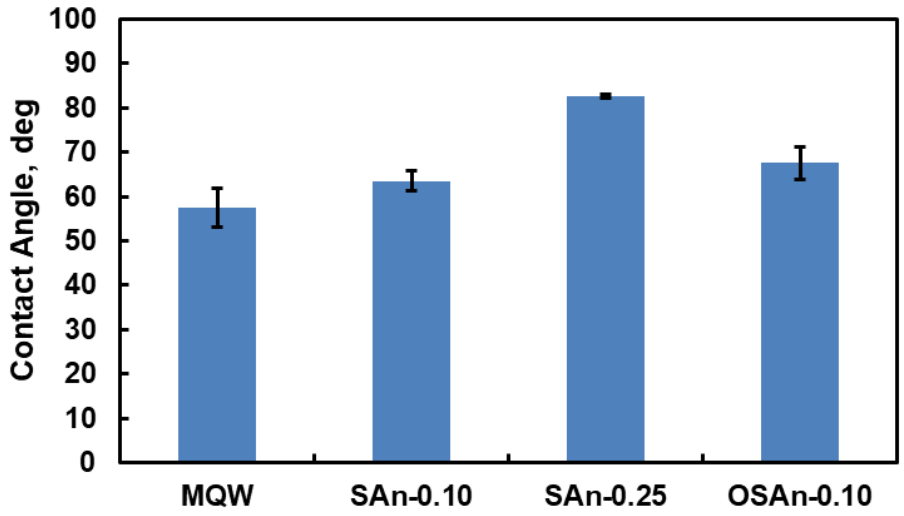

Figure 5.3: Contact angle (CA) measurements for hydrophobized SNPs following drying of an SNP suspension on a leaf surface.

The effect of anhydride functionalization of SNPs on the particle size and dispersion stability of the SNPs is summarized in **Table 5.1.** Hydrophobization of the SNPs results in an increase in interparticle interactions, leading to higher particle sizes by intensity (which especially weights the presence of larger aggregates in calculating the overall particle size). This size increase is particularly notable at higher SNP concentrations since particle-particle interactions are more likely to occur. SNPs functionalized with more anhydride (i.e. higher DS values) and/or the anhydrides with longer alkyl chains (i.e. OSAn instead of SAn) resulted in reduced colloidal stability at these SNP concentrations in aqueous suspension, consistent with increasing interfacial hydrophobicity that reduces the steric stabilization that leads to SNP dispersion in polar solvents. Of note, when comparing DMSO and MQW results, DMSO can much better disperse the hydrophobized SNPs, justifying use of the 50:50 DMSO:MQW mixture used during synthesis to enable pH control but also reduce overall polarity in the system and thus the aggregation/swellability of the particles in solution. The DLS data reported herein used a refractive index of 1.34 (for starch) to convert the intensity averaged data (which is independent of the particle refractive indices) to the number averaged data [285]. However, the trends in the data will remain the same irrespective of the refractive index used for processing.

Table 5.1: Dynamic light scattering (DLS) results for 0.5 wt% anhydride-functionalized and unmodified SNPs reported in terms of intensity averages or number averages. Results are given for dispersions in DMSO (left) and Milli Q water (right) with the standard deviations given.

Sample	DMSO		5 mM KCl		
	Avg. Diam. (intensity), nm	**Avg. Diam. (number), nm**	**Avg. Diam (intensity), nm**	**Avg. Diam (number), nm**	**Mobility, (μ/s)/(V/cm)**
SAn-0.25	465 ± 162	20 ± 1	975 ± 126	21 ± 1	-1.31 ± 0.09
SAn-0.10	236 ± 28	15 ± 3	338 ± 32	18 ± 6	-0.64 ± 0.04
OSAn-0.25	498 ± 104	17 ± 9	978 ± 259	12 ± 3	-1.67 ± 0.07
OSAn-0.10	267 ± 150	11 ± 6	430 ± 159	23 ± 6	-1.10 ± 0.14
Unmodified SNP	194 ± 8	19 ± 6	237 ± 12	21 ± 8	0.03 ± 0.15

The extent of differences in charge between the unmodified and hydrophobized SNPs was assessed by measuring the electrophoretic mobility measurements. In general, the hydrophobized SNPs exhibited a more negative charge than the unfunctionalized SNPs, consistent with the generation of a residual -COOH group on the SNP for every SAn or OSAn grafted to the SNP; however, the magnitude of the measured electrophoretic mobilities suggest that even the modified SNPs are only weakly anionic (< 2 (μ/s)/(V/cm)) and are not expected to induce large charge-charge repulsion on the naturally anionic plant membrane surfaces. Coupled with the maintained small size of the modified SNPs these results suggest that SNPs may have desirable properties for functional delivery of the nanoparticles to plants.

It is important to note the significantly lower number average particle size measured for OSAn-0.25 compared to OSAn-0.10. We hypothesize that the significantly higher concentration of alkyl chains attached to the surface OSAn-0.25 induces significantly stronger hydrophobic interactions that induce dewatering of the nanogel-like SNPs, resulting in the overall number average diameter of the SNP decreasing from 23 ± 6 nm by number in 5 mM KCl (OSAn-0.10) to 12 ± 3 nm by number in 5 mM KCl (OSAn-0.25); in comparison, the much less hydrophobic SAn grafts do not add sufficient hydrophobicity to drive such deswelling at the same DS values of 0.10 (18 ± 6 nm) and 0.25 (21 ± 1 nm).

5.3.2 Photodegradation Testing

Prior to using fluorescein-labeled SNPs (FITC-SNPs) for probing the adhesion and penetrability of the hydrophobized SNPs in plants, the photodegradation of FITC-SNPs was assessed to ensure the fluorescence signal from the SNP was maintained following exposure to typical sunlight/simulated sunlight light wavelengths. Scintillation vials of the FITC-tagged hydrophobized SNPs were left in both natural greenhouse conditions

(**Fig. 5.4a**) and simulated sunlight on the bench in the lab (**Fig. 5.4b**), with the trends in relative fluorescence intensity over time shown in the figures below.

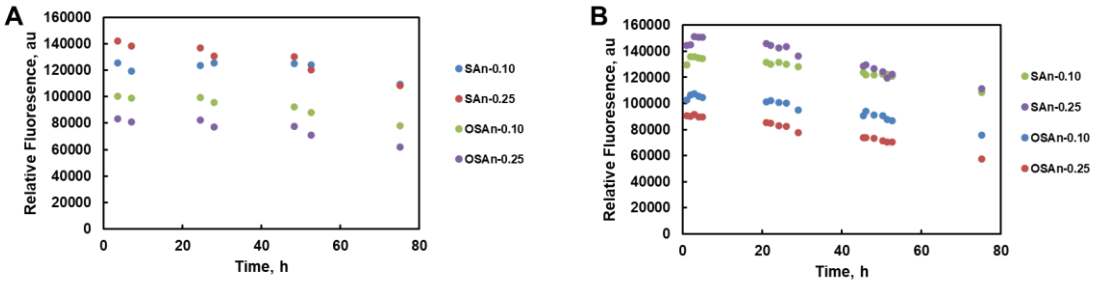

Figure 5.4 (a,b): Photodegradation of the FITC-SNP fluorescence signal for hydrophobized SNPs tagged with 2 mg of FITC isomer I (A) in natural greenhouse conditions; and (B) under simulated sunlight on benchtop.

By comparing the general trends in photodegradation in **Fig. 5.4a** (greenhouse) to that of **Fig. 5.4b** (Helios), the relative rates of degradation are comparable under both growth conditions; while all samples did see a decrease in fluorescent signal over the course of the ~80 hour experiment in both the greenhouse (13-26% decrease) and under simulated light (16-36% decrease), the decreases were relatively modest and the residual fluorescence would still allow for facile tracking of nanoparticle distribution on a timescale relevant to the growth schedules of the plants selected for screening [516]. Given the results presented herein, it appears as if photodegradation is not a major concern given the time frame of the release studies that will be performed acutely (2 weeks or less).

5.3.3 Humic Acid Encapsulation & Release

To assess the potential of the hydrophobized SNPs to enhance the delivery of bioactive agents to plants, humic acid (HA) was selected as the model bioactive given its key biological roles in plant growth and attractive combination of water solubility and highly aromatic internal structure (exploiting both the swellability of SNPs and the hydrophobic domains in the hydrophobized SNPs to enhance HA loading and control subsequent HA release) [508,517]. HA was loaded into SNPs via passive diffusion (as is commonly used to load hydrated nanoparticles with bioactives) and centrifugal loading strategies, with **Table 5.2** showing the resulting encapsulation efficiencies observed using both strategies. High HA loadings corresponding to 60–70% encapsulation were achieved via centrifugal loading, a result attributed to the role of the hydrophobic grafts in enhancing physical interactions between HA and the SNPs. Given that the centrifugal method is both faster and more effective than the lengthy passive diffusion method, centrifugal loading was used for all future tests. Of note, when HA was centrifuged alone in the absence of SNPs, no pellet whatsoever was formed; as such, we expect that all the HA that co-localizes with the SNP pellet is loaded into (or on the surface of) the SNPs and not simply

precipitated by the centrifugation process. For each sample, three centrifuge runs at the speeds and times indicated previously were performed and the %EE was calculated after each to determine if longer centrifugation spinning would further improve loading. Note that, due to the very high specific surface area of SNPs and the very broad molecular weight distribution of HA, this high EE value could correspond to the uptake of HA inside of SNPs or the adsorption of HA to the SNP surface, either of which can enable efficient HA delivery.

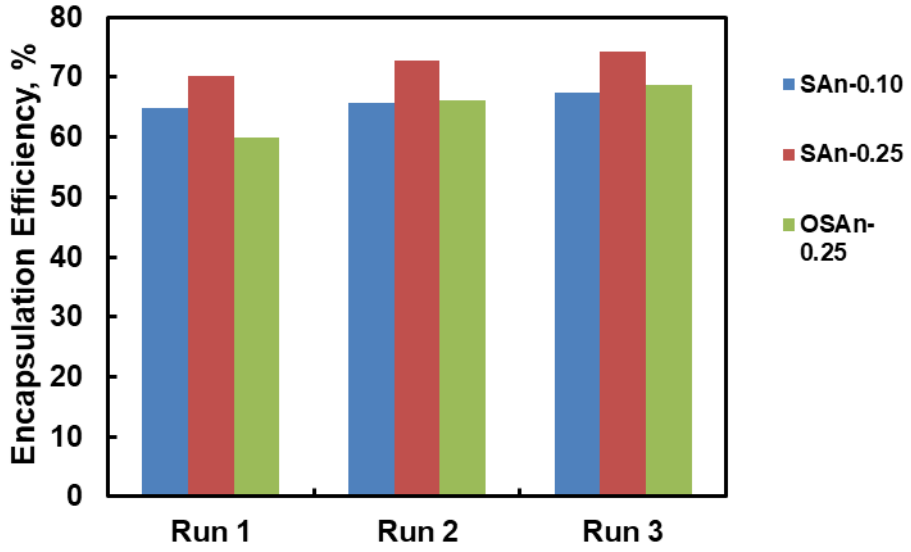

Figure 5.5: Encapsulation efficiencies of humic acid in hydrophobized SNPs following centrifugal loading. Three runs were performed for each sample, and the EE% was calculated for each. Note that the data for runs 1-3 were collected using three independent samples and centrifuge tubes (i.e. three independent samples tested for each functionality).

The release kinetics of the loaded HA from the hydrophobized SNPs are shown in **Figure 5.6.** Given the broad molecular weight distribution of the loaded HA, release was tracked using a 100 kDa dialysis membrane based on the large MWD of humic acid. A very small amount of HA was released in the first 350 h (<1 mg), likely due to hydrophobic interactions that could occur with the cellulose ester membranes of the Float-a-Lyzers or due to strong interactions between the HA and the SNPs. The latter hypothesis is supported by the observation that SNPs prepared with lower DS values and/or shorter hydrophobes (i.e. SAn instead of OSAn) release more drug faster, with the most hydrophobized SNP (OSAn-0.25) being particularly efficient at reducing burst HA release given its more condensed state (**Table 5.1**) As such, hydrophobized SNPs can both enhance the loading and prolong the release of HA. It is anticipated similar benefits would be exhibited with other low solubility and/or amphiphilic bioactives that would benefit from the amphiphilic internal structure of the hydrophobized SNPs.

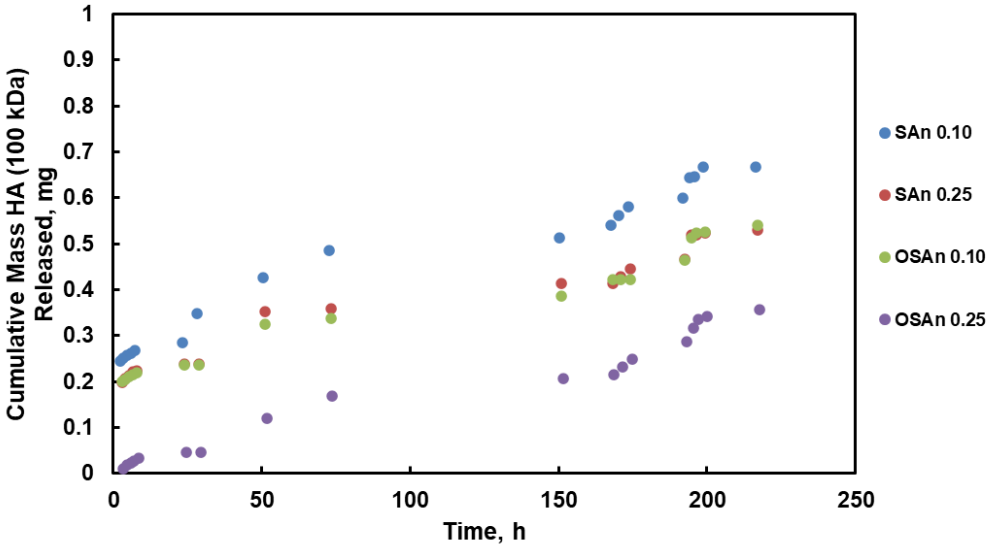

Figure 5.6: Humic acid (HA) release from hydrophobized SNPs as measured through a 100 kDa Float-a-Lyzer dialysis membrane.

5.3.4 Plant Experiments

Suspensions of (unloaded) FITC-SNPs were sprayed on both the stomal and cuticular sides of pumpkin and watermelon leaves followed by fluorescence microscopy analysis of SNP retention on the leaf using a plate reader (see **Supporting Information Figure S5.7** for a picture of a representative experiment). Representative results for SNP retention are shown in **Fig. 5.7A** (for pumpkin leaves) and **Fig. 5.7B** (for watermelon leaves). In general, stomatal side retention was significantly higher than cuticular retention, consistent with the presence of the waxy barrier on the cuticular side as well as the known role of the stomata in promoting particle transport into leaves. While the DS did not significantly alter the apparent retention of the SNPs in SAn-functionalized SNPs, the higher DS OSAn-functionalized SNPs retained significantly better on the stomatal side in both pumpkin and watermelon leaves. This result is consistent with the higher interfacial hydrophobicity of OSAn-0.25 enhancing the interfacial interaction with the waxy barrier on the leaf.

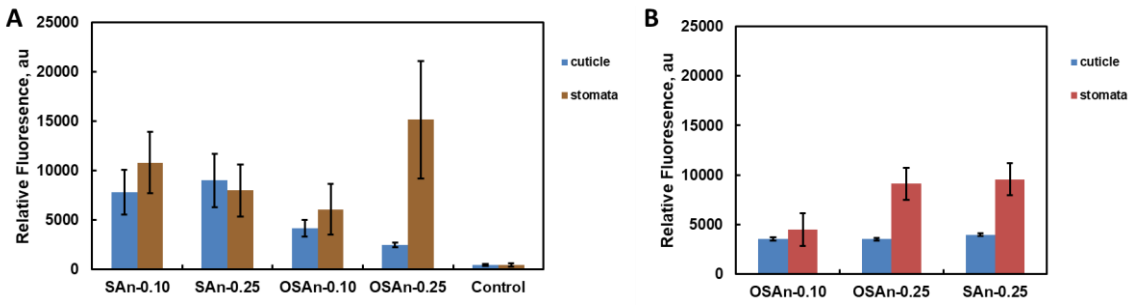

Figure 5.7: Retention data of hydrophobized FITC-SNPs following foliar spray for (A) pumpkin leaves and (B) watermelon leaves. The control group in image A is a pumpkin leaf which was sprayed with water containing no SNPs or bioactives, confirming that the leaf itself does not exhibit any autofluorescence.

To get a better assessment of the potential for hydrophobized SNPs to penetrate and even translocate within plant tissues, *Arabidopsis* was selected as the plant model given that it has the highest average number of stomata per square mm of tissue and its stomata is the largest in diameter among common crops (30- 60 μm) [3]; both these factors can promote improved nanoparticle transport. Furthermore, relative to pumpkin and watermelon leaves, *Arabidopsis* leaves are thinner and easier to image the underlying plant tissue for better contrast and better assessments of penetration deeper into the leaf. Based on OSAn-0.25 exhibiting both the highest retention on both watermelon and pumpkin leaves (**Fig. 5.7**) and the smallest size (and thus the hypothesized highest transport potential, **Table 5.1**), FITC-OSAn-0.25 was probed for its translocation potential using confocal microscopy; note that in this case the plant cells are also visible (in red) due to imaging also being conducted using the TRITC filter in which the autofluorescence of the chloroplasts can be visualized independently of the FITC-labeled hydrophobized SNPs. **Fig. 5.9A** shows a strong retention of the SNPs immediately after they are sprayed on the surface of an *Arabidopsis* leaf, confirming their high retention in a third plant model with different properties from the hairy pumpkin and watermelon plants. Following washing of the surface three times with water (**Fig. 5.9B**), much of the green color disappears as weakly adsorbed particles are washed away; however, there is clear evidence of SNPs persisting in the intercellular gaps between the cells, indicating successful penetration of the SNPs into the leaf. SNPs are also clearly visible in the stomata of the leaves as indicated by the green O-ring visible in **Figs. 5.9C** and **5.9D**, suggesting that SNPs can both transport through the micrometer stomatal openings as well as penetrate cellular gaps once there. Of note, to our knowledge, no other bio-based nanoparticles have previously been reported to not only adhere to plant surfaces and penetrate through cellular junctions but also penetrate into the stomata and related membranes when sprayed foliarly, a combination of properties that would facilitate the protection and active transport of agrochemicals from the point of administration into the body of the leaf. The most hydrophobic and smallest number average diameter (**Table 5.1**) FITC-OSAn-0.25 SNPs can also penetrate through the root cells, with **Fig. 5.9E** showing clear

evidence of the SNPs transporting up and down the length of a root and **Fig. 5.9F** suggesting that the SNPs could penetrate the first few epithelial layers of the root; we attribute this result to hydrophobic interactions with the hairy roots that are rich in secreted mucilage both dry and wet [518].

The hydrophobized SNPs offer several biological benefits for penetration into and through plants. First, the outside surface of leaves are rich in waxes and lipids that help promote water droplet roll-off so the leaf cells can remain isotonic [182]. The natural microscopic ridges and roughness of plant leaves [519] also help to mechanically trap applied nanoparticles, with hydrophobized nanoparticles more likely to adhere given the leaf surface chemistry. Once the SNP has penetrated a leaf, the fluid mosaic model [520] of plants suggests that the hydrophobic surface also helps promote translocation throughout the plant since the native plant cell membranes are lipid-rich and charge sensitive (making the near-neutral charge of the hydrophobized SNPs beneficial for promoting intra-leaf transport). As such, the hydrophobized SNPs offer clear translational benefits for both foliar and root-based agrochemical delivery in terms of increasing the penetration of bioactives into plants via multiple transport routes.

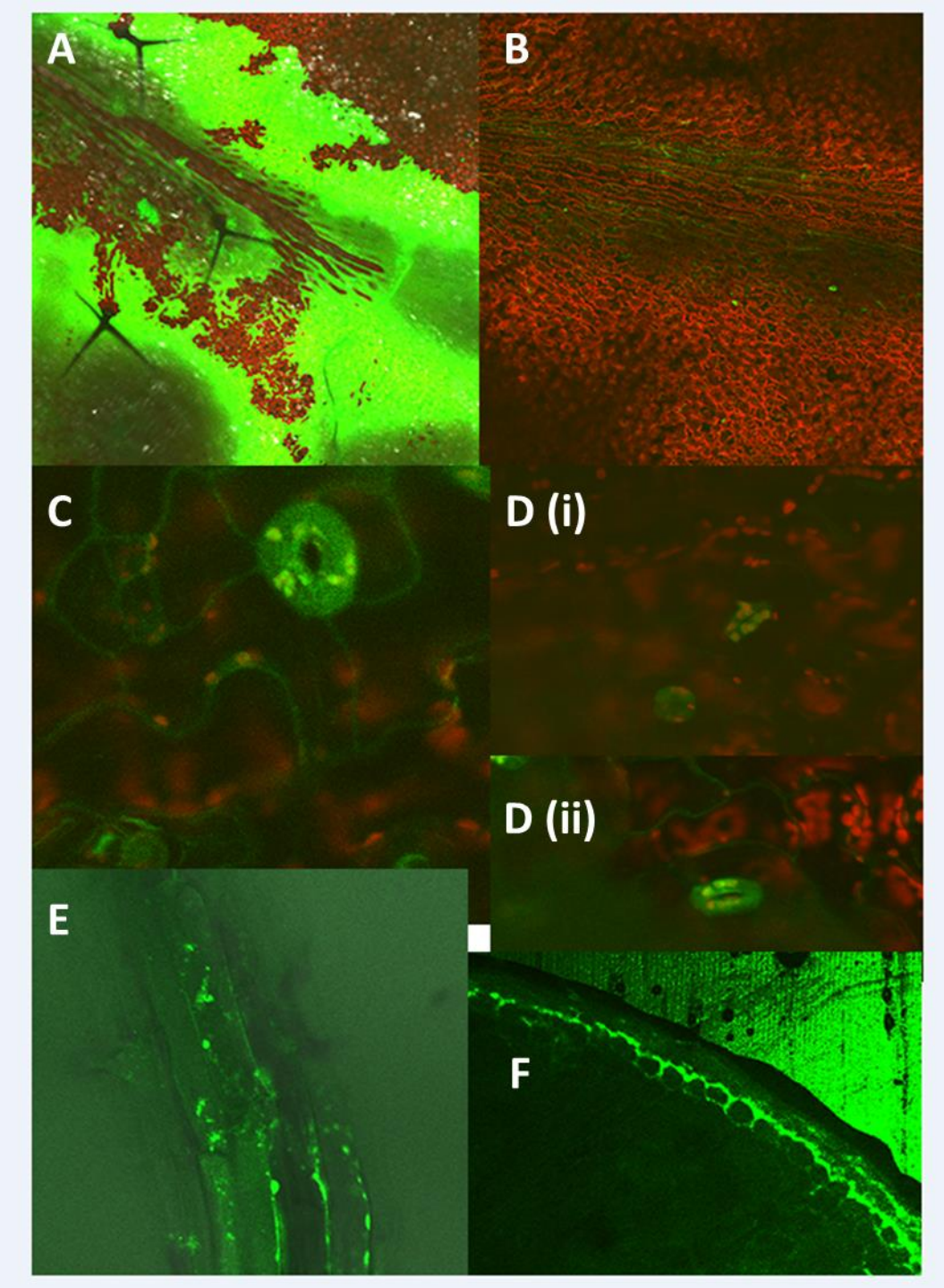

Figure 5.9 (a-f): Confocal images of transport of FITC-OSAn-0.25 starch nanoparticles following foliar spray on (A,B) the leaf surface; (C,D) the stomata (note that D(i) and D(ii) represent two different images on different parts of the leaf showing the same phenomenon); and (E,F) the root capillary. Green coloration represents the location of the SNPs (FITC filter) while red represents chloroplasts (TRITC filter).

5.4 Conclusions and Acknowledgements

Hydrophobized starch nanoparticles are promising vehicles for foliar or soil-based agrichemical delivery given their favorable size, deformabililty, and charge for promoting both leaf adhesion and subsequent translocation into plants. Hydrophobization of the commercial SNPs via grafting of succinic anhydride (SAn) or octenyl succinic anhydride (OSAn) at two degrees of substitution (DS = 0.10 and 0.25) was demonstrated to increase the contact angle and, by extension, enhance adhesion of the SNPs on the surfaces of both pumpkin (*Cucurbita pepo*) and watermelon (*Citrullus lanatus*) leaves. Humic acid uptake and delivery is enabled by the amphiphilic internal structure of the hydrophobized SNPs. Preliminary penetration tests suggest that FITC-tagged hydrophobic SNPs are not detectable in the stems or roots 24 h post spraying but can be seen in the leaf vasculature. A further test with the *Arabsidopsis* plant suggests that the most hydrophobized SNP can effectively penetrate into the leaf, into the stomata, and through the root hairs of the plants. Coupled with the fact that SNPs are made from a sustainable source (corn) and can be fabricated on large industrial scales (via reactive co-extrusion), the use of hydrophobized SNPs as a sprayable delivery vehicle for large-scale agricultural applications offers a renewable and functional option for functional agrochemical delivery.

5.5 Acknowledgements

The Natural Sciences and Engineering Research Council of Canada (NSERC) is acknowledged for funding this work (Strategic Project Grant 463327-14). *EcoSynthetix Inc.* is acknowledged for its in-kind contributions of the starch nanoparticles used in this study. Dr. Wenzi Ckurshumova is acknowledged for her assistance with designing and collecting the confocal microscopy data on *Arabsidopsis* and Dr. Madeline Simpson is acknowledged for collecting the initial electrophoretic mobility measurements of unfunctionalized and hydrophobized SNPs.

Appendix 5S: Supporting Information to Chapter 5

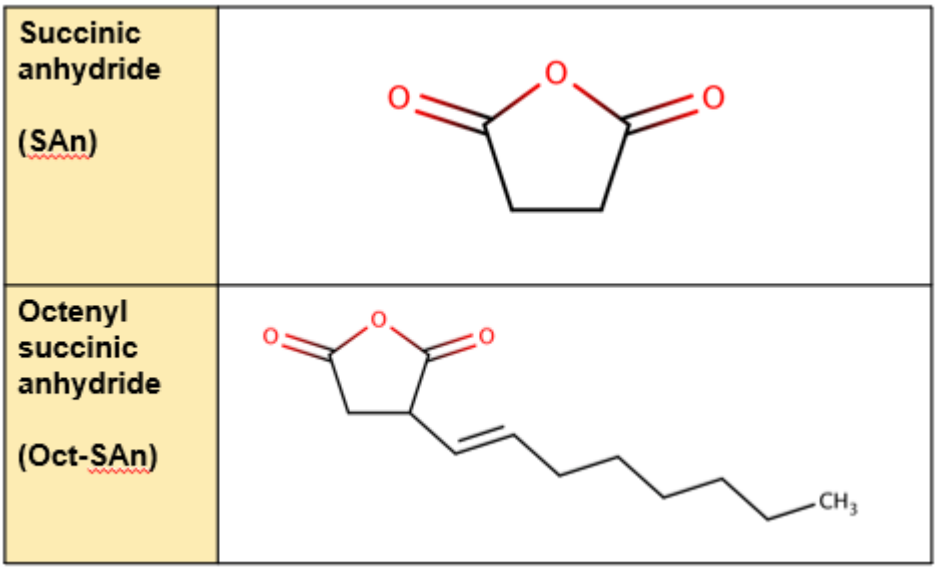

Figure S5.1: The chemical structures for the main additives used in this study, succinic anhydride or SAn (top) and octenyl succinic anhydride or OSAn (bottom).

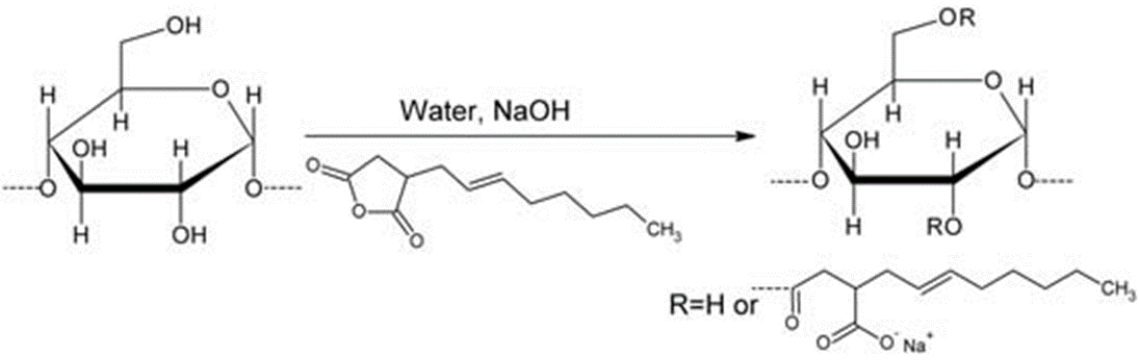

Figure S5.2: The functionalization reaction scheme for OSAn-modified starch, adapted from Sweedman et al. (2013) [501]. The same reaction would also take place with the SAn-modified starch, just without the extra alkenyl chain.

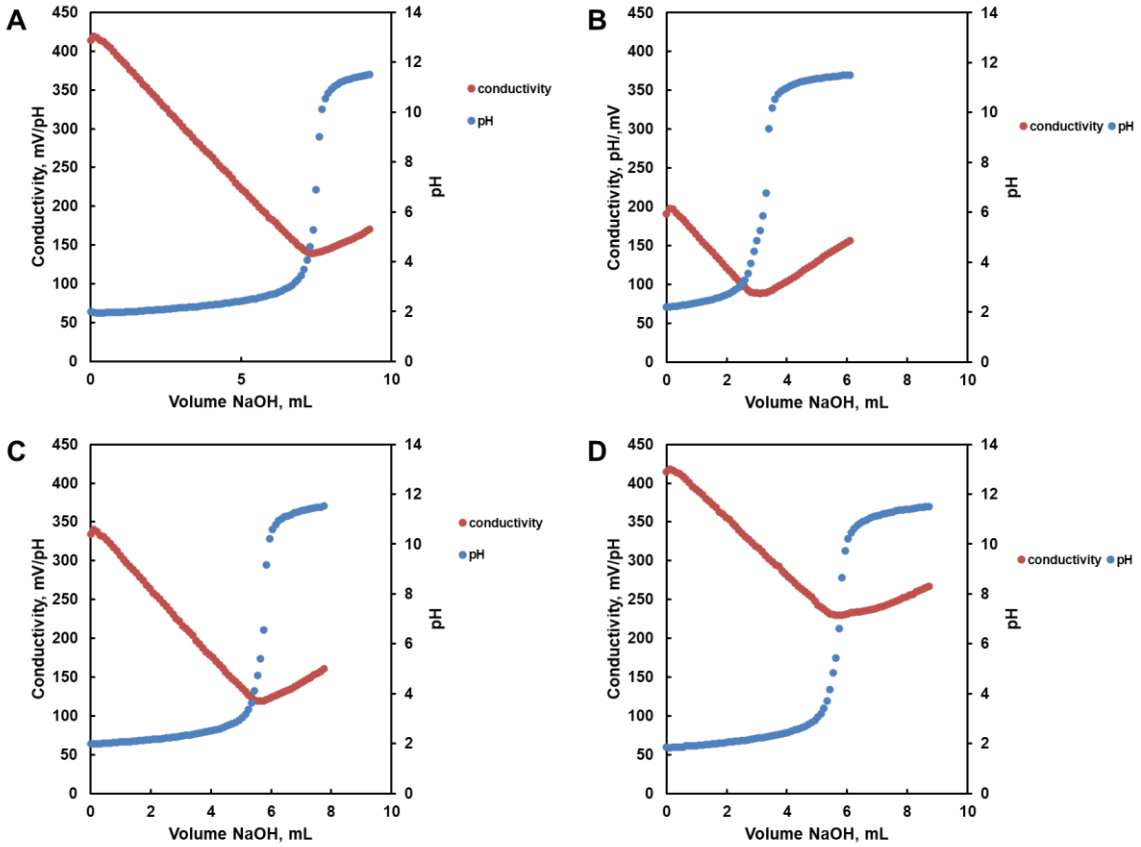

Figure S5.3 (A-D): Conductometric titration data (pH and conductivity vs. volume of NaOH added) for SAn-0.10 (a), SAn-0.25 (b), OSAn-0.10 (c), and OSAn-0.25 (d).

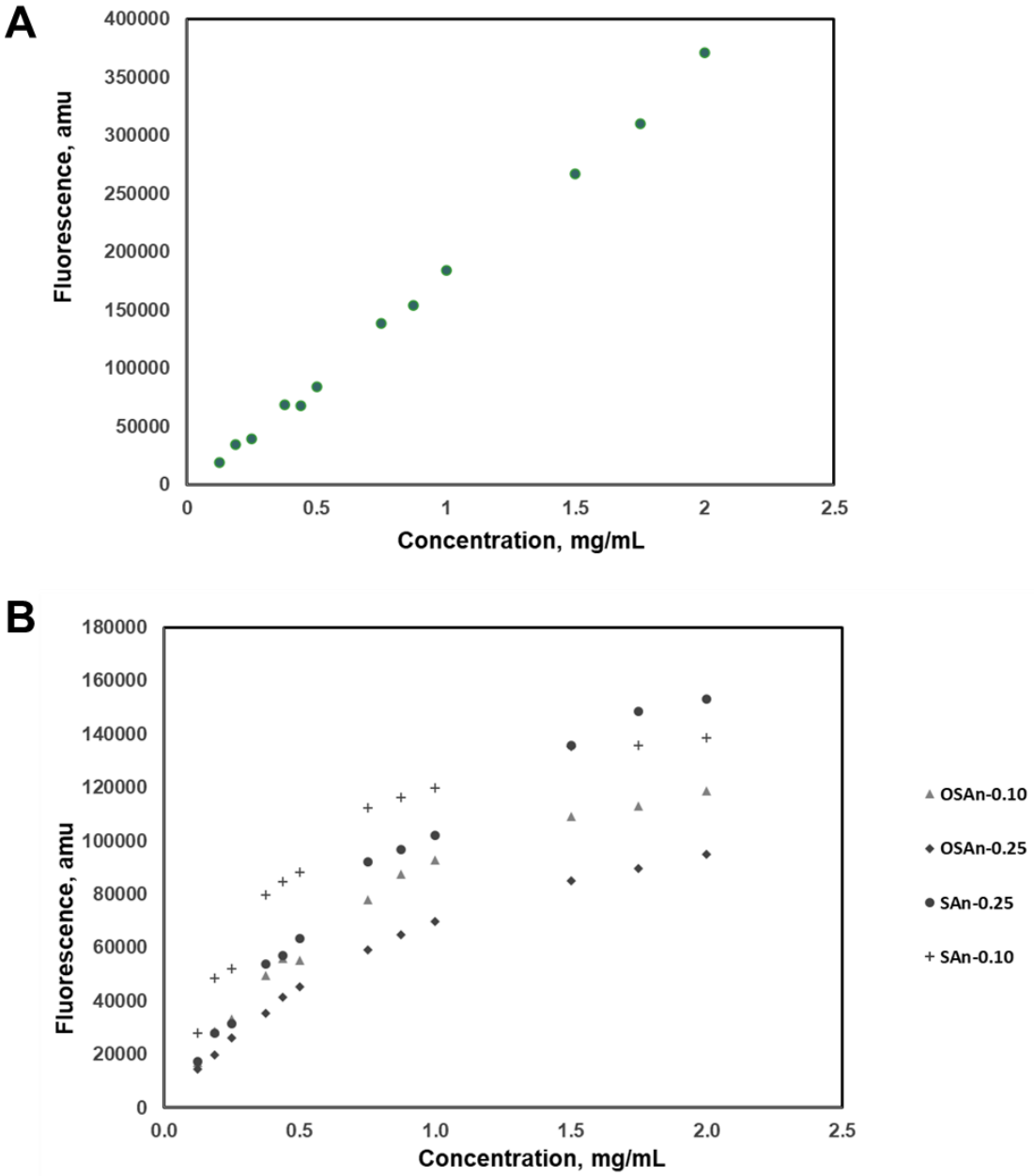

Figure S5.4: Standard curves for (a) FITC-tagged neutral SNPs and (b) the relative fluorescence for the hydrophobized SNPs (all at 2 mg FITC/50 mg polymer) post-hydrophobization at comparable concentrations.

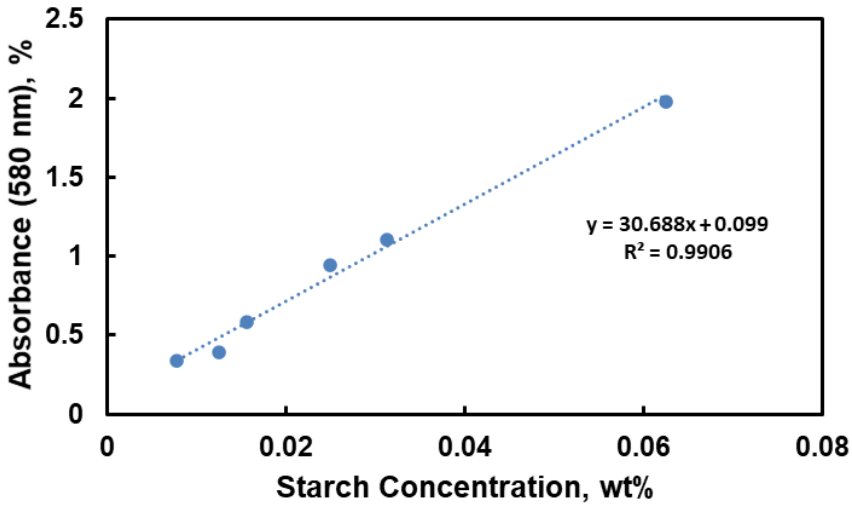

Figure S5.5: Standard curve for the starch-iodine test using 0.0125 M iodine and varying wt%'s of HA. Note that concentrations of up to 0.5 wt% were tested, but concentrations above the range of this graph did not give a linear calibration.

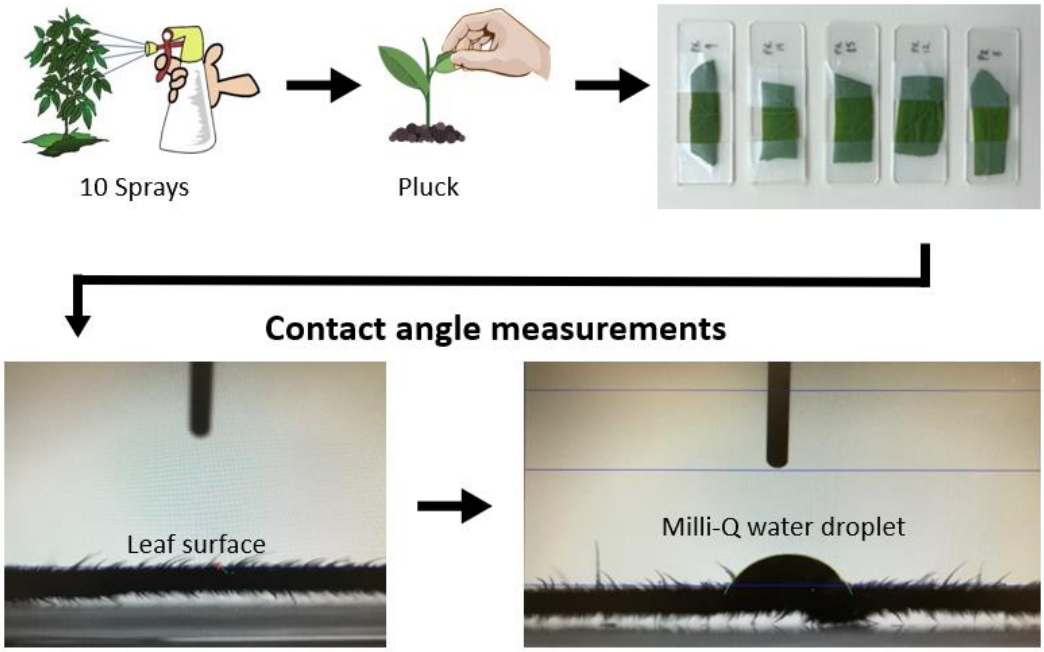

Figure S5.6: Schematic of the experimental protocol for the contact angle measurements to clear up any confusion with the measurements on top of the leaf surface.

Figure S5.7: Example of the leaf sections in their 48 well plate before being quantified for their relative FITC fluorescent intensity values.

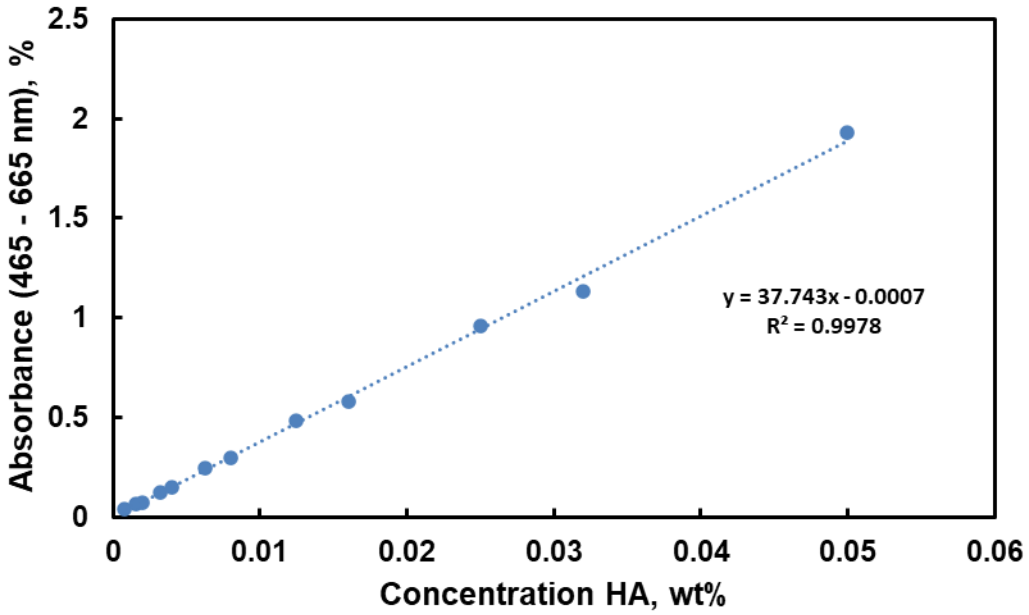

Figure S5.8: Calibration curve run using UV-vis spectroscopy (plotting the difference in absorbances at 465 and 665 nm) for humic acid (HA).

Chapter 6: Conclusions, Significance, and Future Perspectives

The research presented in this thesis describes the characterization and modification of industrially-synthesized starch nanoparticles (SNPs) for the purpose of fabricating novel hydrogel morphologies. The central design of all projects described herein involves imparting some functionality, and thus crosslinking capability, onto the hydroxyl (-OH) rich starch surface (and bulk) which can then be further exploited to create plum pudding or colloidal nanoparticle network hydrogels. By utilizing different crosslinking mechanisms including free radical polymerization (FRP), *in situ* reactive chemistries (i.e. imine formation), and physical interactions (e.g. electrostatic interactions or hydrophobic domains), hydrogels on different length scales (bulk to nano) were designed that demonstrated unique physical and biological properties for applications in biomedicine, *in vivo* drug delivery, and agricultural delivery, with the utility of the hydrogels in each case linked to the nanoparticle network gel morphology formed using SNPs as the hydrogel building block.

Chapter 2 described a method for creating starch nanoparticles with available vinyl groups (methacrylates, SNP-MAAn) that could be subsequently crosslinked under long-wave UV light to fabricate the first reported starch nanoparticle network hydrogels (NNHs). While SNPs have been used as an additive or crosslinker in hydrogel systems before, our work showed how having the entire gel made from nanoscale building blocks has inherent benefits for allowing for higher wt% dispersions, lower non-specific cell adhesion, improved mechanical properties, and lower swelling ratios compared to gels made from branched (soluble) starch alternatives. Due to the large scale (kg/hr) production enabled by the reactive extrusion method used to fabricate the SNP building blocks, such hydrogels could be made at any desired scale to enable further performance testing of SNP-based gels for broad applications.

Future Work & Perspectives (Chapter 2): This paper has been published in *Carbohydrate Polymers*. The major contributions this work are (1) the use of functional anhydrides to promote crosslinking and gelation between starch nanoparticles and (2) the demonstration of macroscopic gel differences for a nanoparticle network hydrogel made from nanoscale building blocks compared to other gel morphologies or nanocomposites. Additionally, this is the first report of the fabrication of stable covalently crosslinked hydrogels made from only SNPs without the need for another crosslinking polymer. Future work to compare the protein repellency performance of SNP-only hydrogels compared to hybrid gels (SNP + polymer) and the current "gold-standard" synthetic hydrogels (i.e. PEG analogues) would be of interest to see the relevance of the extremely high SNP concentration (and thus packing density) in terms of improving anti-fouling to hydrogel-coated surfaces would be of interest. Alternatively, some type of flow experiment aimed at assessing gel porosity (e.g. assessing transport of proteins or FITC-dextran probes with well-defined molecular weights) would be useful to determine the differences in porosity in these gels compared to hybrid or synthetic alternatives, again to better understand the impact of the NP spacing and packing within the macroscopic gel on the resulting hydrogel properties. The potential use of these hydrogels for tissue

engineering applications (also exploiting the intra-particle porosity of these systems which is unique to other hydrogels) would also be of interest, particularly if the SNPs are RGD functionalized to promote cell adhesion. Degradation tests using estersases/enzymes (i.e. amylases) would also be relevant to learn about the erosion and degradation patterns of these bulk gels, with ultimate applications in regulating the degradation of the hydrogel in tandem with cell infiltration within the tissue matrix formed.

In addition to exploring the use of the hydrogels as bulk materials, the use of these hydrogels as surface coatings would also be of interest. For example, by using plasma treatment methods that introduce a vinyl group functionality on various types of polymer films, subsequent UV photopolymerization of functionalized SNPs in either dilute (monolayers) or viscous (surface-attached hydrogel) suspensions is expected to covalently link SNP hydrogel coatings to a variety of materials. Since the SNPs are curable by long wave UV, the shape of the hydrogel may be modified or patterned much easier than other synthetic options to improve tissue integration of biomedical implants (if cell adhesive) or maintain non-fibrotic interfaces between implants and the biological environment (if cell/protein repulsive).

Chapter 3 described a further chemical modification of the UV photopolymerized SNP-MAAn by introducing the presence of charge to determine how anionic (pyridinium methyl sulfate functionalized) or cationic (glycidyltrimethylammonium chloride functionalized) starches and different starch morphologies (SS, SNPs, and mixtures thereof) affect both the rate and the structure of nanoparticle network hydrogel formation. It was determined that the presence of charge promotes particle-particle repulsion and increases the time for a gel to form (t_{gel}), as assessed by the amount of time it takes for the storage modulus (G') to overlap the loss modulus (G"), compared to neutral hydrogels. Additionally, the vSANS data demonstrate that notable increases in the fluid correlation length and the fluid scale are demonstrated following irradiation for 10 three second intervals (30 s total irradiation) with long wave (365 nm) UV light *in situ* with the neutron beam, suggesting that the SNPs themselves are deformed by the gelation process; note that this experimental set-up had never been described before in the literature.

Future Work & Perspectives (Chapter 3): The manuscript will be submitted (intended journal *ACS Macromolecules*) at the time of the defence. This is one of the first papers to utilize the very small angle neutron scattering (vSANS) machine at the National Institute of Standards and Technology (NIST) since its introduction in 2017, enabling the first example of *in situ* tracking. of UV photogelation kinetics *in situ* within the neutron beam. Thus, beyond the system-specific physical insights acquired from this work, it is anticipated that this work can aid other researchers in applying SANS analysis to further investigate hydrogel network formation and internal morphology in a time-dependent manner, typically difficult to do with other analytical methods. This is also the first report of generating charged starch nanoparticles, which opens up new avenues for use

and testing in future work for those studying electrostatic-driven interactions in soft materials.

For future work, other scattering methods could be used to corroborate or gain further information about the impact of charge on SNP-SNP and SNP-solvent interactions (e.g. static light scattering). It is well known that nanoparticles have the tendency to aggregate in solution due to their interesting properties at the nanoscale, so further investigations of this nature would be impactful to the study of carbohydrate nanoparticle behaviour. In addition, it is anticipated that the structural and kinetics data from SANS could be leveraged to apply these hydrogels in various biomedical settings.

The neutral, cationic, anionic, and zwitterionic starch nanoparticle network hydrogels, and/or combinations thereof, have been preliminarily tested for their ability to resist the adsorption of various fluorescently tagged proteins of interest (fibrinogen, bovine serum albumin, and lysozyme) as well as human blood plasma, with initial results suggesting promise in the use of these materials as protein-repellent coatings. By exploiting the nanotopology, interesting rheological and viscoelastic properties, and overall charge, it is anticipated that these hydrogels have potential as medical device coatings or thin film hydrogels. Additionally, if the hydrogels were to be used in their dried state post-crosslinking, various SNP-based excipients which exploit the SNP charge and size to make new oral tablets or controlled delivery devices with tunable dissolution kinetics and/or drug interactions could also be envisioned.

Matthew A. Campea in the Hoare lab will be completing more protein adsorption and hemocompatibility experiments with the goal of publishing the performance of charged SNP and SS gels (mechanics of which described herein **Chapter 3**) in a separate study using my preliminary data. It is anticipated that the follow-up study to **Chapter 3** specifically looking at the biological performance of the charged/neutral SS and SNP gels characterized and synthesized here first will be published in mid-2022 (April/May) in a peer-reviewed journal.

Chapter 4 reports a different chemistry to incorporate SNPs into a nanoparticle network hydrogel with highly dynamic crosslinking. SNPs were oxidized to generate dialdehyde groups at the C2 and C3 hydroxyl locations on the anhydrous glucose backbone and then mixed with carboxymethyl chitosan (CMCh) to create self-gelling plum pudding nanoparticle network hydrogels via imine crosslinking. The resulting hydrogels exhibited quick gelation times (< 10 min), tunable mechanical properties (hundred to thousands of Pascals) and relevant rates of degradation (days), nasal mucosal retention, and on-site sprayability that enabled easy intranasal administration (IN). By encapsulating (3R)-2-Oxo-3-[[(2S)-2-Pyrrolidinylcarbonyl]amino]-1-pyrrolidineacetamide (PAOPA) in the gels during the gelation process, the 35 wt% SNP-CHO (DS 0.25 & 0.50) and CMCh (2 and 4 wt%) gels alleviated negative symptoms of schizophrenia (i.e. decreased social interaction time) in rats for up to 72 hours using a low drug dosage (0.5 mg/kg) following MK-801 induced schizophrenia-like symptoms; in comparison, conventional PAOPA

administration via the intraperitoneal route required twice the PAOPA dose to achieve a therapeutic effect that persists for only a few hours. This strategy offers potential for substantially decreasing re-administration frequencies and overall drug doses (and thus side-effects) of a range of potential antipsychotic drugs via a minimally-invasive administration route.

Future Work & Perspectives (Chapter 4): This chapter demonstrates the first sprayable gel formulation that enables controlled delivery of a peptide, which was shown to have favourable biological action in previous papers by our collaborators despite its short clearance time (< 24 h). Bulk gels are less popular for intranasal delivery given the challenges associated with their delivery into the nose; however, the shear-thinning and nanoscale properties of the SNP and CMCh enabled facile delivery of the gel to form a thin film in the nose via a spray-based mechanism. This is also the first report that has determined the proper dosages for PAOPA for IN delivery as well as extended the symptom alleviation for up to 5 days post-injection, which is a notable improvement to previous work done on this peptide/model (typically <1 day).

The simplicity of the hydrogel formulations (one off-the-shelf oral generally recognized as safe (GRAS) oral excipient in CMCh and lightly oxidized SNPs) coupled with the favourable properties of the resulting *in situ*-gelling hydrogels and the facile functionalizability of SNPs for creating hydrogels with high affinities to various types of therapeutics has already initiated further collaborative research projects for delivering other types of antipsychotic bioactive agents, either directly encapsulated in the hydrogel or encapsulated in a secondary nanoparticle (or a modified SNP) that then mediates drug release while the hydrogel enables drug retention in the nasal cavity even longer than 3 days as shown herein. Therapeutics for treating Parkinson's disease as well as schizophrenia are currently under investigation leveraging the basic approach described in **Chapter 4**.

Chapter 5 applies the same anhydride chemistry previously used for methacrylation in **Chapter 2** to create hydrophobized SNPs using succinic (SAn) and octenyl succinic (OSAn) anhydride grafting targeting varying degrees of substitution (DS = 0.10 and 0.25). The particles were fluorescently tagged with FITC isomer I and sprayed onto the surface of pumpkin leaves to assess the potential of the hydrophobized SNPs for leaf adhesion (via a plate reader) and penetration potential into a leaf (via confocal microscopy). Significant improvements in both pumpkin and watermelon leaf adhesion and Arabidopsis penetration (the latter in particular a key challenge with nanoparticle-based agrochemicals) were observed using hydrophobized SNPs. The particles could also be loaded with humic acid (HA), one of the primary components of soil that helps regulate internal plant cell metabolism and related photo transformation processes and help boost growth patterns as a biostimulant; *in vitro* release was observed over the course of at least 13 days, indicating the potential of the hydrophobized SNPs to both

Future Work & Perspectives (Chapter 5): Performing more leaf adhesion measurements by varying not only the number of sprays but also the distance of the spray bottle away from the plant would be beneficial to assess how different types of aerosolization impact the surface coverage and thus the efficacy of the spray-based formulation. In addition, while this chapter provides preliminary evidence to suggest that the SNPs can enter the stomata and roots as well as potentially translocate within the plant, a time-resolved confocal experiment performed at specified time points (ex. 10 minutes, 30 minutes, 1 hour, 2 hours) post-spraying would be required to directly observe the translocation of SNPs within the plant vasculature. Repeats with multiple types of plants would also be required to assess how broadly applicable hydrophobized SNPs are for promoting plant transport. It is suggested also to test the translocation when the SNPs are introduced at either the stomata (leaf surface) or root capillaries to confirm and compare the rates of translocation depending on the administration strategy. Dr. Madeline Simpson in the Hoare lab is currently conducting this research as part of her post-doctroal fellowship research, aiming to finalize a peer-reviewed publication by mid-2022.

The potential of hydrophobized SNPs to deliver other types of bioactives should also be tested. While the use of humic acid (HA) gave some promising initial data, the wide molecular weight distribution of humic acid makes it arduous to quantify; furthermore, it would be nearly impossible to distinguish delivered HA from natural soil-based HA to show unambiguous *in planta* release profiles. Hydrophobic agrochemicals could be selected for delivery to exploit drug-NP hydrophobic interactions for enabling better loading while preserving the softness and external hydrophilicity of starch nanoparticles. Alternately, phosphinothricin is suggested as a cargo since it is an antimicrobial that causes the plant tissue to turn yellow when it is present, allowing direct tracking of the release and location of the SNPs externally without damaging the plant in addition to its inherent potential functional benefits. The further addition of plant-adhesive functional groups/ligands and waxy cuticle dissolvers would also be recommended to improve the release and translocation even more to further broaden the application of SNPs in agriculture.

Cheers.

References for Thesis

[1] L. Kaur, J. Singh, Q. Liu, Starch – A Potential Biomaterial for Biomedical Applications, in: R.M. Mozafari (Ed.), Nanomater. Nanosyst. Biomed. Appl., 2007: pp. 83–99.

[2] A.R. Rauter, B.E. Christensen, L. Somsak, P. Kosma, R. Adamo, Recent Trends in Carbohydrate Chemistry, Elsevier, 2020.

[3] B.M.J. Martens, W.J.J. Gerrits, E.M.A.M. Bruininx, H.A. Schols, Amylopectin structure and crystallinity explains variation in digestion kinetics of starches across botanic sources in an in vitro pig model, J. Anim. Sci. Biotechnol. 9 (2018) 1–13. https://doi.org/10.1186/s40104-018-0303-8.

[4] R. Hoover, Composition, molecular structure, and physicochemical properties of tuber and root starches: A review, Carbohydr. Polym. 45 (2001) 253–267. https://doi.org/10.1016/S0144-8617(00)00260-5.

[5] D. Le Corre, J. Bras, A. Dufresne, Starch nanoparticles: A review, Biomacromolecules. 11 (2010) 1139–1153. https://doi.org/10.1021/bm901428y.

[6] D. Le Corre, H. Angellier-Coussy, Preparation and application of starch nanoparticles for nanocomposites: A review, React. Funct. Polym. 85 (2014) 97–120. https://doi.org/10.1016/j.reactfunctpolym.2014.09.020.

[7] F. Chauhan, K. Seetharaman, On the organization of chains in amylopectin, Starch/Staerke. 65 (2013) 191–199. https://doi.org/10.1002/star.201200132.

[8] K. Wang, J. Hasjim, A.C. Wu, R.J. Henry, R.G. Gilbert, Variation in amylose fine structure of starches from different botanical sources, J. Agric. Food Chem. 62 (2014) 4443–4453. https://doi.org/10.1021/jf5011676.

[9] R.F. Tester, J. Karkalas, X. Qi, Starch - Composition, fine structure and architecture, J. Cereal Sci. 39 (2004) 151–165. https://doi.org/10.1016/j.jcs.2003.12.001.

[10] W.S. Ratnayake, R. Hoover, T. Warkentin, Pea starch: Composition, structure and properties - A review, Starch/Staerke. 54 (2002) 217–234. https://doi.org/10.1002/1521-379X(200206)54:6<217::AID-STAR217>3.0.CO;2-R.

[11] F. Zhu, Isolation, Composition, Structure, Properties, Modifications, and Uses of Yam Starch, Compr. Rev. Food Sci. Food Saf. 14 (2015) 357–386. https://doi.org/10.1111/1541-4337.12134.

[12] I.A. Wani, D.S. Sogi, A.M. Hamdani, A. Gani, N.A. Bhat, A. Shah, Isolation, composition, and physicochemical properties of starch from legumes: A review, Starch/Staerke. 68 (2016) 834–845. https://doi.org/10.1002/star.201600007.

[13] R. Hoover, T. Hughes, H.J. Chung, Q. Liu, Composition, molecular structure, properties, and modification of pulse starches: A review, Food Res. Int. 43 (2010) 399–413. https://doi.org/10.1016/j.foodres.2009.09.001.

[14] R. Fida, G. Pramafisi, Y. Cahyana, Application of banana starch and banana flour in various food product: A review, IOP Conf. Ser. Earth Environ. Sci. 443 (2020). https://doi.org/10.1088/1755-1315/443/1/012057.

[15] P. Zhang, R.L. Whistler, J.N. Bemiller, B.R. Hamaker, Banana starch: Production, physicochemical properties, and digestibility - A review, Carbohydr. Polym. 59

(2005) 443–458. https://doi.org/10.1016/j.carbpol.2004.10.014.
[16] V. V. Lele, S. Kumari, H. Niju, Syntheses, Characterization and Applications of Graft Copolymers of Sago Starch – A Review, Starch/Staerke. 70 (2018) 1–9. https://doi.org/10.1002/star.201700133.
[17] S.M. Chisenga, T.S. Workneh, G. Bultosa, B.A. Alimi, Progress in research and applications of cassava flour and starch: a review, J. Food Sci. Technol. 56 (2019) 2799–2813. https://doi.org/10.1007/s13197-019-03814-6.
[18] F. Zhu, Structures, physicochemical properties, and applications of amaranth starch, Crit. Rev. Food Sci. Nutr. 57 (2017) 313–325. https://doi.org/10.1080/10408398.2013.862784.
[19] E.D.R. Zavareze, A.R.G. Dias, Impact of heat-moisture treatment and annealing in starches: A review, Carbohydr. Polym. 83 (2011) 317–328. https://doi.org/10.1016/j.carbpol.2010.08.064.
[20] E. Šárka, V. Dvořáček, New processing and applications of waxy starch (a review), J. Food Eng. 206 (2017) 77–87. https://doi.org/10.1016/j.jfoodeng.2017.03.006.
[21] J. Ye, X. Hu, S. Luo, W. Liu, J. Chen, Z. Zeng, C. Liu, Properties of Starch after Extrusion: A Review, Starch/Staerke. 70 (2018) 1–8. https://doi.org/10.1002/star.201700110.
[22] G. Moad, Chemical modification of starch by reactive extrusion, Prog. Polym. Sci. 36 (2011) 218–237. https://doi.org/10.1016/j.progpolymsci.2010.11.002.
[23] N. Masina, Y.E. Choonara, P. Kumar, L.C. du Toit, M. Govender, S. Indermun, V. Pillay, A review of the chemical modification techniques of starch, Carbohydr. Polym. 157 (2017) 1226–1236. https://doi.org/10.1016/j.carbpol.2016.09.094.
[24] B.C. Maniglia, N. Castanha, P. Le-Bail, A. Le-Bail, P.E.D. Augusto, Starch modification through environmentally friendly alternatives: a review, Crit. Rev. Food Sci. Nutr. 0 (2020) 1–24. https://doi.org/10.1080/10408398.2020.1778633.
[25] I. Grgić, Đ. Ačkar, V. Barišić, M. Vlainić, N. Knežević, Z. Medverec Knežević, Nonthermal methods for starch modification—A review, J. Food Process. Preserv. 43 (2019) 1–13. https://doi.org/10.1111/jfpp.14242.
[26] A.C. Wu, T. Witt, R.G. Gilbert, Characterization methods for starch-based materials: State of the art and perspectives, Aust. J. Chem. 66 (2013) 1550–1563. https://doi.org/10.1071/CH13397.
[27] G. Liu, Z. Gu, Y. Hong, L. Cheng, C. Li, Structure, functionality and applications of debranched starch: A review, Trends Food Sci. Technol. 63 (2017) 70–79. https://doi.org/10.1016/j.tifs.2017.03.004.
[28] N. Soykeabkaew, C. Thanomsilp, O. Suwantong, A review: Starch-based composite foams, Compos. Part A Appl. Sci. Manuf. 78 (2015) 246–263. https://doi.org/10.1016/j.compositesa.2015.08.014.
[29] A. Jiménez, M.J. Fabra, P. Talens, A. Chiralt, Edible and Biodegradable Starch Films: A Review, Food Bioprocess Technol. 5 (2012) 2058–2076. https://doi.org/10.1007/s11947-012-0835-4.
[30] U. Shah, F. Naqash, A. Gani, F.A. Masoodi, Art and Science behind Modified Starch Edible Films and Coatings: A Review, Compr. Rev. Food Sci. Food Saf. 15 (2016) 568–580. https://doi.org/10.1111/1541-4337.12197.

[31] H. Ismail, M. Irani, Z. Ahmad, Starch-based hydrogels: Present status and applications, Int. J. Polym. Mater. Polym. Biomater. 62 (2013) 411–420. https://doi.org/10.1080/00914037.2012.719141.
[32] B. Biduski, W.M.F. da Silva, R. Colussi, S.L. de M. El Halal, L.T. Lim, Á.R.G. Dias, E. da R. Zavareze, Starch hydrogels: The influence of the amylose content and gelatinization method, Int. J. Biol. Macromol. 113 (2018) 443–449. https://doi.org/10.1016/j.ijbiomac.2018.02.144.
[33] C. Xiao, Current advances of chemical and physical starch-based hydrogels, Starch/Staerke. 65 (2013) 82–88. https://doi.org/10.1002/star.201200113.
[34] M.A.V.T. Garcia, C.F. Garcia, A.A.G. Faraco, Pharmaceutical and Biomedical Applications of Native and Modified Starch: A Review, Starch/Staerke. 72 (2020) 1–15. https://doi.org/10.1002/star.201900270.
[35] M. V. Lawal, Modified Starches as Direct Compression Excipients – Effect of Physical and Chemical Modifications on Tablet Properties: A Review, Starch/Staerke. 71 (2019) 1–10. https://doi.org/10.1002/star.201800040.
[36] B. Khan, M. Bilal Khan Niazi, G. Samin, Z. Jahan, Thermoplastic Starch: A Possible Biodegradable Food Packaging Material—A Review, J. Food Process Eng. 40 (2017). https://doi.org/10.1111/jfpe.12447.
[37] G.A. Valencia, E.N. Zare, P. Makvandi, T.J. Gutiérrez, Self-Assembled Carbohydrate Polymers for Food Applications: A Review, Compr. Rev. Food Sci. Food Saf. 18 (2019) 2009–2024. https://doi.org/10.1111/1541-4337.12499.
[38] A.M. Helbling, M.R. Hills, F.T. Stollmaier, T.M.S. Annen, Use of Starch Dispersions as Binder in Coating Compositions and Process for Preparing the Starch Dispersion, US 2004/0014844 A1, 2004.
[39] S. Bloembergen, E. Strom, R.H. Nebeling, Apparatus and Method for the Production of Corrugated and Laminated Board and Compositions Based Thereon, US 2009/011737.6 A1, 2009.
[40] S. Di Risio, R. De Jong, R. Carlson, Coating for Paper Adapted for Inkjet Printing, US 2015/0110977 A1, 2015.
[41] S. Bloembergen, Methods of Using Biobased Latex Binders for Improved Printing Performance, US 9,157,187 B2, 2015.
[42] H. Li, Y. Qi, Y. Zhao, J. Chi, S. Cheng, Starch and its derivatives for paper coatings: A review, Prog. Org. Coatings. 135 (2019) 213–227. https://doi.org/10.1016/j.porgcoat.2019.05.015.
[43] A. Chemelli, F. Gomernik, F. Thaler, A. Huber, U. Hirn, W. Bauer, S. Spirk, Cationic starches in paper-based applications—A review on analytical methods, Carbohydr. Polym. 235 (2020) 115964. https://doi.org/10.1016/j.carbpol.2020.115964.
[44] B.A. Cinelli, L.R. Castilho, D.M.G. Freire, A.M. Castro, A brief review on the emerging technology of ethanol production by cold hydrolysis of raw starch, Fuel. 150 (2015) 721–729. https://doi.org/10.1016/j.fuel.2015.02.063.
[45] F. Vendruscolo, Starch: a potential substrate for biohydrogen production, Int. Jounral Energy Res. 39 (2015) 293–302. https://doi.org/10.1002/er.
[46] M. Kaseem, K. Hamad, F. Deri, Thermoplastic starch blends: A review of recent

works, Polym. Sci. - Ser. A. 54 (2012) 165–176. https://doi.org/10.1134/S0965545X1202006X.
[47] M.J. Santander-ortega, T. Stauner, B. Loretz, J.L. Ortega-vinuesa, D. Bastos-González, G. Wenz, Nanoparticles made from novel starch derivatives for transdermal drug delivery, J. Control. Release. 141 (2010) 85–92. https://doi.org/10.1016/j.jconrel.2009.08.012.
[48] L. Tuovinen, E. Ruhanen, T. Kinnarinen, S. Ro, Starch acetate microparticles for drug delivery into retinal pigment epithelium — in vitro study, 98 (2004) 407–413. https://doi.org/10.1016/j.jconrel.2004.05.016.
[49] J.Y. Kim, D.J. Park, S.T. Lim, Fragmentation of waxy rice starch granules by enzymatic hydrolysis, Cereal Chem. 85 (2008) 182–187. https://doi.org/10.1094/CCHEM-85-2-0182.
[50] D. Liu, Q. Wu, H. Chen, P.R. Chang, Transitional properties of starch colloid with particle size reduction from micro- to nanometer, J. Colloid Interface Sci. 339 (2009) 117–124. https://doi.org/10.1016/j.jcis.2009.07.035.
[51] S. Wang, L. Copeland, Effect of Acid Hydrolysis on Starch Structure and Functionality: A Review, Crit. Rev. Food Sci. Nutr. 55 (2015) 1081–1097. https://doi.org/10.1080/10408398.2012.684551.
[52] S. Bloembergen, E. Vanegdom, R. Wildi, I.J. Mclennan, D.I. Lee, C.P. Klass, J.V.A.N. Leeuwen, Biolatex Binders for Paper and Paperboard Applications, Jounral Pulp Pap. Sci. 36 (2010) 1–11.
[53] S. Bloembergen, M.P. Santos, P. Greenall, R. Dejong, J.Y. Shin, N. Jones, P.D. Fleming, M.K. Joyce, D.I. Lee, THE EFFECTS OF BIOLATEX BINDERS ON THE DYNAMIC WATER RETENTION PROPERTIES OF PAPER COATING FORMULATIONS, (2013) 8–10.
[54] B.P. Van Ballegooie, V.P. Marketing, B. Development, P. Greenall, V.P.G. Sales, S. Bloembergen, E.V.P. Technology, R. Dejong, EcoSphere ® biolatex ® binders : Next generation solutions for today ' s paper coating industry, (2011) 100–104.
[55] M. Grossutti, C. Miki, J.R. Dutcher, Phytoglycogen Nanoparticles: 1. Key properties relevant to its use as a natural moisturizing ingredient, Househ. Pers. Care Today. 12 (2017) 47–51. http://mirexusbiotech.com/wp-content/uploads/2015/11/Phytoglycogen_HPC.pdf.
[56] J.D. Nickels, J. Atkinson, E. Papp-szabo, C. Stanley, S.O. Diallo, S. Perticaroli, B. Baylis, P. Mahon, G. Ehlers, J. Katsaras, J.R. Dutcher, Structure and Hydration of Highly-Branched, Monodisperse Phytoglycogen Nanoparticles, (2016). https://doi.org/10.1021/acs.biomac.5b01393.
[57] M. Grossutti, E. Bergmann, B. Baylis, J.R. Dutcher, Equilibrium Swelling, Interstitial Forces, and Water Structuring in Phytoglycogen Nanoparticle Films, Langmuir. 33 (2017) 2810–2816. https://doi.org/10.1021/acs.langmuir.7b00025.
[58] C. Bastioli, Properties and applications of Mater-Bi starch-based materials, 59 (1998).
[59] P. Tomasik, C.H. Schilling, Chemical modification of starch, 2004. https://doi.org/10.1016/S0065-2318(04)59005-4.
[60] F. Xie, L. Yu, H. Liu, L. Chen, Starch modification using reactive extrusion,

Starch/Staerke. 58 (2006) 131–139. https://doi.org/10.1002/star.200500407.
[61] E.M. Ahmed, Hydrogel: Preparation, characterization, and applications: A review, J. Adv. Res. 6 (2015) 105–121. https://doi.org/10.1016/j.jare.2013.07.006.
[62] T.S. Anirudhan, J. Parvathy, A.S. Nair, A novel composite matrix based on polymeric micelle and hydrogel as a drug carrier for the controlled release of dual drugs, Carbohydr. Polym. 136 (2016) 1118–1127. https://doi.org/10.1016/j.carbpol.2015.10.019.
[63] T. Gilbert, R.J. Alsop, M. Babi, J. Moran-Mirabal, M.C. Rheinstädter, T. Hoare, Nanostructure of Fully Injectable Hydrazone-Thiosuccinimide Interpenetrating Polymer Network Hydrogels Assessed by Small-Angle Neutron Scattering and dSTORM Single-Molecule Fluorescence Microscopy, ACS Appl. Mater. Interfaces. 9 (2017) 42179–42191. https://doi.org/10.1021/acsami.7b11637.
[64] E. Bakaic, N.M.B. Smeets, O. Barrigar, R. Alsop, M.C. Rheinstädter, T. Hoare, PH-Ionizable in Situ Gelling Poly(oligo ethylene glycol methacrylate)-Based Hydrogels: The Role of Internal Network Structures in Controlling Macroscopic Properties, Macromolecules. 50 (2017) 7687–7698. https://doi.org/10.1021/acs.macromol.7b01505.
[65] C. Chen, L. Wang, L. Deng, R. Hu, A. Dong, Performance optimization of injectable chitosan hydrogel by combining physical and chemical triple crosslinking structure, J. Biomed. Mater. Res. - Part A. 101 A (2013) 684–693. https://doi.org/10.1002/jbm.a.34364.
[66] B. Sarker, J. Rompf, R. Silva, N. Lang, R. Detsch, J. Kaschta, B. Fabry, A.R. Boccaccini, Alginate-based hydrogels with improved adhesive properties for cell encapsulation, Int. J. Biol. Macromol. 78 (2015) 72–78. https://doi.org/10.1016/j.ijbiomac.2015.03.061.
[67] S.S. Stalling, S.O. Akintoye, S.B. Nicoll, Development of photocrosslinked methylcellulose hydrogels for soft tissue reconstruction, Acta Biomater. 5 (2009) 1911–1918. https://doi.org/10.1016/j.actbio.2009.02.020.
[68] S. hee Kim, C.C. Chu, Pore structure analysis of swollen dextran-methacrylate hydrogels by SEM and mercury intrusion porosimetry, J. Biomed. Mater. Res. 53 (2000) 258–266. https://doi.org/10.1002/(SICI)1097-4636(2000)53:3<258::AID-JBM11>3.0.CO;2-O.
[69] A. Shalviri, Q. Liu, M.J. Abdekhodaie, X.Y. Wu, Novel modified starch-xanthan gum hydrogels for controlled drug delivery: Synthesis and characterization, Carbohydr. Polym. 79 (2010) 898–907. https://doi.org/10.1016/j.carbpol.2009.10.016.
[70] J. Kopeček, J. Yang, Smart self-assembled hybrid hydrogel biomaterials, Angew. Chemie - Int. Ed. 51 (2012) 7396–7417. https://doi.org/10.1002/anie.201201040.
[71] M.M. Khansari, L. V. Sorokina, P. Mukherjee, F. Mukhtar, M.R. Shirdar, M. Shahidi, T. Shokuhfar, Classification of Hydrogels Based on Their Source: A Review and Application in Stem Cell Regulation, Jom. 69 (2017) 1340–1347. https://doi.org/10.1007/s11837-017-2412-9.
[72] V. Brar, G. Kaur, Biopolymers as Carriers for Nasal Drug Delivery, Polym. - Plast. Technol. Eng. 53 (2014) 1518–1531.

https://doi.org/10.1080/03602559.2014.912327.
[73] S.K.. Gulrez, S. Al-Assaf, G.O. Phillips, Hydrogels: Methods of Preparation, Characterisation and Applications in Molecular and Environmental Bioengineering, Prog. Mol. Environ. Bioeng. - From Anal. Moddelling to Technol. Appl. (2011) 646. https://doi.org/10.5772/24553.
[74] J. jiang Duan, L. na Zhang, Robust and smart hydrogels based on natural polymers, Chinese J. Polym. Sci. (English Ed. 35 (2017) 1165–1180. https://doi.org/10.1007/s10118-017-1983-9.
[75] M. Burek, I. Wandzik, Synthetic Hydrogels with Covalently Incorporated Saccharides Studied for Biomedical Applications–15 Year Overview, Polym. Rev. 58 (2018) 537–586. https://doi.org/10.1080/15583724.2018.1443122.
[76] M. Patenaude, T. Hoare, Injectable, mixed natural-synthetic polymer hydrogels with modular properties, Biomacromolecules. 13 (2012) 369–378. https://doi.org/10.1021/bm2013982.
[77] B.M. Discher, Y.Y. Won, D.S. Ege, J.C.M. Lee, F.S. Bates, D.E. Discher, D.A. Hammer, Polymersomes: Tough vesicles made from diblock copolymers, Science (80-.). 284 (1999) 1143–1146. https://doi.org/10.1126/science.284.5417.1143.
[78] K. Haraguchi, Nanocomposite hydrogels, Curr. Opin. Solid State Mater. Sci. 11 (2007) 47–54. https://doi.org/10.1016/j.cossms.2008.05.001.
[79] P. Thoniyot, M.J. Tan, A.A. Karim, D.J. Young, X.J. Loh, Nanoparticle–Hydrogel Composites: Concept, Design, and Applications of These Promising, Multi-Functional Materials, Adv. Sci. 2 (2015) 1–13. https://doi.org/10.1002/advs.201400010.
[80] S.R. Sershen, S.L. Westcott, N.J. Halas, J.L. West, Independent optically addressable nanoparticle-polymer optomechanical composites, Appl. Phys. Lett. 80 (2002) 4609–4611. https://doi.org/10.1063/1.1481536.
[81] N. Ravi, H.A. Aliyar, P.D. Hamilton, Hydrogel nanocomposite as a synthetic intra-ocular lens capable of accommodation, Macromol. Symp. 227 (2005) 191–202. https://doi.org/10.1002/masy.200550919.
[82] M. Liu, Y. Ishida, Y. Ebina, T. Sasaki, T. Aida, Photolatently modulable hydrogels using unilamellar titania nanosheets as photocatalytic crosslinkers, Nat. Commun. 4 (2013) 1–7. https://doi.org/10.1038/ncomms3029.
[83] L. Sheeney-Haj-Ichia, G. Sharabi, I. Willner, Control of the electronic properties of thermosensitive poly(N-isopropylacrylamide) and Au-nanoparticle/poly(N-isopropylacrylamide) composite hydrogels upon phase transition, Adv. Funct. Mater. 12 (2002) 27–32. https://doi.org/10.1002/1616-3028(20020101)12:1<27::AID-ADFM27>3.0.CO;2-T.
[84] Y.G. Guo, J.S. Hu, H.P. Liang, L.J. Wan, C.L. Bai, Highly Dispersed Metal Nanoparticles in Porous Anodic Alumina Films Prepared by a Breathing Process of Polyacrylamide Hydrogel, Chem. Mater. 15 (2003) 4332–4336. https://doi.org/10.1021/cm0343397.
[85] C.D. Jones, L.A. Lyon, Photothermal patterning of microgel/gold nanoparticle composite colloidal crystals, J. Am. Chem. Soc. 125 (2003) 460–465. https://doi.org/10.1021/ja027431x.

[86] P.S.K. Murthy, Y. Murali Mohan, K. Varaprasad, B. Sreedhar, K. Mohana Raju, First successful design of semi-IPN hydrogel-silver nanocomposites: A facile approach for antibacterial application, J. Colloid Interface Sci. 318 (2008) 217–224. https://doi.org/10.1016/j.jcis.2007.10.014.
[87] Y. Xiang, D. Chen, Preparation of a novel pH-responsive silver nanoparticle/poly(HEMA-PEGMA-MAA) composite hydrogel, Eur. Polym. J. 43 (2007) 4178–4187. https://doi.org/10.1016/j.eurpolymj.2007.08.005.
[88] K. Varaprasad, G. Siva Mohan Reddy, J. Jayaramudu, R. Sadiku, K. Ramam, S.S. Ray, Development of microbial resistant Carbopol nanocomposite hydrogels via a green process, Biomater. Sci. 2 (2014) 257–263. https://doi.org/10.1039/c3bm60185d.
[89] D. Zhang, J. Yang, S. Bao, Q. Wu, Q. Wang, Semiconductor nanoparticle-based hydrogels prepared via self-initiated polymerization under sunlight, even visible light, Sci. Rep. 3 (2013) 1–7. https://doi.org/10.1038/srep01399.
[90] G.D. Prestwich, A. Skardal, J. Zhang, L. McCoard, S. Oottamasathien, Dynamically crosslinked gold nanoparticle-hyaluronan hydrogels, Adv. Mater. 22 (2010) 4736–4740. https://doi.org/10.1002/adma.201001436.
[91] H. Wu, G. Yu, L. Pan, N. Liu, M.T. McDowell, Z. Bao, Y. Cui, Stable Li-ion battery anodes by in-situ polymerization of conducting hydrogel to conformally coat silicon nanoparticles, Nat. Commun. 4 (2013). https://doi.org/10.1038/ncomms2941.
[92] A.O. Moughton, M.A. Hillmyer, T.P. Lodge, Multicompartment block polymer micelles, Macromolecules. 45 (2012) 2–19. https://doi.org/10.1021/ma201865s.
[93] D. Sivakumaran, D. Maitland, T. Hoare, Injectable microgel-hydrogel composites for prolonged small-molecule drug delivery, Biomacromolecules. 12 (2011) 4112–4120. https://doi.org/10.1021/bm201170h.
[94] R.T. Chacko, J. Ventura, J. Zhuang, S. Thayumanavan, Polymer nanogels: A versatile nanoscopic drug delivery platform, Adv. Drug Deliv. Rev. 64 (2012) 836–851. https://doi.org/10.1016/j.addr.2012.02.002.
[95] G.L. Li, H. Möhwald, D.G. Shchukin, Precipitation polymerization for fabrication of complex core-shell hybrid particles and hollow structures, Chem. Soc. Rev. 42 (2013) 3628–3646. https://doi.org/10.1039/c3cs35517a.
[96] A.D. Schlüter, A. Halperin, M. Kröger, D. Vlassopoulos, G. Wegner, B. Zhang, Dendronized polymers: Molecular objects between conventional linear polymers and colloidal particles, ACS Macro Lett. 3 (2014) 991–998. https://doi.org/10.1021/mz500376e.
[97] I. Postnova, V. Silant'ev, M.H. Kim, G.Y. Song, I. Kim, C.S. Ha, Y. Shchipunov, Hyperbranched polyglycerol hydrogels prepared through biomimetic mineralization, Colloids Surfaces B Biointerfaces. 103 (2013) 31–37. https://doi.org/10.1016/j.colsurfb.2012.10.026.
[98] J.R. Yu, M. Janssen, B.J. Liang, H.C. Huang, J.P. Fisher, A liposome/gelatin methacrylate nanocomposite hydrogel system for delivery of stromal cell-derived factor-1α and stimulation of cell migration, Acta Biomater. 108 (2020) 67–76. https://doi.org/10.1016/j.actbio.2020.03.015.

[99] T. Kashiwagi, F. Du, J.F. Douglas, K.I. Winey, R.H. Harris, J.R. Shields, Nanoparticle networks reduce the flammability of polymer nanocomposites., Nat. Mater. 4 (2005) 928–933. https://doi.org/10.1038/nmat1502.
[100] Q. Wang, R. Hou, Y. Cheng, J. Fu, Super-tough double-network hydrogels reinforced by covalently compositing with silica-nanoparticles, Soft Matter. 8 (2012) 6048. https://doi.org/10.1039/c2sm07233e.
[101] S.-H. Hu, T.-Y. Liu, D.-M. Liu, S.-Y. Chen, Nano-ferrosponges for controlled drug release, J. Control. Release. 121 (2007) 181–189. https://doi.org/10.1016/j.jconrel.2007.06.002.
[102] G. Hon, B.R. Goldstein, J. J. Thomson's plum-pudding atomic model: The making of a scientific myth, Ann. Phys. 525 (2013) A129–A133. https://doi.org/10.1002/andp.201300732.
[103] I. Lynch, K.A. Dawson, Synthesis and Characterization of an Extremely Versatile Structural Motif Called the "Plum-Pudding" Gel, J. Phys. Chem. B. 107 (2003) 9629–9637. https://doi.org/10.1021/jp022008w.
[104] N. Sahiner, Colloidal nanocomposite hydrogel particles, Colloid Polym. Sci. 285 (2007) 413–421. https://doi.org/10.1007/s00396-006-1583-7.
[105] M.A. Campea, M.J. Majcher, A. Lofts, T. Hoare, A Review of Design and Fabrication Methods for Nanoparticle Network Hydrogels for Biomedical, Environmental, and Industrial Applications, Adv. Funct. Mater. 2102355 (2021). https://doi.org/10.1002/adfm.202102355.
[106] I. Lynch, K.A. Dawson, Release of model compounds from "plum-pudding"-type gels composed of microgel particles randomly dispersed in a gel matrix, J. Phys. Chem. B. 108 (2004) 10893–10898. https://doi.org/10.1021/jp0487105.
[107] D. Maitland, S.B. Campbell, J. Chen, T. Hoare, Controlling the resolution and duration of pulsatile release from injectable magnetic "plum-pudding" nanocomposite hydrogels, RSC Adv. 6 (2016) 15770–15781. https://doi.org/10.1039/c6ra01665k.
[108] Q. Wang, Z. Gu, S. Jamal, M.S. Detamore, C. Berkland, Hybrid hydroxyapatite nanoparticle colloidal gels are injectable fillers for bone tissue engineering, Tissue Eng Part A. 19 (2013) 2586–2593. https://doi.org/10.1089/ten.TEA.2013.0075.
[109] W. Xu, F. Lu, S. Chen, X. Lin, S. Zhou, W. Wu, Synthesis of polymer macrogels with rapid and significant response to glucose concentration changes, RSC Adv. 7 (2017) 55945–55956. https://doi.org/10.1039/c7ra11920h.
[110] O.S. Fenton, M.W. Tibbitt, E.A. Appel, S. Jhunjhunwala, M.J. Webber, R. Langer, Injectable Polymer-Nanoparticle Hydrogels for Local Immune Cell Recruitment, Biomacromolecules. 20 (2019) 4430–4436. https://doi.org/10.1021/acs.biomac.9b01129.
[111] A. Shimoda, S. ichi Sawada, A. Kano, A. Maruyama, A. Moquin, F.M. Winnik, K. Akiyoshi, Dual crosslinked hydrogel nanoparticles by nanogel bottom-up method for sustained-release delivery, Colloids Surfaces B Biointerfaces. 99 (2012) 38–44. https://doi.org/10.1016/j.colsurfb.2011.09.025.
[112] S.H. Cho, J.H. Hong, Y.W. Noh, E. Lee, C.S. Lee, Y.T. Lim, Raspberry-like poly(γ-glutamic acid) hydrogel particles for ph-dependent cell membrane passage

and controlled cytosolic delivery of antitumor drugs, Int. J. Nanomedicine. 11 (2016) 5621–5632. https://doi.org/10.2147/IJN.S117862.
[113] G. Huang, J. Gao, Z. Hu, J. V. St. John, B.C. Ponder, D. Moro, Controlled drug release from hydrogel nanoparticle networks, J. Control. Release. 94 (2004) 303–311. https://doi.org/10.1016/j.jconrel.2003.10.007.
[114] Z. Hu, X. Xia, M. Marquez, H. Weng, L. Tang, Controlled release from and tissue response to physically bonded hydrogel nanoparticle assembly, Macromol. Symp. 227 (2005) 275–284. https://doi.org/10.1002/masy.200550927.
[115] K. Zhai, F. Zhang, C. Wang, X. Pei, Y. Tan, Y. Bai, B. Zhang, Y. Wang, K. Xu, P. Wang, Synthesis of millimeter-sized hydrogel beads by inverse Pickering polymerization using starch-based nanoparticles as emulsifier, Polym. Adv. Technol. (2020) 1321–1329. https://doi.org/10.1002/pat.4861.
[116] Y. Li, C. Liu, Y. Tan, K. Xu, C. Lu, P. Wang, In situ hydrogel constructed by starch-based nanoparticles via a Schiff base reaction, Carbohydr. Polym. 110 (2014) 87–94. https://doi.org/10.1016/j.carbpol.2014.03.058.
[117] Y. Li, Y. Tan, K. Xu, C. Lu, X. Liang, P. Wang, In situ crosslinkable hydrogels formed from modified starch and O-carboxymethyl chitosan, RSC Adv. 5 (2015) 30303–30309. https://doi.org/10.1039/c4ra14984j.
[118] G. Saragih, T. Tamrin, Marpongahtun, D.Y. Nasution, Abdillah, Preparation of semi-IPN hydrogel from starch nanoparticles of magrove fruit and monomer acrylic acid using crosslinker N,N' methylene bisacrylamide, AIP Conf. Proc. 2049 (2018). https://doi.org/10.1063/1.5082454.
[119] X. Ma, R. Jian, P.R. Chang, J. Yu, Fabrication and characterization of citric acid-modified starch nanoparticles/plasticized-starch composites, Biomacromolecules. 9 (2008) 3314–3320. https://doi.org/10.1021/bm800987c.
[120] Erizal, Synthesis of poly(acrylamide-co-acrylic acid)-starch based superabsorbent hydrogels by gamma radiation: Study its swelling behavior, Indo. J Chem. 12 (2012).
[121] I. Puspita, C. Winarti, A. Maddu, M. Kurniati, Synthesis of cassava starch based nano-hydrogels using gamma irradiation, IOP Conf. Ser. Earth Environ. Sci. 299 (2019). https://doi.org/10.1088/1755-1315/299/1/012009.
[122] S. Li, Y. Xia, Y. Qiu, X. Chen, S. Shi, Preparation and property of starch nanoparticles reinforced aldehyde–hydrazide covalently crosslinked PNIPAM hydrogels, J. Appl. Polym. Sci. 135 (2018) 1–13. https://doi.org/10.1002/app.45761.
[123] J.M. Anderson, A.K. McNally, Biocompatibility of implants: Lymphocyte/macrophage interactions, Semin. Immunopathol. 33 (2011) 221–233. https://doi.org/10.1007/s00281-011-0244-1.
[124] P.A. Markov, D.S. Khramova, K. V. Shumikhin, I.R. Nikitina, V.S. Beloserov, E.A. Martinson, S.G. Litvinets, S. V. Popov, Mechanical properties of the pectin hydrogels and inflammation response to their subcutaneous implantation, J. Biomed. Mater. Res. - Part A. 107 (2019) 2088–2098. https://doi.org/10.1002/jbm.a.36721.
[125] L.T. Kuhn, Chapter 5 - Biomaterials, in: Introd. to Biomed. Eng. (Third Ed., 2012:

pp. 219–271. https://doi.org/10.1016/B978-0-12-374979-6.00005-8.
[126] S.R. Meyers, M.W. Grinstaff, Biocompatible and bioactive surface modifications for prolonged in vivo efficacy, Chem Rev. 112 (2012) 1615–1632.
[127] S. Barr, E.W. Hill, A. Bayat, Functional biocompatibility testing of silicone breast implants and a novel classification system based on surface roughness, J. Mech. Behav. Biomed. Mater. 75 (2017) 75–81. https://doi.org/10.1016/j.jmbbm.2017.06.030.
[128] T.A. Horbett, J.L. Brash, Proteins at Interfaces: Current Issues and Future Prospects, (1987) 1–33. https://doi.org/10.1021/bk-1987-0343.ch001.
[129] J.L. Brash, T.A. Horbett, No Title, in: Proteins at Interfaces, 1995: pp. 1–23.
[130] I. Lynch, E. Al., The nanoparticle-protein complex as a biological entity; a complex fluids and surface science challenge for the 21st century, Adv Colloid Interface Sci. 134 (2007) 167–174.
[131] J.M. Anderson, Biological Responses to Materials, Annu. Rev. Mater. Res. 31 (2000) 81–110.
[132] J.M. Anderson, A. Rodriguez, D.T. Chang, Foreign body reaction to biomaterials, Semin Immunol. 20 (2008) 86–100.
[133] Z. Sheikh, P.J. Brooks, O. Barzilay, N. Fine, M. Glogauer, Macrophages, foreign body giant cells and their response to implantable biomaterials, Materials (Basel). 8 (2015) 5671–5701. https://doi.org/10.3390/ma8095269.
[134] B.D. Ratner, Replacing and renewing synthetic materials, biomimetics, and tissue engineering in implant dentistry, Jounral Dent. Eduction. 65 (2001) 1340–1347.
[135] K.C. Dee, R. Bizios, Protein-Surface Interactions in An Introduction to Tissue-Biomateral Interactions, John Wiley & Sons Inc., 2002.
[136] J. Ladd, Z. Zhang, S. Chen, J.C. Hower, S. Jiang, Zwitterionic polymers exhibiting high resistance to nonspecific protein adsorption from human serum and plasma, Biomacromolecules. 9 (2008) 1357–1361. https://doi.org/10.1021/bm701301s.
[137] K.P. García, K. Zarschler, L. Barbaro, J.A. Barreto, W. O'Malley, L. Spiccia, H. Stephan, B. Graham, Zwitterionic-coated "stealth" nanoparticles for biomedical applications: Recent advances in countering biomolecular corona formation and uptake by the mononuclear phagocyte system, Small. 10 (2014) 2516–2529. https://doi.org/10.1002/smll.201303540.
[138] S. Sharma, R.W. Johnson, T.A. Desai, Evaluation of the Stability of Nonfouling Ultrathin Poly(ethylene glycol) Films for Silicon-Based Microdevices, Langmuir. 20 (2004) 348–356. https://doi.org/10.1021/la034753l.
[139] F. Kawai, Microbial degradation of polyethers, Appl. Microbiol. Biotechnol. 58 (2002) 30–38. https://doi.org/10.1007/s00253-001-0850-2.
[140] J.K. Armstrong, G. Hempel, S. Koling, L.S. Chan, T. Fisher, H.J. Meiselman, G. Garratty, Antibody against poly(ethylene glycol) adversely affects PEG-asparaginase therapy in acute lymphoblastic leukemia patients, Cancer. 110 (2007) 103–111. https://doi.org/10.1002/cncr.22739.
[141] F. Variola, J. Brunski, G. Orsini, P.T. De Oliveira, A. Nanci, Nanoscale surface modifications of medically-relevant metals: state-of-the art and perspectives, Nanoscale. 3 (2012) 335–353. https://doi.org/10.1039/c0nr00485e.Nanoscale.

[142] A.A. Vertegel, R.W. Siegel, J.S. Dordick, Silica nanoparticle size influences the structure and enzymatic activity of adsorbed lysozyme, Langmuir. 20 (2004) 6800–6807. https://doi.org/10.1021/la0497200.
[143] J.E. Gagner, M.D. Lopez, J.S. Dordick, R.W. Siegel, Effect of gold nanoparticle morphology on adsorbed protein structure and function, Biomaterials. 32 (2011) 7241–7252. https://doi.org/10.1016/j.biomaterials.2011.05.091.
[144] P. Roach, D. Eglin, K. Rohde, C.C. Perry, Modern biomaterials: A review - Bulk properties and implications of surface modifications, J. Mater. Sci. Mater. Med. 18 (2007) 1263–1277. https://doi.org/10.1007/s10856-006-0064-3.
[145] A. Kondo, F. Murakami, M. Kawagoe, K. Higashitani, Kinetic and circular dichroism studies of enzymes adsorbed on ultrafine silica particles, Appl. Microbiol. Biotechnol. 39 (1993) 726–731. https://doi.org/10.1007/BF00164457.
[146] B. Kasemo, J. Gold, Implant surfaces and interface processes., Adv. Dent. Res. 13 (1999) 8–20. https://doi.org/10.1177/08959374990130011901.
[147] D. V. Sotnikov, A.N. Berlina, V.S. Ivanov, A. V. Zherdev, B.B. Dzantiev, Adsorption of proteins on gold nanoparticles: One or more layers?, Colloids Surfaces B Biointerfaces. 173 (2019) 557–563. https://doi.org/10.1016/j.colsurfb.2018.10.025.
[148] E. Colangelo, J. Comenge, D. Paramelle, M. Volk, Q. Chen, R. Lévy, Characterizing self-assembled monolayers on gold nanoparticles, Bioconjug. Chem. 28 (2017) 11–22. https://doi.org/10.1021/acs.bioconjchem.6b00587.
[149] Y. Mao, Q. Sun, X. Wang, Q. Ouyang, L. Han, L. Jiang, D. Han, In vivo nanomechanical imaging of blood-vessel tissues directly in living mammals using atomic force microscopy, Appl. Phys. Lett. 95 (2009). https://doi.org/10.1063/1.3167546.
[150] H. Fan, P. Chen, R. Qi, J. Zhai, J. Wang, L. Chen, L. Chen, Q. Sun, Y. Song, D. Han, L. Jiang, Greatly improved blood compatibility by microscopic multiscale design of surface architectures, Small. 5 (2009) 2144–2148. https://doi.org/10.1002/smll.200900345.
[151] S.G. Lévesque, M.S. Shoichet, Synthesis of enzyme-degradable, peptide-cross-linked dextran hydrogels, Bioconjug. Chem. 18 (2007) 874–885. https://doi.org/10.1021/bc0602127.
[152] P.M. Kharkar, K.L. Kiick, A.M. Kloxin, Designing degradable hydrogels for orthogonal control of cell microenvironments., Chem. Soc. Rev. 42 (2013) 7335–72. https://doi.org/10.1039/c3cs60040h.
[153] D. Dong, J. Li, M. Cui, J. Wang, Y. Zhou, L. Luo, Y. Wei, L. Ye, H. Sun, F. Yao, In Situ "Clickable" Zwitterionic Starch Based Hydrogel for 3D Cell Encapsulation, ACS Appl. Mater. Interfaces. (2016) acsami.5b12141. https://doi.org/10.1021/acsami.5b12141.
[154] H. Meng, Q. Cheng, H. Wang, C. Li, Improving anti-protein-fouling property of polyacrylonitrile ultrafiltration membrane by grafting sulfobetaine zwitterions, J. Chem. 2014 (2014). https://doi.org/10.1155/2014/304972.
[155] L. Zhang, Z. Cao, T. Bai, L. Carr, J.R. Ella-Menye, C. Irvin, B.D. Ratner, S. Jiang, Zwitterionic hydrogels implanted in mice resist the foreign-body reaction, Nat.

Biotechnol. 31 (2013) 553–556. https://doi.org/10.1038/nbt.2580.
[156] L. Ye, Y. Zhang, B. Yang, X. Zhou, J. Li, Z. Qin, D. Dong, Y.-L. Cui, F. Yao, Zwitterionic-modified starch-based stealth micelles for prolonging circulation time and reducing macrophage response, ACS Appl. Mater. Interfaces. (2016) acsami.5b10811. https://doi.org/10.1021/acsami.5b10811.
[157] K.H.A. Lau, Peptoids for biomaterials science, Biomater. Sci. 2 (2014) 627–633. https://doi.org/10.1039/c3bm60269a.
[158] A. Laschewsky, Structures and synthesis of zwitterionic polymers, Polymers (Basel). 6 (2014) 1544–1601. https://doi.org/10.3390/polym6051544.
[159] S. Chen, J. Zheng, L. Li, S. Jiang, Strong resistance of phosphorylcholine self-assembled monolayers to protein adsorption: Insights into nonfouling properties of zwitterionic materials, J. Am. Chem. Soc. 127 (2005) 14473–14478. https://doi.org/10.1021/ja054169u.
[160] W. Yang, G. Cheng, S. Jiang, Film thickness dependence of protein adsorption from blood serum and plasma onto poly(sulfobetaine) and poly(carboxybetaine)-grafted surfaces, AIChE Annu. Meet. Conf. Proc. (2008) 9211–9214.
[161] G. Cheng, G. Li, H. Xue, S. Chen, J.D. Bryers, S. Jiang, Zwitterionic carboxybetaine polymer surfaces and their resistance to long-term biofilm formation, Biomaterials. 30 (2009) 5234–5240. https://doi.org/10.1016/j.biomaterials.2009.05.058.
[162] C.R. Emmenegger, E. Brynda, T. Riedel, Z. Sedlakova, M. Houska, A.B. Alles, Interaction of blood plasma with antifouling surfaces, Langmuir. 25 (2009) 6328–6333. https://doi.org/10.1021/la900083s.
[163] A. Lewis, Y. Tang, S. Brocchini, J.W. Choi, A. Godwin, Poly(2-methacryloyloxyethyl phosphorylcholine) for protein conjugation, Bioconjug. Chem. 19 (2008) 2144–2155. https://doi.org/10.1021/bc800242t.
[164] Z. Zhang, S. Chen, Y. Chang, S. Jiang, Surface grafted sulfobetaine polymers via atom transfer radical polymerization as superlow fouling coatings, J. Phys. Chem. B. 110 (2006) 10799–10804. https://doi.org/10.1021/jp057266i.
[165] W. Yang, H. Xue, W. Li, J.Z. And, S. Jiang, Pursuing “zero” protein adsorption of poly(carboxybetaine) from undiluted blood serum and plasma, Langmuir. 25 (2009) 11911–11916. https://doi.org/10.1021/la9015788.
[166] W.F. Lee, Y.M. Chen, Poly(sulfobetaine)s and Corresponding Cationic Polymers. X. Viscous Properties of Zwitterionic Poly(sulfobetaine) Derived from Styrene-(N,N-Dimethylammopropyl maleamidic acid) Copolymer in Aqueous Salt Solutions, J. Appl. Polym. Sci. 91 (2004) 726–734. https://doi.org/10.1002/app.13206.
[167] L. Mi, M.T. Bernards, G. Cheng, Q. Yu, S. Jiang, pH responsive properties of non-fouling mixed-charge polymer brushes based on quaternary amine and carboxylic acid monomers, Biomaterials. 31 (2010) 2919–2925. https://doi.org/10.1016/j.biomaterials.2009.12.038.
[168] L. Mi, S. Jiang, Integrated antimicrobial and nonfouling zwitterionic polymers, Angew. Chemie - Int. Ed. 53 (2014) 1746–1754. https://doi.org/10.1002/anie.201304060.

[169] V.B. Damodaran, S.N. Murthy, Bio-inspired strategies for designing antifouling biomaterials, Biomater. Res. 20 (2016). https://doi.org/10.1186/s40824-016-0064-4.
[170] Z.G. Estephan, P.S. Schlenoff, J.B. Schlenoff, Zwitteration as an alternative to PEGylation, Langmuir. 27 (2011) 6794–6800. https://doi.org/10.1021/la200227b.
[171] R. Esmaeely Neisiany, M.S. Enayati, P. Sajkiewicz, Z. Pahlevanneshan, S. Ramakrishna, Insight Into the Current Directions in Functionalized Nanocomposite Hydrogels, Front. Mater. 7 (2020) 1–8. https://doi.org/10.3389/fmats.2020.00025.
[172] T. Abitbol, E.D. Cranston, Chiral Nematic Self-Assembly of Cellulose Nanocrystals in Suspensions and Solid Films, in: Handb. Green Mater., 2014: pp. 37–56. https://doi.org/10.1142/9789814566469_0035.
[173] X. Wang, H. Gan, T. Sun, B. Su, H. Fuchs, D. Vestweber, S. Butz, Stereochemistry triggered differential cell behaviours on chiral polymer surfaces, Soft Matter. 6 (2010) 3851–3855. https://doi.org/10.1039/c0sm00151a.
[174] K. Tang, H. Gan, Y. Li, L. Chi, T. Sun, H. Fuchs, Stereoselective interaction between DNA and chiral surfaces, J. Am. Chem. Soc. 130 (2008) 11284–11285. https://doi.org/10.1021/ja8044184.
[175] H. Gan, K. Tang, T. Sun, M. Hirtz, Y. Li, L. Chi, S. Butz, H. Fuchs, Selective adsorption of DNA on chiral surfaces: Supercoiled or relaxed conformation, Angew. Chemie - Int. Ed. 48 (2009) 5282–5286. https://doi.org/10.1002/anie.200806295.
[176] T. Sun, G. Qing, B. Su, L. Jiang, Functional biointerface materials inspired from nature, Chem. Soc. Rev. 40 (2011) 2909–2921. https://doi.org/10.1039/c0cs00124d.
[177] K. Wang, C. Zhou, Y. Hong, X. Zhang, A review of protein adsorption on bioceramics, Interface Focus. 2 (2012) 259–277. https://doi.org/10.1098/rsfs.2012.0012.
[178] P. Sen, S. Yamaguchi, T. Tahara, New insight into the surface denaturation of proteins: Electronic sum frequency generation study of cytochrome c at water interfaces, J. Phys. Chem. B. 112 (2008) 13473–13475. https://doi.org/10.1021/jp8061288.
[179] J.H. Park, J.A. Jackman, A.R. Ferhan, G.J. Ma, B.K. Yoon, N.J. Cho, Temperature-Induced Denaturation of BSA Protein Molecules for Improved Surface Passivation Coatings, ACS Appl. Mater. Interfaces. 10 (2018) 32047–32057. https://doi.org/10.1021/acsami.8b13749.
[180] Q. Yu, Y. Zhang, H. Wang, J. Brash, H. Chen, Anti-fouling bioactive surfaces, Acta Biomater. 7 (2011) 1550–1557. https://doi.org/10.1016/j.actbio.2010.12.021.
[181] J.L. Brash, Exploiting the current paradigm of blood-material interactions for the rational design of blood-compatible materials, J Biomater Sci Polym Ed. 11 (2000). https://doi.org/doi: 10.1163/156856200744237.
[182] G. Wang, Z. Guo, W. Liu, Interfacial effects of superhydrophobic plant surfaces: A Review, J. Bionic Eng. 11 (2014) 325–345. https://doi.org/10.1016/S1672-6529(14)60047-0.
[183] M.J. Kreder, J. Alvarenga, P. Kim, J. Aizenberg, Design of anti-icing surfaces:

Smooth, textured or slippery?, Nat. Rev. Mater. 1 (2016). https://doi.org/10.1038/natrevmats.2015.3.
[184] J.L. Drury, D.J. Mooney, Hydrogels for tissue engineering: Scaffold design variables and applications, Biomaterials. 24 (2003) 4337–4351. https://doi.org/10.1016/S0142-9612(03)00340-5.
[185] J. Rouwkema, N.C. Rivron, C.A. van Blitterswijk, Vascularization in tissue engineering, Trends Biotechnol. 26 (2008) 434–441. https://doi.org/10.1016/j.tibtech.2008.04.009.
[186] J.P. Vacanti, R. Langer, Tissue engineering: The design and fabrication of living replacement devices for surgical reconstruction and transplantation, Lancet. 354 (1999) 32–34. https://doi.org/10.1016/s0140-6736(99)90247-7.
[187] Z. Mirzakhanian, K. Faghihi, A. Barati, H.R. Momeni, Synthesis of superabsorbent hydrogel nanocomposites for use as hemostatic agent, Int. J. Polym. Mater. Polym. Biomater. 65 (2016) 779–788. https://doi.org/10.1080/00914037.2016.1171218.
[188] S.J. Hollister, Porous scaffold design for tissue engineering, Nat. Mater. 4 (2005) 518–524. https://doi.org/10.1038/nmat1421.
[189] N. Annabi, J.W. Nichol, X. Zhong, C. Ji, S. Koshy, A. Khademhosseini, F. Dehghani, Controlling the porosity and microarchitecture of hydrogels for tissue engineering, Tissue Eng. - Part B Rev. 16 (2010) 371–383. https://doi.org/10.1089/ten.teb.2009.0639.
[190] A. Sergeeva, N. Feoktistova, V. Prokopovic, D. Gorin, D. Volodkin, Design of Porous Alginate Hydrogels by Sacrificial CaCO3 Templates: Pore Formation Mechanism, Adv. Mater. Interfaces. 2 (2015) 1–10. https://doi.org/10.1002/admi.201500386.
[191] B. Tan, J.Y. Lee, A.I. Cooper, Synthesis of emulsion-templated poly(acrylamide) using CO 2-in-water emulsions and poly(vinyl acetate)-based block copolymer surfactants, Macromolecules. 40 (2007) 1945–1954. https://doi.org/10.1021/ma062518e.
[192] J. Xue, T. Wu, Y. Dai, Y. Xia, Electrospinning and electrospun nanofibers: Methods, materials, and applications, Chem. Rev. 119 (2019) 5298–5415. https://doi.org/10.1021/acs.chemrev.8b00593.
[193] J. Li, A. He, C.C. Han, D. Fang, B.S. Hsiao, B. Chu, Electrospinning of hyaluronic acid (HA) and HA/ gelatin blends, Macromol. Rapid Commun. 27 (2006) 114–120. https://doi.org/10.1002/marc.200500726.
[194] L. Li, Y. Lo Hsieh, Ultra-fine polyelectrolyte hydrogel fibres from poly(acrylic acid)/poly(vinyl alcohol), Nanotechnology. 16 (2005) 2852–2860. https://doi.org/10.1088/0957-4484/16/12/020.
[195] J.Y. Lee, B. Tan, A.I. Cooper, CO2-in-water emulsion-templated poly(vinyl alcohol) hydrogels using poly(vinyl acetate)-based surfactants, Macromolecules. 40 (2007) 1955–1961. https://doi.org/10.1021/ma0625197.
[196] K. anne Johnson, N. Muzzin, S. Toufanian, R.A. Slick, M.W. Lawlor, B. Seifried, P. Moquin, D. Latulippe, T. Hoare, Drug-impregnated, pressurized gas expanded liquid-processed alginate hydrogel scaffolds for accelerated burn wound healing, Acta Biomater. 112 (2020) 101–111. https://doi.org/10.1016/j.actbio.2020.06.006.

[197] V. Saez-Martinez, G. Atorrasagasti, B. Olalde, I. Madarieta, F. Morin, N. Garagorri, Fabrication and characterization of macroporous poly(ethylene glycol) hydrogels generated by several types of porogens, Int. J. Polym. Mater. Polym. Biomater. 62 (2013) 502–508. https://doi.org/10.1080/00914037.2012.734353.
[198] K.R. Coogan, P.T. Stone, N.D. Sempertegui, S.S. Rao, Fabrication of micro-porous hyaluronic acid hydrogels through salt leaching, Eur. Polym. J. 135 (2020) 109870. https://doi.org/10.1016/j.eurpolymj.2020.109870.
[199] R.A. Quirk, R.M. France, K.M. Shakesheff, S.M. Howdle, Supercritical fluid technologies and tissue engineering scaffolds, Curr. Opin. Solid State Mater. Sci. 8 (2004) 313–321. https://doi.org/10.1016/j.cossms.2003.12.004.
[200] E.G. Lima, K.M. Durney, R.S. Shashank, A.B. Nover, G.A. Ateshian, M.A. Borden, C.T. Hung, Microbubbles as Biocompatible Porogens for Hydrogel Scaffolds, Acta Biomater. 8 (2012) 4334–4341. https://doi.org/doi:10.1016/j.actbio.2012.07.007.
[201] J. Li, C. Wu, P.K. Chu, M. Gelinsky, 3D printing of hydrogels: Rational design strategies and emerging biomedical applications, Mater. Sci. Eng. R Reports. 140 (2020) 100543. https://doi.org/10.1016/j.mser.2020.100543.
[202] V.M. Pathak, Navneet, Review on the current status of polymer degradation: a microbial approach, Bioresour. Bioprocess. 4 (2017). https://doi.org/10.1186/s40643-017-0145-9.
[203] FDA, Substances Generally Recognized as Safe - 21 CFR Parts 20, 25, 170, 184, 186, and 570, 81 (2016) 54960–55055.
[204] A. Göpferich, Polymer bulk erosion, Macromolecules. 30 (1997) 2598–2604. https://doi.org/10.1021/ma961627y.
[205] J.M. Anderson, M.S. Shive, Biodegradation and biocompatibility of PLA and PLGA microspheres, Adv. Drug Deliv. Rev. 64 (2012) 72–82. https://doi.org/10.1016/j.addr.2012.09.004.
[206] N.M.B. Smeets, E. Bakaic, M. Patenaude, T. Hoare, Injectable and tunable poly(ethylene glycol) analogue hydrogels based on poly(oligoethylene glycol methacrylate)., Chem. Commun. (Camb). 50 (2014) 3306–9. https://doi.org/10.1039/c3cc48514e.
[207] E. Bakaic, N.M.B. Smeets, T. Hoare, Injectable hydrogels based on poly(ethylene glycol) and derivatives as functional biomaterials, RSC Adv. 5 (2015) 35469–35486. https://doi.org/10.1039/C4RA13581D.
[208] S. Kim, K.E. Healy, Synthesis and characterization of injectable poly(N-isopropylacrylamide-co-acrylic acid) hydrogels with proteolytically degradable cross-links, Biomacromolecules. 4 (2003) 1214–1223. https://doi.org/10.1021/bm0340467.
[209] N. V. Tsarevsky, K. Matyjaszewski, Combining atom transfer radical polymerization and disulfide/thiol redox chemistry: A route to well-defined (bio)degradable polymeric materials, Macromolecules. 38 (2005) 3087–3092. https://doi.org/10.1021/ma050020r.
[210] P.M. Kharkar, A.M. Kloxin, K.L. Kiick, Dually degradable click hydrogels for controlled degradation and protein release, J Mater Chem B Mater Biol Med. 2

(2014) 5511–5521. https://doi.org/10.1016/j.physbeh.2017.03.040.
[211] V.M. Weaver, Cell and tissue mechanics: The new cell biology frontier, Mol. Biol. Cell. 28 (2017) 1815–1818. https://doi.org/10.1091/mbc.E17-05-0320.
[212] D.E. Discher, P. Janmey, Y.L. Wang, Tissue cells feel and respond to the stiffness of their substrate, Science (80-.). 310 (2005) 1139–1143. https://doi.org/10.1126/science.1116995.
[213] K.H. Vining, D.J. Mooney, Mechanical forces direct stem cell behaviour in development and regeneration, Nat Rev Mol Cell Biol. 18 (2017) 728–742. https://doi.org/10.1038/nrm.2017.108.Mechanical.
[214] A. Kumar, J.K. Placone, A.J. Engler, Understanding the extracellular forces that determine cell fate and maintenance, Dev. 144 (2017) 4261–4270. https://doi.org/10.1242/dev.158469.
[215] E. Ruoslahti, RGD and other recognition sequences for integrins, Annu. Rev. Cell Dev. Biol. 12 (1996) 697–715. https://doi.org/10.1146/annurev.cellbio.12.1.697.
[216] J.A. Rowley, G. Madlambayan, D.J. Mooney, Alginate hydrogels as synthetic extracellular matrix materials, Biomaterials. 20 (1999) 45–53. https://doi.org/10.1016/S0142-9612(98)00107-0.
[217] C.A. DeForest, K.S. Anseth, Photoreversible patterning of biomolecules within click-based hydrogels, Angew. Chemie - Int. Ed. 51 (2012) 1816–1819. https://doi.org/10.1002/anie.201106463.
[218] D.J. Lee, A. Fontaine, X. Meng, D. Park, Biomimetic nerve guidance conduit containing intraluminal microchannels with aligned nanofibers markedly facilitates in nerve regeneration, (2016). https://doi.org/10.1021/acsbiomaterials.6b00344.
[219] L.L. Kiessling, J.E. Gestwicki, L.E. Strong, Synthetic Multivalent Ligands as Probes of Signal Transduction, Angew Chem Int Ed Engl. 45 (2006) 2348–2368. https://doi.org/10.1002/anie.200502794.
[220] A. Arsiwala, A. Castro, S. Frey, M. Stathos, R.S. Kane, Designing multivalent ligands to control biological interactions: From vaccines and cellular effectors to targeted drug delivery, Aust. J. Public Adm. 78 (2019) 244–255. https://doi.org/10.1002/asia.201801677.
[221] E. Caló, V. V. Khutoryanskiy, Biomedical applications of hydrogels: A review of patents and commercial products, Eur. Polym. J. 65 (2015) 252–267. https://doi.org/10.1016/j.eurpolymj.2014.11.024.
[222] N.S. Satarkar, D. Biswal, J.Z. Hilt, Hydrogel nanocomposites: a review of applications as remote controlled biomaterials, Soft Matter. 6 (2010) 2364. https://doi.org/10.1039/b925218p.
[223] M. Hamidi, A. Azadi, P. Rafiei, Hydrogel nanoparticles in drug delivery, Adv. Drug Deliv. Rev. 60 (2008) 1638–1649. https://doi.org/10.1016/j.addr.2008.08.002.
[224] T.R. Hoare, D.S. Kohane, Hydrogels in drug delivery: Progress and challenges, Polymer (Guildf). 49 (2008) 1993–2007. https://doi.org/10.1016/j.polymer.2008.01.027.
[225] Y.K. Katare, J.E. Piazza, J. Bhandari, R.P. Daya, K. Akilan, M.J. Simpson, T. Hoare, R.K. Mishra, Intranasal delivery of antipsychotic drugs, Schizophr. Res.

184 (2017) 2–13. https://doi.org/10.1016/j.schres.2016.11.027.
[226] M. Ghori, M. Mahdi, A. Smith, B. Conway, Nasal drug delivery: An overview, Am. J. Pharmacol. Sci. 3 (2015) 110–119. https://doi.org/http://dx.doi.org/10.12691/ajps-3-5-2.
[227] T.P. Crowe, M.H.W. Greenlee, A.G. Kanthasamy, W.H. Hsu, Mechanism of intranasal drug delivery directly to the brain, Life Sci. 195 (2018) 44–52. https://doi.org/10.1016/j.lfs.2017.12.025.
[228] M.T. am Ende, D. Hariharan, N.A. Peppas, Factors influencing drug and protein transport and release from ionic hydrogels, React. Polym. 25 (1995) 127–137. https://doi.org/10.1016/0923-1137(94)00040-C.
[229] M. Romanini, M. Lorente, B. Schammé, L. Delbreilh, V. Dupray, G. Coquerel, J.L. Tamarit, R. Macovez, Enhancement of the Physical and Chemical Stability of Amorphous Drug-Polymer Mixtures via Cryogenic Comilling, Macromolecules. 51 (2018) 9382–9392. https://doi.org/10.1021/acs.macromol.8b01271.
[230] J. Huang, R.J. Wigent, J.B. Schwartz, Drug-polymer interaction and its significance on the physical stability of nifedipine amorphous dispersion in microparticles of an ammonio methacrylate copolymer and ethylcellulose binary blend, J. Pharm. Sci. 97 (2008) 251–262. https://doi.org/10.1002/jps.21072.
[231] K. Nakamae, T. Nishino, K. Kato, T. Miyata, A.S. Hoffman, Synthesis and characterization of stimuli-sensitive hydrogels having a different length of ethylene glycol chains carrying phosphate groups: Loading and release of lysozyme, J. Biomater. Sci. Polym. Ed. 15 (2004) 1435–1446. https://doi.org/10.1163/1568562042368095.
[232] T. Sato, R. Uchida, H. Tanigawa, K. Uno, A. Murakami, Application of polymer gels containing side-chain phosphate groups to drug-delivery contact lenses, J. Appl. Polym. Sci. 98 (2005) 731–735. https://doi.org/10.1002/app.22080.
[233] R. Weissleder, K. Poss, R. Wilkinson, C. Zhou, A. Bogdanov, Quantitation of slow drug release from an implantable and degradable gentamicin conjugate by in vivo magnetic resonance imaging, Antimicrob. Agents Chemother. 39 (1995) 839–845. https://doi.org/10.1128/AAC.39.4.839.
[234] U.G.T.M. Sampath, Y.C. Ching, C.H. Chuah, J.J. Sabariah, P.C. Lin, Fabrication of porous materials from natural/synthetic biopolymers and their composites, Materials (Basel). 9 (2016) 1–32. https://doi.org/10.3390/ma9120991.
[235] M.V. Dinu, M. Přádný, E.S. Drăgan, J. Michálek, Ice-templated hydrogels based on chitosan with tailored porous morphology, Carbohydr. Polym. 94 (2013) 170–178. https://doi.org/10.1016/j.carbpol.2013.01.084.
[236] Y. Liu, W. He, Z. Zhang, B. Lee, Recent Developments in Tough Hydrogels for Biomedical Applications, Gels. 4 (2018) 46. https://doi.org/10.3390/gels4020046.
[237] K.A. Pacheco, Allergy to Surgical Implants, J. Allergy Clin. Immunol. Pract. 3 (2015) 683–695. https://doi.org/10.1016/j.jaip.2015.07.011.
[238] A. Chyzy, M. Tomczykowa, M.E. Plonska-Brzezinska, Hydrogels as potential nano-, micro- and macro-scale systems for controlled drug delivery, Materials (Basel). 13 (2020) 188. https://doi.org/10.3390/ma13010188.
[239] G. Zhou, Z. Luo, X. Fu, Preparation of starch nanoparticles in a water-in-ionic

liquid microemulsion system and their drug loading and releasing properties, J. Agric. Food Chem. 62 (2014) 8214–8220. https://doi.org/10.1021/jf5018725.
[240] R. L. Shinde, A. B. Jindal, P. V. Devarajan, Microemulsions and Nanoemulsions for Targeted Drug Delivery to the Brain, Curr. Nanosci. 7 (2011) 119–133. https://doi.org/10.2174/157341311794480282.
[241] W. Gao, D. Vecchio, J. Li, J. Zhu, Q. Zhang, V. Fu, J. Li, S. Thamphiwatana, D. Lu, L. Zhang, Hydrogel containing nanoparticle-stabilized liposomes for topical antimicrobial delivery, ACS Nano. 8 (2014) 2900–2907. https://doi.org/10.1021/nn500110a.
[242] L. Hosta-Rigau, R. Chandrawati, E. Saveriades, P.D. Odermatt, A. Postma, F. Ercole, K. Breheney, K.L. Wark, B. Städler, F. Caruso, Noncovalent liposome linkage and miniaturization of capsosomes for drug delivery, Biomacromolecules. 11 (2010) 3548–3555. https://doi.org/10.1021/bm101020e.
[243] Y. Zhang, B. Ren, F. Yang, Y. Cai, H. Chen, T. Wang, Z. Feng, J. Tang, J. Xu, J. Zheng, Micellar-incorporated hydrogels with highly tough, mechanoresponsive, and self-recovery properties for strain-induced color sensors, J. Mater. Chem. C. 6 (2018) 11536–11551. https://doi.org/10.1039/c8tc03914c.
[244] A. Salvati, O. Söderman, I. Lynch, Plum-pudding gels as a platform for drug delivery: understanding the effects of the different components on the diffusion behavior of solutes., J. Phys. Chem. B. 111 (2007) 7367–76. https://doi.org/10.1021/jp069051u.
[245] Z. Hu, X. Lu, J. Gao, C. Wang, Polymer gel nanoparticle networks, Adv. Mater. 12 (2000) 1173–1176. https://doi.org/10.1002/1521-4095(200008)12:16<1173::AID-ADMA1173>3.0.CO;2-Z.
[246] N.M.B. Smeets, E. Bakaic, F.M. Yavitt, F. Yang, M.C. Rheinsta, Probing the Internal Morphology of Injectable Poly(oligoethylene glycol methacrylate) Hydrogels by Light and Small-Angle Neutron Scattering, (2014).
[247] M. Norouzi, B. Nazari, D.W. Miller, Injectable hydrogel-based drug delivery systems for local cancer therapy, Drug Discov. Today. 21 (2016) 1835–1849. https://doi.org/10.1016/j.drudis.2016.07.006.
[248] I. Urosev, E. Bakaic, R.J. Alsop, M.C. Rheinstädter, T. Hoare, Tuning the properties of injectable poly(oligoethylene glycol methacrylate) hydrogels by controlling precursor polymer molecular weight, J. Mater. Chem. B. 4 (2016) 6541–6551. https://doi.org/10.1039/C6TB02197B.
[249] M. Peroglio, S. Grad, D. Mortisen, C.M. Sprecher, S. Illien-Jünger, M. Alini, D. Eglin, Injectable thermoreversible hyaluronan-based hydrogels for nucleus pulposus cell encapsulation, Eur. Spine J. 21 (2012) 839–849. https://doi.org/10.1007/s00586-011-1976-2.
[250] C.A. DeForest, D.A. Tirrell, A photoreversible protein-patterning approach for guiding stem cell fate in three-dimensional gels., Nat. Mater. 14 (2015) 523–531. https://doi.org/10.1038/nmat4219.
[251] H. Zhan, H. De Jong, D.W.P.M. Löwik, Comparison of Bioorthogonally Cross-Linked Hydrogels for in Situ Cell Encapsulation, ACS Appl. Bio Mater. 2 (2019) 2862–2871. https://doi.org/10.1021/acsabm.9b00253.

[252] L. Yu, J. Ding, Injectable hydrogels as unique biomedical materials, Chem. Soc. Rev. 37 (2008) 1473–1481. https://doi.org/10.1039/b713009k.
[253] J.A. Yang, J. Yeom, B.W. Hwang, A.S. Hoffman, S.K. Hahn, In situ-forming injectable hydrogels for regenerative medicine, Prog. Polym. Sci. 39 (2014) 1973–1986. https://doi.org/10.1016/j.progpolymsci.2014.07.006.
[254] R. Mavlyanova, R. Yang, T. Tao, M. Aquib, S. Kesse, M.B.J. Maviah, K.O. Boakye-Yiadom, M.A. Farooq, B. Wang, Injectable hydrogels for targeted delivering of therapeutic molecules for tissue engineering and disease treatment, Polym. Adv. Technol. 31 (2020) 192–203. https://doi.org/10.1002/pat.4763.
[255] A.S. Hoffman, Hydrogels for biomedical applications, Adv. Drug Deliv. Rev. 64 (2012) 18–23. https://doi.org/10.1016/j.addr.2012.09.010.
[256] J. Li, D.J. Mooney, Designing hydrogels for controlled drug delivery, Nat Rev Mater. 1 (2016) 1–38. https://doi.org/10.1097/IOP.0b013e31819ac7c5.
[257] H.K.S. Yadav, N. Anwar, A. Halabi, G.A. Alsalloum, Nanogels as Novel Drug Delivery Systems - A Review Properties of Nanogels Keywords : Introduction Advantages of Nanogels, Insight Pharma Res. 1 (2017) 1–8. http://www.imedpub.com/articles/nanogels-as-novel-drug-delivery-systems--a-review.php?aid=18950.
[258] M.W. Tibbitt, C.B. Rodell, J.A. Burdick, K.S. Anseth, Progress in material design for biomedical applications, Proc. Natl. Acad. Sci. U. S. A. 112 (2015) 14444–14451. https://doi.org/10.1073/pnas.1516247112.
[259] N.J. Yang, M.J. Hinner, Getting Across the Cell Membrane: An Overview for Small Molecules, Peptides, and Proteins, Methods Mol Biol. 1266 (2015) 29–53. https://doi.org/10.1007/978-1-4939-2272-7_3.
[260] X. Pang, X. Yang, G. Zhai, Polymer-drug conjugates: Recent progress on administration routes, Expert Opin. Drug Deliv. 11 (2014) 1075–1086. https://doi.org/10.1517/17425247.2014.912779.
[261] M. Shiwnarain, Difference Between Plant And Animal Cells, Sci. Trends. (2017). https://doi.org/10.31988/scitrends.7132.
[262] M.J. Majcher, T. Hoare, Hydrogel Synthesis and Design, 2019. https://doi.org/10.1007/978-3-319-95990-0_9.
[263] I. Mingneault, C. Dartiguenave, M.J. Bertrand, K.C. Waldron, Glutaraldehyde: behavior in aqueous solution, reaction with proteins, and application to enzyme crosslinking, Biotechniques. 37 (2004) 790–802. https://doi.org/10.1039/C6TA07211A.
[264] F. Atyabi, S. Manoochehri, S.H. Moghadam, R. Dinarvand, Cross-linked starch microspheres: effect of cross-linking condition on the microsphere characteristics., Arch. Pharm. Res. 29 (2006) 1179–1186. https://doi.org/10.1007/BF02969311.
[265] L. Gao, J. Chen, X. Han, S. Yan, Y. Zhang, W. Zhang, Z. Gao, Electro-response characteristic of starch hydrogel crosslinked with Glutaraldehyde, J. Biomater. Sci. Polym. Ed. 26 (2015) 545–557. https://doi.org/10.1080/09205063.2015.1037587.
[266] Z. Emami Meybodi, M. Imani, M. Atai, Kinetics of dextran crosslinking by epichlorohydrin: A rheometry and equilibrium swelling study, Carbohydr. Polym. 92 (2013) 1792–1798. https://doi.org/10.1016/j.carbpol.2012.11.030.

[267] G. Mocanu, D. Mihai, L. Picton, D. LeCerf, G. Muller, Associative pullulan gels and their interaction with biological active substances, J. Control. Release. 83 (2002) 41–51. https://doi.org/10.1016/S0168-3659(02)00169-4.
[268] G. Hamdi, G. Ponchel, D. Duchêne, Formulation of epichlorohydrin cross-linked starch microspheres, 2048 (2016). https://doi.org/10.1080/02652040010019505.
[269] V. Wintgens, C. Lorthioir, P. Dubot, B. Sébille, C. Amiel, Cyclodextrin/dextran based hydrogels prepared by cross-linking with sodium trimetaphosphate., Carbohydr. Polym. 132 (2015) 80–8. https://doi.org/10.1016/j.carbpol.2015.06.038.
[270] F.M. Hsieh, C. Huang, T.F. Lin, Y.M. Chen, J.C. Lin, Study of sodium tripolyphosphate-crosslinked chitosan beads entrapped with Pseudomonas putida for phenol degradation, Process Biochem. 43 (2008) 83–92. https://doi.org/10.1016/j.procbio.2007.10.016.
[271] H.J. Chung, K.S. Woo, S.T. Lim, Glass transition and enthalpy relaxation of cross-linked corn starches, Carbohydr. Polym. 55 (2004) 9–15. https://doi.org/10.1016/j.carbpol.2003.04.002.
[272] J. Ma, K. Fu, J. Shi, Y. Sun, X. Zhang, L. Ding, Ultraviolet-Assisted synthesis of polyacrylamide-grafted chitosan nanoparticles and flocculation performance, Carbohydr. Polym. 151 (2016) 565–575. https://doi.org/10.1016/j.carbpol.2016.06.002.
[273] T. Takigawa, Y. Endo, Effects of glutaraldehyde exposure on human health, J. Occup. Health. 48 (2006) 75–87. https://doi.org/10.1539/joh.48.75.
[274] A.K. Giri, Genetic toxicology of epichlorohydrin: A review, Mutat. Res. - Rev. Mutat. Res. 386 (1997) 25–38. https://doi.org/10.1016/S1383-5742(96)00042-7.
[275] B.M. Louie, G.M. Carratt, D.S. Soong, Modeling the free radical solution and bulk polymerization of methyl methacrylate, J. Appl. Polym. Sci. 30 (1985) 3985–4012. https://doi.org/10.1002/app.1985.070301004.
[276] T.S. Yang, D.B. Min, Quenching mechanism and kinetics of ascorbic acid on the photosensitizing effects of synthetic food colorant FD & C Red Nr 3, J. Food Sci. 74 (2009). https://doi.org/10.1111/j.1750-3841.2009.01364.x.
[277] P. Garra, C. Dietlin, F. Morlet-Savary, F. Dumur, D. Gigmes, J.P. Fouassier, J. Lalevée, Redox two-component initiated free radical and cationic polymerizations: Concepts, reactions and applications, Prog. Polym. Sci. 94 (2019) 33–56. https://doi.org/10.1016/j.progpolymsci.2019.04.003.
[278] P. Kumar, A.L. Ganure, B.B. Subudhi, S. Shukla, Preparation and characterization of pH-sensitive methyl methacrylate-g-starch/hydroxypropylated starch hydrogels: in vitro and in vivo study on release of esomeprazole magnesium, Drug Deliv. Transl. Res. 5 (2015) 243–256. https://doi.org/10.1007/s13346-015-0221-7.
[279] V.D. Athawale, V. Lele, Thermal Studies on Granular Maize Starch and its Graft Copolymers with Vinyl Monomers, Starch - Stärke. 52 (2000) 205–213. https://doi.org/10.1002/1521-379X(200007)52:6/7<205::AID-STAR205>3.0.CO;2-3.
[280] Y. Hong, H. Song, Y. Gong, Z. Mao, C. Gao, J. Shen, Covalently crosslinked chitosan hydrogel: Properties of in vitro degradation and chondrocyte

encapsulation, Acta Biomater. 3 (2007) 23–31. https://doi.org/10.1016/j.actbio.2006.06.007.
[281] B. Singh, D.K. Sharma, A. Gupta, Controlled release of thiram fungicide from starch-based hydrogels., J. Environ. Sci. Health. B. 42 (2007) 677–695. https://doi.org/10.1080/03601230701465825.
[282] S. Das, A. Pandey, S. Pal, H. Kolya, T. Tripathy, Green synthesis, characterization and antibacterial activity of gold nanoparticles using hydroxyethyl starch-g-poly (methylacrylate-co-sodium acrylate): A novel biodegradable graft copolymer, J. Mol. Liq. 212 (2015) 259–265. https://doi.org/10.1016/j.molliq.2015.09.020.
[283] Y. Zhao, C. Shi, X. Yang, B. Shen, Y. Sun, Y. Chen, X. Xu, H. Sun, K. Yu, B. Yang, Q. Lin, pH and Temperature Sensitive Hydrogel Nanoparticles with Dual Photoluminescence for Bioprobes, ACS Nano. (2016). https://doi.org/10.1021/acsnano.6b00770.
[284] I. Mironi-Harpaz, D.Y. Wang, S. Venkatraman, D. Seliktar, Photopolymerization of cell-encapsulating hydrogels: Crosslinking efficiency versus cytotoxicity, Acta Biomater. 8 (2012) 1838–1848. https://doi.org/10.1016/j.actbio.2011.12.034.
[285] M.J. Majcher, C.L. McInnis, S. Himbert, R.J. Alsop, D. Kinio, M. Bleuel, M.C. Rheinstädter, N.M.B. Smeets, T. Hoare, Photopolymerized Starchstarch Nanoparticle (SNP) network hydrogels, Carbohydr. Polym. 236 (2020) 115998. https://doi.org/10.1016/j.carbpol.2020.115998.
[286] D. Missirlis, N. Tirelli, J.A. Hubbell, Amphiphilic hydrogel nanoparticles. Preparation, characterization, and preliminary assessment as new colloidal drug carriers, Langmuir. 21 (2005) 2605–2613. https://doi.org/10.1021/la047367s.
[287] D.J.P.J.J.P.K.K.R. Karki S.B., Mechanism of oxidative amine dealkylation of substituted N,N-dimethylanilines by cytochrome P-450: Application of isotope effect profiles, J. Am. Chem. Soc. 117 (1995) 3657–3664. https://doi.org/10.1021/ja00118a001.
[288] Y. Kato, J. Kaminaga, R. Matsuo, A. Isogai, TEMPO-mediated oxidation of chitin, regenerated chitin and N-acetylated chitosan, Carbohydr. Polym. 58 (2004) 421–426. https://doi.org/10.1016/j.carbpol.2004.08.011.
[289] G. Babaladimath, B. Vishalakshi, Silver nanoparticles embedded gum ghatti-graft-poly(N,N-dimethylacrylamide) biodegradable hydrogel: evaluation as matrix for controlled release of 2,4-dichlorophenoxyacetic acid, J. Polym. Res. 24 (2017) 1–9. https://doi.org/10.1007/s10965-017-1314-4.
[290] J.B. Leach, K.A. Bivens, C.W. Patrick, C.E. Schmidt, Photocrosslinked hyaluronic acid hydrogels: Natural, biodegradable tissue engineering scaffolds, Biotechnol. Bioeng. 82 (2003) 578–589. https://doi.org/10.1002/bit.10605.
[291] J. Hedin, Å. Östlund, M. Nydén, UV induced cross-linking of starch modified with glycidyl methacrylate, Carbohydr. Polym. 79 (2010) 606–613. https://doi.org/10.1016/j.carbpol.2009.09.019.
[292] M. Diolosà, I. Donati, G. Turco, M. Cadenaro, R. Di Lenarda, L. Breschi, S. Paoletti, Use of methacrylate-modified chitosan to increase the durability of dentine bonding systems, Biomacromolecules. 15 (2014) 4606–4613. https://doi.org/10.1021/bm5014124.

[293] J. Han, K. Wang, D. Yang, J. Nie, Photopolymerization of methacrylated chitosan/PNIPAAm hybrid dual-sensitive hydrogels as carrier for drug delivery, Int. J. Biol. Macromol. 44 (2009) 229–235. https://doi.org/10.1016/j.ijbiomac.2008.12.009.
[294] E.A. Kamoun, N-succinyl chitosan-dialdehyde starch hybrid hydrogels for biomedical applications, J. Adv. Res. 7 (2015) 69–77. https://doi.org/10.1016/j.jare.2015.02.002.
[295] K.C.F. Leung, S. Xuan, C.M. Lo, Reversible switching between hydrophilic and hydrophobic superparamagnetic iron oxide microspheres via one-step supramolecular dynamic dendronization: Exploration of dynamic wettability, ACS Appl. Mater. Interfaces. 1 (2009) 2005–2012. https://doi.org/10.1021/am900367a.
[296] G. Godeau, T. Darmanin, F. Guittard, Switchable surfaces from highly hydrophobic to highly hydrophilic using covalent imine bonds, J. Appl. Polym. Sci. 133 (2016) 1–6. https://doi.org/10.1002/app.43130.
[297] H. Ghafuri, M.M. Hashemi, One-pot reductive amination of aldehydes by the dihydropyridine in water, Sci. Iran. 19 (2012) 1591–1593. https://doi.org/10.1016/j.scient.2012.10.030.
[298] H. Zhang, A. Qadeer, W. Chen, In situ gelable interpenetrating double network hydrogel formulated from binary components: Thiolated chitosan and oxidized dextran, Biomacromolecules. 12 (2011) 1428–1437. https://doi.org/10.1021/bm101192b.
[299] M.A. Winnik, A. Yekta, Associative polymers in aqueous solution, Curr. Opin. Colloid Interface Sci. 2 (1997) 424–436. https://doi.org/10.1016/s1359-0294(97)80088-x.
[300] P. Sheikholeslami, B. Muirhead, D.S.H. Baek, H. Wang, X. Zhao, D. Sivakumaran, S. Boyd, H. Sheardown, T. Hoare, Hydrophobically-modified poly(vinyl pyrrolidone) as a physically-associative, shear-responsive ophthalmic hydrogel, Exp. Eye Res. 137 (2015) 18–31. https://doi.org/10.1016/j.exer.2015.05.021.
[301] M. Jamard, T. Hoare, H. Sheardown, Nanogels of methylcellulose hydrophobized with N-tert-butylacrylamide for ocular drug delivery, Drug Deliv. Transl. Res. 6 (2016) 648–659. https://doi.org/10.1007/s13346-016-0337-4.
[302] T. Nishikawa, K. Akiyoshi, J. Sunamoto, Supramolecular assembly between nanoparticles of hydrophobized polysaccharide and soluble protein complexation between the self-aggregate of cholesterol-, Macromolecules. 27 (1994) 7654–7659. https://doi.org/10.1021/ma00104a021.
[303] A.K. Hellström, R. Bordes, Reversible flocculation of nanoparticles by a carbamate surfactant, J. Colloid Interface Sci. 536 (2019) 722–727. https://doi.org/10.1016/j.jcis.2018.10.057.
[304] S. Kumar, V.K. Aswal, J. Kohlbrecher, Small-Angle Neutron Scattering Study of Interplay of Attractive and Repulsive Interactions in Nanoparticle-Polymer System, Langmuir. 32 (2016) 1450–1459. https://doi.org/10.1021/acs.langmuir.5b03998.
[305] Q. Wang, S. Jamal, M.S. Detamore, C. Berkland, PLGA-chitosan/PLGA-alginate

nanoparticle blends as biodegradable colloidal gels for seeding human umbilical cord mesenchymal stem cells, J. Biomed. Mater. Res. - Part A. 96 A (2011) 520–527. https://doi.org/10.1002/jbm.a.33000.
[306] W. Wang, S.A. Sande, A dynamic light scattering study of hydrogels with the addition of surfactant: A discussion of mesh size and correlation length, Polym. J. 47 (2015) 302–310. https://doi.org/10.1038/pj.2014.114.
[307] D.C. Schoenmakers, A.E. Rowan, P.H.J. Kouwer, Crosslinking of fibrous hydrogels, Nat. Commun. 9 (2018) 1–8. https://doi.org/10.1038/s41467-018-04508-x.
[308] M. Trudicova, J. Smilek, M. Kalina, M. Smilkova, K. Adamkova, K. Hrubanova, V. Krzyzanek, P. Sedlacek, Multiscale experimental evaluation of agarose-based semi-interpenetrating polymer network hydrogels as materials with tunable rheological and transport performance, Polymers (Basel). 12 (2020) 1–27. https://doi.org/10.3390/polym12112561.
[309] S. Khandai, R.A. Siegel, S.S. Jena, Probing the microenvironment of polyacrylamide hydrogel matrix using turbidity and fluorescence recovery after photobleaching: One versus Two phases, Colloids Surfaces A Physicochem. Eng. Asp. 593 (2020) 124618. https://doi.org/10.1016/j.colsurfa.2020.124618.
[310] J. Kärger, M. Avramovska, D. Freude, J. Haase, S. Hwang, R. Valiullin, Pulsed field gradient NMR diffusion measurement in nanoporous materials, Springer US, 2021. https://doi.org/10.1007/s10450-020-00290-9.
[311] Z. Kaberova, E. Karpushkin, M. Nevoralová, M. Vetrík, M. Šlouf, M. Dušková-Smrcková, Microscopic structure of swollen hydrogels by scanning electron and light microscopies: Artifacts and reality, Polymers (Basel). 12 (2020). https://doi.org/10.3390/polym12030578.
[312] W. Zhang, I. Gaberman, M. Ciszkowska, Diffusion and concentration of molecular probes in thermoresponsive poly(N-isopropylacrylamide) hydrogels: Effect of the volume phase transition, Anal. Chem. 74 (2002) 1343–1348. https://doi.org/10.1021/ac0107857.
[313] S. Kumar, V.K. Aswal, J. Kohlbrecher, Size-dependent interaction of silica nanoparticles with different surfactants in aqueous solution., Langmuir. 28 (2012) 9288–97. https://doi.org/10.1021/la3019056.
[314] A.J. Jackson, Introduction to Small-Angle Neutron Scattering and Neutron Reflectometry, NIST Cent. Neutron Res. (2008) 1–24. ftp://ftp.ncnr.nist.gov/pub/sans/kline/Tutorials/P85_vs_Temp_NG3_2008.zip.
[315] B. Chu, T. Liu, Characterization of nanoparticles by scattering techniques, J. Nanoparticle Res. 2 (2000) 29–41. https://doi.org/10.1023/A:1010001822699.
[316] Small Angle Scattering with Neutrons and X-Rays, (2021). https://sites.google.com/site/sanssaxsaba/home/neutrons-vs-x-rays.
[317] N.C. for N. Research, Chapter 6 - INTRODUCTION TO NEUTRON SCATTERING, (n.d.) 1–5.
[318] M.M. Castellanos, A. McAuley, J.E. Curtis, Investigating Structure and Dynamics of Proteins in Amorphous Phases Using Neutron Scattering, Comput. Struct. Biotechnol. J. 15 (2017) 117–130. https://doi.org/10.1016/j.csbj.2016.12.004.

[319] H. Tanaka, K. Yamauchi, H. Hasegawa, N. Miyamoto, S. Koizumi, T. Hashimoto, In situ and real-time small-angle neutron scattering studies of living anionic polymerization process and polymerization-induced self-assembly of block copolymers, Phys. B Condens. Matter. 385-386 I (2006) 742–744. https://doi.org/10.1016/j.physb.2006.06.049.
[320] S.U. Egelhaaf, U. Olsson, P. Schurtenberger, Time-resolved SANS for surfactant phase transitions, Phys. B Condens. Matter. 276–278 (2000) 326–329. https://doi.org/10.1016/S0921-4526(99)01527-6.
[321] P.D.T. Huibers, L.E. Bromberg, B.H. Robinson, T.A. Hatton, Reversible gelation in semidilute aqueous solutions of associative polymers: a small-angle neutron scattering study, Macromolecules. 32 (1999) 4889–4894. https://doi.org/10.1021/ma990181t.
[322] A.Y.C. Koh, B.R. Saunders, Small-angle neutron scattering study of temperature-induced emulsion gelation: The role of sticky microgel particles, Langmuir. 21 (2005) 6734–6741. https://doi.org/10.1021/la050600h.
[323] S. Chodankar, V.K. Aswal, J. Kohlbrecher, R. Vavrin, A.G. Wagh, Small-angle neutron scattering study of structure and kinetics of temperature-induced protein gelation, Phys. Rev. E - Stat. Nonlinear, Soft Matter Phys. 79 (2009) 1–7. https://doi.org/10.1103/PhysRevE.79.021912.
[324] K. Hashimoto, K. Fujii, K. Nishi, M. Shibayama, Ion Gel Network Formation in an Ionic Liquid Studied by Time-Resolved Small-Angle Neutron Scattering, J. Phys. Chem. B. 122 (2018) 9419–9424. https://doi.org/10.1021/acs.jpcb.8b08111.
[325] H. Ismail, M. Irani, Z. Ahmad, Starch-Based Hydrogels: Present Status and Applications, Int. J. Polym. Mater. 4037 (2012) 121010064447009. https://doi.org/10.1080/00914037.2012.719141.
[326] P. Chen, W. Zhang, W. Luo, Y. Fang, Synthesis of superabsorbent polymers by irradiation and their applications in agriculture, J. Appl. Polym. Sci. 93 (2004) 1748–1755. https://doi.org/10.1002/app.20612.
[327] N. Sahiner, S. Butun, O. Ozay, B. Dibek, Utilization of Smart Hydrogel-Metal Composites as Catalysis Media, J. Colloid Interface Sci. 373 (2012) 122–128. https://doi.org/10.1016/j.jcis.2011.08.080.
[328] U. Hersel, C. Dahmen, H. Kessler, RGD modified polymers: Biomaterials for stimulated cell adhesion and beyond, Biomaterials. 24 (2003) 4385–4415. https://doi.org/10.1016/S0142-9612(03)00343-0.
[329] C. Elvira, J. Mano, J. San Román, R. Reis, Starch-based biodegradable hydrogels with potential biomedical applications as drug delivery systems, Biomaterials. 23 (2002) 1955–1966. https://doi.org/10.1016/S0142-9612(01)00322-2.
[330] P.B. Malafaya, G.A. Silva, R.L. Reis, Natural – origin polymers as carriers and scaffolds for biomolecules and cell delivery in tissue engineering applications, Adv. Drug Deliv. Rev. 59 (2007) 207–233. https://doi.org/10.1016/j.addr.2007.03.012.
[331] S. Van Vlierberghe, P. Dubruel, E. Schacht, Biopolymer-based hydrogels as scaffolds for tissue engineering applications: A review, Biomacromolecules. 12 (2011) 1387–1408. https://doi.org/10.1021/bm200083n.

[332] B. Ramaraj, G. Radhakrishnan, Modification of the dynamic swelling behaviour of poly(2-hydroxyethyl methacrylate) hydrogels in water through interpenetrating polymer networks (IPNs), Polymer (Guildf). 35 (1994) 2167–2173. https://doi.org/10.1016/0032-3861(94)90245-3.
[333] T. Norisuye, N. Masui, Y. Kida, D. Ikuta, E. Kokufuta, S. Ito, S. Panyukov, M. Shibayama, Small angle neutron scattering studies on structural inhomogeneities in polymer gels: irradiation cross-linked gels vs chemically cross-linked gels., Polymer (Guildf). 43 (2002) 5289–5297. https://doi.org/https://doi.org/10.1016/S0032-3861(02)00343-9.
[334] C. Dannert, B.T. Stokke, R.S. Dias, Nanoparticle-hydrogel composites: From molecular interactions to macroscopic behavior, Polymers (Basel). 11 (2019) 1–35. https://doi.org/10.3390/polym11020275.
[335] Qiu, C., et al., Preparation and characterization of size-controlled starch nanoparticles based on short linear chains from debranched waxy corn starch., LWT - Food Sci. Technol. 74 (2016) 303–310.
[336] et al Zhang, Z., Synthesis of pH-responsive starch nanoparticles grafted poly (l-glutamic acid) for insulin controlled release., Eur. Polym. J. 49 (n.d.) 2082–2091.
[337] S. Bel Haaj, W. Thielemans, A. Magnin, S. Boufi, Starch nanocrystals and starch nanoparticles from waxy maize as nanoreinforcement: A comparative study, Carbohydr. Polym. 143 (2016) 310–317. https://doi.org/10.1016/j.carbpol.2016.01.061.
[338] N. Lin, J. Huang, A. Dufresne, Preparation, properties and applications of polysaccharide nanocrystals in advanced functional nanomaterials: a review, Nanoscale. 4 (2012) 3274–3294. https://doi.org/10.1039/c2nr30260h.
[339] S.A. Kheradvar, J. Nourmohammadi, H. Tabesh, B. Bagheri, Starch nanoparticle as a vitamin E-TPGS carrier loaded in silk fibroin-poly(vinyl alcohol)-Aloe vera nanofibrous dressing, Colloids Surfaces B Biointerfaces. 166 (2018) 9–16. https://doi.org/10.1016/j.colsurfb.2018.03.004.
[340] Sheeja, O. Manaf, K. Juraij, P. Sneha Sundaran, K. Ashitha, L.S. Aleena, A. Sujith, Polyethylene-g-starch nanoparticle biocomposites: Physicochemical properties and biodegradation studies, Polym. Compos. 39 (2018) E426–E440. https://doi.org/10.1002/pc.24503.
[341] M.K. Lima-Tenório, E.T. Tenório-Neto, F.P. Garcia, C. V. Nakamura, M.R. Guilherme, E.C. Muniz, E.A.G. Pineda, A.F. Rubira, Hydrogel nanocomposite based on starch and Co-doped zinc ferrite nanoparticles that shows magnetic field-responsive drug release changes, J. Mol. Liq. 210 (2015) 100–105. https://doi.org/10.1016/j.molliq.2014.11.027.
[342] S. Jia, Z. Tang, Y. Guan, Y. Zhang, Order-Disorder Transition in Doped Microgel Colloidal Crystals and Its Application for Optical Sensing, ACS Appl. Mater. Interfaces. 10 (2018) 14254–14258. https://doi.org/10.1021/acsami.8b01326.
[343] M.K. Maurer, D.E. Condon, H.E. McKinney, J.K. Kim, Photoresponsive interpenetrating network photonic crystal, Proc. IEEE Sensors. (2009) 418–421. https://doi.org/10.1109/ICSENS.2009.5398256.
[344] S. Thaiboonrod, A.H. Milani, B.R. Saunders, Doubly crosslinked poly(vinyl

amine) microgels: Hydrogels of covalently inter-linked cationic microgel particles, J. Mater. Chem. B. 2 (2014) 110–119. https://doi.org/10.1039/c3tb21579b.
[345] R. Absil, S. Çakir, S. Gabriele, P. Dubois, C. Barner-Kowollik, F. Du Prez, L. Mespouille, Click reactive microgels as a strategy towards chemically injectable hydrogels, Polym. Chem. 7 (2016) 6752–6760. https://doi.org/10.1039/c6py01663d.
[346] J.C. Gaulding, M.H. Smith, J.S. Hyatt, A. Fernandez-Nieves, L.A. Lyon, Reversible inter- and intra-microgel cross-linking using disulfides, Macromolecules. 45 (2012) 39–45. https://doi.org/10.1021/ma202282p.
[347] Y. Tan, K. Xu, L. Li, C. Liu, C. Song, P. Wang, Fabrication of size-controlled starch-based nanospheres by nanoprecipitation, ACS Appl. Mater. Interfaces. 1 (2009) 956–959. https://doi.org/10.1021/am900054f.
[348] J.-Y. Kim, S.-T. Lim, Preparation of nano-sized starch particles by complex formation with n-butanol, Carbohydr. Polym. 76 (2009) 110–116. https://doi.org/10.1016/j.carbpol.2008.09.030.
[349] S. Bel Haaj, A. Magnin, C. Pétrier, S. Boufi, Starch nanoparticles formation via high power ultrasonication, Carbohydr. Polym. 92 (2013) 1625–1632. https://doi.org/10.1016/j.carbpol.2012.11.022.
[350] H.Y. Kim, J.A. Han, D.K. Kweon, J.D. Park, S.T. Lim, Effect of ultrasonic treatments on nanoparticle preparation of acid-hydrolyzed waxy maize starch, Carbohydr. Polym. 93 (2013) 582–588. https://doi.org/10.1016/j.carbpol.2012.12.050.
[351] J. Zhu, L. Li, L. Chen, X. Li, Study on supramolecular structural changes of ultrasonic treated potato starch granules, Food Hydrocoll. 29 (2012) 116–122. https://doi.org/10.1016/j.foodhyd.2012.02.004.
[352] X. Li, Y. Qin, C. Liu, S. Jiang, L. Xiong, Q. Sun, Size-controlled starch nanoparticles prepared by self-assembly with different green surfactant: The effect of electrostatic repulsion or steric hindrance, Food Chem. 199 (2016) 356–363. https://doi.org/10.1016/j.foodchem.2015.12.037.
[353] Q. Sun, G. Li, L. Dai, N. Ji, L. Xiong, Green preparation and characterisation of waxy maize starch nanoparticles through enzymolysis and recrystallisation, Food Chem. 162 (2014) 223–228. https://doi.org/10.1016/j.foodchem.2014.04.068.
[354] J.D. Nickels, J. Atkinson, E. Papp-Szabo, C. Stanley, S.O. Diallo, S. Perticaroli, B. Baylis, P. Mahon, G. Ehlers, J. Katsaras, J.R. Dutcher, Structure and Hydration of Highly-Branched, Monodisperse Phytoglycogen Nanoparticles, Biomacromolecules. 17 (2016) 735–743. https://doi.org/10.1021/acs.biomac.5b01393.
[355] A.C.F. Ip, T.H. Tsai, I. Khimji, P.J.J. Huang, J. Liu, Degradable starch nanoparticle assisted ethanol precipitation of DNA, Carbohydr. Polym. 110 (2014) 354–359. https://doi.org/10.1016/j.carbpol.2014.04.007.
[356] A. Tseitlin, D. Van Alstyne, S. Bloembergen, US Patent Application US2012/0309246 A1, 2012.
[357] H. Bae, A.F. Ahari, H. Shin, J.W. Nichol, C.B. Hutson, M. Masaeli, S.-H. Kim, H. Aubin, S. Yamaniar, A. Khademhosseini, NIH Public Access, Soft Matter. 7

(2011) 1903–1911. https://doi.org/10.1039/C0SM00697A.
[358] M. Stieger, J.S. Pedersen, P. Lindner, W. Richtering, Are thermoresponsive microgels model systems for concentrated colloidal suspensions? A rheology and small-angle neutron scattering study, Langmuir. 20 (2004) 7283–7292. https://doi.org/10.1021/la049518x.
[359] K.C. Sharma, R. V.; Sharma, The structure factor and the transport properties of dense fluids having molecules with square well potential, a possible generalization, Physica. 89 (1977) 213–218. https://doi.org/https://doi.org/10.1016/0378-4371(77)90151-0.
[360] B. Hammouda, D.L. Ho, S. Kline, Insight into clustering in poly(ethylene oxide) solutions, Macromolecules. 37 (2004) 6932–6937. https://doi.org/10.1021/ma049623d.
[361] B. Hammouda, Scattering from Fractal Systems. In Probing Nanoscale Structures, SANS Toolbox; Natl. Inst. Stand. Technol. (2004). https://www.ncnr.nist.gov/staff/hammouda/the_sans_toolbox.pdf.
[362] P.A. Jackson, J.C. Widen, D.A. Harki, K.M. Brummond, Covalent Modifiers: A Chemical Perspective on the Reactivity of α,β-Unsaturated Carbonyls with Thiols via Hetero-Michael Addition Reactions, J. Med. Chem. 60 (2017) 839–885. https://doi.org/10.1021/acs.jmedchem.6b00788.
[363] V. Ansteinsson, H.B. Kopperud, E. Morisbak, J.T. Samuelsen, Cell toxicity of methacrylate monomers-The role of glutathione adduct formation, J. Biomed. Mater. Res. - Part A. 101 (2013) 3504–3510. https://doi.org/10.1002/jbm.a.34652.
[364] T.R. Hoare, D.S. Kohane, Hydrogels in drug delivery: Progress and challenges, Polymer (Guildf). 49 (2008) 1993–2007. https://doi.org/10.1016/j.polymer.2008.01.027.
[365] M. Rabe, D. Verdes, S. Seeger, Understanding protein adsorption phenomena at solid surfaces, Adv. Colloid Interface Sci. 162 (2011) 87–106. https://doi.org/10.1016/j.cis.2010.12.007.
[366] S. Campuzano, M. Pedrero, P. Yáñez-Sedeño, J.M. Pingarrón, Antifouling (Bio)materials for electrochemical (bio)sensing, Int. J. Mol. Sci. 20 (2019). https://doi.org/10.3390/ijms20020423.
[367] N. Liu, Z. Xu, A. Morrin, X. Luo, Low fouling strategies for electrochemical biosensors targeting disease biomarkers, Anal. Methods. 11 (2019) 702–711. https://doi.org/10.1039/c8ay02674b.
[368] X. Deng, M. Korogiannaki, B. Rastegari, J. Zhang, M. Chen, Q. Fu, H. Sheardown, C.D.M. Filipe, T. Hoare, "click" Chemistry-Tethered Hyaluronic Acid-Based Contact Lens Coatings Improve Lens Wettability and Lower Protein Adsorption, ACS Appl. Mater. Interfaces. 8 (2016). https://doi.org/10.1021/acsami.6b07433.
[369] N.M.B. Smeets, E. Bakaic, M. Patenaude, T. Hoare, Injectable poly(oligoethylene glycol methacrylate)-based hydrogels with tunable phase transition behaviours: Physicochemical and biological responses, Acta Biomater. 10 (2014) 4143–4155. https://doi.org/10.1016/j.actbio.2014.05.035.
[370] J. Wang, H. Sun, J. Li, D. Dong, Y. Zhang, F. Yao, Ionic starch-based hydrogels for the prevention of nonspecific protein adsorption, Carbohydr. Polym. 117

(2015) 384–391. https://doi.org/10.1016/j.carbpol.2014.09.077.
[371] X. Deng, N.M.B. Smeets, C. Sicard, J. Wang, J.D. Brennan, C.D.M. Filipe, T. Hoare, Poly(oligoethylene glycol methacrylate) dip-coating: Turning cellulose paper into a protein-repellent platform for biosensors, J. Am. Chem. Soc. 136 (2014) 12852–12855. https://doi.org/10.1021/ja507372v.
[372] S.M. Russell, G. Carta, Multicomponent protein adsorption in supported cationic polyacrylamide hydrogels, AIChE J. 51 (2005) 2469–2480. https://doi.org/10.1002/aic.10482.
[373] M. Pekař, Hydrogels with micellar hydrophobic (nano)domains, Front. Mater. 1 (2015) 1–14. https://doi.org/10.3389/fmats.2014.00035.
[374] J.R.S.I. 12 (2015). https://doi. org/10. 1098/rsif. 2015. 0226. Y. Huang, [1] Y. Huang, Y. Wang, L. Sun, R. Agrawal, M. Zhang, Sundew adhesive: A naturally occurring hydrogel, Y. Wang, L. Sun, R. Agrawal, M. Zhang, Sundew adhesive: A naturally occurring hydrogel, J. R. Soc. Interface. 12 (2015). https://doi.org/10.1098/rsif.2015.0226.
[375] C. Rochas, E. Geissler, Measurement of dynamic light scattering intensity in gels, Macromolecules. 47 (2014) 8012–8017. https://doi.org/10.1021/ma501882d.
[376] E. Vanden Bussche, Y. De Deene, P. Dubruel, K. Vergote, E. Schacht, C. De Wagter, The use of static light scattering for the structure analysis of radiosensitive polymer gels: a literature survey, J. Phys. Conf. Ser. 3 (2004) 180–183. https://doi.org/10.1088/1742-6596/3/1/022.
[377] C. Gomes, R.C.S. Dias, M.R.P.F.N. Costa, Static light scattering monitoring and kinetic modeling of polyacrylamide hydrogel synthesis, Processes. 7 (2019) 1–25. https://doi.org/10.3390/pr7040237.
[378] D.J. Water, K. Engbergm, R. Parke-Houben, L. Hartmann, C.N. Ta, M.F. Toney, C.W. Frank, Poly(ethylene, Morphology of Photopolymerized End-linked Scattering, glycol) Hydrogels by Small Angle X-ray, Macromolecules. 43 (2010) 6861–6870. https://doi.org/doi:10.1021/ma101070s.
[379] A. Nack, J. Seifert, C. Passow, J. Wagner, Hindered nematic alignment of hematite spindles in poly(N-isopropylacrylamide) hydrogels: A small-angle X-ray scattering and rheology study: A, J. Appl. Crystallogr. 51 (2018) 87–96. https://doi.org/10.1107/S1600576717017411.
[380] A. Tripathi, G.N. Parsons, S.A. Khan, O.J. Rojas, Synthesis of organic aerogels with tailorable morphology and strength by controlled solvent swelling following Hansen solubility, Sci. Rep. 8 (2018) 1–12. https://doi.org/10.1038/s41598-018-19720-4.
[381] R.A. Pouliot, B.M. Young, P.A. Link, H.E. Park, A.R. Kahn, K. Shankar, M.B. Schneck, D.J. Weiss, R.L. Heise, Porcine Lung-Derived Extracellular Matrix Hydrogel Properties Are Dependent on Pepsin Digestion Time, Tissue Eng. - Part C Methods. 26 (2020) 332–346. https://doi.org/10.1089/ten.tec.2020.0042.
[382] J. Tian, T.A.P. Seery, R.A. Weiss, Physically cross-linked alkylacrylamide hydrogels: Phase behavior and microstructure, Macromolecules. 37 (2004) 9994–10000. https://doi.org/10.1021/ma049475r.
[383] B. Hammouda, D.L. Ho, Insight into Chain Dimensions in PEO/Water Solutions, J.

Polym. Sci., Part B Polym. Phys. 45 (2007) 2196−2200. https://doi.org/10.1002/polb.
[384] N. Sanson, J. Rieger, Synthesis of nanogels/microgels by conventional and controlled radical crosslinking copolymerization, Polym. Chem. 1 (2010) 965–977. https://doi.org/10.1039/c0py00010h.
[385] et al. Smeets, Niels M. B., Probing the internal morphology of injectable poly(oligoethylene glycol methacrylate) hydrogels by light and small-angle neutron scattering, Macromolecules. 47 (2014) 6017–6027.
[386] M. Shibayama, Small-angle neutron scattering on polymer gels: Phase behavior, inhomogeneities and deformation mechanisms, Polym. J. 43 (2011) 18–34. https://doi.org/10.1038/pj.2010.110.
[387] T. Hoare, S. Young, M.W. Lawlor, D.S. Kohane, Thermoresponsive nanogels for prolonged duration local anesthesia, Acta Biomater. 8 (2012) 3596–3605. https://doi.org/10.1016/j.actbio.2012.06.013.
[388] V. Barbier, M. Hervé, J. Sudor, A. Brulet, D. Hourdet, J.L. Viovy, Thermally induced gelation of poly(acrylamide) grafted with poly(N-isopropylacrylamide): A small-angle neutron scattering study, Macromolecules. 37 (2004) 5682–5691. https://doi.org/10.1021/ma049182y.
[389] B.D. Butler, C.D. Muzny, H.J.M. Hanley, Scaling of small-angle neutron scattering intensities from gelling colloidal silica, Int. J. Thermophys. 20 (1999) 35–43. https://doi.org/10.1023/A:1021465827468.
[390] M. Shibayama, H. Kawada, T. Kume, T. Matsunaga, H. Iwai, T. Sano, N. Osaka, S. Miyazaki, S. Okabe, H. Endo, In situ small-angle neutron scattering and rheological measurements of shear-induced gelation, J. Chem. Phys. 127 (2007). https://doi.org/10.1063/1.2790900.
[391] S.R. Kline, Reduction and analysis of SANS and USANS data using IGOR Pro, J. Appl. Crystallogr. 39 (2006) 895–900. https://doi.org/10.1107/S0021889806035059.
[392] E.W. Gomez, N.G. Clack, H.J. Wu, J.T. Groves, Like-charge interactions between colloidal particles are asymmetric with respect to sign, Soft Matter. 5 (2009) 1931–1936. https://doi.org/10.1039/b821510c.
[393] F.E. Giezen, R.O.J. Jongboom, H. Feil, K.F. Gotlieb, A. Boersma, Process for producing biopolymer nanoparticles, PCT Int. Appl. (2000) 17 pp.
[394] R. Takano, T. Nagai, X. Wu, X.Y. Xu, N.T. Huy, K. Kamei, S. Hara, Sulfation of polysaccharides using monomethyl sulfate, J. Carbohydr. Chem. 19 (2000) 1185–1190. https://doi.org/10.1080/07328300008544142.
[395] S.A.S. Criag, C.C. Maningat, P.A. Seib, R.C. Hoseney, Starch paste clarity, Cereal Chem. 66 (1989) 173–182.
[396] F. Mousseau, L. Vitorazi, L. Herrmann, S. Mornet, J.F. Berret, Polyelectrolyte assisted charge titration spectrometry: Applications to latex and oxide nanoparticles, J. Colloid Interface Sci. 475 (2016) 36–45. https://doi.org/10.1016/j.jcis.2016.04.036.
[397] O. Sakurada, Y. Kato, N. Kito, K. Kameyama, T. Hattori, M. Hashiba, Colloidal Titration of Aqueous Zirconium Solutions with Poly(vinyl sulfate) by

Potentiometric Endpoint Detection Using a Toluidine Blue Selective Electrode, Anal. Sci. 20 (2004) 311–314. https://doi.org/10.2116/analsci.20.311.
[398] J. Duffy, Measuring the rheology of polymer solutions, Malvern Instruments Ltd. (2015) 1–13. www.malvern.com/contact.
[399] T. Chen, UV Curing Analysis Using A Rheometer, TA Instruments. (n.d.) 2–6.
[400] N.M.B. Smeets, E. Bakaic, F.M. Yavitt, F.C. Yang, M.C. Rheinstädter, T. Hoare, Probing the internal morphology of injectable poly(oligoethylene glycol methacrylate) hydrogels by light and small-angle neutron scattering, Macromolecules. 47 (2014) 6017–6027. https://doi.org/10.1021/ma5011827.
[401] K. Gorska, A. Horzela, K.A. Penson, G. Dattoli, G.H.E. Duchamp, The stretched exponential behavior and its underlying dynamics. The phenomenological approach, Fract. Calc. Appl. Anal. 20 (2017) 260–283. https://doi.org/https://doi.org/10.1515/fca-2017-0014.
[402] G.C. Berry, D.J. Plazek, On the use of stretched-exponential functions for both linear viscoelastic creep and stress relaxation, Rheol. Acta. 36 (1997) 320–329. https://doi.org/10.1007/BF00366673.
[403] L. Toppozini, F. Roosen-Runge, R.I. Bewley, R.M. Dalgliesh, T. Perring, T. Seydel, H.R. Glyde, V. García Sakai, M.C. Rheinstädter, Anomalous and anisotropic nanoscale diffusion of hydration water molecules in fluid lipid membranes, Soft Matter. 11 (2015) 8354–8371. https://doi.org/10.1039/c5sm01713k.
[404] P. De Gennes, Pierre-giles De Gennes - Scaling concepts in polymer physics (1979, Cornell University Press), (1979) 324. https://www.eng.uc.edu/~beaucag/Classes/Properties/Books/Pierre-giles De Gennes - Scaling concepts in polymer physics-Cornell University Press (1979).pdf.
[405] E.M. Saffer, M.A. Lackey, D.M. Griffin, S. Kishore, G.N. Tew, S.R. Bhatia, SANS Study of Highly Resilient Poly(ethylene glycol) Hydrogels, Soft Matter. 10 (2008) 1905–1916. https://doi.org/doi:10.1039/C3SM52395K.
[406] D.H. Le, C.K. Pham, T.T.T. Nguyen, T.T. Bui, Parameter extraction and optimization using Levenberg-Marquardt algorithm, 2012 4th Int. Conf. Commun. Electron. ICCE 2012. (2012) 434–437. https://doi.org/10.1109/CCE.2012.6315945.
[407] S. Finsterle, M.B. Kowalsky, A truncated Levenberg-Marquardt algorithm for the calibration of highly parameterized nonlinear models, Comput. Geosci. 37 (2011) 731–738. https://doi.org/10.1016/j.cageo.2010.11.005.
[408] E.K. Chamberlain, M.A. Rao, C. Cohen, Shear thinning and antithixotropic behavior of a heated cross-linked waxy maize starch dispersion, Int. J. Food Prop. 2 (1999) 63–77. https://doi.org/10.1080/10942919909524590.
[409] M.J. Majcher, A. Babar, A. Lofts, A. Leung, X. Li, F. Abu-Hijleh, N.M.B. Smeets, R.K. Mishra, T. Hoare, In situ-gelling starch nanoparticle (SNP)/O-carboxymethyl chitosan (CMCh) nanoparticle network hydrogels for the intranasal delivery of an antipsychotic peptide, J. Control. Release. 330 (2020) 738–752. https://doi.org/10.1016/j.jconrel.2020.12.050.
[410] H.A. Whiteford, A.J. Ferrari, L. Degenhardt, V. Feigin, T. Vos, The global burden

of mental, neurological and substance use disorders: An analysis from the global burden of disease study 2010, PLoS One. 10 (2015) 1–14. https://doi.org/10.1371/journal.pone.0116820.

[411] W. Tong Chien, S. Fong Leung, F. Kk Yeung, W. Kit Wong, Current approaches to treatments for schizophrenia spectrum disorders, part II: psychosocial interventions and patient-focused perspectives in psychiatric care, Neuropsychiatr. Dis. Treat. 9 (2013) 1463–1481. https://doi.org/10.2147/NDT.S49263.

[412] J. McGrath, S. Saha, D. Chant, J. Welham, Schizophrenia: A concise overview of incidence, prevalence, and mortality, Epidemiol. Rev. 30 (2008) 67–76. https://doi.org/10.1093/epirev/mxn001.

[413] R. Tandon, M.D. Jibson, Efficacy of newer generation antipsychotics in the treatment of schizophrenia, Psychoneuroendocrinology. 28 (2003) 9–26. https://doi.org/10.1016/S0306-4530(02)00110-5.

[414] J.S. McIntyre, C.C. Sara Charles, V.-C.J. Daniel Anzia, I.A. Cook, M.T. Finnerty, B.R. Johnson, J.E. Nininger, P. Summergrad, S.M. Woods, J. Yager, M. Ann Barnovitz, S. Hafter Gray, S. Saxena, T. Tonnu, M.B. First, L.J. Fochtmann, Treating schizophrenia: A quick reference guide, (2004). http://psychiatryonline.org/pb/assets/raw/sitewide/practice_guidelines/guidelines/schizophrenia-guide.pdf.

[415] P. Mason, G. Harrison, C. Glazebrook, I. Medley, T. Croudace, The course of schizophrenia over 13 years: A report from the International Study on Schizophrenia (ISoS) coordinated by the World Health Organization, Br. J. Psychiatry. 169 (1996) 580–586. https://doi.org/10.1192/bjp.169.5.580.

[416] J. Karagianis, D. Novick, J. Pecenak, J.M. Haro, M. Dossenbach, T. Treuer, W. Montgomery, R. Walton, A.J. Lowry, Worldwide-Schizophrenia Outpatient Health Outcomes (W-SOHO): Baseline characteristics of pan-regional observational data from more than 17,000 patients, Int. J. Clin. Pract. 63 (2009) 1578–1588. https://doi.org/10.1111/j.1742-1241.2009.02191.x.

[417] K. Higashi, G. Medic, K.J. Littlewood, T. Diez, O. Granström, M. de Hert, Medication adherence in schizophrenia: Factors influencing adherence and consequences of nonadherence, a systematic literature review, Ther. Adv. Psychopharmacol. 3 (2013) 200–218. https://doi.org/10.1177/2045125312474019.

[418] S. Grassin-Delyle, A. Buenestado, E. Naline, C. Faisy, S. Blouquit-Laye, L.J. Couderc, M. Le Guen, M. Fischler, P. Devillier, Intranasal drug delivery: An efficient and non-invasive route for systemic administration - Focus on opioids, Pharmacol. Ther. 134 (2012) 366–379. https://doi.org/10.1016/j.pharmthera.2012.03.003.

[419] S.P. van Kessel, A.K. Frye, A.O. El-Gendy, M. Castejon, A. Keshavarzian, G. van Dijk, S. El Aidy, Gut bacterial tyrosine decarboxylases restrict levels of levodopa in the treatment of Parkinson's disease, Nat. Commun. 10 (2019) 1–11. https://doi.org/10.1038/s41467-019-08294-y.

[420] E. Samaridou, M.J. Alonso, Nose-to-brain peptide delivery – The potential of nanotechnology, Bioorganic Med. Chem. 26 (2018) 2888–2905. https://doi.org/10.1016/j.bmc.2017.11.001.

[421] M. Vajdy, D.T. O'Hagan, Microparticles for intranasal immunization, Adv. Drug Deliv. Rev. 51 (2001) 127–141. https://doi.org/10.1016/S0169-409X(01)00167-3.
[422] L.B. Rene Holm, United States Patent, US 9,610,287 B2, 2014.
[423] K. Maeda, H. Sugino, H. Akazawa, N. Amada, J. Shimada, T. Futamura, H. Yamashita, N. Ito, R.D. McQuade, A. Mørk, A.L. Pehrson, M. Hentzer, V. Nielsen, C. Bundgaard, J. Arnt, T.B. Stensbøl, T. Kikuchi, Brexpiprazole I: In vitro and in vivo characterization of a novel serotonin-dopamine activity modulator, J. Pharmacol. Exp. Ther. 350 (2014) 589–604. https://doi.org/10.1124/jpet.114.213793.
[424] K. Maeda, L. Lerdrup, H. Sugino, H. Akazawa, N. Amada, R.D. McQuade, T.B. Stensbøl, C. Bundgaard, J. Arnt, T. Kikuchi, Brexpiprazole II: Antipsychotic-like and procognitive effects of a novel serotonin-dopamine activity modulator, J. Pharmacol. Exp. Ther. 350 (2014) 605–614. https://doi.org/10.1124/jpet.114.213819.
[425] L. Rajagopal, S. Kwon, M. Huang, E. Michael, L. Bhat, M. Cantillon, H.Y. Meltzer, RP5063, an atypical antipsychotic drug with a unique pharmacologic profile, improves declarative memory and psychosis in mouse models of schizophrenia, Behav. Brain Res. 332 (2017) 180–199. https://doi.org/10.1016/j.bbr.2017.02.036.
[426] D.C. Goff, Bitopertin The Good News and Bad News The Social Brain , Stress , and Psychopathology, 71 (2014) 6–7. https://doi.org/10.1001/jamapsychiatry.2014.163.2.
[427] L.S. Köster, M. Carbon, C.U. Correll, Emerging drugs for schizophrenia: An update, Expert Opin. Emerg. Drugs. 19 (2014) 511–531. https://doi.org/10.1517/14728214.2014.958148.
[428] R.P. Daya, J. Bhandari, S.K. Kooner, J. Ho, C.D. Rowley, N.A. Bock, T. Farncombe, R.K. Mishra, The Dopamine Allosteric Agent, PAOPA, Demonstrates Therapeutic Potential in the Phencyclidine NMDA Pre-clinical Rat Model of Schizophrenia, Front. Behav. Neurosci. 12 (2018) 1–10. https://doi.org/10.3389/fnbeh.2018.00302.
[429] M.G.R. Beyaert, R.P. Daya, B.A. Dyck, R.L. Johnson, R.K. Mishra, PAOPA, a potent dopamine D2 receptor allosteric modulator, prevents and reverses behavioral and biochemical abnormalities in an amphetamine-sensitized preclinical animal model of schizophrenia, Eur. Neuropsychopharmacol. 23 (2013) 253–262. https://doi.org/10.1016/j.euroneuro.2012.04.010.
[430] D. Basu, Y. Tian, J. Bhandari, J.R. Jiang, P. Hui, R.L. Johnson, R.K. Mishra, Effects of the Dopamine D2 Allosteric Modulator, PAOPA, on the Expression of GRK2, Arrestin-3, ERK1/2, and on Receptor Internalization, PLoS One. 8 (2013) 1–11. https://doi.org/10.1371/journal.pone.0070736.
[431] B. Dyck, K. Guest, C. Sookram, D. Basu, R. Johnson, R.K. Mishra, PAOPA, a potent analogue of Pro-Leu-glycinamide and allosteric modulator of the dopamine D2 receptor, prevents NMDA receptor antagonist (MK-801)-induced deficits in social interaction in the rat: Implications for the treatment of negative symptoms in schi, Schizophr. Res. 125 (2011) 88–92.

https://doi.org/10.1016/j.schres.2010.09.025.
[432] J. Piazza, T. Hoare, L. Molinaro, K. Terpstra, J. Bhandari, P.R. Selvaganapathy, B. Gupta, R.K. Mishra, Haloperidol-loaded intranasally administered lectin functionalized poly(ethylene glycol)-block-poly(D,L)-lactic-co-glycolic acid (PEG-PLGA) nanoparticles for the treatment of schizophrenia, Eur. J. Pharm. Biopharm. 87 (2014) 30–39. https://doi.org/10.1016/j.ejpb.2014.02.007.
[433] D. Basu, Y. Tian, P. Hui, J. Bhandari, R.L. Johnson, R.K. Mishra, Change in expression of vesicular protein synapsin II by chronic treatment with D2 allosteric modulator PAOPA, Peptides. 66 (2015) 58–62. https://doi.org/10.1016/j.peptides.2015.01.004.
[434] M.L. Tan, D. Basu, J.M. Kwiecien, R.L. Johnson, R.K. Mishra, Preclinical pharmacokinetic and toxicological evaluation of MIF-1 peptidomimetic, PAOPA: Examining the pharmacology of a selective dopamine D2 receptor allosteric modulator for the treatment of schizophrenia, Peptides. 42 (2013) 89–96. https://doi.org/10.1016/j.peptides.2013.02.004.
[435] M.E. Meredith, T.S. Salameh, W.A. Banks, Intranasal Delivery of Proteins and Peptides in the Treatment of Neurodegenerative Diseases, AAPS J. 17 (2015) 780–787. https://doi.org/10.1208/s12248-015-9719-7.
[436] M. Agrawal, S. Saraf, S. Saraf, S.G. Antimisiaris, M.B. Chougule, S.A. Shoyele, A. Alexander, Nose-to-brain drug delivery: An update on clinical challenges and progress towards approval of anti-Alzheimer drugs, J. Control. Release. 281 (2018) 139–177. https://doi.org/10.1016/j.jconrel.2018.05.011.
[437] M.S.A. Tan, H.S. Parekh, P. Pandey, D.J. Siskind, J.R. Falconer, Nose-to-brain delivery of antipsychotics using nanotechnology: a review, Expert Opin. Drug Deliv. 17 (2020) 839–853. https://doi.org/10.1080/17425247.2020.1762563.
[438] J.J. Lochhead, R.G. Thorne, Intranasal delivery of biologics to the central nervous system., Adv. Drug Deliv. Rev. 64 (2012) 614–28. https://doi.org/10.1016/j.addr.2011.11.002.
[439] F. Chengcheng, S. Xiayan, Z. Chi, L. Qingfeng, C. Jie, S. Yehong, Z. Qizhi, J. Xinguo, Effect of absorption enhancers on nasal delivery of basic fibroblast growth factor, African J. Pharm. Pharmacol. 5 (2011) 1070–1079. https://doi.org/10.5897/AJPP11.157.
[440] N. Kamei, T. Shingaki, Y. Kanayama, M. Tanaka, R. Zochi, K. Hasegawa, Y. Watanabe, M. Takeda-Morishita, Visualization and Quantitative Assessment of the Brain Distribution of Insulin through Nose-to-Brain Delivery Based on the Cell-Penetrating Peptide Noncovalent Strategy, Mol. Pharm. 13 (2016) 1004–1011. https://doi.org/10.1021/acs.molpharmaceut.5b00854.
[441] D. Yang, Y.Y. Sun, X. Lin, J.M. Baumann, R.S. Dunn, D.M. Lindquist, C.Y. Kuan, Intranasal delivery of cell-penetrating anti-NF-κB peptides (Tat-NBD) alleviates infection-sensitized hypoxic-ischemic brain injury, Exp. Neurol. 247 (2013) 447–455. https://doi.org/10.1016/j.expneurol.2013.01.015.
[442] N. Nonaka, S.A. Farr, T. Nakamachi, J.E. Morley, M. Nakamura, S. Shioda, W.A. Banks, Intranasal administration of PACAP: Uptake by brain and regional brain targeting with cyclodextrins, Peptides. 36 (2012) 168–175.

https://doi.org/10.1016/j.peptides.2012.05.021.
[443] S.T. Charlton, S.S. Davis, L. Illum, Evaluation of bioadhesive polymers as delivery systems for nose to brain delivery: In vitro characterisation studies, J. Control. Release. 118 (2007) 225–234. https://doi.org/10.1016/j.jconrel.2006.12.014.
[444] V.K. Mourya, N.N. Inamdar, A. Tiwari, Carboxymethyl chitosan and its applications, Adv. Mater. Lett. 1 (2010) 11–33. https://doi.org/10.5185/amlett.2010.3108.
[445] A. Kumar, R.K. Khar, F.J. Ahmed, P. V Diwan, Effective insulin delivery using starch nanoparticles as a potential trans-nasal mucoadhesive carrier, 69 (2008) 426–435. https://doi.org/10.1016/j.ejpb.2007.12.001.
[446] S. Mao, J. Chen, Z. Wei, H. Liu, D. Bi, Intranasal administration of melatonin starch microspheres, 272 (2004) 37–43. https://doi.org/10.1016/j.ijpharm.2003.11.028.
[447] L. Qi, G. Ji, Z. Luo, Z. Xiao, Q. Yang, Characterization and Drug Delivery Properties of OSA Starch-Based Nanoparticles Prepared in [C3OHmim]Ac-in-Oil Microemulsions System, ACS Sustain. Chem. Eng. 5 (2017) 9517–9526. https://doi.org/10.1021/acssuschemeng.7b02727.
[448] P. Watts, L. Illum, Drug Delivery Composition for the Nasal Administration of Antiviral Agents, US 2001/0053359 A1, 2001.
[449] A. Momeni, M.H. Mohammadi, Respiratory delivery of theophylline by size-targeted starch microspheres for treatment of asthma, J. Microencapsul. 26 (2009) 701–710. https://doi.org/10.3109/02652040802685043.
[450] S. Barua, S. Mitragotri, Challenges associated with Penetration of Nanoparticles across Cell and Tissue Barriers: A Review of Current Status and Future Prospects, Nano Today. 9 (2014) 223–243. https://doi.org/10.1038/jid.2014.371.
[451] T.M.M. Ways, W.M. Lau, V. V. Khutoryanskiy, Chitosan and its derivatives for application in mucoadhesive drug delivery systems, Polymers (Basel). 10 (2018). https://doi.org/10.3390/polym10030267.
[452] J. Maia, R.A. Carvalho, J.F.J. Coelho, P.N. Simões, M.H. Gil, Insight on the periodate oxidation of dextran and its structural vicissitudes, Polymer (Guildf). 52 (2011) 258–265. https://doi.org/10.1016/j.polymer.2010.11.058.
[453] K.C. Lee, S.Y. Lee, Preparation of highly cross-linked, monodisperse poly(methyl methacrylate) microspheres by dispersion polymerization; Part II. Semi-continuous processes, Macromol. Res. 16 (2008) 293–302. https://doi.org/10.1007/BF03218520.
[454] S. Gizurarson, Anatomical and Histological Factors Affecting Intranasal Drug and Vaccine Delivery, Curr. Drug Deliv. 9 (2012) 566–582. https://doi.org/10.2174/156720112803529828.
[455] G.K. Reznik, Comparative anatomy, physiology, and function of the upper respiratory tract, Environ. Health Perspect. 85 (1990) 171–176. https://doi.org/10.2307/3430681.
[456] Y. Liu, M.R. Johnson, E.A. Matida, S. Kherani, J. Marsan, Creation of a standardized geometry of the human nasal cavity, J. Appl. Physiol. 106 (2009) 784–795. https://doi.org/10.1152/japplphysiol.90376.2008.

[457] B.K. Lipska, J.A. Gogos, Animal Models of Schizophrenia, Schizophr. Third Ed. (2011) 462–481. https://doi.org/10.1002/9781444327298.ch22.
[458] M.A. Geyer Moghaddam, Bita, Animal models relevant to schizophrenia, Neuropsychopharmacol. Fifth Gener. Prog. (2002) 689–702.
[459] S.E. File, The use of social interaction as a method for detecting anxiolytic activity of chlordiazepoxide-like drugs, J. Neurosci. Methods. 2 (1980) 219–238. https://doi.org/10.1016/0165-0270(80)90012-6.
[460] F. Sams-Dodd, Effects of continuous D-amphetamine and phencyclidine administration on social behaviour, stereotyped behaviour, and locomotor activity in rats, Neuropsychopharmacology. 19 (1998) 18–25. https://doi.org/10.1016/S0893-133X(97)00200-5.
[461] J.R. Harkema, S.A. Carey, J.G. Wagner, The Nose Revisited: A Brief Review of the Comparative Structure, Function, and Toxicologic Pathology of the Nasal Epithelium, Toxicol. Pathol. 34 (2006) 252–269. https://doi.org/10.1080/01926230600713475.
[462] M.A. Kaliner, Human nasal host defense and sinusitis, J. Allergy Clin. Immunol. 90 (1992) 424–430. https://doi.org/10.1016/0091-6749(92)90162-U.
[463] Y. Majima, T. Harada, T. Shimizu, K. Takeuchi, Y. Sakakura, S. Yasuoka, S. Yoshinaga, Effect of biochemical components on rheologic properties of nasal mucus in chronic sinusitis, Am. J. Respir. Crit. Care Med. 160 (1999) 421–426. https://doi.org/10.1164/ajrccm.160.2.9805117.
[464] J.P. Rung, A. Carlsson, K.R. Markinhuhta, M.L. Carlsson, (+)-MK-801 induced social withdrawal in rats; A model for negative symptoms of schizophrenia, Prog. Neuro-Psychopharmacology Biol. Psychiatry. 29 (2005) 827–832. https://doi.org/10.1016/j.pnpbp.2005.03.004.
[465] J.C. Neill, S. Barnes, S. Cook, B. Grayson, N.F. Idris, S.L. McLean, S. Snigdha, L. Rajagopal, M.K. Harte, Animal models of cognitive dysfunction and negative symptoms of schizophrenia: Focus on NMDA receptor antagonism, Pharmacol. Ther. 128 (2010) 419–432. https://doi.org/10.1016/j.pharmthera.2010.07.004.
[466] F. Sams-Dodd, (+) MK-801 and phencyclidine induced neurotoxicity do not cause enduring behaviours resembling the positive and negative symptoms of schizophrenia in the rat, Basic Clin. Pharmacol. Toxicol. 95 (2004) 241–246. https://doi.org/10.1111/j.1742-7843.2004.pto950507.x.
[467] C.M. Powell, T. Miyakawa, Schizophrenia-Relevant Behavioral Testing in Rodent Models: A Uniquely Human Disorder?, Biol. Psychiatry. 59 (2006) 1198–1207. https://doi.org/doi:10.1016/j.biopsych.2006.05.008.
[468] H. Yasar, D.K. Ho, C. De Rossi, J. Herrmann, S. Gordon, B. Loretz, C.M. Lehr, Starch-chitosan polyplexes: A versatile carrier system for anti-infectives and gene delivery, Polymers (Basel). 10 (2018) 1–21. https://doi.org/10.3390/polym10030252.
[469] N.L. Vanier, S.L.M. El Halal, A.R.G. Dias, E. da Rosa Zavareze, Molecular structure, functionality and applications of oxidized starches: A review, Food Chem. 221 (2017) 1546–1559. https://doi.org/10.1016/j.foodchem.2016.10.138.
[470] M. Nasrollahzadeh, N. Shafiei, Z. Nezafat, N.S. Soheili Bidgoli, F. Soleimani,

Recent progresses in the application of cellulose, starch, alginate, gum, pectin, chitin and chitosan based (nano)catalysts in sustainable and selective oxidation reactions: A review, Carbohydr. Polym. 241 (2020) 116353. https://doi.org/10.1016/j.carbpol.2020.116353.

[471] B. Singh, D.K. Sharma, A. Gupta, A study towards release dynamics of thiram fungicide from starch-alginate beads to control environmental and health hazards, J. Hazard. Mater. 161 (2009) 208–216. https://doi.org/10.1016/j.jhazmat.2008.03.074.

[472] J.J. Perez, N.J. Francois, Chitosan-starch beads prepared by ionotropic gelation as potential matrices for controlled release of fertilizers, Carbohydr. Polym. 148 (2016) 134–142. https://doi.org/10.1016/j.carbpol.2016.04.054.

[473] K. Zhong, Z.T. Lin, X.L. Zheng, G.B. Jiang, Y.S. Fang, X.Y. Mao, Z.W. Liao, Starch derivative-based superabsorbent with integration of water-retaining and controlled-release fertilizers, Carbohydr. Polym. 92 (2013) 1367–1376. https://doi.org/10.1016/j.carbpol.2012.10.030.

[474] P.C. Parvathy, A.N. Jyothi, K.S. John, J. Sreekumar, Cassava Starch Based Superabsorbent Polymer as Soil Conditioner: Impact on Soil Physico-Chemical and Biological Properties and Plant Growth, Clean - Soil, Air, Water. 42 (2014) 1610–1617. https://doi.org/10.1002/clen.201300143.

[475] N.C. Dafader, H.Z. Sonia, S.M.N. Alam, Synthesis of a Superwater Absorbent and Studies of its Properties, Nucl. Sci. Appl. 2 (2014) 15–19.

[476] F. Nnadi, C. Brave, Environmentally friendly superabsorbent polymers for water conservation in agricultural lands, J. Soil Environ. Manag. 2 (2011) 206–211.

[477] J. Woodhouse, M.S. Johnson, Effect of superabsorbent polymers on survival and growth of crop seedlings, Agric. Water Manag. 20 (1991) 63–70. https://doi.org/10.1016/0378-3774(91)90035-H.

[478] R. Rajakumar, J. Sankar, Hydrogel : Novel Soil Conditioner and Safer Delivery Vehicle for Fertilizers and Agrochemicals – A Review, (2016) 163–172.

[479] W. Abobatta, Impact of hydrogel polymer in agricultural sector, Adv. Agric. Environ. Sci. Open Access. 1 (2018) 59–64. https://doi.org/10.30881/aaeoa.00011.

[480] T. Eichert, A. Kurtz, U. Steiner, H.E. Goldbach, Size exclusion limits and lateral heterogeneity of the stomatal foliar uptake pathway for aqueous solutes and water-suspended nanoparticles, Physiol. Plant. 134 (2008) 151–160. https://doi.org/10.1111/j.1399-3054.2008.01135.x.

[481] F. Schwab, G. Zhai, M. Kern, A. Turner, J.L. Schnoor, M.R. Wiesner, Barriers, pathways and processes for uptake, translocation and accumulation of nanomaterials in plants - Critical review, Nanotoxicology. 10 (2016) 257–278. https://doi.org/10.3109/17435390.2015.1048326.

[482] R.C. Kirkwood, Recent developments in our understanding of the plant cuticle as a barrier to the foliar uptake of pesticides, Pestic. Sci. 55 (1999) 69–77. https://doi.org/10.1002/(SICI)1096-9063(199901)55:1<69::AID-PS860>3.0.CO;2-H.

[483] P. Zhao, T. Zhu, B. Liang, M. Hu, L. Kang, J. Gong, Characteristics of mass distributions of aerosol particle and its inorganic water-soluble ions in summer

over a suburb farmland in Beijing, Front. Environ. Sci. Eng. China. 1 (2007) 159–165. https://doi.org/10.1007/s11783-007-0028-y.
[484] T.M. Nordgren, C. Charavaryamath, Agriculture Occupational Exposures and Factors Affecting Health Effects, Curr. Allergy Asthma Rep. 18 (2018). https://doi.org/10.1007/s11882-018-0820-8.
[485] W. Lopes Soares, M. Firpo de Souza Porto, Estimating the social cost of pesticide use: An assessment from acute poisoning in Brazil, Ecol. Econ. 68 (2009) 2721–2728. https://doi.org/10.1016/j.ecolecon.2009.05.008.
[486] P. Vega-Vásquez, N.S. Mosier, J. Irudayaraj, Nanoscale Drug Delivery Systems: From Medicine to Agriculture, Front. Bioeng. Biotechnol. 8 (2020) 1–16. https://doi.org/10.3389/fbioe.2020.00079.
[487] L. Zhang, H. Chen, J. Xie, M. Becton, X. Wang, Interplay of Nanoparticle Rigidity and Its Translocation Ability through Cell Membrane, J. Phys. Chem. B. 123 (2019) 8923–8930. https://doi.org/10.1021/acs.jpcb.9b07452.
[488] H.M. Ding, Y.Q. Ma, Theoretical and computational investigations of nanoparticle-biomembrane interactions in cellular delivery, Small. 11 (2015) 1055–1071. https://doi.org/10.1002/smll.201401943.
[489] G. Chichiriccò, A. Poma, Penetration and toxicity of nanomaterials in higher plants, Nanomaterials. 5 (2015) 851–873. https://doi.org/10.3390/nano5020851.
[490] P. Wang, E. Lombi, F.J. Zhao, P.M. Kopittke, Nanotechnology: A New Opportunity in Plant Sciences, Trends Plant Sci. 21 (2016) 699–712. https://doi.org/10.1016/j.tplants.2016.04.005.
[491] P. Hu, J. An, M.M. Faulkner, H. Wu, Z. Li, X. Tian, J.P. Giraldo, Nanoparticle Charge and Size Control Foliar Delivery Efficiency to Plant Cells and Organelles, ACS Nano. 14 (2020) 7970–7986. https://doi.org/10.1021/acsnano.9b09178.
[492] J. Lin, A. Alexander-Katz, Cell membranes open "doors" for cationic nanoparticles/ biomolecules: Insights into uptake kinetics, ACS Nano. 7 (2013) 10799–10808. https://doi.org/10.1021/nn4040553.
[493] P. Zhang, Y. Ma, C. Xie, Z. Guo, X. He, E. Valsami-Jones, I. Lynch, W. Luo, L. Zheng, Z. Zhang, Plant species-dependent transformation and translocation of ceria nanoparticles, Environ. Sci. Nano. 6 (2019) 60–67. https://doi.org/10.1039/C8EN01089G.
[494] A.H. Moghimi, J. Hamdan, J. Shamshuddin, A.W. Samsuri, A. Abtahi, Physicochemical properties and surface charge characteristics of arid soils in southeastern Iran, Appl. Environ. Soil Sci. 2013 (2013). https://doi.org/10.1155/2013/252861.
[495] N.S. Bolan, R. Naidu, J.K. Syers, R.W. Tillman, Surface Charge and Solute Interactions in Soils, Adv. Agron. 67 (1999) 87–140.
[496] E. Spielman-Sun, A. Avellan, G.D. Bland, R. V. Tappero, A.S. Acerbo, J.M. Unrine, J.P. Giraldo, G. V. Lowry, Nanoparticle surface charge influences translocation and leaf distribution in vascular plants with contrasting anatomy, Environ. Sci. Nano. 6 (2019) 2508–2519. https://doi.org/10.1039/c9en00626e.
[497] Z.J. Zhu, H. Wang, B. Yan, H. Zheng, Y. Jiang, O.R. Miranda, V.M. Rotello, B. Xing, R.W. Vachet, Effect of surface charge on the uptake and distribution of gold

nanoparticles in four plant species, Environ. Sci. Technol. 46 (2012) 12391–12398. https://doi.org/10.1021/es301977w.
[498] H. Chen, Metal based nanoparticles in agricultural system: Behavior, transport, and interaction with plants, Chem. Speciat. Bioavailab. 30 (2018) 123–134. https://doi.org/10.1080/09542299.2018.1520050.
[499] D. Šubarić, Đ. Ačkar, J. Babić, N. Sakač, A. Jozinović, Modification of wheat starch with succinic acid/acetic anhydride and azelaic acid/acetic anhydride mixtures I. Thermophysical and pasting properties, J. Food Sci. Technol. 51 (2014) 2616–2623. https://doi.org/10.1007/s13197-012-0790-0.
[500] S. Jiang, L. Dai, Y. Qin, L. Xiong, Q. Sun, Preparation and Characterization of Octenyl Succinic Anhydride Modified Taro Starch Nanoparticles, (2016) 1–11. https://doi.org/10.1371/journal.pone.0150043.
[501] M.C. Sweedman, M.J. Tizzotti, C. Schäfer, R.G. Gilbert, Structure and physicochemical properties of octenyl succinic anhydride modified starches: A review, Carbohydr. Polym. 92 (2013) 905–920. https://doi.org/10.1016/j.carbpol.2012.09.040.
[502] L. Altuna, M.L. Herrera, M.L. Foresti, Synthesis and characterization of octenyl succinic anhydride modified starches for food applications. A review of recent literature, Food Hydrocoll. 80 (2018) 97–110. https://doi.org/10.1016/j.foodhyd.2018.01.032.
[503] Q. Zhang, D. Kim, L. Li, S. Patel, J. Duhamel, Surfactant Structure-Dependent Interactions with Modified Starch Nanoparticles Probed by Fluorescence Spectroscopy, Langmuir. 35 (2019) 3432–3444. https://doi.org/10.1021/acs.langmuir.8b03794.
[504] L. Li, D. Kim, X. Zhai, J. Duhamel, A Pyrene Excimer Fluorescence (PEF) Study of the Interior of Amylopectin in Dilute Solution, Macromolecules. 53 (2020) 6850–6860. https://doi.org/10.1021/acs.macromol.0c01280.
[505] D. Kim, R. Amos, M. Gauthier, J. Duhamel, Applications of Pyrene Fluorescence to the Characterization of Hydrophobically Modified Starch Nanoparticles, Langmuir. 34 (2018) 8611–8621. https://doi.org/10.1021/acs.langmuir.8b01591.
[506] Z. Xu, D. Yang, T. Long, L. Yuan, S. Qiu, D. Li, C. Mu, L. Ge, pH-Sensitive nanoparticles based on amphiphilic imidazole/cholesterol modified hydroxyethyl starch for tumor chemotherapy, Carbohydr. Polym. 277 (2021). https://doi.org/10.1016/j.carbpol.2021.118827.
[507] P. Calza, D. Vione, C. Minero, The role of humic and fulvic acids in the phototransformation of phenolic compounds in seawater, Sci. Total Environ. 493 (2014) 411–418. https://doi.org/10.1016/j.scitotenv.2014.05.145.
[508] L.P. Canellas, F.L. Olivares, N.O. Aguiar, D.L. Jones, A. Nebbioso, P. Mazzei, A. Piccolo, Humic and fulvic acids as biostimulants in horticulture, Sci. Hortic. (Amsterdam). 196 (2015) 15–27. https://doi.org/10.1016/j.scienta.2015.09.013.
[509] E. Evgenidou, K. Fytianos, Photodegradation of triazine herbicides in aqueous solutions and natural waters, J. Agric. Food Chem. 50 (2002) 6423–6427. https://doi.org/10.1021/jf0202887.
[510] M. Mansour, E.A. Feicht, A. Behechti, K.W. Schramm, A. Kettrup, Determination

of Photostability of Selected Agrochemicals in Water and Soil, Chemosphere. 39 (1999) 575–585.
[511] F. Orgaz, M.D. Fernández, S. Bonachela, M. Gallardo, E. Fereres, Evapotranspiration of horticultural crops in an unheated plastic greenhouse, Agric. Water Manag. 72 (2005) 81–96. https://doi.org/10.1016/j.agwat.2004.09.010.
[512] D. Yavuz, N. Yavuz, M. Seymen, Ö. Türkmen, Evapotranspiration, crop coefficient and seed yield of drip irrigated pumpkin under semi-arid conditions, Sci. Hortic. (Amsterdam). 197 (2015) 33–40. https://doi.org/10.1016/j.scienta.2015.11.010.
[513] A. Javanshah, A. Saidi, Determination of Humic Acid by Spectrophotometric Analysis in the Soils, Int. J. Adv. Biotechnol. Res. 7 (2016) 19–23. http://www.bipublication.com.
[514] Q. Duan, Y. Lin, W. Jiang, D. Huang, Stomatal development and associated photosynthetic characteristics of watermelon (Citrullus lanatus) plug seedlings during light storage, HortScience. 49 (2014) 881–885. https://doi.org/10.21273/hortsci.49.7.881.
[515] H. Zhu, J. Han, J.Q. Xiao, Y. Jin, Uptake, translocation, and accumulation of manufactured iron oxide nanoparticles by pumpkin plants, J. Environ. Monit. 10 (2008) 713–717. https://doi.org/10.1039/b805998e.
[516] F.R. Kulcheski, R. Córrea, I.A. Gomes, J.C. De Lima, R. Margis, NPK macronutrients and microRNA homeostasis, Front. Plant Sci. 6 (2015) 1–19. https://doi.org/10.3389/fpls.2015.00451.
[517] Z.H. Shah, H.M. Rehman, T. Akhtar, H. Alsamadany, B.T. Hamooh, T. Mujtaba, I. Daur, Y. Al Zahrani, H.A.S. Alzahrani, S. Ali, S.H. Yang, G. Chung, Humic substances: Determining potential molecular regulatory processes in plants, Front. Plant Sci. 9 (2018) 1–12. https://doi.org/10.3389/fpls.2018.00263.
[518] T. Zeppenfeld, N. Balkenhol, K. Kóvacs, A. Carminati, Rhizosphere hydrophobicity: A positive trait in the competition for water, PLoS One. 12 (2017) 1–18. https://doi.org/10.1371/journal.pone.0182188.
[519] L.F. Wang, Z.D. Dai, Effects of the natural microstructures on the wettability of leaf surfaces, Biosurface and Biotribology. 2 (2016) 70–74. https://doi.org/10.1016/j.bsbt.2016.06.001.
[520] S.J. Singer, G.L. Nicolson, The Fluid Mosaic Model of the Structure of Cell Membranes, Science (80-.). 175 (1972) 720–731. https://doi.org/10.1126/science.175.4023.720.